Transactions of the ASME

Journal of Fluids Engineering

Published Quarterly by The American Society of Mechanical Engineers

VOLUME 108 • NUMBER 3 • SEPTEMBER 1986

FLUIDS ENGINEERING DIVISION
Technical Editor
FRANK M. WHITE (1989)
Executive Secretary
L. T. NELSON (1989)
Calendar Editor
M. F. ACKERSON

Associate Editors
Fluid Machinery
WIDEN TABAKOFF (1988)
RICHARD F. SALANT (1987)
Fluid Measurements
ALEXANDER DYBBS (1987)
Fluid Mechanics
J. A. MILLER (1987)
HUGH W. COLEMAN (1987)
STANLEY F. BIRCH (1988)
WILLIAM W. DURGIN (1986)
Fluid Transients
FREDERICK J. MOODY (1986)
Numerical Methods
PATRICK J. ROACHE (1988)
Multiphase Flow
M. C. ROCO (1988)
GEORGES L. CHAHINE (1986)
Review Articles
K. N. GHIA (1986)

BOARD ON COMMUNICATIONS
Chairman and Vice President
K. N. REID, Jr.

Members-at-Large
W. BEGELL
J. T. COKONIS
W. G. GOTTENBERG
M. KUTZ
J. R. LLOYD
T. C. MIN
R. E. NICKELL
C. F. PHILLIPS
R. E. REDER
F. W. SCHMIDT

President, **N. D. FITZROY**
Executive Director
PAUL ALLMENDINGER
Treasurer,
ROBERT A. BENNETT

PUBLISHING STAFF
Mng. Dir. Publ., **J. J. FREY**
Dep. Mng. Dir. Publ.,
JOS. SANSONE
Managing Editor,
CORNELIA MONAHAN
Editorial Production Assistant,
MARISOL ANDINO

Technical Briefs

Announcements and Special Notices

The Journal of Fluids Engineering (ISSN 0098-2202) is published quarterly for $100 per year by The American Society of Mechanical Engineers, 345 East 47th Street, New York, NY 10017. Second class postage paid at New York, NY and additional mailing offices. POSTMASTER: Send address changes to The Journal of Fluids Engineering, c/o THE AMERICAN SOCIETY OF MECHANICAL ENGINEERS, 22 Law Drive, Box 2300, Fairfield, NJ 07007-2300.

CHANGES OF ADDRESS must be received at Society headquarters seven weeks before they are to be effective. Please send old label and new address.

PRICES: To members, $24.00, annually; to nonmembers, $100. Add $6.00 for postage to countries outside the United States and Canada.

STATEMENT from By-Laws. The Society shall not be responsible for statements or opinions advanced in papers or . . . printed in its publications (B7.1, Par. 3).

COPYRIGHT © 1986 by The American Society of Mechanical Engineers. Reprints from this publication may be made on condition that full credit be given the TRANSACTIONS OF THE ASME, JOURNAL OF FLUIDS ENGINEERING and the author, and date of publication be stated.

INDEXED by Engineering Information

Downloaded 03 Jun 2010 to 171.66.16.159. Redistribution subject to ASME license or copyright; see http://www.asme.org/terms/Terms_Use.cfm

A Review of Holography Applications in Multiphase Flow Visualization Study

Y. J. Lee
Kaiser Engineers, Inc.,
Oakland, CA 94623

J. H. Kim
Electric Power Research Institute,
Palo Alto, CA 94303

Holographic techniques are used in many fields of science and engineering including flow observation. The purpose of this paper is to review applications of holography to multiphase flow study with emphasis on gas-solid and gas-liquid two-phase flows. The application of holography to multiphase flow has been actively explored in the areas of particle sizing in particulate flows and nuclei population measurements in cavitation study. It is also recognized that holography holds great potential as a means of visualizing dynamic situations inherent in multiphase flows. This potential has been demonstrated by holographic flow visualization studies of coal combustion processes in gas-solid flows, gas-liquid two-phase critical flow measurements, and flashing flows in a nozzle. More effective and refined holographic techniques as well as efficient image processing methods are very much in need to facilitate and enhance the understanding of complex physical phenomena occurring in multiphase flows.

Introduction

Holography, which was a mere scientific curiosity when first discovered, has now become a practical means of recording image. Because of its vast potential for practical applications, holography has also earned its place even in popular magazines. The science and art of holography truly has come a long way since Gabor first conceptualized it in 1947 to improve the electron microscope (Gabor, 1948, 1949, and 1971).

Holography did not gain immediate popularity until the laser, with its great temporal and spatial coherence of light, became generally available. Leith and Upatnieks (1964) introduced the use of the laser in holography, and subsequent advances by many scientists led to a burgeoning development in holography. As a result, applications of holographic techniques now can be found in many areas of art, science, and engineering. Some of the applications in science and engineering include stress analysis (Fourney, 1968 and Holloway, 1971), nondestructive testing (Erf, 1974; Doty and Hildebrand, 1982), combustion study (Trolinger and Heap, 1979; Craig et al., 1984), heat and mass transfer study (Mayinger and Panknin, 1974), aerodynamics study (Trolinger, 1982), and marine biology studies (Knox, 1966; Knox and Brooks, 1969; Beers, et al., 1973; Stewart et al., 1973; Heflinger et al., 1978), to name just a few areas.

Holography records an image of an object by using the entire content of the light, i.e., the intensity, wavelength and phase, reflected or transmitted by the object, thus capturing the entire message of the scene in all its visual properties, including the vivid realism of three dimensions. Holograms can store a vast amount of information that cannot be stored by using conventional imagery. Thus holography will be particularly suited for visualizing multiphase flow systems that contain myriads of "objects" such as bubbles, droplets, or particles. The fine resolution of holography also allows direct observation of microbubbles or microparticulates in a flowing system.

A conventional optical system (photograph) can resolve an element R (such as a particle of radius R) if the element lies within a distance $R^2/2\lambda$ of a single focused plane, where λ is the wavelength of the incident light. When the element lies more than $R^2/2\lambda$ from the plane, it is out of focus and the system can no longer resolve the element R. This places severe limitations on the capability of all conventional image recording and analyzing techniques when the situation is dynamic such as in fluid flow. In contrast, a hologram will resolve an element R if the element lies within about RD/λ of the hologram, where D is the effective hologram diameter. The ratio of the two sample volumes is RD/λ to $R^2/2\lambda$ which is $2D/R$. This ratio places the capacity of holograms for recording volumetric data many orders of magnitude above photographs. This ratio is essentially the number of photographs that would be needed to capture the same amount of information contained in one hologram (Trolinger, 1980). The ratio can be of the order of 10,000 (Deason and Fincke, 1981). Thus, when an extended volume contains a large number of small elements of interest such as bubbles or droplets in multiphase flow, holography can be immensely powerful because it can record high resolution optical information over a large volume in a short time. By storing the entire information in a hologram, one can reduce data later at one's convenience. The image can be photographed or videotaped, examined by microscope, analyzed by other optical methods, or simply observed by the naked eye.

Contributed by the Fluids Engineering Division and presented at the ASME/ASCE Mechanics Conference, Albuquerque, NM, June 24–26, 1985 of THE AMERICAN SOCIETY OF MECHANICAL ENGINEERS. Manuscript received by the Fluids Engineering Division, March 21, 1985.

In multiphase flow study, the first successful application of holographic technique was achieved in the recording and imaging of particle fields (Thompson and Ward, 1966; Thompson et al., 1966). Soon after, other investigators applied holography to particle field diagnosis (Trolinger et al., 1969; Belz and Dougherty, 1972; Trolinger, 1980; Trolinger and Field, 1980), to visualization study of cavitation nuclei (Feldberg and Shlemenson, 1973; Peterson et al., 1975; van der Meulen, 1976; Gates and Bacon, 1978; Billet and Gates, 1981, Katz and Acosta, 1982; Katz and O'Hern, 1983; Katz et al., 1984), and to the study of gas-liquid flows (Lee, 1973; Lee et al., 1974; Deason and Fincke, 1981; Deason, 1982). Other techniques, such as the light-scattering method for particle sizing, suffer from the difficulty of differentiating between different objects such as particulates from bubbles, whereas holography makes direct observation possible. Diffraction methods are only effective if the particle size range is very narrow and if the particles are spherical; other particle shapes are difficult to handle, especially if their orientations are random.

Holography provides a powerful tool for helping to visualize the basic physical processes of many complex phenomena encountered in multiphase flows. Holography is the only known method by which high resolution images of individual particles in a dynamic field can be produced. In studying multiphase flows, information on the entire flow field is often necessary, e.g., spatial and instantaneous distribution of bubbles, droplets, or particles. Holography can provide such information by capturing the whole flow field and freezing the image in time.

The purpose of this article is to review the state of the art of the applications of holographic techniques to multiphase flow study and to discuss and recommend areas for further research.

Description of Holographic Techniques

The term "hologram" was first applied by Gabor (1948) to a film that records the interference pattern formed by the interaction between a coherent reference light and the diffracted or reflected light from an object. When the hologram is illuminated by the reference beam, it acts as a special type of diffraction grating and changes the reference beam into several components, one of which is nearly identical to the original object beam in information content. This, in turn, forms the three-dimensional image of the object. Detailed analytical descriptions of holographic recording and reconstruction processes can be found in several monograms published on holography (DeVelis and Reynolds, 1967; Caulfield and Lu, 1970, Collier et al., 1971). In this section of the paper, the typical optical arrangement for recording and reconstructing the image that can be directly applicable to multiphase flow study will be discussed briefly.

Holographic recording process can be divided into two categories depending on whether reflected or diffracted light from the object is used as the information beam. The holography formed by the diffracted light as the information beam can be further divided into in-line or off-axis holography depending on the selection of the reference beam.

Figure 1 shows a schematic diagram of the optical arrangement for recording a hologram by using the reflected light as the reference beam. As shown, the laser beam is split into two parts, and each part passes through the spatial filter to make a spatially coherent beam. Both beams pass through a number of lenses in order to be expanded and collimated to a desirable size. One beam is directed to the object, and the reflected light from it reaches the film plate; the other travels directly to the film plate. The intensities of both the reflected and the reference beams at the film plate are desired to match in order to make a good quality hologram.

A schematic diagram of recording a hologram using the in-line technique is shown in Fig. 2(*a*). An in-line hologram is made by passing a coherent light through a volume of object and recording the resulting wave front. When the light passes through the object, part of it is diffracted by the object, and the remainder is unscattered. The unscattered light acts as a reference light and interferes with the scattered light. This interference pattern is recorded on a photographic medium and reconstructed for later viewing.

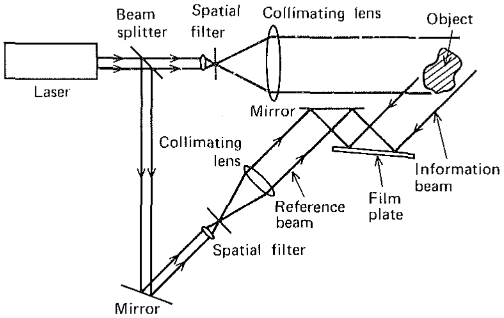

Fig. 1 Schematic diagram of holographic recording using reflected light as information beam

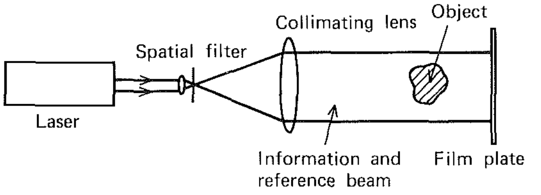

(a) In-Line Recording

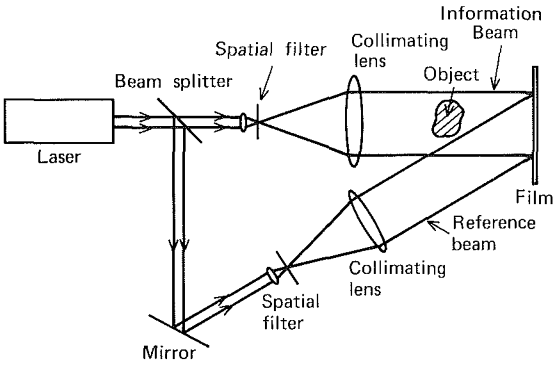

(b) Off-Axis Recording

Fig. 2 Schematic diagram of holographic recording using diffracted light as information beam

An off-axis hologram, as shown in Fig. 2(*b*), is formed by introducing the reference beam separated from the light passing through the object, a process somewhat similar to recording from the reflected information beam as illustrated in Fig. 1. In the arrangement shown in Fig. 2(*b*), the reference beam can even be introduced to the back side of the film plate in order to increase the aperture of the system (Lee et al., 1974). In-line holography is the simplest type of holography and should be explored first when the holographic technique is applied to a new field. However, there are many cases in which an off-axis arrangement is desirable. For example, the off-axis method is superior when the object is crowded with a large number of particles or has a large total cross-sectional area, or when the object field modulates the phase of the light significantly. To produce a good in-line hologram for such cases, a significant amount of light (about 80 percent) must pass through the field without modulation to serve as an effective reference beam (Trolinger, 1975); this percentage may not always be attainable.

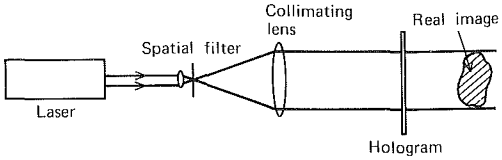

Fig. 3 Reconstruction of a hologram

A typical image reconstruction system is shown in Fig. 3. The location of the reconstructed image depends on the recording technique. Figure 3 shows the location of the reconstructed image recorded by an in-line technique. The dimension of the reconstructed image can be magnified or contracted by various reconstruction arrangements, such as utilizing a different source of light or varying the distance between the light source and the film plate. The relationship governing the location and magnification of the constructed image of in-line holography with or without a lens has been thoroughly discussed by Fourney et al. (1969).

As previously mentioned, holographic recording and reconstruction requires a coherent light source. At present, the laser is the only source that can provide temporally and spatially coherent light. In general, there are two types of laser: gas and solid. The gas laser produces a continuous light, and the solid laser generates a strong short-pulse light. Because the optical components of the holographic apparatus, as well as the object, must not move more than 1/8 of a wavelength during the recording of a hologram, the laser source must provide a short-pulsed, high-powered light if a dynamic field is to be recorded. A Q-switched solid laser producing a pulse with a duration of 20–50 ns can be used for such purposes. Also, such pulses can be repeated within microsec to achieve a desirable time interval for recording the object in motion. Koechner (1979) has presented a review on the application of a pulsed laser to holographic recording. The hologram is reconstructed by a continuous gas laser to provide a stable image.

Photographic plates are commonly used as the holographic recording medium. However, the nature of the holographic process and the development of high-powered coherent light sources have enabled other materials besides photographic emulsions to be used. As a result, photoresist, electro-optical crystals and other materials have been tried as holographic recording materials. An extensive review on holographic recording materials has been presented by Kurtz and Owen (1975).

Applications to Fluid-Particle System

Solid particles present many engineering problems: fluidized bed combustion, particle motions in rocket exhaust, electrostatic precipitation of dust, ignition of gun powder, and aerosol transport, to name a few examples. These problems involve a wide variety of particle shapes and a broad range of sizes. In the biological sciences, researchers also need to investigate the behavior and movement of microplanktons in marine environment, swimming motion of organisms, and blood cells, all of which are similar to a fluid-particle system. In understanding these systems, the information of primary importance is particle size and particle velocity distributions. For instance, in fluidized bed studies, information on drift flux, flow regime, local bed quantities, and effect of particle size is very important in model development (Staub et al., 1980). The existing information in this area clearly indicates the need for first identifying the nature of the two-phase flow regime and then developing models based on the observed flow behavior. Measurement of local and average bed expansion (void fraction), of particle circulation rates, and of local velocities is necessary for such predictions.

Flows with small particles moving in various directions are difficult to measure by conventional techniques. The conventional imaging system is severely limited by its narrow depth field when one tries to resolve a small object such as a particle. Therefore, it is not surprising that one of the first applications of holography in multiphase flow was particle size analysis (Thompson and Ward, 1966; Thompson et al., 1966). Holographic techniques allow a vast amount of information to be stored in a hologram, e.g., the size, number density and relative position of particles in a dynamic three-dimensional field. Such information is frozen as a stationary image and can be reproduced later for detailed study.

Thompson (1974) and Trolinger (1975) reviewed holographic particle-sizing techniques and discussed the basic principles and practical limitations of in-line Fraunhofer holography and off-axis holography in particle sizing.

The fundamental idea behind the in-line Fraunhofer holography is to consider the diffracted field associated with groups of particles in a three-dimensional sample and to record the diffracted field as a hologram by using a collinear background beam. This hologram can then be used to form an image of the original three-dimensional sample. Normally, the particles are moving and thus, with an appropriate exposure time, a hologram can be made of this sample and a stationary image of the dynamic object distribution then can be formed that has much greater depth of field than a normal image. Hence, this method is a two-step image-forming process that reproduces a three-dimensional particle distribution. The in-line Fraunhofer holography has been used successfully in aerosol analysis by Thompson et al. (1967). They used pulse lengths of approximately 20 ns. Trolinger, et al. (1969) used a similar technique in their study of rocket injectors. The use of the Fraunhofer plane for particle measurement is now well established (Cornillault, 1971; Swithenbank et al., 1977; Ewan, 1979).

Also, particle holography has been applied to the study of weather and pollution. The techniques that were introduced for studying water droplet distribution in fog have now been extended to the observation of snow particles in clouds.

Theoretically, the holographic technique can record a particle whose size is equivalent to the wavelength of the recording light. However, when conventional film plate has been used, the holographic technique has only been capable of recording down to a particle size of few microns (Lee, 1973; Briones et al., 1978). With the aid of computer, Hickling (1968) has produced Fraunhofer holograms of submicrometer-size particles and has successfully formed images. He computed the holograms by using the classical Mie solution and suggested that the method might be used for particles in the size range 0.5–20 μm. This method was subsequently applied to small clouds of ultrasonically generated water droplets but using a separate reference beam to make the holograms (Hickling, 1969).

It is often necessary to measure the velocity spectrum simultaneously with the particle-size spectrum. Fraunhofer hololgraphy can readily be extended to perform such tasks by using a double exposure of the particle field with a predetermined time interval between the exposing light pulses. This idea apparently was adopted by Trolinger et al. (1968, 1969), Menzel et al. (1968), and Fourney et al. (1969). Double-pulsed ruby lasers with pulse lengths of 7–50 ns and pulse separations as low as 10 μs have been used to record 5–100 μm particles in concentrations up to $10^5/\text{cm}^2$ moving with velocities of 15 m/sec. The instantaneous velocity vector is determined by knowing the time interval between pulses and measuring the vector distance between the particle images. Presently, the pulse from the laser can be repeated within a fraction of a microsec and upward, and it has been demonstrated that particles moving at a velocity in excess of 2000 m/s can be determined by the holographic technique (Trolinger, 1975).

Generally, the in-line holographic technique has been applied to the recording of particles if the particle field is not too dense. Also, the off-axis holographic technique has been tried occasionally for crowded particle fields. The off-axis holography, in which the reference beam is added separately, has also been used by Wuerker et al. (1968) and by Wuerker and Heflinger (1970) for particle sizing in rocket engine studies. They used a pulsed ruby laser for illuminating, with the reference beam passing through a separate enclosed path. Mathews (1971) used reflected light methods to study limestone clouds in a pulverized coal furnace. Field depths of up to 15 m reportedly have been achieved. The major advantages of the off-axis holography are that the two images are entirely separate and that the sample volume need not actually transmit the beam and hence can be used in reflected light. However, the method requires a higher resolution film, and an undisturbed path has to be provided for the reference beam.

Table 1 Comparison of known and measured peak velocities over a range of the distribution width parameter σ/A (Ewan, 1979)

σ /A	Known peak velocity A (m/sec)	Measured peak velocity A (m/sec)
<0.01	2.43 ± 0.04	2.40 ± 0.03
0.04	2.40 ± 0.04	2.37 ± 0.03
0.08	1.90 ± 0.06	1.84 ± 0.036
0.14	1.90 ± 0.06	1.85 ± 0.036

A velocity-synchronized Fourier transform hologram camera also has been developed (Klaubert and Ward, 1969; Dyes et al., 1970). Such a method can be used to analyze hypervelocity particles. The hologram is the interference pattern between a Fraunhofer diffraction pattern of the particle formed by a lens and a reference beam produced by back reflection from the particle.

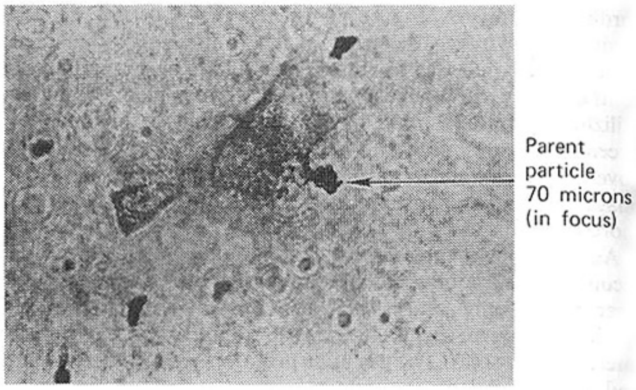

Fig. 4 Hologram of a disintegrating coal particle; Trolinger and Heap (1979)

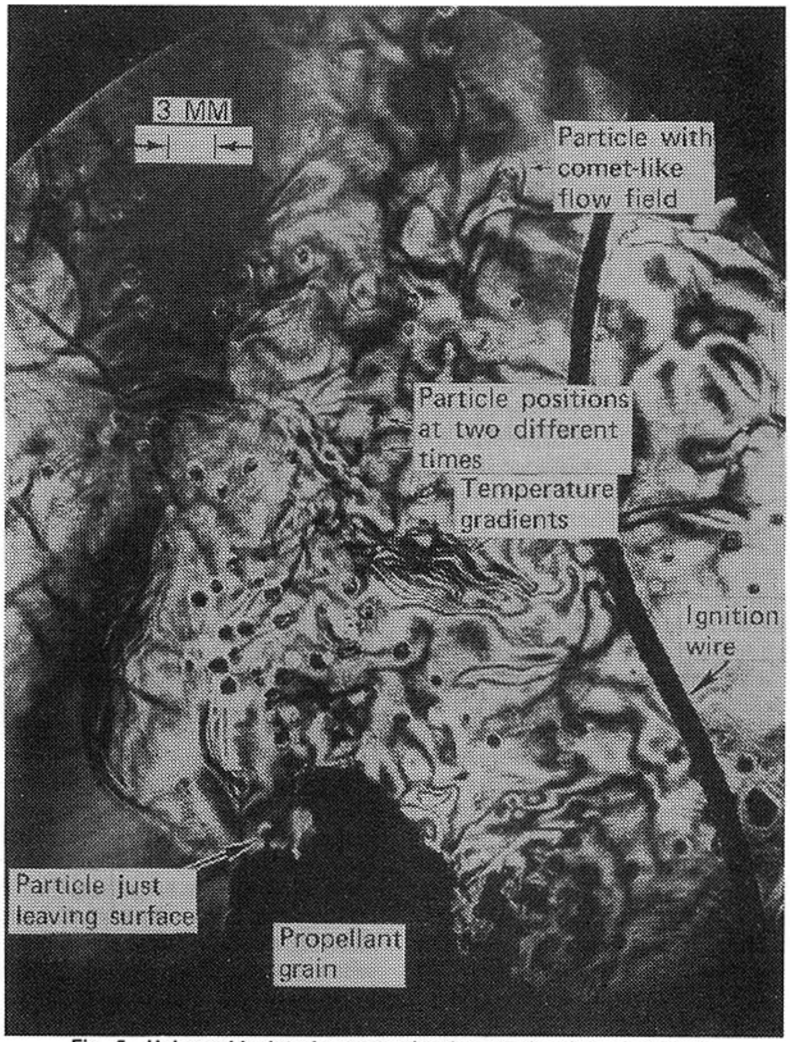

Fig. 5 Holographic interferogram showing combustion of a black powder pellet; Trolinger and Field (1980)

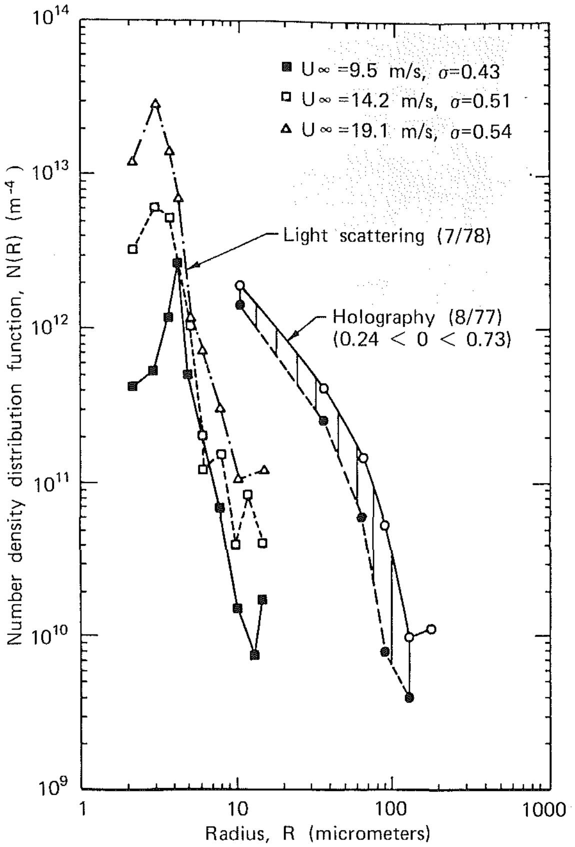

Fig. 6 Comparison of measurements of nuclei populations; Billet and Gates (1981)

Briones et al. (1978) developed an off-axis transmission holographic scheme and report that they achieved a 2-micron resolution of the combustion of solid rocket propellents at high pressures at a working distance of 6 cm.

Ewan (1979) produced double exposure holograms of a moving particle field having a one-dimensional velocity distribution. Table 1 compares the known peak velocities and measured peak velocities of his holograms over a range of the distribution width parameter σ/A. An excellent agreement is shown between the two. His method is based on the fact that the Fraunhofer diffraction patterns, produced in the back focal plane of a lens, for particles which are related by a displacement in a plane parallel to the recording plane, differ by an explicit phase factor that is a linear function of position in the recording plane. The double aperture type of parallel fringe structure, which results when the amplitudes from two particles are combined, can be used to calculate the particle separation. For velocity measurement, the two waves corresponding to the particle's position at two different times are recorded holographically by using a double-pulsed ruby laser. This approach can yield velocity distribution information while permitting rapid data-handling procedures to be used, thus eliminating the procedure of particle pair counting that was necessary in previous methods. A summary of particle field holography may be found in Trolinger and Field (1980).

Holography has been successfully used to visualize the basic combustion processes of a variety of particle types such as coal particles and explosive particles. Understanding the physics of coal combustion and soot formation is important in producing more efficient and clean energy, and holography is beginning to provide new and valuable insights into such processes by way of direct visualization. In investigations of basic combustion phenomena, holography has enabled observation not only of particle size and velocity but also of how particles separate from a parent particle and disintegrate while burning; their subsequent growth after combustion can be observed by using holography, and its application in this area opened a new data source for studying fluid-particle systems (Trolinger and Heap, 1979). Holography has indeed provided visualization of combustion from beginning to end, which has hitherto never been possible by any other techniques. Trolinger and Heap (1979) studied burning of coal particles in free flight by using holography. They attained a resolution of about 3 μm in the combustion zone of a flat flame burner at a working distance of 20 cm. Both the size and velocity of particles up to 75 μm in diameter were measured holographically. They were able to observe burning coal particles in free flight with nearly diffraction-limited performance. Figure 4 shows a hologram of a disintegrating coal particle during the combustion process. Trolinger and Heap also compared in-line and off-axis images of various types of particles, and concluded that relative image quality varies significantly depending on the type of particles and the environment. In some instances, in-line image resolution was higher than off-axis resolution. However, they report that the signal-to-noise ratio was always higher for off-axis images, thus providing images that were more pleasing and easy to record. Especially, the gas density gradients near particles were more sharply defined in off-axis images where interferometry was used.

Table 2 Comparison of nuclei measurements obtained in the LTWT (Billet and Gates, 1981)

Number of nuclei/cubic centimeter
Nuclei diameter (micrometers)

Test number	<20 Holo.	<20 Scat.	20-50 Holo.	20-50 Scat.	>50 Holo.	>50 Scat.	Cumulative Holo.	Cumulative Scat.
16	221	82	39	4.6	1.2	1.0	261	88
17	290	208	116	4.2	3.2	0.8	409	212
24	308	126	106	3.6	1.6	0.6	416	128
25	312	172	81	2.8	1.6	-	394	176
34	204	166	66	0.6	2.8	0.6	273	168
35	242	146	64	1.6	4.4	-	310	148

Trolinger and Field (1980) produced holograms at several stations, beginning at the point of introduction of coal particles and continuing downstream. They were able to observe the microscopic details of everything in the stream with a spatial resolution of about 10 μm and a temporal resolution of approximately 20 ns. The time history of the coal-combustion process could be observed from time zero to about 100 ms. Their holographic interferogram, showing combustion of a black powder pellet, is reproduced in Fig. 5. The capability to repeatedly view the physical processes occurring in combustion phenomena in microscopic detail under controlled conditions makes holographic techniques enormously attractive for use in discovering the precise mechanics and chemistry of combustion and many other related phenomena.

The most tedious part in applying holography to particle measurement may be in comparing samples and in counting and sizing particles. Limited successes have been reported in applying a computer-aided technique to automate such procedures (Haussmann and Lauterborn, 1980; Feinstein and Girard, 1981); further development in this area is clearly desirable in the future.

Applications to Gas-Liquid System

Compared to the applications in fluid-particle systems, the applications of holography to gas-liquid flows had not drawn much attention until the 1970s when cavitation researchers began to investigate cavitation nuclei by using holographic techniques (Peterson, 1972; Feldberg and Shlemenson, 1973; Peterson et al., 1975). Since then, a bulk of pioneering work in the use of holography has been attained in cavitation studies (van der Meulen, 1976; Lauterborn and Ebeling, 1977; Gates and Bacon, 1978; Ebeling, 1980; Billet and Gates, 1981; Katz and Acosta, 1982; Katz and O'Hern, 1983; Katz et al., 1984; Katz, 1984). The initial application of hologarphy to cavitation studies was to measure the population density of nuclei in flow to investigate the onset of cavitation because free-stream nuclei are recognized to be important in cavitation inception.

Peterson and others (1972, 1975), and Feldberg and Shlemenson (1973) developed an experimental apparatus to measure nuclei distributions by using holograms. Holograms of a sample volume of a water tunnel test section were recorded on a special high-resolution film by holocamera, and a three-dimensional image of the original volume was reconstructed from the developed holograms. The frozen image was then studied. Such a method is described by Gates and Bacon (1978).

Comparison of the light-scattering and holographic techniques in cavitation nuclei measurement is given by Peterson et al. (1975), and by Billet and Gates (1978). Using the two different techniques in the same facility, Billet and Gates measured particulate and bubble distributions. Their results on nuclei measurements are shown in Fig. 6. In this comparison, in the overlapping size range of 10–50 μm in diameter, the light-scattering technique recorded substantially fewer nuclei than the holographic method. It can be assumed that holography results are essentially correct for nuclei larger than 20 μm because the holography technique allows direct observation of the reconstructed image of the nuclei. Small particles with diameters of less than 20 μm may induce some uncertainty because of background noise in the original hologram and in the reconstructed system. Table 2 presents a further comparison of the results obtained by the two techniques.

The holographic method is advantageous in resolving the controversy surrounding the relative importance of particulates versus bubbles as cavitation nuclei because the nuclei can be directly visualized and inspected; in contrast, the light-scattering technique cannot distinguish between particulates and bubbles.

Lauterborn and Ebeling (1977) and Ebeling (1980) developed and applied high-speed holocinematography to the study of cavitation. Lauterborn (1982) utilized a high-speed holocinematography to investigate the dynamics of a bubble vortex ring in front of a plane solid boundary. A holographic series was taken at 25,000 frame/s, and images were reconstructed. The arrangement used a pulsed ruby laser and an off-axis reference beam. From these experiments, and supplemented by the ordinary high-speed cinematography, he was able to verify that the originally spherical bubble near the solid boundary forms oscillating torus-like bubbles that seem to appear in conjunction with jet formation.

Katz et al. (1984) used an underwater holographic camera system to detect microparticulates in their study on cavitation inception. Reconstruction of the test holograms at 16X magnificiation produced sharp images of macroscopic objects, whereas 150X magnification clearly showed microscopic nuclei. They used an off-axis holography utilizing a high-energy pulsed ruby laser of 20–50 ns duration to shorten the exposure time of the sample volume and were able to identify moving microscopic objects on the order of 10 μm.

Katz (1984) used the lensless Fraunhofer holography in his study of the onset of cavitation. The exposure time was on the order of 20 ns, and the wavelength of the generated light was 0.6943 μm. Reconstruction of these holograms then enabled the population of microbubbles in the flow field to be quantitatively evaluated. The location and the nature of the subsequent visible cavitation originating from these microbubbles was also determined from these holograms. The direct holographic flow visualization confirmed that cavitation inception occurs when a free-stream bubble is brought to instability by the pressure-fluctuation peaks.

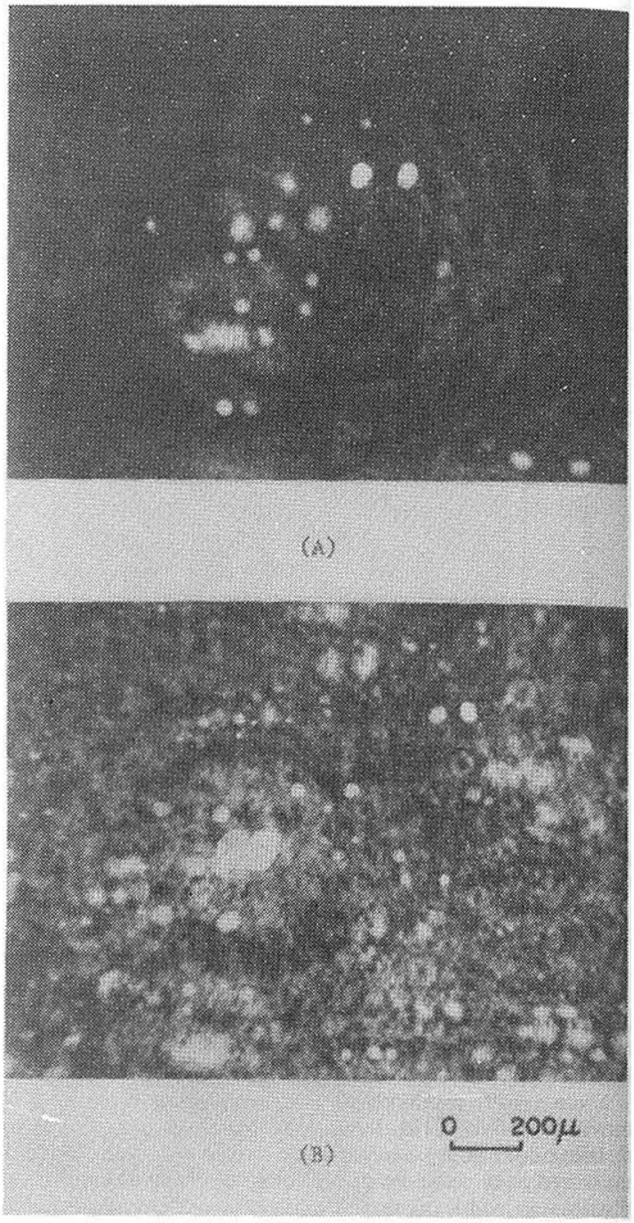

Fig. 7 Giant double-pulse exposed holograms showing water droplets in air-water two-phase flow; Lee (1973)

Other than in cavitation research, the application of holography to a gas-liquid system has not been widespread. Yet, holographic techniques can potentially offer a great deal in investigating the fundamentals of two-phase, gas-liquid flows. For instance, accurate information about void distribution in channel flows will greatly help model developers. In two-phase drift flux models, the void distribution parameter is an important empirical quantity to be specified. Such information may be obtained from holographic measurements of void distribution. Currently, the phase distribution is usually measured by a gamma densitometer. Gamma densitometer normally requires many beams to accurately measure void distribution, and furthermore, is not adapted for measuring phasic velocities which are also a meaningful quantity in two-phase flows. In two-phase channel flow, such as occurs in boiling water reactor fuel assemblies or in steam generators,

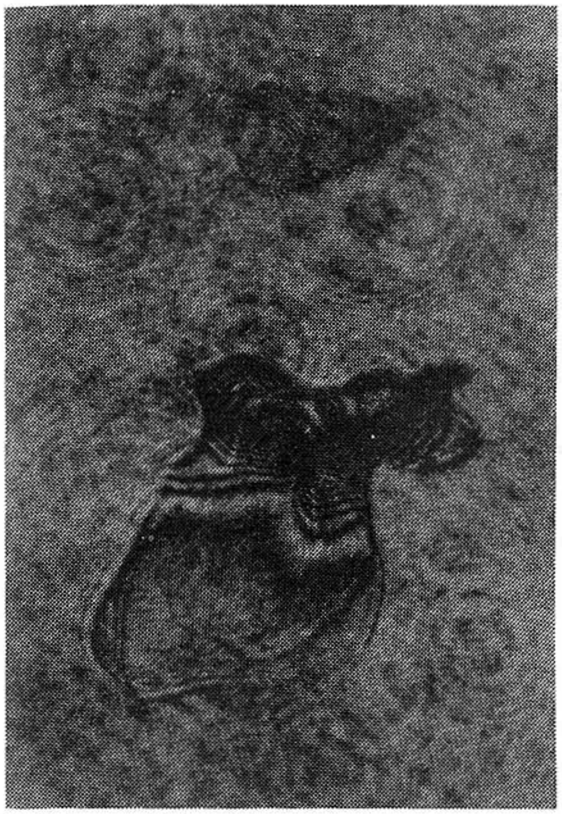

Fig. 8 Hologram of alcohol droplet breakup using double pulse ($\Delta T = 25$ μs); Craig (1984)

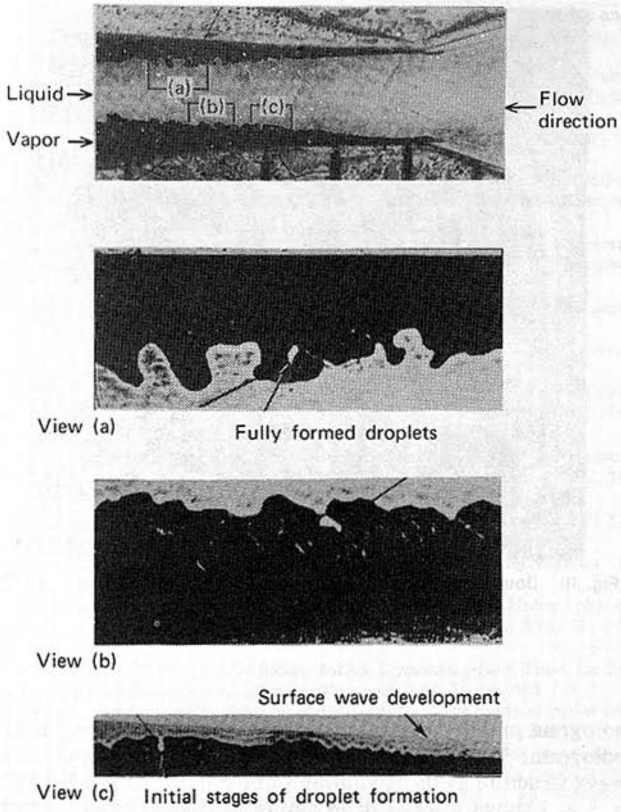

Fig. 9 Details of cavitating (flashing) flow in a nozzle; Deason and Fincke (1981)

information on the lateral drift of bubbles and droplets can be extremely valuable in developing models. It is possible to obtain such information with holography more than with any other technique. The potential for holography application to the study of such dynamic behavior of dispersed two-phase flows is becoming increasingly recognized.

In dispersed gas-liquid, two-phase flow studies, Lee (1973) and Lee et al. (1974) successfully employed holography to determine slip ratios in air-water, two-phase critical flow at quality levels above 0.95. They determined the slip ratios by directly measuring liquid droplet size and velocity based on the holograms exposed to double pulses from a ruby laser with a minimum separation time of 5 μs. Their holographic recording technique for small drops was substantially improved by using a large aperture. They further experimented and created triple-exposed holograms by using a triple pulse from the ruby laser and demonstrated that such techniques could be used to measure droplet accelerations. The drop-size distribution could be measured by the microscope to an accuracy of a few microns. Information on the size distribution of drops is also important in two-phase flow studies, and a direct measurement based on holographic visualization will shed much light in this direction. Figure 7 shows the reconstructed image of a double-exposed hologram of air-water, two-phase flow taken by Lee (1973). The drop velocities were calculated by measuring the distance the drops traversed within the interval of time produced between the two pulses. Later, Ju et al. (1982) have extended this technique to the study of steam-water, two-phase flow.

Trolinger (1980) and Trolinger and Field (1980) used the technique of multiple-exposure recording for air bubbles in air-water dispersed two-phase flow. They studied air bubbles in a simulated cooling channel, using a double-pulsed hologram. From their visualization studies, Trolinger and Field observed that bubbles were not necessarily spheres; therefore, optical instruments such as those used in conventional diffraction methods, which must assume the bubbles are spheres, would produce erroneous results. They also studied liquid particle breakup in a liquid fuel injector nozzle and the disintegration of a molten slag droplet by air jet. The technique of multiple-exposure holography is useful in producing velocity, acceleration, and information on shape change. Craig (1984) used pulsed laser holography to observe liquid and liquid metal breakup phenomena and was able to obtain great resolution. Figure 8 shows his hologram of alcohol droplets during breakup.

With the important role of interfacial area concentration and particle shape factor in two-phase flow modeling (Kocamustafaogullari and Ishii, 1983), information on bubble size and shape obtainable from holographic visualization can provide valuable insights for two-phase flow investigators and will greatly help to advance these studies.

When the bubble number density becomes increasingly large, multiple scattering and shadowing effects make it difficult to observe individual bubbles. Trolinger and Field (1980) suggest a way to extend the range of applicability by illuminating the field with a sheet of light instead of a column of light. This method considerably reduces the amount of light and information recorded by the hologram. Bubbles or droplets that might otherwise be blocked from view or lost in the bright background can be seen by this technique. The overall sheet of light passing through the channel can be observed from a wide range of views, thereby providing a measure of density or a closeup view that reveals the individual bubbles.

Deason and Fincke (1981) used pulsed ruby holography to obtain detailed, three-dimensional images of the phase change process in a two-dimensional converging-diverging nozzle. Figure 9 shows views of various flow structures observed in the nozzle. All these views were photographed from the same

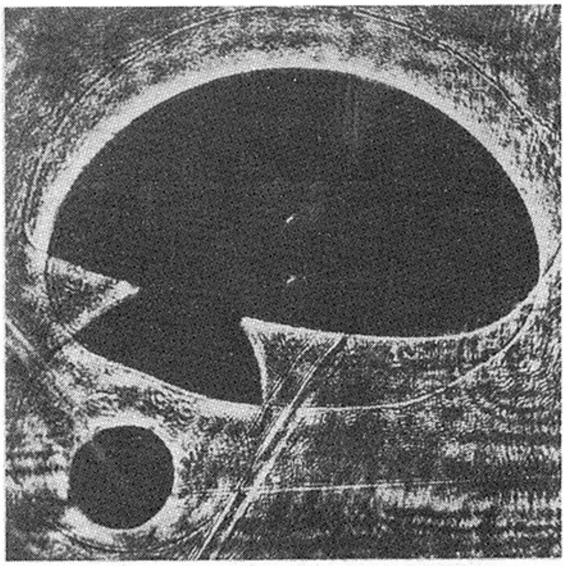

Fig. 10 Double-exposed hologram of steam bubbles; Deason (1982)

hologram and demonstrate the great resolution present in the hologram. View (*c*) in Fig. 9 shows the gradual growth of wavy structure as the cavitation bubble itself grows. View (*b*) in Fig. 9 shows a water drop almost separated from the bulk liquid. In View (*a*) in Fig. 9, a droplet appears to be entrained in the vapor phase while other droplets are in the process of formation. These examples powerfully demonstrate the capability of holographic technique for recording an entire scene instantaneously that later can be analyzed by using conventional photographic methods. Deason and Fincke also used double-pulsed holograms with a time interval of 50 μs between pulses to determine the time-of-flight velocity of the interface movement. Such a visualization technique can provide detailed local velocities throughout a volume of space at a particular instant in time. This capability is a distinct advantage over the LDA technique, which provides continuous velocity information at a particular point in space. Velocities at other locations must be obtained by traversing the LDA probe or by using several LDA systems simultaneously. The accuracy of Deason and Fincke's measurements was limited by the precision with which a particular point can be relocated on the two instantaneous images and by how accurately the reference beams have been collimated. Their error was estimated to be ±8 percent in the velocity determination. The pulsed holographic images of the phase change process in a two-dimensional, converging-diverging nozzle showed the details of vapor generation and collapse as well as the location of these events within the nozzle for various temperatures and flow rates. Their portable holographic camera contains a double-pulsed ruby laser with a pulse length of 20 ns and a maximum pulse energy of 750 mJ.

Deason (1982) used holography to further investigate air-water bubbly flows. His main interest was to determine bubble shapes and distributions for various flow regimes as well as to discover which flow conditions might prove to be optically too opaque to make usable holograms. He has concluded that dispersed bubbly flows, when a maximum void fraction of 0.2 is attained, image quality becomes too poor to be useful except for bubbles near the walls. This image degradation is due to multiple reflections from air-water interfaces. Figure 10 shows the results of a double exposed hologram with 50 ms between exposures. The double image permits measurements of the speed and direction of each bubble because the bubble displacement can be directly measured and the time interval is known. Shown in the figure are two bubbles: one remains attached to the heated wire and grows between exposures; the second has released and is rising under buoyant forces. Such revealing visualization is possible only by using holography.

Ooi and Acosta (1984) made an interesting application of holography by using it to determine instantaneous local static pressure in a liquid jet. They injected air bubbles into the jet and traced the change of volume shape of the bubbles by taking a series of holograms from which they deduced the fluctuating pressure in the jet.

Concluding Remarks

This paper has reviewed the state of the art in holography applications to multiphase flow studies. The application of holographic techniques to visualize multiphase flow, although limited at present, is very promising because of the potential for freezing and recording dynamic situations; holography gives three-dimensional images and a pulse laser as the light source makes an extremely short image formation time possible. Reconstructed images from holograms can be photographed, videotaped, examined by microscopy, analyzed by Schlieren techniques, or simply observed by the naked eye.

Some of the limitations of current holographic techniques in multiphase flow study are as follows:

- Their application is limited to the field where the dispersed phase is sparsely populated. This limitation is caused by the recording technique as well as by the recording material.
- The present method of viewing the reconstructed image through either TV screen or microscope and recording the desired data manually is extremely tedious when thousands of pieces of information stored in one holographic plate must be examined.
- The reconstructed image is somewhat degraded by the speckle patterns in the reconstructed laser light. Improvement can be made in this area by using a rotating diffuser and by other methods, but further improvement is desirable.

Recommendations for improving the applications of holography to multiphase flow visualization are as follows:

- Information-processing and data-analysis techniques for the reconstructed image should be vastly improved. The computer-aided automatic process techniques such as the one developed by Haussmann and Lauterborn (1980) need further improvement.
- The feasibility of using reflected light, instead of diffracted light, as an information beam should be further explored with the aim of recording a densely populated field of multiphase flow. The problem with recording the densely populated field by using diffracted light as an information beam is that the beam is disturbed and loses its information as it passes through layers of objects such as droplets or bubbles. This difficulty could conceivably be alleviated by taking a hologram using reflected light as an information beam, although such a method might prove to be ineffective if the field is overly populated and the depth of field is too deep.
- To enhance the understanding of multiphase flow phenomena, combining holography with holographic interferometry is also recommended. This technique will allow one to visualize not only the movement of the dispersed phase but also the movement, density, and velocity gradient of the continuous, ambient phase.

Acknowledgments

The authors wish to thank Mr. Vance A. Deason of EG&G Idaho/INEL, and Drs. James E. Craig and James D. Trolinger of Spectron Development Laboratories, who generously permitted the authors to use their reconstructed hologram prints in this paper and provided other valuable information and suggestions. We also wish to thank Izetta Grisham of Kaiser Engineers for typing the manuscript.

References

Beers, J. R., Reid, F. M. H., and Stewart, G. L., 1973, "Microplankton of North Pacific Central Gyre. Population, Structure, and Abundance," *Int. Revue. Ges. Hydrobio.*, Vol. 60, No. 5, pp. 607-638.

Belz, R. A., and Dougherty, N. S., 1972, "In-line Holography of Reacting Liquid Spray," *Proceedings Symp. Eng. Appl. of Holography*, R. Aprahamian, Ed., Redondo Beach, CA: SPIE, pp. 209-218.

Billet, M. L., and Gates, E. M., 1981, "A Comparison of Two Optical Techniques for Measuring Cavitation Nuclei," ASME Journal of Fluids Engineering, Vol. 103, No. 1, pp. 8-13.

Briones, R. A., Heflinger, L. O., and Wuerker, R. F., 1978, "Holographic Microscopy," *Applied Optics*, Vol. 17, No. 6, pp. 944-950.

Caulfield, H. J., and Lu, S., 1970, *The Application of Holography*, Wiley-Interscience.

Collier, J. W., Burckhardt, C. B., and Lin, L. H., 1971, *Optical Holography*, Academic Press.

Cornillault, J., 1971, "Particle Size Analyzer," *Applied Optics*, Vol. 11, No. 2, pp. 265-268.

Craig, J. E., 1984, "Conventional and Liquid Metal Droplet Breakup in Aerodynamic Nozzle Contractions," AIAA Paper No. 84-0201, AIAA 22nd Aerospace Sciences Meeting, January 9-12, Reno, NV.

Craig, J. E., Azzazy, M., and Poon, C. C., 1984, "Resonant Holographic Tomography for Detection of Hydroxyl Radicals in Reacting Flows," AIAA Paper No. 84-0202, AIAA 22nd Aerospace Sciences Meeting, January 9-12, Reno, NV.

Deason, V. A., and Fincke, J. R., 1981, "A Study of Cavitation Process in a Two-Dimensional Nozzle Using Pulsed Ruby Holography," NUREG/CR-2276, EG&G-2120, EG&G Idaho, Inc.

Deason, V. A., 1982, "Applications of Holography and Holographic Interferometry at the INEL," EGG-ID-5693, EG&G Idaho, Inc.

DeVelis, J. B., and Reynolds, G. O., 1967, *Theory and Application of Holography*, Addison-Wesley Publishing Co.

Doty, J. L., and Hildebrand, B. P., 1982, "The Use of Sandwich Hologram Interferometry for Nondestructive Testing of Nuclear Reactor Components," *Optical Eng.*, Vol. 21, No. 3, pp. 542-547.

Dyes, W. A., Kellen, P. F., and Klaubert, E. C., 1970, "Velocity Synchronized Fourier Transform Hologram Camera System," *Applied Optics*, Vol. 9, pp. 1105-1112.

Ebeling, K. J., 1980, "Application of High-Speed Holocinematographical Methods in Cavitation Research," *Cavitation and Inhomogeneities in Underwater Acoustics*, W. Lauterborn, Ed., Springer, Berlin, pp. 35-41.

Erf, R. K., 1974, *Holographic Non-Destructive Testing*, Academic Press.

Ewan, B. C. R., 1979, "Holographic Particle Velocity Measurement in the Fraunhofer Plane," *Applied Optics*, Vol. 18, No. 5, pp. 623-626.

Feinstein, S. P., and Girard, M. A., March 1981, "Automated Holographic Drop-Size Analyzer," *Applied Optics*, Vol. 20, No. 6, pp. A52.

Feldberg, L. A., and Shlemenson, K. T., 1973, "The Holographic Study of Cavitation Nuclei," Discussion to Proceedings IUTAM Symposium on Non-Steady Flow of Water at High Speeds, Leningrad, USSR (English Version; Moscow, 1973), pp. 106-111.

Fourney, M. E., 1968, "Application of Holography to Photoelasticity," *Experimental Mechanics*, Vol. 8, No. 1, pp. 33-38.

Fourney, M. E., Matkin, J. H., and Waggoner, A. P., 1969, "Aerosol Size and Velocity Determination Via Holography," *Rev. Sci. Instrum.*, Vol. 40, pp. 205-213.

Gabor, D., 1948, "A New Microscope Principle," *Nature*, Vol. 161, pp. 777-778.

Gabor, D., 1949, "Microscopy by Reconstructed Wavefronts," *Proceedings of the Royal Society, London*, Series A, Vol. 197, pp. 454-487.

Gabor, D., 1971, "Holography, Past, Present and Future," *Proceedings Semin. Developments in Holography*, Redondo Beach, CA:SPIE, B. J. Thompson and J. B. DeVelis, Eds., Vol. 25, pp. 129-133.

Gates, E. M., and Bacon, J., 1978, "Determination of Cavitation Nuclei Distribution by Holography," *J. Ship Research*, Vol. 22, No. 1, pp. 29-31.

Haussmann, G., and Lauterborn, W., 1980, "Determination of Size and Position of Fast Moving Gas Bubbles in Liquids by Digital 3-D Image Processing of Hologram Reconstructions," *Applied Optics*, Vol. 19, No. 20, pp. 3529-3535.

Heflinger, L. O., Stewart, G. L., and Booth, C. R., 1978, "Holographic Motion Pictures of Microscopic Plankton," *Applied Optics*, Vol. 17, No. 6, pp. 951-954.

Hickling, R., 1968, "Scattering of Light by Spherical Liquid Droplets Using Computer-Synthesized Holograms," *J. Opt. Soc. Am.*, Vol. 58, pp. 455-460.

Hickling, R., 1969, "Holography of Liquid Droplets," *J. Opt. Soc. Am.*, Vol. 59, pp. 1334-1339.

Holloway, D. C., 1971, "Simultaneous Determination of the Isophachic and Fringe Patterns for Dynamic Loadings by Holographic Photoelasticity," University of Illinois-Urbana, T&AM Report No. 349.

Ju, Y., Moulton, R. W., and Garlid, K. L., 1982, "Holographic and Photographic Studies of High-Quality Steam-Water Critical Flow," *AIChE Journal*, Vol. 28, No. 2, pp. 597-603.

Katz, J., and Acosta, A. J., 1982, "Observation of Nuclei in Cavitating Flows," *J. Applied Scientific Research*, Vol. 38, pp. 123-132.

Katz, J., and O'Hern, T. J., 1983, "Holographic Observations of Cavitating Flows Within Regions of Flow Separation," Eighth Biennial Symposium on Turbulence, Rolla, MO.

Katz, J., O'Hern, T. J., and Acosta, A. J., 1984, "An Underwater Holographic Camera System for Detection of Microparticulates," *Cavitation and Multiphase Flow Forum-1984*, J. W. Hoyt, Ed., pp. 22-25.

Katz, J., 1984, "Cavitation Phenomena Within Regions of Flow Separation," *Journal of Fluid Mechanics*, Vol. 140, 1984, pp. 397-436.

Klaubert, E. C., and Ward, J. H., 1969, *Proceedings Semin. on Evaluation of Motion Degraded Images*, Washington, DC:NASA, pp. 119-122.

Knox, C., and Brooks, R. E., 1969, "Holographic Motion Picture Microscopy," *Proceedings of the Royal Society, London*, Series B, Vol. 174, pp. 115-121.

Kocamustafaogullari, G., and Ishii, M., 1983, "Interfacial Area and Nucleation Site Density in Boiling Systems," *Int. J. Heat and Mass Transfer*, Vol. 26, No. 9, pp. 1377-1387.

Koechner, W., 1979, "Pulsed Holography," *Laser Handbook*, Vol. 3, M. Stitch, Ed., North-Holland Publishing Co., pp. 577-626.

Kurtz, R. L., and Owen, R. B., 1975, "Holographic Recording Material–A Review," *Optical Eng.*, Vol. 14, No. 5, pp. 393-401.

Lauterborn, W., and Ebeling, K. J., 1977, "High-Speed Holography of Laser-Induced Breakdown in Liquids," *Appl. Phys. Letters*, Vol. 31, pp. 663-664.

Lauterborn, W., 1982, "Cavitation Bubble Dynamics–New Tools for Intriciate Problem," *J. Applied Scientific Research*, Vol. 38, pp. 165-178.

Lee, Y. J., 1973, "An Application of Holography to the Study of Air-Water Two-Phase Critical Flow," PhD thesis, University of Washington, Seattle, WA.

Lee, Y. J., Fourney, M. E., and Moulton, R. W., 1974, "Determination of Slip Ratios in Air-Water Two-Phase Critical Flow at High Quality Levels Utilizing Holographic Techniques," *AIChE Journal*, Vol. 20, No. 2, pp. 209-219.

Leith, E. N., and Upatnieks, J., 1964, "Wavefront Reconstruction With Diffused Illumination and Three-Dimensional Objects," *J. Opt. Soc. Am.*, Vol. 54, pp. 1295-1301.

Mathews, B. J., 1971, "Measurement of Fine Particulate in Pollution Control," *Proceedings Semin. Developments in Holography*, Rendondo Beach, CA:SPIE, B. J., Thompson and J. B. DeVelis, Eds., Vol. 25, pp. 157-168.

Mayinger, F., and Panknin, W., 1974, "Holography in Heat and Mass Transfer," Paper No. 49-3, *Heat Transfer 1974*, Vol. 6, pp. 28-43; *Proceedings of the 5th International Heat Transfer Conference*, Tokyo, 1974.

Menzel, R., Russell, T. G., and Shofner, F. M., 1968, "Recording Fluid Velocity Fields Holography," *Proceedings Semin. on Holography*, Redondo Beach, CA:SPIE, Vol. 15, pp. 167-170.

Mesler, R., 1982, "Research on Nucleate Boiling," *Chemical Engineering Education*, Vol. 16, No. 4, pp. 152-156.

Ooi, K. K., and Acosta, A. J., 1984, "The Utilization of Specially Tailored Air Bubbles as Static Pressure Sensors in a Jet," ASME Journal of Fluids Engineering, Vol. 106, No. 4, pp. 459-465.

Peterson, F. B., 1972, "Hydrodynamic Cavitation and Some Considerations of the Influence of Free Gas Content," *9th Symposium on Naval Hydrodynamics*, Paris.

Peterson, F. B., Daniel, F., Keller, A. P., and Lecoffre, Y., 1975, "Determination of Bubbles and Particulate Spectra and Number Density in a Water Tunnel With Three Optical Techniques," *Proceedings 14th ITTC*, Ottawa, Vol. 2, pp. 27-52.

Staub, F. W., Wood, R. T., Canada, G. S., and McLaughlin, M. H., 1980, "Two-Phase Flow and Heat Transfer in Fluidized Beds," EPRI CS-1456, Electric Power Research Institute.

Stewart, G. L., Beers, J. R., and Knox, C., 1973, "Application of Holographic Techniques to the Study of Marine Plankton in the Field and in the Laboratory," Developments in Laser Technology-II, *Proceedings Soc. Photo-Opt. Instru. Eng.*, San Diego, Vol. 41, pp. 183.

Swithenbank, J., Beer, J. M., Taylor, D. S., Abbot, D., and McCreath, G. C., 1977, *Prog. Astro. Aero.*, Vol. 53, pp. 421.

Thompson, B. J., and Ward, J. H., 1966, "Particle Sizing–The First Direct Use of Holography," *Scientific Research*, Vol. 37, No. 10, pp. 37-40.

Thompson, B. J., Parrent, G. B., Ward, J. H., and Justh, B., 1966, "A Readout Technique for the Laser Fog Disdrometer," *J. Appl. Meteor.*, Vol. 5, pp. 343-348.

Thompson, B. J., Ward, J. H., and Zinky, W. R., 1967, "Application of Hologram Techniques for Particle Size Analysis," *Applied Optics*, Vol. 6, No. 3, pp. 519-526.

Thompson, B. J., 1974, "Holographic Particle Sizing Techniques," *J. of Phys., E.*, Vol. 7, pp. 781-788.

Trolinger, J., Farmer, W. M., and Belz, R. A., 1968, "Multiple Exposure Holography of Time Varying Three-Dimensional Fields," *Applied Optics*, Vol. 7, No. 8, pp. 1640-1641.

Trolinger, J., Belz, R. A., and Farmer, W. M., 1969, "Holographic Techniques for the Study of Dynamic Particle Fields," *Applied Optics*, Vol. 8, No. 5, pp. 957-961.

Trolinger, J., 1975, "Particle Field Holography," *Optical Eng.*, Vol. 14, No. 5, pp. 383–392.

Trolinger, J. D., and Heap, M. P., 1979, "Coal Particle Combustion Studied by Holography," *Applied Optics*, Vol. 18.

Trolinger, J., and Field, R., 1980, "Particle Field Diagnostics by Holography," AIAA Paper No. 80-0018, AIAA 18th Aerospace Sciences Meeting, Pasadena, CA.

Trolinger, J. D., 1980, "Analysis of Holographic Diagnostics Systems," *Optical Eng.*, Vol. 19, No. 5, pp. 722–726.

Trolinger, J. D., 1982, "Aero-Optical Characterization of Aircraft Optical Turrets by Holography, Interferometry, and Shadowgraph," *Aero-Optical Phenomena*, Prog. Astro. Aero., K. G. Gilbert and L. J. Otten, Eds., Vol. 80, pp. 200–217.

van der Meulen, J. H. J., 1976, "A Holographic Study of Cavitation on Axisymmetric Bodies and the Influence on Polymer Additives," Netherlands Ship Model Basin Pub. 509, Wageningen, The Netherlands.

Wuerker, R. F., Heflinger, L. O., and Zivi, S. M., 1969, "Holographic Interferometry and Pulsed Laser Holography," *Proceedings Seminar on Holography*, Redondo Beach, CA:SPIE, Vol. 15, pp. 97–104.

Wuerker, R. F., and Heflinger, L. O., 1970, "Pulsed Laser Holography," *Proceedings on Engineering Uses of Holography*, E. R. Robertson and J. M. Harvey, Eds., Cambridge University Press, pp. 99–114.

Yukimaru Shimizu
Associate Professor.

Makoto Nagafusa
Graduate Student.

Koichi Sugino
Assistant.

Fusanobu Nakamura
Graduate Student.

Department of Mechanical Engineering,
Mie University,
Kamihama-cho, Tsu-shi,
Mie-ken, Japan 514

Studies on Performance and Internal Flow of Twisted *S*-Shaped Bend Diffuser—The So-Called Coiled Bend Diffuser: 1st Report

This paper is the result of our research into the twisted S*-shaped bend diffuser – the so-called coiled bend diffuser. It is a diffuser with a centerline in the shape of a twisted "*S.*" Our studies show that the performance characteristics of this bend diffuser are greatly improved when interaction by the bend elements generates an adequate secondary flow inside the diffuser. Full consideration was given to the influence of the divergent angle of the bend elements, consisting of the diffuser or curvature radius ratio of the bend, on these performance characteristics. The relation between diffuser performance and internal flow also was studied. Some guidelines for designing such a high performance diffuser is given.*

1 Introduction

This paper discusses the twisted *S* shaped bend diffuser, or the so-called coiled bend diffuser; i.e., a diffuser with a center line in the shape of a twisted "*S*." Our studies show that the performance characteristics of this bend diffuser [1-3] are greatly improved when interaction by the bend elements creates adequate secondary flow inside the diffuser. It is also made clear, however, that performance characteristics of the same diffuser may vary by 30-40 percent according to the inlet velocity distribution and that high performance is not always obtained.

In this study, a bend diffuser is proposed, in which high and stable performance is guaranteed even when the distribution of inlet velocity is varied. The reasons for this are explained from measurement results on internal velocity distribution. We also will present our guidelines for designing such a high performance diffuser. Before this study, the influence of the divergent angle of the bend elements consisting of diffuser or curvature radius ratio of the bend on the performance characteristics was mostly unknown; full consideration was given to this. The relation between such elements and diffuser performance was thoroughly studied.

2 Experimental Method and Apparatus

2.1 Experimental Apparatus. Figure 1 is the schematic diagram of the apparatus to measure the pressure recovery performance of the diffuser. Water is pumped up and passes through rectifying tank *A*, the orifice, rectifying tank *B*, the pipe of inlet length and the distorted flow generator, and enters into the test bend diffuser. The test bend diffuser is submerged in the wide water tank with no tailpipe connected so that the pressure recovery of the diffuser can be measured. However, it is difficult to measure velocity distribution in water and, therefore, this conventional apparatus was modified: A diffuser outlet was installed on the sidewall of the water tank. Pressure taps for measuring pressure recovery performance were put at the inlet section, p_{w1}, and the outlet section of the test diffuser, p_n. The water column manometer is used to measure the pressure at each section. The diffuser was made by bending a straight conical diffuser into a semicircular shape, with a constant curvature radius ratio of 3 and 6. This was further divided into four equal parts as shown in Fig. 2. The data for these elements are shown in Table 1. The diffuser was made of zinc alloy casting and its inner wall was hydraulically smooth.

2.2 Shapes of Twisted *S* Bend Diffusers. At first, twisted

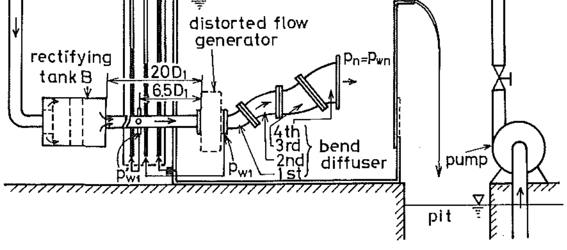

Fig. 1 Schematic diagram of experiment apparatus

Contributed by the Fluids Engineering Division for publication in the JOURNAL OF FLUIDS ENGINEERING. Manuscript received by the Fluids Engineering Division April 12, 1985.

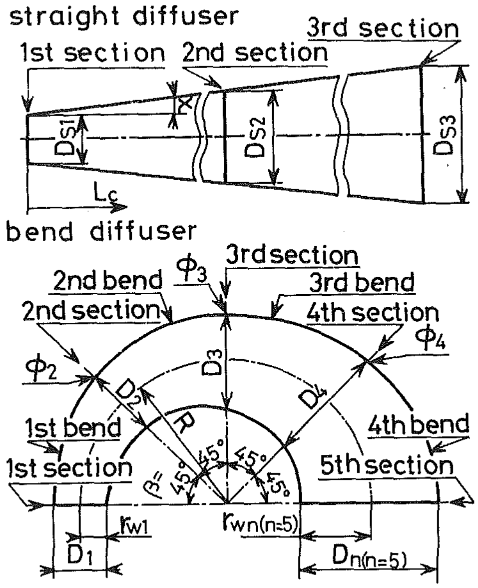

Fig. 2 Various definitions of bend diffuser elements and method of producing sample bend diffuser elements

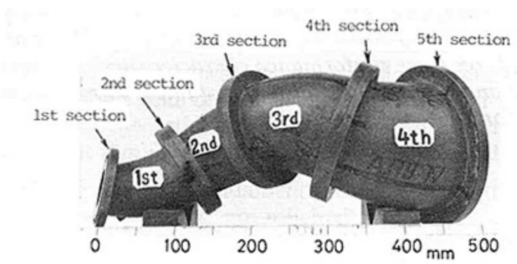

Fig. 3 Example of a 90° coil bend diffuser ($\phi_2=\phi_3=\phi_4=90°$ or $\phi_n=90°$), $R/r_{w1}=6$, $2\chi=12°$

Table 1 Area ratio for each section of bend diffuser (uncertainty in $R/r_{w1}=6\pm0.1$, in $AR=15.9\pm0.3$)

bend curvature ratio R/r_{wl}	3	6	3	6	3	6
	$2\chi=6°$ diffuser area ratio AR		$2\chi=12°$ diffuser area ratio AR		$2\chi=18°$ diffuser area ratio AR	
2nd section	1.3	1.5	1.6	2.2	1.9	3.1
3rd section	1.6	2.2	2.3	3.8	3.1	6.3
4th section	1.9	2.9	3.1	5.8	4.6	10.6
5th section	2.3	3.8	4.0	8.2	6.2	15.9

Diameter of inlet section ($=2r_{wl}$) : 0.054 m

Length of one bend element : in case of $R/r_{wl}=3$: $2\pi R/8=0.0636$ m

in case of $R/r_{wl}=6$: $2\pi R/8=0.127$ m

Table 2 Ordinary shape of bend diffuser in the experiment (uncertainty in $\phi_n=10°\pm10'$)

divergent angle 2χ	6°, 12° and 18°		
connection angle	ϕ_2	ϕ_3	ϕ_4
U bend diffuser	0°	0°	0°
twisted S shape bend diffuser, so called, coiled bend diffuser	45°	45°	45°
	90°	90°	90°
	135°	135°	135°
snake bend diffuser	180°	180°	180°

Table 3 Data for bend element of modified diffuser (uncertainty in $\phi_n=10°\pm10'$, in $2\chi=12°\pm10'$, in $R/r_{w1}=6\pm0.1$, in $AR=15.9\pm0.3$)

diffusers \ sequence of bend		1	2	3	4	5	6	representative connecting angle ϕ_n
(A)	2χ	6°	6°	12°	12°	18°	18°	45° 90° 135° 180°
	R/r_{wl}	6	6	6	6	6	6	
	AR	1.5	2.2	3.8	5.8	10.6	15.9	

S-shaped bend diffusers with equal connecting angles ($\phi_2=\phi_3=\phi_4,=\phi_n$), as shown in Table 2, were used in the experiment; these diffusers were composed of bend elements with an equal divergent angle from 1st to 4th bends. Finally, a modified diffuser (A), as shown in Table 3, was used. Because of modified diffuser was formed by combining various bend elements, there may have been some differences in the diameters of the connecting sections of the bend elements depending on the circumstances. In such cases, a certain divergent angle was given to the spacer with a thickness of 10 mm , which was inserted between bend elements to prevent rapid expansion. Figure 3 shows an example of a twisted S-shaped bend diffuser (connecting angle $\phi_2=\phi_3=\phi_4=90°$). The connecting angle ϕ_n is defined as follows. In Fig. 4, $(n-1)$th and nth bend elements are selected as examples and the connecting angle ϕ_n between the bend elements is shown. ϕ_n is an angle formed by the planes of the bend element's curvature on the upstream and downstream sides, with the

Nomenclature

AR = area ratio between inlet and outlet; $=(r_{wn}/r_{w1})^2$; Fig. 2
D_n = diameter of nth section in coil bend diffuser; Fig. 2
L_c = length of centerline of coil bend diffuser
N = number of bend elements
p_{wn} = mean wall pressure of nth section in coil bend diffuser
Q = flow rate measured by orifice; Fig. 1
r_n = any radius position in nth section
r_{wn} = radius of nth section; $=D_n/2$
R = curvature radius ratio of bend diffuser element
Re_1 = inlet Reynolds number; $=V_{m1}D_1/\nu$
V_{m1} = mean axial velocity at diffuser inlet section; $=Q/\pi r_{w1}{}^2$
v_{zn}, $v_{\alpha n}$ = axial and peripheral velocities in nth section
α_1 = angular position of eccentric center of distorted flow at inlet section of coil bend diffuser; Fig. 4; equation (5)
ϕ_n = connecting angle of both $(n-1)$th and nth bend elements and is called the representative connecting angle of coil bend diffuser; Fig. 4
2χ = apparent divergent angle of bend diffuser element; Fig. 2
δ^* = mean displacement thickness; Table 4 and Fig. 5

Subscript

n = number of section; Figs. 2–4

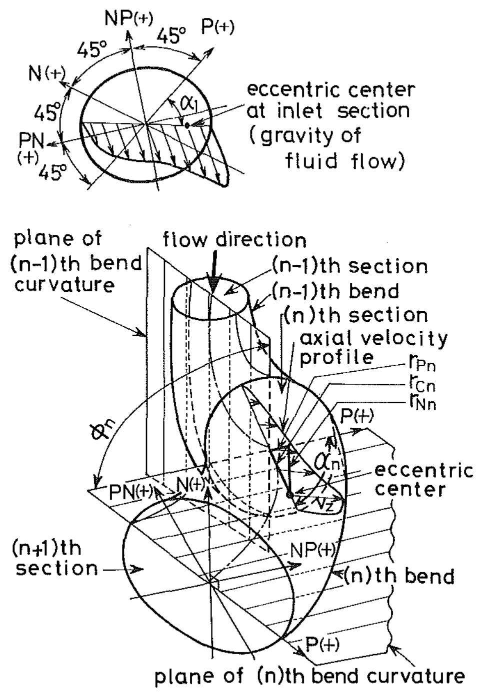

Fig. 4 Definitions of connecting angle of bend diffuser elements ϕ_n, angular position of eccentric center of distorted flow α_n, length from eccentric center to center of section r_{Cn} and four measuring directions of velocity *P*, *NP*, *N*, and *PN*

counterclockwise direction being regarded as positive. ϕ_2, ϕ_3, ϕ_4, ϕ_5, and ϕ_6 indicate the angles formed by 1st and 2nd bends, 2nd and 3rd bends, 3rd and 4th bends, 4th and 5th bends, and 5th and 6th bends, respectively. In our experiment, all connecting angles are equal to each other ($\phi_2 = \phi_3 = \ldots = \phi_n$), and ϕ_n is called the representative connecting angle.

2.3 Inlet Velocity Distributions Used in Experiment. The five types of flow which were used as inlet velocity distribution of the diffuser are shown in Fig. 5. These velocity profiles are often found at complicatedly bent pipelines or at the outlets of fluid machinery. Table 4 shows the characteristics of inlet velocity distribution Types I to V as well as the mean displacement thickness (mean value of 8 points around the peripheral wall), swirl strength of inflow M_1', maximum gradient of axial velocity distribution $[(v_{z\max}/V_{m1})-1]/(r/r_{w1})$, kinetic energy correction coefficient β_1 (inlet), β_n (outlet) and pressure correction coefficient π_1 (inlet), π_n (outlet); see equation (3). Reynolds number at the inlet section is maintained about 1.5 × 10^5 throughout the experiment. The method of generating these velocity profiles are also detailed in Table 4. The measurement of velocity distribution was carried out consecutively from the 1st section of diffuser to the outlet section as shown in Fig. 3. There were four measuring directions on each section, *N*, *NP*, *PN*, and *P* as shown in Fig. 4. Measurement was carried out using a 3-hole cylindrical pitot tube, with an outer diameter of 3 mm.

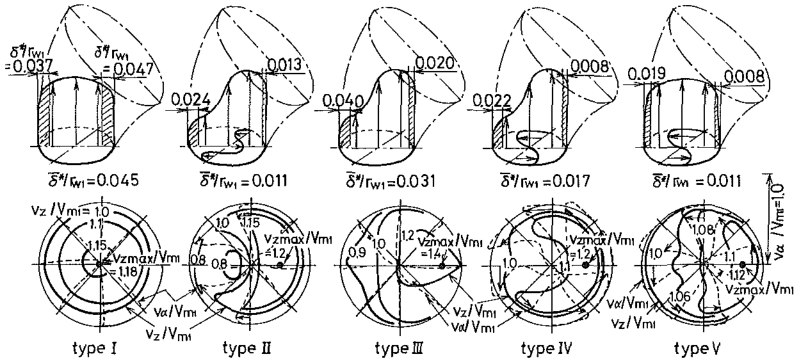

Fig. 5 Five types of flow used in the experiment as inlet velocity distributions of the coil bend diffuser, Types I, II, III, IV, and V and mean displacement thickness (mean value of eight points on periphery); (uncertainty in $\delta^*/r_{w1} = 0.047 \pm 0.0007$, in $v_z/V_{m1} = 1.0 \pm 0.015$, in $v_\alpha/V_{m1} = 0.2 \pm 0.003$)

Table 4 Inlet velocity distribution of 5 types used in the experiment, generating method, each correction coefficient and etc. (Uncertainty in $Re_1 = 1.5 \times 10^5 \pm 2.5 \times 10^3$, in $\bar{\delta}^*/r_{w1} = 0.045 \pm 0.0007$, in $M_l' = 0.413 \pm 0.006$, in $\beta_1 = 1.12 \pm 0.015$, in $\pi_1 = 1.0 \pm 0.015$)

On outlet section, $\beta_n = \pi_n = 1$ for all cases of types I-V

types of inlet velocity distribution		generating method	inlet Reynolds number	displacement thickness (mean value of 8 points)	swirl strength	maximum gradient of axial velocity	kinetic energy correction coefficient		pressure correction coefficient	
			Re_1	$\bar{\delta}^*/r_{w1}$	M_1'	$\frac{(v_{z\max}/V_{m1})-1}{r/r_{w1}}$	β_1	β_n	π_1	π_n
type I	developed turbulent saturated flow	after fully inlet length	1.5×10^5	0.045	0		1.06	1.0	1.0	1.0
type II	deviated flow accompanying by left-right symmetrical secondary flow	downstream tangent 1d outlet of single bend $R/r_w=3$	1.5×10^5	0.011	nearly 0	0.35	1.10	1.0	1.0	1.0
type III	deviated flow having no secondary flow (having cross flow)	lattice pipe	1.5×10^5	0.031	nearly 0	0.40	1.12	1.0	1.0	1.0
type IV	deviated flow accompanying by uni-directional swirling flow	second bend outlet downstream 1d section when two 90°-bends ($R/r_w=3$) are combined in twisted S shape	1.5×10^5	0.017	0.404	0.26	1.11	1.0	0.98	1.0
type V	flow accompanying by unidirectional swirling flow, but having almost uniform axial velocity distribution	second bend outlet downstream 10d section when two 90°-bends ($R/r_w=2$) are combined in twisted S shape	1.5×10^5	0.011	0.413	0.05	1.10	1.0	0.98	1.0

3 Formulas to Represent Experiment Results

Representative formulas to represent the experiment results are given. Approximated energy efficiency[1] of the diffuser (hereinafter referred to as "energy efficiency" or "efficiency")

$$\eta = (p_{wn} - \pi_1 p_{w1})/(\rho V_{m1}{}^2/2)\{\beta_1 - (1/AR)^2\} \quad (1)$$

Relation between energy efficiency and pressure recovery coefficient C_p

$$C_p = \eta\{1 - 1/(\beta_1 AR)^2\} \quad (2)$$

pressure and kinetic energy correction coefficients π_1, β_1 at inlet section

$$\begin{aligned} \pi_1 &= \int_0^{r_{w1}} \int_0^{2\pi} p_1 v_{z1} r_1 dr d\alpha / p_{w1} Q \\ \beta_1 &= \left\{\frac{\rho}{2} \int_0^{r_{w1}} \int_0^{2\pi} (v_{z1}{}^2 + v_{\alpha 1}{}^2) v_{z1} r_1 dr d\alpha \right\} \Big/ \frac{\rho}{2} V_{m1}{}^2 Q \end{aligned} \quad (3)$$

The strength of unidirectional swirling flow (dimensionless angular momentum flow rate) M'_{n1} at nth section

$$M'_{n1} = \rho \int_0^{2\pi} \int_0^{r_{wn}} v_{zn} v_{\alpha n} r_n{}^2 dr d\alpha / \rho V_{m1}{}^2 r_{w1}{}^3 \quad (4)$$

The definition of the angle position α_1 at the eccentric center of distorted flow (gravity center position of the flow) in the inlet section

$$\begin{aligned} \alpha_1 &= \tan^{-1}(r_{N1}/r_{P1}) \\ r_{c1}{}^2 &= r_{N1}{}^2 + r_{P1}{}^2 \\ r_{N1}/r_{w1} &= \int_0^{2\pi} \int_0^{r_{w1}} v_{z1} r_1^2 \sin\alpha \, d\alpha dr / \pi V_{m1} r_{w1}{}^3 \\ r_{P1}/r_{w1} &= \int_0^{2\pi} \int_0^{r_{w1}} v_{z1} r_1^2 \cos\alpha \, d\alpha dr / \pi V_{m1} r_{w1}{}^3 \end{aligned} \quad (5)$$

4 Experimental Results and Considerations

4.1 Performance Characteristics of a Twisted *S*-Shaped Bend Diffuser With Equal Divergent Angle.

4.1.1 Relation Between Energy Efficiency and Various Shapes of Bend Diffusers. Figure 6 shows the energy efficiency of various bend diffusers each with equal divergent and connecting angles; data as in Tables 1 and 2. Four bend elements were used. The inlet velocity was Type I. The efficiency when the curvature radius ratio $R/r_{w1} = 6$ is generally higher than when it is 3. Maximum efficiency is obtained when $R/r_{w1} = 6$; $2\chi = 6°$ and connecting angle ϕ_n is between 90° and 180°. Even when the divergent angle is increased to 12° or 18°, the efficiency in the range of $90° \leqq \phi_n \leqq 180°$ becomes higher. On the other hand, when $R/r_{w1} = 3$, the maximum value is obtained when $2\chi = 6°$ and $\phi_n = 90°$, but it becomes smaller with other connecting angles. This trend is observed also when the divergent angle is gradually increased to 12° or 18°, with efficiency being lowered as 2χ is increased. The reason why efficiency is lowered in proportion to ϕ_n between 90° and 180° when $R/r_{w1} = 3$ can be explained as follows. Separation is very likely to occur at the 1st bend outlet because the bend has been sharpened. When $\phi_n = 135°$ and 180°, secondary flow generated by mutual interaction between bends is weakened as compared to $\phi_n = 90°$, and the action to reduce the development of separation becomes weak (see Fig. 10). It is clear from Fig. 6 that high efficiency is obtained using $\phi_n = 90°$ connection when the inlet velocity is Type I. In the following explanations, therefore, the $\phi_n = 90°$ coil diffuser is selected as a representative example of a twisted *S*-shaped bend diffuser, and the correlations among inlet velocity distribution, curvature radius ratio, divergent angle and energy efficiency are studied. A plane bend diffuser with $\phi_n = 0°$ and 180° is not discussed here as it is discussed in detail in another report.

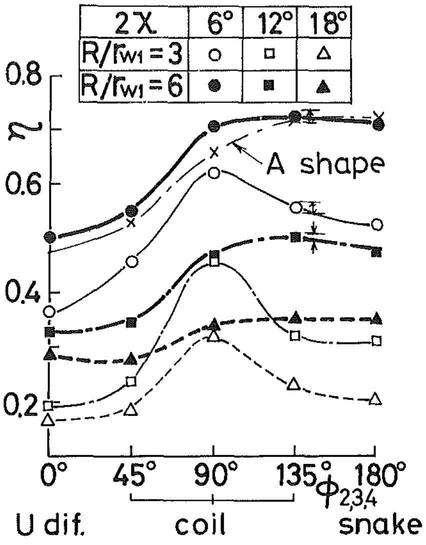

Fig. 6 Inlet velocity Type I. Relation between efficiency η and various shapes of bend diffusers (connecting angle ϕ_n is varied). All four bend elements are connected ($N = 4$) (uncertainty in $\eta = 0.7 \pm 0.01$, ϕ_n, R/r_{w1}, 2χ; see Table 3).

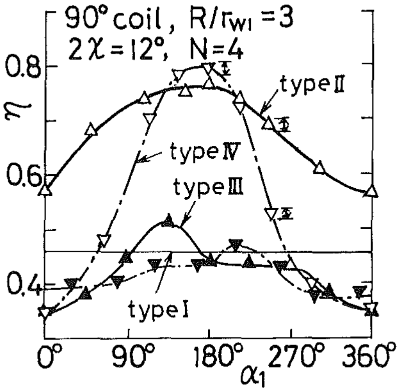

Fig. 7 Relation between efficiency η of 90° coil diffuser and angular position α_1 of high axial velocity zone of distorted flow; inlet velocity: Types II, III, and IV, $N = 4$ (uncertainty in $\eta = 0.7 \pm 0.01$, in $\alpha_1 = 10° \pm 10'$)

4.1.2 Relation Between Energy Efficiency and Inlet Velocity. When the inlet velocity is the distorted flow, such as Types II, III, and IV, the efficiency of the coil bend diffuser changes according to the angular position α_1 (see Fig. 4) of the high axial velocity zone of distorted flow at the inlet section. Figure 7 shows the relation between η and α_1 for any bend shape. High efficiency is obtained when angular position $\alpha_1 \fallingdotseq 180°$ which corresponds to the inner wall of the bend plane. It worsens when α_1 is decreased and reaches its lowest point when $\alpha_1 \fallingdotseq 0°$, the outer wall of the bend plane. This phenomenon is caused by secondary flow which accompanies the distorted flow of Types II and IV. The reason is detailed later in Fig. 13.

In the following explanations, we have adopted the value at inflow angle $\alpha_1 (\fallingdotseq 180°)$, at which energy efficiency reaches

---

[1] Real energy efficiency η_R is defined as $\eta_R = (\pi_n p_{wn} - \pi_1 p_{w1})/(\rho V_{m1}{}^2/2)\{\beta_1 - \beta_n(1/AR)^2\}$. When energy efficiency of the diffuser has a high value and the area ratio AR is large, $\beta_n(1/AR)^2$ will be smaller than 1; i.e., $\beta_n(1/AR)^2 \ll 1$. As a result, real energy efficiency η_R is almost equal to approximately one η, equation (1); see Fig. 17. One-dimensional efficiency η_0 as shown in Fig. 17 is defined as $\eta_0 = (p_{wn} - p_{w1})/(\rho V_{m1}{}^2/2)\{1 - (1/AR)^2\}$.

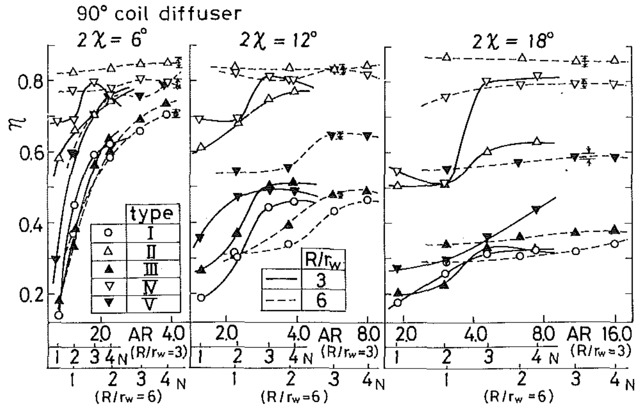

Fig. 8 Relation between efficiency η of 90° coil diffusers and area ratio AR, inlet velocity is varied, Types II and IV; $\alpha_1 = 180°$, Type III; $\alpha_1 = 135°$); (uncertainty in $\eta = 0.7 \pm 0.01$, AR: see Table 1)

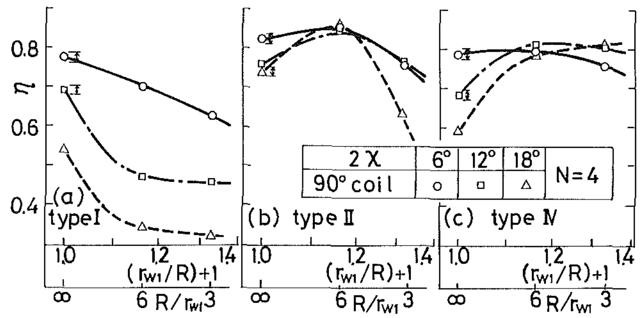

Fig. 9 Relation between the efficiency η of 90° coil diffusers and curvature radius ratio of the bend element R/r_{w1}, $\alpha_1 = 180°$, $N = 4$; inlet velocity: Types I, II, and IV; (uncertainty in $\eta = 0.7 \pm 0.01$, R/r_{w1}, 2χ: see Table 3)

maximum for any bend shape. Figure 8 shows the relation between the efficiency of the 90° coil diffuser and the area ratio when the inlet velocity is changed from Type I to Type V. The divergent angle is 6°, 12°, and 18°, and the curvature radius ratio is 3 and 6. In all these cases, the efficiency is high in Types II and IV and is decreased with Types V and III. It reaches its lowest value with Type I. The smaller the curvature radius ratio is, the greater the change of efficiency according to area ratio. This change reaches its highest value when the divergent angle is 6°. Figure 9 shows the relation between the efficiency of 90° coil diffusers and the curvature radius ratio. In this figure, 90° coil diffusers connected with all four bend elements are compared, while the area ratio of each diffuser varies according to the curvature radius ratio and the divergent angle. In this figure, $R/r_{w1} = \infty$ means a straight-line-type conical diffuser. With inlet Type I, efficiency goes down as the bending of the diffuser element becomes sharper. On the contrary, with Type II, efficiency reaches maximum value when $R/r_{w1} = 6$ and is lowered a little when $R/r_{w1} = 3$. It is interesting to see that, with Type IV, efficiency is increased to $R/r_{w1} = 3$ even when the bending becomes sharper. The reason for this will be explained in the next paragraph, Fig. 14.

4.2 Velocity Distribution of 90° Coil Bend Diffuser.

4.2.1 A Flow in Case of Inlet Velocity Type I. Figure 10 shows a model of Type I flow inside a 90° coil diffuser when $R/r_{w1} = 6$. The velocity profiles approximately correspond with the measured values. Separation is generated near the outlet of the 1st bend, and the deviation of the flow becomes great. When this distorted flow reaches the 2nd bend, it becomes a comparatively strong unidirectional swirling flow for the reason indicated in Fig. 11. The separation at the inlet of the 2nd bend is dragged into the unidirectional swirling flow at the 3rd bend and is moved toward the center of the

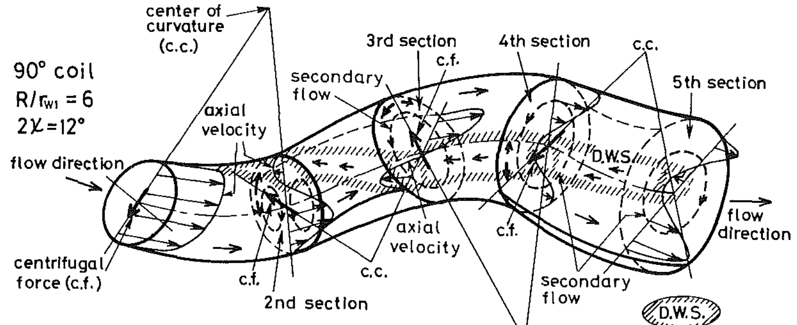

Fig. 10 Flow model of 90° coil diffuser with $R/r_{w1} = 6$ and $2\chi = 12°$; inlet velocity is Type I; $N = 4$

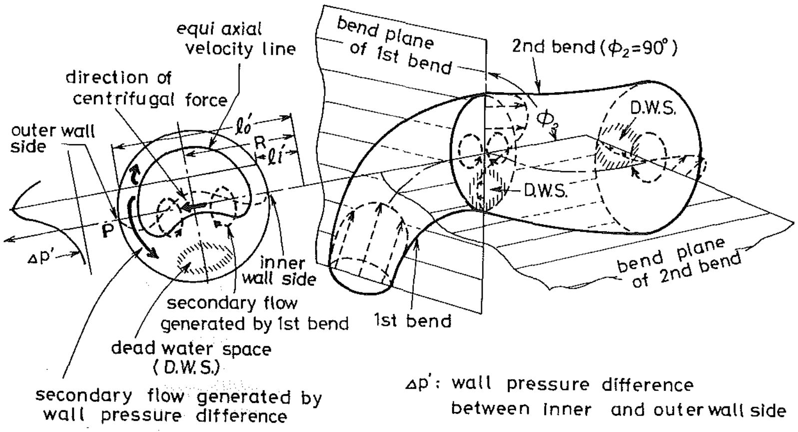

Fig. 11 Explanatory drawing of the generation of unidirectional swirling secondary flow in the 2nd bend of 90° coil diffuser; inlet velocity: Type I

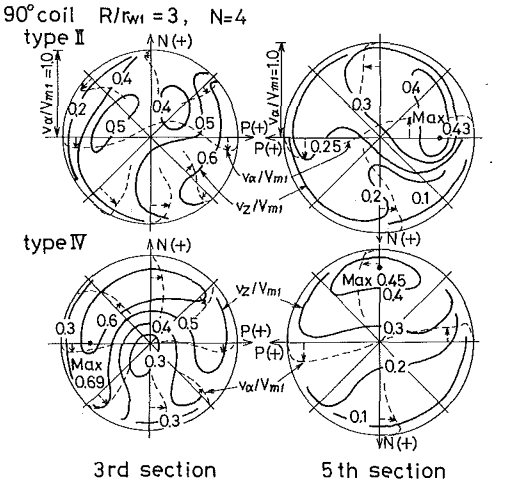

Fig. 12 Velocity distribution in 3rd and 5th sections of 90° coil diffuser with $R/r_{w1}=3$ and $2\chi=12°$; inlet velocity: Types II and IV, $\alpha_1=180°$; (uncertainty in $v_z/V_{m1}=0.6\pm0.01$, in $v_\alpha/V_{m1}=0.2\pm0.003$)

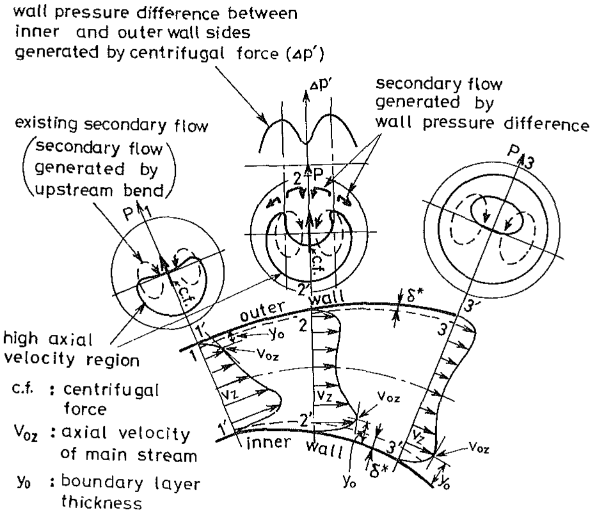

Fig. 13 Explanatory drawing of the generation of secondary flow to suppress separation in the 2nd bend; Type II, $\alpha_1=180°$

pipe. It then forms a reverse flow zone all the way to the bend outlet. The separation at the inlet bend and the reverse flow zone in the middle and downstream region of the diffuser cause a dramatic reduction in energy efficiency. Further, this separation causes a strengthening of the unidirectional swirling flow at the 2nd bend and beyond. This phenomenon is explained by Fig. 11. The left portion of the figure illustrates the equiaxial velocity distribution at the 2nd bend inlet, the operating direction of centrifugal force based on bend curvature, which exerts influence on the flow, and the distribution of dimensionless pressure difference $\Delta p'$ between the inner and outer walls, which is generated by centrifugal force. This can be expressed as

$$\Delta p' = \Delta p/\rho(V_{m1}^2/R) = \int_{l_1'}^{l_0'} [(v_z/V_{m1})^2/l'dl'],\ l' = l/r_{w1}$$

The axial velocity distribution at the 2nd bend inlet is extensively deviated by the separation generated at the 1st bend outlet. Because of this, $\Delta p'$ distribution also becomes extremely asymmetrical to the bending plane of the 2nd bend. Left-right asymmetrical secondary flow is generated by this asymmetrical $\Delta p'$ distribution to the directions shown by the thicker arrows within the boundary layer around the wall surface. This is overlapped by the existing secondary flow, and is turned into unidirectional swirling flow as the stronger flow absorbs the weaker. The size of the separation generated at the 1st bend has a direct influence on the deviation of the flow at the 2nd bend inlet. If the separation is big, the deviation becomes big. As a result, the unidirecitonal swirling flow at the 2nd bend is also strengthened. Consequently, when the separation at the 1st bend is big, strong unidirectional swirling flow is generated; in addition to the loss from separation, friction loss is also increased. Furthermore, discharging kinetic energy is also increased. Hence, energy efficiency is decreased.

4.2.2 Flows in Case of Inlet Velocities Types II and IV. Figure 12 shows the velocity distribution in the 3rd and 5th sections when Type II and Type IV flows are introduced into a 90° coil diffuser with $R/r_{w1}=3$. Unlike the case of Type I, as shown in Fig. 10, neither separation nor any reverse flow zone is generated inside the bend even if the bending is sharper, and the flow streams over the entire section. As a result, energy efficiency is improved. Also, a 90° coil diffuser with a more gentle curvature, $R/r_{w1}=6$, gives similar results. In these circumstances, the reason why separation is not generated in Types II or IV may be explained by Fig. 13. When Type II flow is introduced into the inner wall of 1-1′ section of the 1st bend, $\alpha_1 \doteqdot 180°$, $\Delta p'$ distribution between the inner and outer walls at 2-2′ section a little downstream from 1-1′ section becomes low at the central portion and high at both the right and left sides. By this $\Delta p'$ distribution, secondary flow is generated in the directions shown by thicker arrows within the boundary layer around the wall surface. This is overlapped by the existing secondary flow. As a result, the existing secondary flow is strengthened and occupies all the sections downstream as shown by the broken lines at 3-3′ section. This secondary flow moves high velocity fluid to the inner wall side of the 1st bend, and hinders the generation of separation. Hence, energy efficiency is improved. On the contrary, when the high velocity zone of Type II flow is introduced into the outer wall of the 1st section, $\alpha_1=0°$, the existing secondary flow is strengthened, and the high velocity zone moves to the outer wall side of the 1st bend and low velocity fluid in the boundary layer around the wall accumulates in the inner wall side of the 1st bend due to this strong secondary flow. The force caused by the reverse pressure gradient along the inner wall acts on the accumulated low velocity fluid, and separation develops in the inner wall. Hence, energy efficiency is decreased. In the case of Type IV flow, the flow pattern is similar to that of Type II previously described. However, when the flow is not accompanied by any secondary flow, as in Type III, even though it is the distorted flow, the generation of separation is only slightly hindered even if the high velocity flow streams to the inner wall side of the bend, the efficiency is lessened.

4.2.3. Relation Between Strength of Uniswirling Flow and Inlet Velocity Distributions. Figure 14 shows the change of the strength M_n' in a dimensionless unidirectional swirling flow at 1st-5th sections when flows of Types I, II, and IV are introduced into a 90° coil diffuser of $2\chi=12°$, $R/r_{w1}=3$ and 6. M_n' becomes the strongest in Type I for both the values of curvature radius ratio R/r_{w1}, while it is smaller in Types II and IV, where separation is not generated. Also, in Type IV, M_n' is lowered down to 0.2 or less in the center of the bend. In this way, if swirling is weakened without separation, friction loss is lowered in comparison when there is a strong swirling flow; discharging kinetic energy is also decreased, thus improving efficiency. The reason why efficiency is increased though the curvature radius ratio becomes smaller, as described in Fig. 9, can be explained in terms of these observations. In Fig. 9, M_n', shown by mark • (Type IV′), when a swirling component moving in a direction opposite to the coil winding direction enters the diffuser (the strength of M_n' is the same as in Type

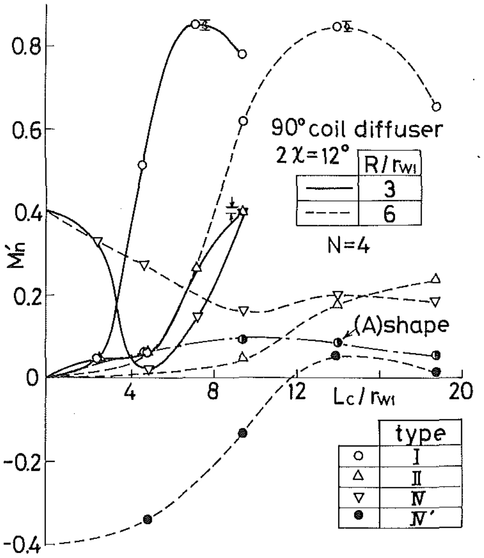

Fig. 14 Change of the strength of swirling flow M_n' moving in a downstream direction in 90° coil diffuser; inlet velocity: Types I, II, IV, and IV'. (A) shape is: $\phi_n = 135°$, $N = 4$ (uncertainty in $M_n' = 0.8 \pm 0.01$; in $L_C/r_{w1} = 10 \pm 0.15$, R/r_{w1}: see Table 3)

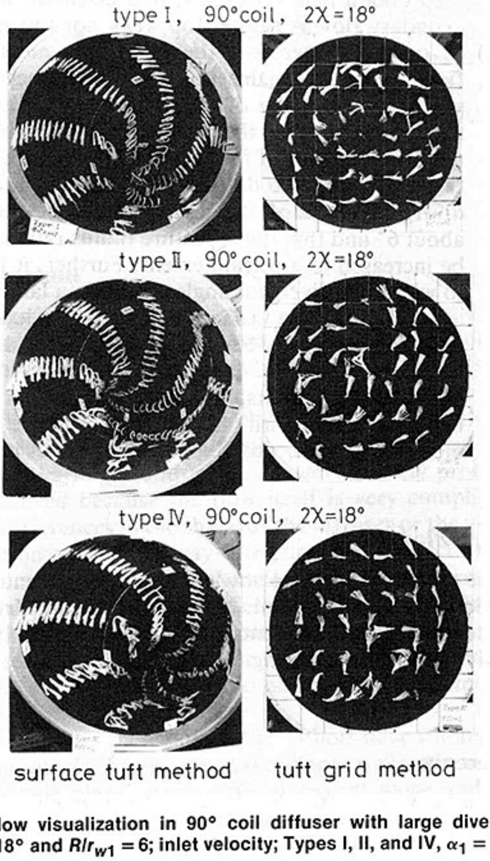

Fig. 15 Flow visualization in 90° coil diffuser with large divergent angle $2\chi = 18°$ and $R/r_{w1} = 6$; inlet velocity; Types I, II, and IV, $\alpha_1 = 180°$; $N = 4$

IV, but the swirling direction is reversed), in the middle of the bend, becomes a swirling flow moving in the coil winding direction. Even when the swirling direction is reversed, the loss is still small and efficiency is also not much lower than in the case of Type IV. Figure 15 shows flow visualization pictures of a 90° coil bend diffuser with a large divergent angle $2\chi = 18°$. The surface tuft method and tuft grid method were used. The types of inlet velocity distribution are Types I, II, and IV. The unidirectional swirling flow pattern can be clearly seen.

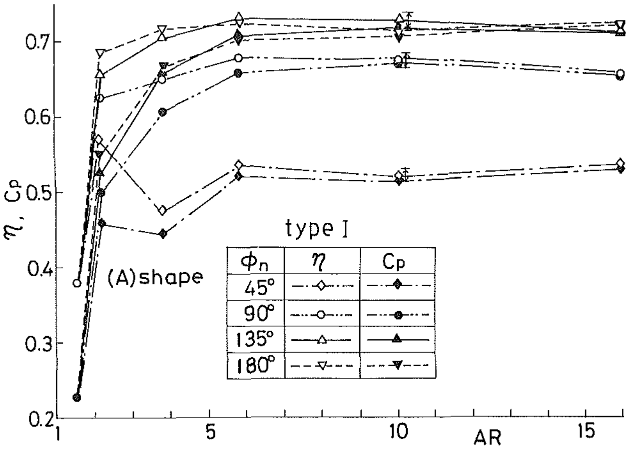

Fig. 16 Relation between area ratio AR and efficiency η (white mark) or pressure recovery coefficient C_p (black mark) of modified (A)-shaped diffusers (Table 3). Connecting angle ϕ_n is varied; (uncertainty in $\eta = 0.7 \pm 0.01$, in $C_p = 0.7 \pm 0.01$, AR, ϕ_n: see Table 3)

4.3 Performance of a Modified Type Twisted S-Shaped Bend Diffuser (Energy Efficiency and Velocity Distribution).

4.3.1 How to Design High Performance Twisted S-Shaped Diffusers. The shape of the diffuser as discussed in the preceding paragraph is as follows: A straight-line diffuser with an equal divergent angle was bent into a *U*-shape with a fixed curvature radius ratio. It was further divided into four equal parts by every 45°, and these four bend elements were connected together with equal connecting angles. The feature of this shape is that secondary flow is generated as a result of mutual interference between bend elements and this acts to suppress the expansion of separation after the generation of secondary flow and to improve diffuser performance. There are, however, limitations on performance improvement because the separation generated at the 1st and 2nd bends on the upstream side cannot be suppressed with Types I and III inlet velocity distributions. Taking this into account, a high efficiency diffuser is proposed in this paragraph, in which the aforementioned defects are excluded as far as is practical. With this kind of diffuser, diffuser efficiency can be improved by hindering the generation of separation at the 1st bend. One way of achieving this is to connect a bend element with a comparatively gentle curve and a small divergent angle to the upstream portion. The divergent angle is gradually widened as the secondary flow develops and the area ratio is increased. In this case, the bending on the downstream side may be sharp.

4.3.2. Experiment Results of High Performance Twisted S-Shaped Bend Diffuser. Based on the foregoing method, the (*A*)-shaped diffuser with a high efficiency, as shown in Table 3, was studied as a representative example of such diffusers. In Fig. 16, the energy efficiency of the (*A*)-shaped diffuser (six bend elements connected) is shown as a white mark. For reference purposes, the pressure recovery coefficient C_p is shown as a black mark. Connection status; $\phi_n = 45°$ coil, $\phi_n = 90°$ coil, $\phi_n = 135°$ coil and $\phi_n = 180°$ wave shape diffusers; inlet velocity distribution is Type I. High efficiency is obtained under all bending conditions when $\phi_n > 45°$. Maximum value is attained when $\phi_n = 135°$ or $\phi_n = 180°$, and it reaches 73 percent when the area ratio $AR = 8$–16. This value is 26 percent higher than the efficiency (47 percent) of a 90° coil diffuser with $2\chi = 12°$, $R/r_{w1} = 6$, $AR = 8$ as shown in Fig. 6. It also is approximately equal to the efficiency of 90° coils, 135° coils and 180° wave-shape diffusers with $2\chi = 6°$, $R/r_{w1} = 6$, $AR = 4$, 72–73 percent; see Fig. 6. In other words, these results mean that the area ratio can be increased by 2 to nearly 4 times without lowering the efficiency.

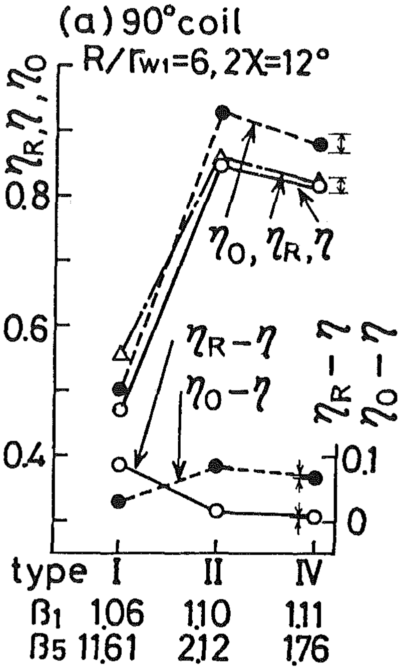

Fig. 17 Comparison of real energy efficiency η_R, approximated energy efficiency η and one-dimensional energy efficiency η_0; see equation (1) and footnote #1; (uncertainty in η_E, η, η_0 = 1.0 ± 0.015)

When inlet velocity distributions are Type II, Type IV, and Type V, the maximum and the minimum values, $\eta_{\max}$ and $\eta_{\min}$, of modified type coil diffuser (*A*) are described as the following (the figure is omitted to shorten the paper). $\eta_{\max} = 0.86$ at $\phi_n = 135°\text{-}225°$ and $\eta_{\min} = 0.78$ at $\phi_n = 270°$ in Type II, $\eta_{\max} = 0.8$ at $\phi_n = 180°\text{-}225°$ and $\eta_{\min} = 0.73$ at $\phi_n = 90°$ in Type IV, and $\eta_{\max} = 0.88$ at $\phi_n = 180°$ and $\eta_{\min} = 0.71$ at $\phi_n = 90°$, respectively. In the foregoing results, the efficiencies are more improved, and the difference between the maximum and the minimum values is very small.

The difference between the flow in the (*A*)-shaped diffuser and the flow in the 90° coil diffuser before modification, as shown in Fig. 10, lies in the separation which develops after the 2nd section and in the strength of the generated unidirectional swirling flow; see Fig. 14. We can say therefore that the separation generated at the 2nd section in the 90° coil diffuser before modification does not fade away at the 3rd section but is sustained all the way down to the diffuser outlet in the form of a reverse flow zone at the center of the pipe, and energy efficiency is thus decreased. On the otherhand, with the (*A*)-shaped diffuser [3], the weak separation which is generated at the 2nd section disappears on or around the 3rd section due to secondary flow, and the expansion of the separation is hindered. Further, the strength of the secondary swirling flow generated inside the bend is also weakened (see Fig. 14). Consequently, the efficiency of the (*A*)-shaped diffuser is raised. When the flow in the (*A*)-shaped diffuser is of Types II, IV, and V, the flow is further improved compared with Type I. The separation at the 2nd section disappears and the flowing condition is extremely good. Therefore, high energy efficiency is obtained as previously mentioned.

5 Conclusion

From the foregoing study on the performance of twisted *S*-shaped bend diffusers and internal flow, the following conclusions have been drawn.

(1) Energy efficiency varies in a complicated manner according to the inlet velocity distribution, curvature radius ratio, and divergent angle of the bend element. It roughly corresponds to the following two types of flow:

(*a*) When substantial separation is generated in the upstream portion of the diffuser, distortion of the flow is increased by this separation, and a strong unidirectional swirling flow is produced because of a corresponding growth in the mutual interaction between bend elements. Consequently, in addition to the loss due to separation, wall surface friction loss and discharge loss are increased, and energy efficiency is thus decreased.

(*b*) On the contrary, when separation is not generated in the upstream portion of the bend, distortion of the flow is small and mutual interaction between bend elements is weakened. The unidirectional swirling flow also becomes weak. For this reason, the aforementioned losses are small, and energy efficiency shows a high value of 80 percent or more. In order to obtain high efficiency, it is essential that the secondary flow is neither too weak nor too strong.

(2) In order to overcome the previously mentioned difficulties and to maintain energy efficiency at a high value for any value of inlet velocity distribution, it is necessary to hinder the generation of separation in the upstream portion of the bend or to minimize the size of this separation. To do this, it is recommended that the divergent angle of the diffuser inlet be decreased to about 6° and that the curvature radius ratio of the bend be increased to a certain extent. Further, it is desirable to widen the divergent angle to obtain a large area ratio as secondary flow inside the bend is developed. In this case, curvature may be made sharper in the downstream portion as required. If full consideration and care are given to these points, it is quite possible to produce a bend diffuser with higher performance than the modified diffuser described in the present report.

Acknowledgment

The authors greatly acknowledge the support and assistance provided by Mr. M. Yasui, Mr. M. Kato, and Mr. A. Saito, Graduate Research Students of Mie University, Department of Mechanical Engineering.

References

1 Shimizu, Y., et al., May 1981, "Studies on Three-Dimensional Curved Diffusers," *Transaction of JSME*, Vol. 47-417B, pp. 729–738 (in Japanese).

2 Shimizu, Y., et al., April 1983, "Studies on *U*-Bend and Snake-Bend Diffusers," *Transaction of JSME*, Vol. 49-440B, pp. 747–756 (in Japanese).

3 Shimizu, Y., et al., December 1984, "Studies on the Twisted *S*-Shaped Bend Diffusers With High Energy Efficiency," *Transaction of JSME*, Vol. 50-460B, pp. 2935–2942 (in Japanese).

Yukimaru Shimizu
Associate Professor.

Makoto Nagafusa
Graduate Student.

Koichi Sugino
Assistant.

Department of Mechanical Engineering,
Mie University,
Kamihama-cho, Tsu-shi,
Mie-ken, Japan 514

Takashi Kubota
Chief Engineer,
Fuji Electric Co.,
Tanabeshinden, Kawasaki-ku,
Kawasaki-shi, Kanagawa-ken,
Japan 210

Studies on Performance and Internal Flow of *U*-Shaped and Snake-Shaped Bend Diffusers: 2nd Report

This paper describes the relation between bend diffuser characteristics and internal flow. Diffusers were bent into U *and snake shapes within the limitation of a single plane. In these experiments, area ratio, divergent angle and curvature radius ratio of bend elements were varied. Five types of inlet velocity profiles also were used, and their effects on diffuser performance and internal flow were investigated in detail. The following is a report on the fruitful and interesting results we have obtained.*

1 Introduction

Several studies [1-4] on bend diffusers have been published in the past. For example, the study by Sprenger [1] on the pressure recovery characteristics and internal flow of a single bend with a small bending angle. The present authors have also published a study [2] on the characteristics of the twisted *S*-shaped bend diffuser. The bend diffuser has thus been studied from various standpoints. However, many problems remain unsolved because the flow itself is very complicated and slight differences in the shape of the diffuser or the velocity distribution at the inlet may often have a big effect on diffuser characteristics. Typical examples of such problems are the relation between bend diffuser shape and the secondary flow, the relation between the separation inside the bend diffuser and secondary flow, and the influence of the divergent angle or the curvature radius ratio on diffuser characteristics and internal flow.

In order to clarify these points, the authors have studied diffusers, bent into *U*-shapes and snake-shapes within the limitation of a single plane. Area ratio, divergent angle and curvature radius ratio of bend elements were varied along with the velocity distribution at the inlet in an experimental study on the relation between diffuser characteristics and internal flow. The following is a report on the fruitful and interesting results we have obtained.

2 Experiment Method and Apparatus

In this experiment, the apparatus shown in Fig. 1(*a*) was used. To measure energy efficiency, a sample diffuser was submerged in an open-top water tank without a tailpipe. Figure 1(*b*) shows examples of the sample *U* bend diffuser (with bend elements connected in the same bending direction, $\phi_n = 0°$) and the snake bend diffuser (bend elements alternately connected in reverse direction, $\phi_n = 180°$). When the area ratio was changed, the number of connected bend elements N was changed. There were three different angles 2χ : 6°, 12° and 18°. Curvature radius ratio R/r_{w1} of the bend element was 3 or 6 (see Table 1). To measure the velocity distribution inside the diffuser, a cylindrical Pitot tube with three holes was used, and the measurement was carried out on the connecting section of the bend element. In this case, the diffuser outlet was fixed onto the outer wall of the water tank. As the flow was not uniform, measurement was made from four directions: *P*, *NP*, *N* and *PN*; see Fig. 2. In the present study, the flow as observed in the pipeline or at the outlet portion of fluid machinery, was roughly divided into 5 types, and was used for diffuser inlet velocity distribution. In Fig. 3, velocity distribution for Types I-V is schematically illustrated.[1]

3 Formulas to Represent Results of the Experiments

Diffuser real energy efficiency is defined as follows:

$$\eta_R = (\pi_n p_{wn} - \pi_1 p_{w1})/[(\rho V_{m1}{}^2/2)\{\beta_1 - \beta_n(1/AR)^2\}] \qquad (1)$$

where β_1 and β_n express the kinetic energy correction coefficients at diffuser inlet and outlet. π_1 and π_n express the pressure correction coefficients at inlet and outlet.

Contributed by the Fluids Engineering Division for publication in the JOURNAL OF FLUIDS ENGINEERING. Manuscript received by the Fluids Engineering Division April 12, 1985.

---

[1] For details of the generating method of the 5 types of velocity distribution, see the 1st Report: Fig. 5, Table 4 or reference [2].

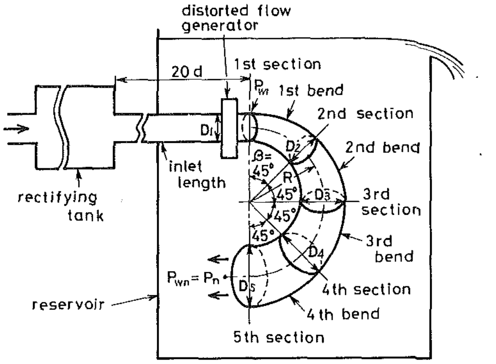

Fig. 1(*a*) Schematic diagram of experiment apparatus

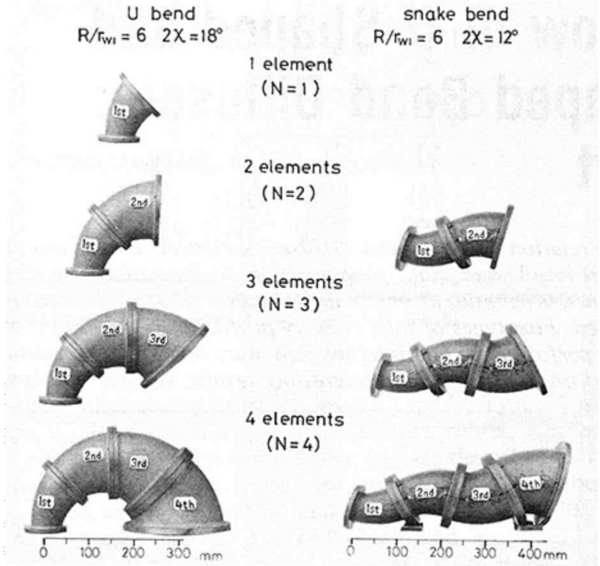

Fig. 1(*b*) Sample *U* and snake bend diffusers, see Table 1

$$\beta_1 = \left\{ \frac{\rho}{2} \int_0^{r_{w1}} \int_0^{2\pi} (v_{z1}{}^2 + v_{\alpha 1}{}^2) v_{z1} r_1 dr\, d\alpha \right\} \Big/ \frac{\rho}{2} V_{m1}{}^2 Q \tag{2}$$

$$\pi_1 = \int_0^{r_{w1}} \int_0^{2\pi} p\, v_z\, r\, dr\, d\alpha / p_{w1} Q \tag{3}$$

In the present report, the approximated value of η_R, where β_n and π_n are approximated to 1,

$$\eta = (p_{wn} - \pi_1 p_{w1})/(\rho V_{m1}{}^2/2)\{\beta_1 - (1/AR)^2\} \tag{4}$$

Table 1 Area ratio of each section of bend diffuser; Uncertainty in $R/r_{w1} = 6 \pm 0.1$, in $AR = 15.9 \pm 0.3$

bend curvature ratio R/r_{w1}	3	6	3	6	3	6
	$2\chi=6°$ diffuser area ratio AR		$2\chi=12°$ diffuser area ratio AR		$2\chi=18°$ diffuser area ratio AR	
2nd section	1.3	1.5	1.6	2.2	1.9	3.1
3rd section	1.6	2.2	2.3	3.8	3.1	6.3
4th section	1.9	2.9	3.1	5.8	4.6	10.6
5th section	2.3	3.8	4.0	8.2	6.2	15.9

Diameter of inlet section ($=2r_{w1}$) : 0.054 m

Length of one bend element : in case of $R/r_{w1}=3$: $2\pi R/8 \approx 0.0636$ m

in case of $R/r_{w1}=6$: $2\pi R/8 \approx 0.127$ m

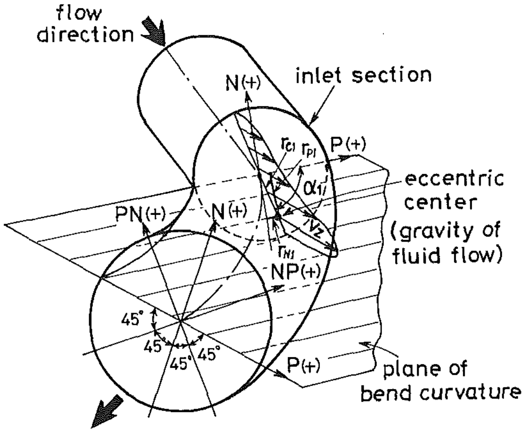

Fig. 2 Definitions of measuring directions (*P*, *NP*, *N* and *PN*) of velocity distribution and angle position α_1 at the eccentric center in the inlet section of the bend diffuser

was used. β_1 and π_1 are shown in Fig. 3. η_R and η are compared to Fig. 4.[2] The difference between the values is small when the energy efficiency is high. As a result, approximate energy efficiency η is used, representatively, in the following, and is called energy efficiency or efficiency. Angle position α_1 of the eccentric center (gravity center position of the flow) of distorted flow at the inlet section and the strength of unidirectional swirling flow (dimensionless angular momentum flow

---

[2] One-dimensional energy efficiency η_0 is defined as follows: $\eta_0 = (p_{wn} - p_{w1})/(\rho\, V_{m1}{}^2/2)\{1-(1/AR)^2\}$.

Nomenclature

AR = area ratio between inlet and outlet, $= (r_{wn}/r_{w1})^2$, Table 1

D_n = diameter of nth section, $= 2r_{wn}$, Table 1, Fig. 1(*a*)

N = number of bend elements

p_{w1}, p_{wn} = mean wall pressure at inlet and outlet, Fig. 1

p_{tn} = total pressure at radius r in nth section

Q = flow rate measured from orifice

R = curvature radius of bend diffuser element

V_{m1} = mean axial velocity at inlet section, $= Q/\pi\, r_{w1}{}^2$

$v_{zn}, v_{\alpha n}$ = axial and peripheral velocities

y_0 = thickness from wall surface to outer end of boundary layer

δ^* = displacement thickness of boundary layer

ρ = fluid density

ϕ_n = connecting angle of both $(n-1)$th and nth bend elements ($\phi_n = 0°$: *U* bend diffuser and $\phi_n = 180°$: snake bend diffuser)

2χ = apparent divergent angle of bend diffuser element

Subscript

n = number of section

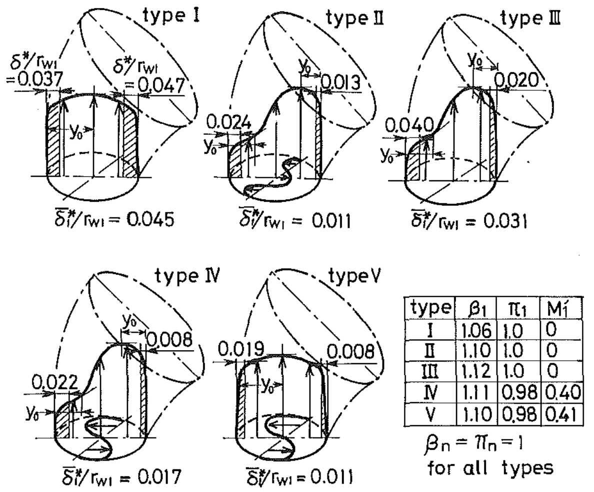

type	β_1	π_1	M_1'
I	1.06	1.0	0
II	1.10	1.0	0
III	1.12	1.0	0
IV	1.11	0.98	0.40
V	1.10	0.98	0.41

$\beta_n = \pi_n = 1$
for all types

Fig. 3 Five types of inlet velocity distribution as used in the experiment; δ^*_1; mean displacement thickness (mean value at 8 measuring points on the periphery of inlet (1st) section); uncertainty in δ^*/r_{w1} = 0.047 ± 0.0007, in δ^*/r_{w1} = 0.045 ± 0.0007

rate) M_1' are expressed by the following formulas. The clockwise rotation from $P(+)$-axis is regarded as positive; see Fig. 2.

$$\left.\begin{aligned} \alpha_1 &= \tan^{-1}(r_{N1}/r_{P1}) \\ r_{C1}{}^2 &= r_{N1}{}^2 + r_{P1}{}^2 \\ r_{N1}/r_{w1} &= \int_0^{2\pi}\int_0^{r_{w1}} v_{z1} r_1{}^2 \sin\alpha \, d\alpha \, dr/\pi \; V_{m1} r_{w1}{}^3 \\ r_{P1}/r_{w1} &= \int_0^{2\pi}\int_0^{r_{w1}} v_{z1} r_1{}^2 \cos\alpha \, d\alpha \, dr/\pi \; V_{m1} r_{w1}{}^3 \end{aligned}\right\} \quad (5)$$

$$M_1' = \rho \int_0^{2\pi}\int_0^{r_{w1}} v_{z1} v_{\alpha 1} r_1{}^2 dr \, d\alpha/\rho \; V_{m1}{}^2 r_{w1}{}^3 \quad (6)$$

4 Experiment Results and Considerations

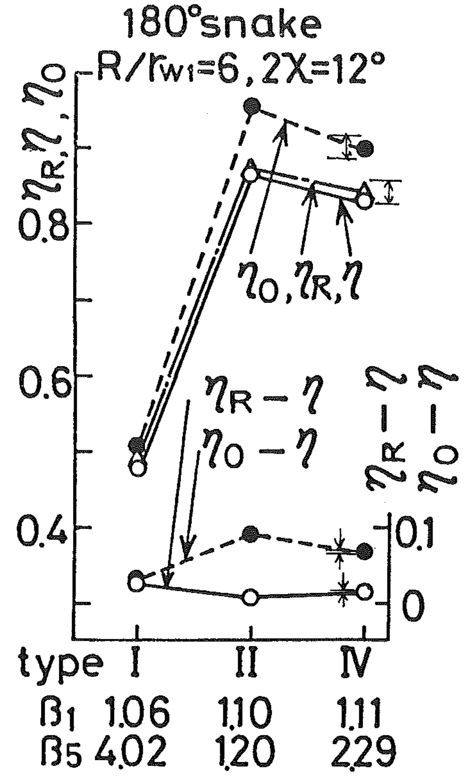

Fig. 4 Comparison of real, one-dimensional and approximate energy efficiencies η_R, η_0 and η; uncertainty in η_R, η_0, η = 0.9 ± 0.014

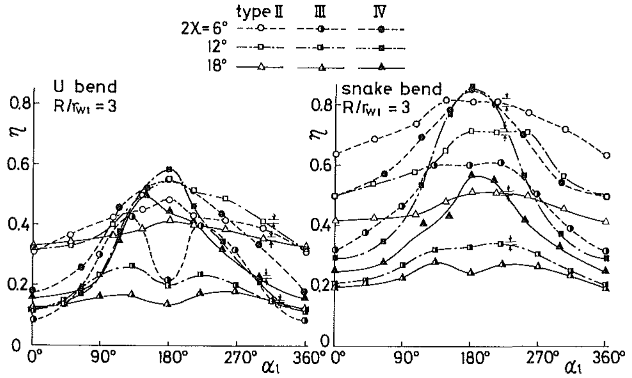

Fig. 5 Relation between efficiency η and the angle of the eccentric center's position α_1 (high velocity zone) at the inlet section; $N = 4$ (four bend elements connected). This figure shows the results for both U and snake bend diffusers; uncertainty in $\eta = 0.8 \pm 0.012$, in α_1 = 10° ± 10′.

4.1 Energy Efficiency. *4.1.1 Relation Between Efficiency and Distorted Inlet Flow.* When the flow enters the bend diffuser, its efficiency shows complex variations according to the angle position α_1 of the eccentric center of distorted flow at the inlet as defined in Fig. 2. Figure 5 shows the relation between α_1 and efficiency for both U bend and snake bend diffusers. From this figure, it is clear that efficiency varies greatly according to the angle position α_1 on the inlet section, to which the eccentric center of distorted flow (high axial velocity zone) comes up. This is closely related to the generation of secondary flow in the diffuser. The relation between α_1 and efficiency also depends a great deal upon the type of secondary flow which goes with the flow at the inlet portion. In other words, for all U and snake bend diffusers with inlet flow Types II and IV, efficiency is increased when the high-speed zone of distorted flow streams into the inner side (α_1 = 180°) of the 1st bend, and is lowered when the flow streams into outer side of this bend (α_1 = 0°). The reason is briefly explained as follows: In the case of Types II and IV, the secondary flow[3] which suppresses separation at α_1 = 180° is generated, while the secondary flow which promotes separation is generated at α_1 = 0°. With inlet flow Type III, the angle position α_1, at which efficiency becomes maximum, deviates to 135° or 225°. The reason for this is that the Type III flow is distorted, but is not accompanied by any secondary swirling component. In this case, efficiency is far below that of Types II or IV. So far, we have studied inflow angle position α_1 and efficiency. The experimental results (explained in the following mentioned figures) relate to α_1, which indicates maximum efficiency.

4.1.2 Relation Between Efficiency and Area Ratio. Figure 6 shows the relation between efficiency η and area ratio AR on the U bend diffuser (or U diffuser) and snake bend diffuser (or snake diffuser). As regards to the U diffuser, when efficiency is as high as 80 percent, η reaches its maximum value on a small area ratio AR. As AR is increased, η tends to decrease gradually. In such a case, as we will report in

---

[3] Separation-suppressing-type secondary flow is the secondary flow which pushes the flow into the inner side of the bend. The reason why such a secondary flow is generated is not explained here because it is described in detail in the 1st Report, Fig. 13.

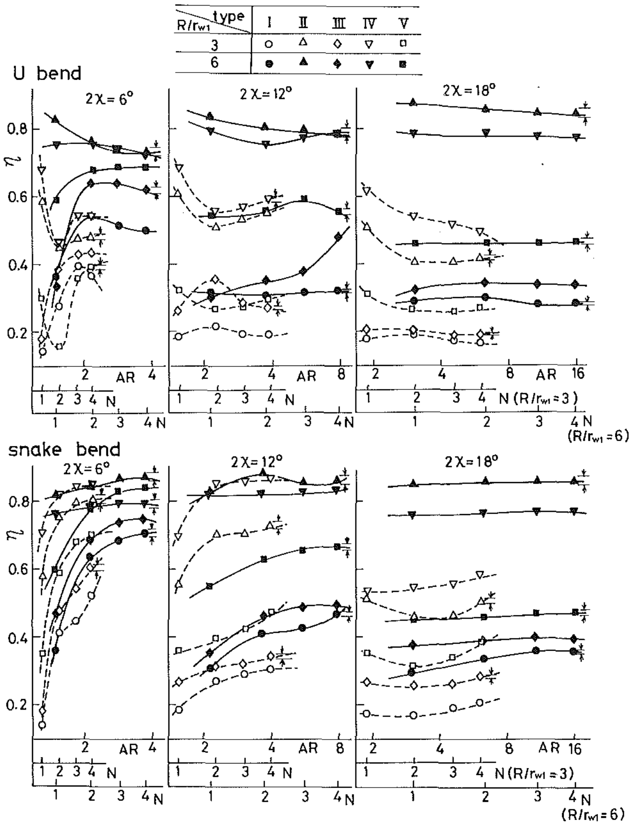

Fig. 6 Relation between efficiency η and area ratio AR for U and snake bend diffusers (Types II and IV: α_1 = 180°, Type III: α_1 = 135°); uncertainty in η = 0.8 ± 0.012, in AR = 16 ± 0.3

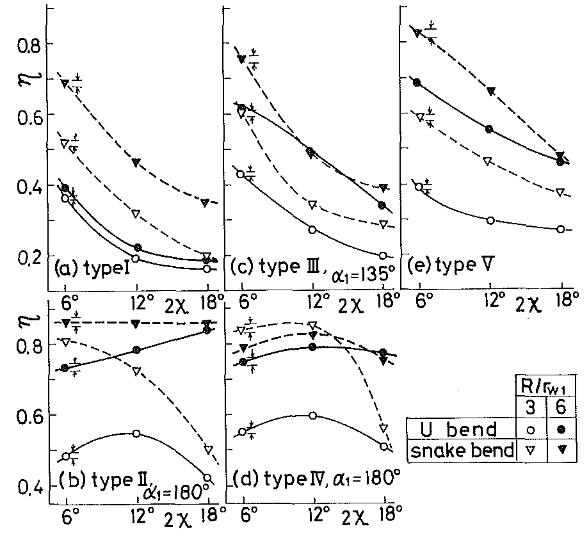

Fig. 7 Relation between efficiency η and divergent angle 2χ for U and snake bend diffusers with inlet Types I, II, III, IV and V. N = 4 (four bend elements connected); uncertainty in η = 0.8 ± 0.012, in 2χ = 12° ± 10′.

detail later (Figs. 11 and 12), separation in the diffuser is not generated upstream but in a far downstream section. In this downstream section, however, the flow velocity is drastically reduced, and the influence of the separation on efficiency is relatively small. When efficiency is 70 percent or lower and the divergent angle is small, 2χ = 6°, efficiency changes dramatically according to AR. As the divergent angle is increased, the change of efficiency becomes smaller, and reaches an almost constant value at 2χ = 18°. Such changes are closely related to the generation of separation inside the diffuser.

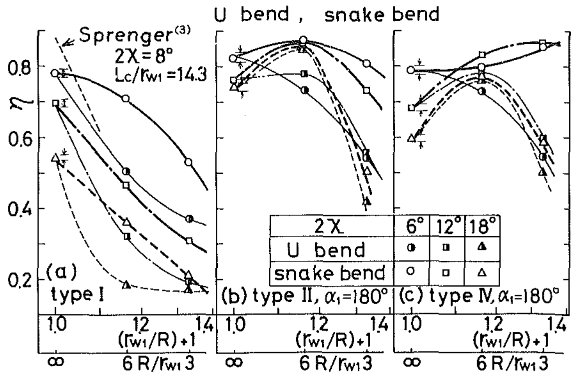

Fig. 8 Relation between efficiency η and curvature radius ratio R/r_{w1} or curvature $(r_{w1}/R + 1)$ for U and snake bend diffusers with inlet Types I, II and IV; uncertainty in η = 0.8 ± 0.012, in R/r_{w1} = 6.0 ± 0.1

We will discuss separation later (Fig. 12). In the case of the snake diffuser, the bend element N = 1 is exempted because it corresponds to the U diffuser. Here, we shall consider $N \geqq 2$. The changes in η are relatively uniform, and the changes according to AR are small in both high and low efficiencies. The reason why the change, according to AR, is small in the case of the snake diffuser will be explained later (Fig. 12). When separation occurs at the 1st bend, such separation does not fade away but continues to exist all the way downstream to the outlet of the diffuser. If this separation at the 1st bend is prevented, the secondary flow ceases to cause any separation, which might have occurred because of the snake bending. In short, any separation in the diffuser is remakably influenced by the existence of separation at the 1st bend. If the length of the diffuser is short, the flow inside the U and snake bend diffusers varies greatly according to the existence of separation. There is no substantial difference caused by the shape of the bend. If the length of the diffuser is long, however, efficiency is closely related to the shape of the diffuser, even if separation occurs in the inlet portion, the flow inside the diffuser stands under a constant moving condition corresponding to the shape of the diffuser. Therefore, we will discuss efficiency with regard to each different shape of diffuser where N = 4, i.e., four bend elements are connected.

4.1.3 Relation Between Efficiency and Divergent Angle. In Fig. 7, the relation between efficiency η and divergent angle 2χ is illustrated for U and snake diffusers. For inlet velocity Types I, III, and V, as shown in Fig. 7(a, c, e), the relation between η and 2χ is similar when the curvature radius ratios R/r_{w1} = 3 and 6, and η is decreased as 2χ is increased. On the other hand, the trends of Types II and IV, Fig. 7(b, d), are different. In U and snake diffusers with a curvature radius ratio R/r_{w1} = 6, efficiency is not decreased even if the divergent angle is widened from 12° to 18°. On the contrary, it may sometimes be increased. The reason for such an increase of efficiency when the divergent angle is widened can be explained as follows: When the flow inside the diffuser shows almost no separation all the way downstream, the swirling flow which occurs at the inlet portion is decreased downstream in the diffuser, because the area of the section is enlarged, the length of periphery is long and the friction effect increases. The ratio of this decrease becomes greater as the angle is widened. In other words, the greater the divergent angle, the weaker the strength of the swirling at the outlet portion. As the conversion ratio of kinetic energy to pressure energy increases, so efficiency is increased in a like proportion. In a diffuser with a curvature radius ratio R/r_{w1} = 3, η is increased up to 2χ = 12°. When it reaches 2χ = 18°, the separation on the inner sidewall of the bend plane can no longer be suppressed, and η begins to decrease rapidly.

4.1.4 Relation Between Efficiency and Curvature Radius

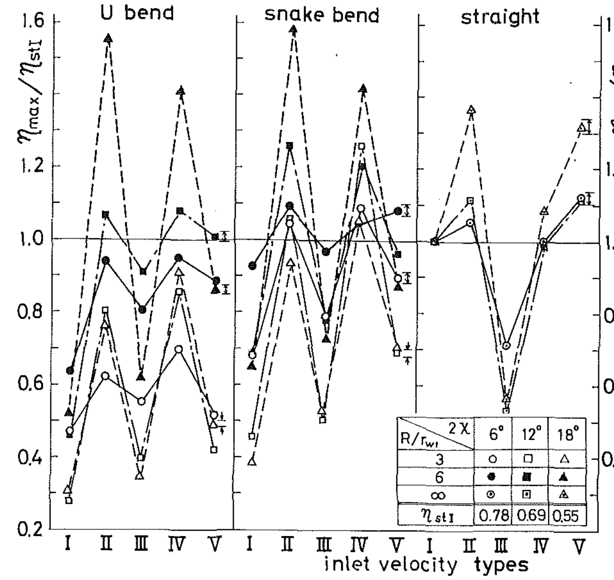

Fig. 9 Comparison of dimensionless efficiency $\eta_{max}/\eta_{st\,I}$ in *U* bend, snake bend, and straight conical diffusers with inlet velocity Types I, II, III, IV and V. N = 4; $\eta_{st\,I}$ = efficiency of each straight conical diffuser in inlet velocity Type I; η_{max} = maximum efficiency of each diffuser with inlet velocity varied (Types II and IV: α_1 = 180°, Type III: α_1 = 135°); Uncertainty in $\eta_{max}/\eta_{st\,I}$ = 1.3 ± 0.02.

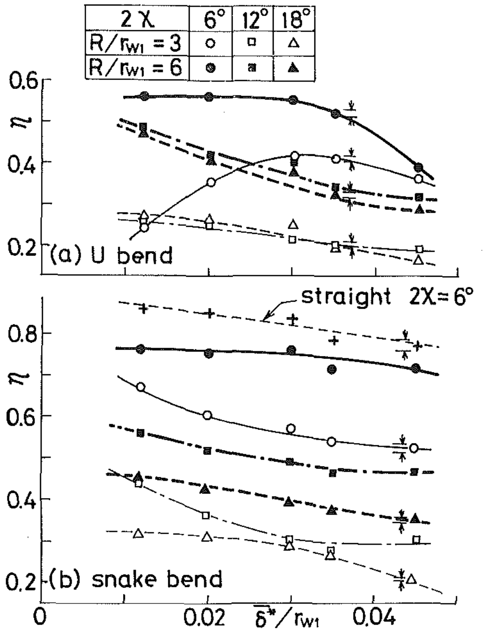

Fig. 10 Relation between efficiency η and mean displacement thickness δ^*_1/r_{w1} in the inlet section of *U* and snake bend diffusers when inlet velocity distribution is uniform (similar to Type I) with no swirling component. N = 4. Uncertainty in η = 0.8 ± 0.012, in δ^*_1/r_{w1} = 0.045 ± 0.007.

Ratio of a Bend Element. Using Fig. 8, we shall now consider the influence of the curvature radius ratio R/r_{w1}. Figure 8 shows how efficiency changes when the curvature of the bend element is increased from $R/r_{w1} = \infty$ to $R/r_{w1} = 3$ having the sharpness of a turn. The diffuser with $R/r_{w1} = \infty$ corresponds to a straight conical shape. The relation between η and R/r_{w1} is complicated, while the trend of change can be roughly divided into the three following tendencies: 1 Monotonously decreasing tendency; 2 Monotonously increasing tendency; 3 Maximum value tendency showing maximum value at $R/r_{w1} = 6$. In the case of inlet velocity, Type I, as shown in Fig. 8(*a*), tendency 1, the same monotonously decreasing tendency occurs with any of the diffuser shapes. In this figure, the result obtained by Sprenger using a *U* bend diffuser of $2\chi = 8°$ [1] is compared; this is quite similar to the value of $2\chi = 6°$. Inlet velocity Type II, as shown in Fig. 8(*b*), corresponds to tendency 3, the change of maximum value tendency. In Type IV, as shown in Fig. 8(*c*), tendency 3 – maximum value tendency and tendency 2 – monotonously increasing tendency are mingled. Tendency 2 – monotonously increasing tendency – is often seen in the snake diffuser, while the *U* diffuser is almost always of maximum value type. η is often bigger than the value of the straight diffuser ($R/r_{w1} = \infty$) by 10-20 percent. The reason for this is that, as the result of mutual interaction between bend elements, secondary swirling flow occurs inside the diffuser and the separation-suppressing effect is increased. From the foregoing observation, it can be demonstrated that separation can be prevented, without using any special device, but simply by generating adequate secondary flow inside the diffuser and by properly combining inlet velocity type with diffuser shape.

4.1.5 Comparison Among Efficiencies of U-Bend, Snake-Bend and Straight Conical Diffusers. Figure 9 shows $\eta_{max}/\eta_{st\,I}$, which is obtained by dividing the maximum value η_{max} of the efficiencies in *U* bend, snake bend and straight conical diffusers with each of the inlet velocity types by the value $\eta_{st\,I}$ of each straight conical diffuser of inlet velocity Type I. The value of $\eta_{st\,I}$ in relation to the divergent angle is described in this figure. The value of $\eta_{max}/\eta_{st\,I}$ varies according to diffuser shape and curvature radius ratio, while a high value is obtained with inlet Types II or IV for any of the diffuser shapes. As is evident from this figure, it also is difficult to discern which type, II and IV, is superior to the other. With inlet Types I and III, $\eta_{max}/\eta_{st\,I}$ is lessened. In the straight conical diffuser at the right, separation can be effectively prevented and efficiency is higher in the case of Type V, where axial velocity distribution is uniform and unidirectional swirling is contained. In *U* and snake bend diffusers, however, efficiency is higher in Types II or IV, where axial velocity distribution is not uniform and the secondary swirling component is contained; due to the interaction of the bend elements, the secondary swirling component is strengthened and separation is more easily prevented.

4.1.6 Relation Between Efficiency and Inlet Displacement Thickness. Figure 10 shows the relation between efficiency and inlet displacement thickness $\bar{\delta}^*/r_{w1}$ for inlet velocity Type I. Except for the mark ○,[4] efficiency is at the highest when displacement thickness is thin ($\bar{\delta}^*/r_{w1} = 0.012$) for *U* and snake diffusers, while it is decreased as $\bar{\delta}^*/r_{w1}$ is increased. The ratio of decrease depends upon shape of the bend. This relation between efficiency and $\bar{\delta}^*/r_{w1}$ is very similar to that of the straight conical diffuser, which is shown in Fig. 10(*b*) by a broken line with the mark +.

4.2 Velocity Distribution Inside the Diffuser. *4.2.1 In Case of U Bend Diffusers.* Figure 11 shows equiaxial velocity lines and peripheral velocity distributions in each of the 1st, 3rd and 5th sections (see Fig. 1) inside the *U* bend diffuser. The inlet velocity is Types I, II and IV. It is obvious from Fig. 11 that, when efficiency is increased, in Types II and IV, almost no separation occurs as far as the 3rd section in the middle of the diffuser. Figure 12(*a*) shows the separation area ratio from 1st-5th sections in the *U* diffuser, including inlet velocity Type V, which was omitted in Fig. 11. With inlet

---

[4] The *U*-bend diffuser (with $2\chi = 6°$ and $R/r_{w1} = 3$ marked by ○) shows a different trend from the others. The reason for this is unknown. The velocity distribution in a *U* bend diffuser with $R/r_{w1} = 3$ could not be measured because of the restrictions on the shape of the bend.

velocity Type I, the separation area reaches 40-60 percent of the total sectional area when AR is larger than 4, and efficiency is lowered. With Types II and IV, when $\alpha_1 = 180°$, however, it decreases 15-40 percent (see marks □, ◨, △), and efficiency is relatively improved. On the contrary, when $\alpha_1 = 0°$, separation reaches nearly 50 percent, and efficiency is lowered. When a divergent angle is as great as $2\chi = 18°$ (the figure is omitted), separation area is large and reaches 50-60 percent of the sectional area in Type I, while it is markedly decreased with Type IV. In Type IV, efficiency is greatly improved, as shown by mark ● in Fig. 7(*d*). In this way, high efficiency is often obtained even in the case of a *U* bend diffuser with a divergent angle as great as 12° or 18°, and it should be noted that efficiency in the *U* bend diffuser is not always low.

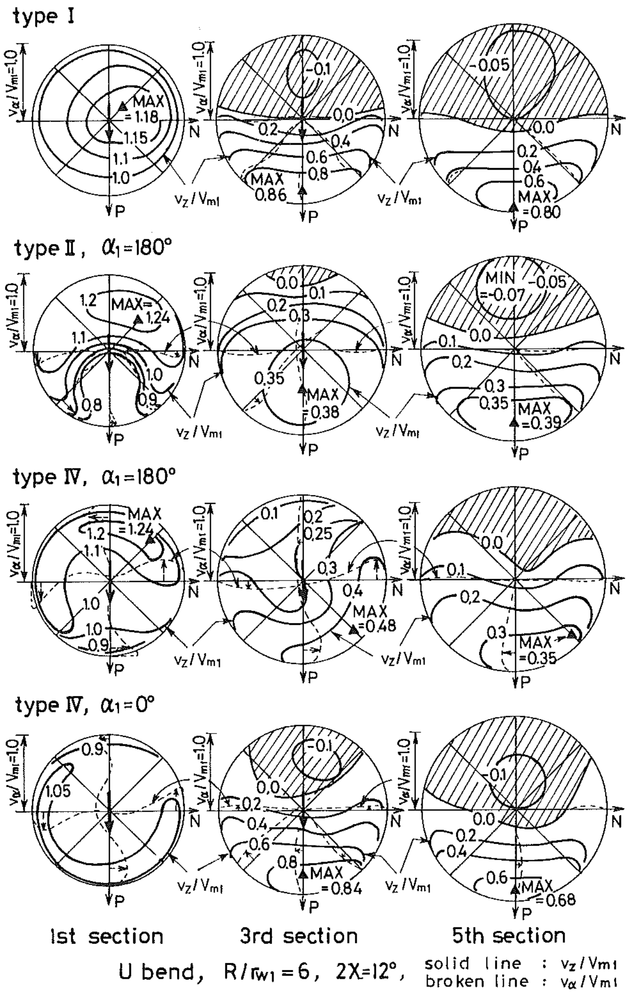

Fig. 11 Velocity distribution in 1st, 3rd and 5th sections inside *U* bend diffuser. $N = 4$. Inlet velocity Types I, II ($\alpha_1 = 180°$) and IV ($\alpha_1 = 180°$ and 0°). Uncertainty in $v_z/V_{m1} = 1.0 \pm 0.015$, in $v_\alpha/V_{m1} = 0.2 \pm 0.003$.

4.2.2 In Case of Snake Bend Diffusers. Figure 13 shows the velocity distribution and flow model when a Type I flow enters the snake bend diffusers. Radius ratio $R/r_{w1} = 3$ and $2\chi = 12°$. The feature of this flow is that, when a dead water region, as shown by the shaded portion, is generated on the inner side of the bend plane of the 1st bend, it develops along the wall surface on the same side, and the separation area is increased or decreased according to the influence of the secondary flow. In other words, in the 3rd and 5th sections, the dead water region tends to be dragged into the center of the pipe by the left-right symmetrical secondary flow. When the curvature radius ratio is increased and reaches $R/r_{w1} = 6$ (although not shown in the figure) the dead water region is almost dragged into the center of the pipe. Figure 12(*b*) shows the separation area ratio of each section of the snake diffuser in the case of Type I. These ratios reach, in downstream sections, 10-20 percent when $R/r_{w1} = 6$, and 20-30 percent when $R/r_{w1} = 3$. Efficiency varies according to the separation area ratio, and deteriorates when the separation is large.

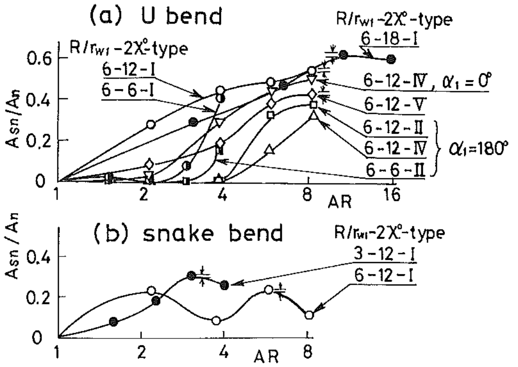

Fig. 12 Change of separation area in downstream direction inside *U* and snake bend diffusers. $N = 4$. (A_{Sn} = separation area of each section, A_n = area of each section.) Uncertainty in $A_{Sn}/A_n = 0.5 \pm 0.008$, in $AR = 8.0 \pm 0.12$.

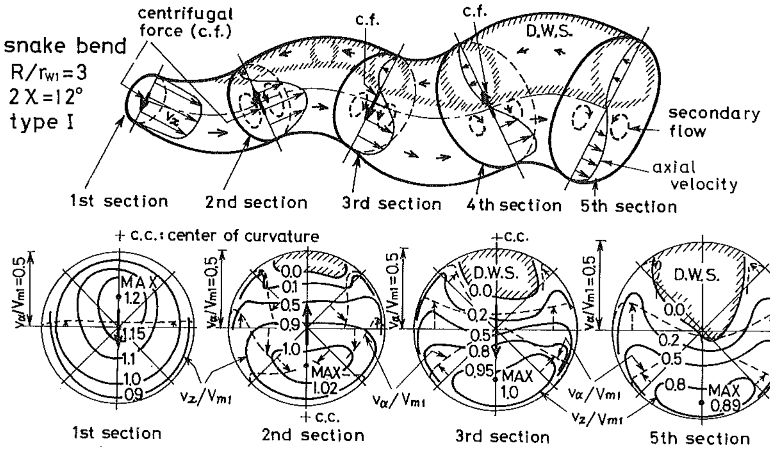

Fig. 13 Flow model and velocity distribution inside snake bend diffuser using inlet Type I. $N = 4$. Uncertainty in $v_z/V_{m1} = 1.0 \pm 0.015$, in $v_\alpha/V_{m1} = 0.2 \pm 0.003$.

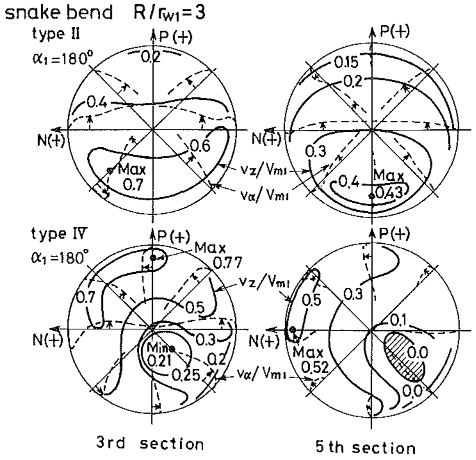

Fig. 14 Velocity distribution inside snake bend diffuser with inlet Types II and IV (3rd and 5th sections). $N = 4$. Uncertainty in $v_z/V_{m1} = 0.7 \pm 0.01$, in $v_\alpha/V_{m1} = 0.2 \pm 0.003$.

Our study was further extended to consider the distorted flow accompanied by the secondary swirling component in the case of Types II and IV. Figure 14 show the velocity distribution in the 3rd and 5th sections of the snake bend (the 1st section is omitted since it is the same as in Fig. 11) in cases of Types II and IV. It is evident from the figure that separation does not occur from inlet to outlet, and efficiency is good. As already stated, when the maximum velocity flow enters the inner side of the bend ($\alpha_1 = 180°$) in Types II and IV, a separation-suppressing-type secondary flow is generated. Therefore, separation is not generated at the outlet portion of the 1st bend. Furthermore, the snake-shaped diffuser means that very little separation occurs in the 2nd and subsequent bends as a result of secondary flow. In short, the flow inside a bend diffuser of this shape will remain stable downstream if separation is hindered at the 1st bend.

5 Conclusion

The following conclusion has been drawn from the results of our study and observations:

1 Even in a *U* bend diffuser, with a big divergent angle and bending angle, which is usually considered to be low in efficiency, energy efficiency can be raised up to around 80 percent by selecting the correct inlet velocity distribution and by generating separation-suppressing-type secondary flow inside the diffuser, without using any special type of device.

2 The snake bend diffuser is much better equipped to generate this separation-suppressing-type secondary flow than the *U* bend diffuser. Consequently, high efficiency of around 80 percent can be obtained, even with a divergent angle bigger than that possible for a *U* bend diffuser and with sharp bending. The influence of area ratio is smaller than it is in the case of the *U* bend diffuser.

3 For both *U* and snake bend diffusers, efficiency may become higher than that in a straight conical diffuser depending on inlet velocity distribution. Interesting phenomena have been observed in both of these diffusers; i.e., the bigger the divergent angle is, or the sharper the bend is, the higher the efficiency can be raised.

4 The relation between efficiency and inlet boundary-layer thickness in these two bend diffusers is approximately the same as that observed in straight conical diffusers.

References

1 Sprenger, H., 1959, "Experimental Investigations of Straight and Curved Diffusers," *Mitt. Inst. Aerodyn.*, Zurich, Vol. 27, pp. 1–80.

2 Shimizu, Y., et al., May 1981, "Studies on Three-Dimensional Curved Diffusers," *Transaction of JSME*, Vol. 47-417B, pp. 729–738, (in Japanese).

3 Murakami, M., and Shimizu, Y., September 1977, "Hydraulic Losses and Flow Patterns in Pipes With Two Bends Combined," *Bulletin of the JSME*, Vol. 20-147, pp. 1136–1144.

4 Shimizu, Y., et al., October 1982, "Effects of Approaching Flow Types on the Performances of Straight Conical Diffusers," *Bulletin of the JSME*, Vol. 25-208, pp. 1506–1512.

Vortex Simulation of Propagating Stall in a Linear Cascade of Airfoils

C. G. Speziale

The George W. Woodruff School
of Mechanical Engineering,
Georgia Institute of Technology,
Atlanta, GA 30332

F. Sisto

S. Jonnavithula

Mechanical Engineering Department,
Stevens Institute of Technology,
Hoboken, NJ 07030

A numerical simulation of propagating stall in a linear cascade of airfoils at high Reynolds numbers is conducted using a vortex method which was first developed by Spalart [7] *for this problem. In this approach, the vorticity is discretized into a large collection of vortex blobs whose motion is tracked in time by the use of a well-known vortex tracing algorithm based on the Euler equation. The near-wall effects of viscosity are accounted for by the creation of discrete vortex sheets at the boundaries of the airfoils consistent with the no-slip condition. These boundary vortices are then released into the flow field downstream of the separation points which are obtained from a boundary-layer routine. Calculations are presented for a variety of flow geometries. It is demonstrated that (for a given cascade of airfoils, disturbance wavelength, and stagger angle) several different flow regimes are obtained: Attached flow at lower angles of attack and a chaotic deep stall configuration at larger angles of attack with a narrow intermediate range of such angles where propagating stall occurs. The physical characteristics of this propagating stall are parameterized and a quantitative study of the effects of camber and imposed wavelength is conducted. Comparisons are made with previous theoretical and experimental studies.*

1 Introduction

With the advent of the Random Vortex Method and other similar vortex techniques, it recently has become possible to simulate high Reynolds number turbulent flows which have large-scale coherent structures that are two-dimensional [1-5]. The stability and excessive storage problems associated with finite-difference techniques at high Reynolds numbers are not encountered here since a spatial grid is not used. Rather, the vorticity is split into a large collection of vortex blobs (i.e., vortices with a small core where the singularity has been smoothed out) whose motion is tracked in time by using a well-known vortex tracing algorithm based on the Euler equation [6]. Since the Reynolds numbers being considered are extremely large, the major effects of viscosity are confined to the boundary-layer region. These viscous effects are simulated by the creation of vortex sheets at the boundaries so that the no-slip condition is satisfied. In this manner, vortices are constantly created to replace those that are "washed away" with the mean flow consistent with the basic physics of the problem.

In a recent paper, Spalart [7] conducted a numerical study of propagating stall in a linear cascade of airfoils. The vortex approach he utilized had several novel features which distinguished it from the more common Random Vortex Method previously cited [1-5]. To be more specific, the conditions of vanishing normal and tangential velocity components at the boundaries of the airfoils were satisfied simultaneously, in an approximate sense, by the introduction at each time step of a chain of new vortices along the walls (i.e., discrete vortex sheets) with the appropriate strengths. Furthermore, a semiempirical boundary-layer routine (Head's method [8]) was introduced in order to determine the approximate location of the separation points. The wall vortices were only released downstream of these predicted separation points in order to enhance the accuracy of the computed large-scale structures. Calculations were conducted with NACA 0009 (i.e., uncambered) airfoils at high Reynolds numbers of the order of 10^7. Various stagger angles and angles of attack were considered in infinite linear cascades with either a three-blade or five-blade flow period. For a given stagger angle, these computations clearly demonstrated the existence of propagating stall for an intermediate range of angles of attack. No previous theoretical studies on propagating stall had so clearly reproduced this phenomenon (while some interesting calculations on cascades were conducted by Lewis and Porthouse [9], they were not able to reproduce propagating stall).

Since this cascade of airfoils represents an idealized stage of a turbomachine (i.e., axial-flow compressors and fans), a better understanding of this phenomenon from a fundamental fluid mechanics standpoint could be of considerable use in the design of such systems. This is extremely important as a result of the fact that propagating stall may give rise to fluid-structure resonances which have profound destructive consequences.

Contributed by the Fluids Engineering Division for publication in the JOURNAL OF FLUIDS ENGINEERING. Manuscript received by the Fluids Engineering Division October 21, 1985.

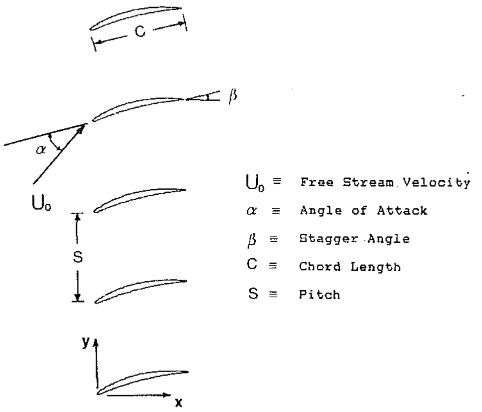

Fig. 1 Flow in a linear cascade of airfoils

The purpose of the present paper is to expand considerably on the initial calculations of Spalart [7] in order to gain more physical insight on this important phenomenon of propagating stall. The same basic vortex method will be used in this study with just a few modifications (the effect of the boundary-layer routine will be explored in more detail and the geometry and periodicity of the cascade will be varied). In order to gain a more quantitative understanding of the physics of the problem, mass flow diagrams and time-filtered drag and lift coefficient graphs will be introduced. A detailed study of the effects of camber and imposed wavelength on the velocity of stall propagation (predictions which are of great technical interest) will also be conducted. Comparisons will be made with the results of previous computational and experimental studies along with a discussion of the prospects for future research.

2 Formulation of the Physical Problem

The problem to be considered is that of viscous incompressible flow past an infinite linear cascade of airfoils at high Reynolds numbers; see Fig. 1. Since the interaction of large-scale separated flow structures with the mean flow (which are approximately two-dimensional) is of primary interest and the Reynolds numbers are extremely large, the two-dimensional inviscid Euler equation will be solved in the interior of the flow domain. In vorticity transport form, this equation is given by

$$\frac{\partial \omega}{\partial t}+u\frac{\partial \omega}{\partial x}+v\frac{\partial \omega}{\partial y}=0 \tag{1}$$

where

$$\mathbf{v}=u(x,y,t)\mathbf{i}+v(x,y,t)\mathbf{j} \tag{2}$$

$$\omega=\left(\frac{\partial v}{\partial x}-\frac{\partial u}{\partial y}\right)\mathbf{k}\equiv\omega(x,y,t)\mathbf{k} \tag{3}$$

are, respectively, the velocity and vorticity vectors. The Euler equation (1) must be solved subject to the continuity equation which, for two-dimensional incompressible flow, takes the form

$$\frac{\partial u}{\partial x}+\frac{\partial v}{\partial y}=0 \tag{4}$$

This equation has the general solution

$$u=-\frac{\partial \psi}{\partial y}, \quad v=\frac{\partial \psi}{\partial x} \tag{5}$$

where ψ is the stream function which can be determined from the Poisson equation

$$\nabla^2\psi=\omega \tag{6}$$

The vorticity ω will be decomposed into a large collection of vortex blobs (i.e, vortices with a small bounded core) in contrast to the finite-difference or finite-element solutions of (1)-(4) where a spatial grid is constructed. For a collection of N vortex blobs, it follows that

$$\omega=\sum_{k=1}^{N}\omega_k=\sum_{k=1}^{N}\nabla^2\psi_k \tag{7}$$

where ω_k and ψ_k are, respectively, the vorticity and stream function associated with the kth vortex blob. In the simpler applications of the Random Vortex Method, ψ_k usually takes the form [2]

$$\psi_k=\begin{cases}\dfrac{\Gamma_k}{2\pi\sigma}\,|\mathbf{r}-\mathbf{r}_k|+\text{constant}, & |\mathbf{r}-\mathbf{r}_k|<\sigma\\[2ex] \dfrac{\Gamma_k}{2\pi}\ln|\mathbf{r}-\mathbf{r}_k|, & |\mathbf{r}-\mathbf{r}_k|\geq\sigma\end{cases} \tag{8}$$

where Γ_k and $\mathbf{r}_k$ are, respectively, the strength and position of the kth vortex blob and σ is its bounded support (i.e., the radius of its small bounded core). While this formulation of ψ_k is suitable for the treatment of isolated bodies, some modifications are needed in order to efficiently treat an infinite array of bodies. The same form for ψ_k as proposed by Spalart [7] will be used. This representation is given by

$$\psi_k=\frac{\Gamma_k}{4\pi}\ln\left\{\left|\sin\left[\frac{2\pi i}{P}(z-z_k)\right]\right|^2+\sigma^2\right\} \tag{9}$$

where $i\equiv\sqrt{-1}$ and the complex variable notation $z=x+iy$ is used. Here, P is the period of the array and the parameter σ smooths out the singularity at $z=z_k$. For $\sigma=0$, equation (9) reduces to the singular form

$$\psi_k=\frac{\Gamma_k}{2\pi}\ln\left|\sin\left[\frac{2\pi i}{P}(z-z_k)\right]\right| \tag{10}$$

which is the stream function induced by a periodic array of vortices (c.f., Lamb [10]).

Nomenclature

C ≡ chord length
C_D ≡ drag coefficient
C_L ≡ lift coefficient
$\bar{C}_D$ ≡ time-filtered drag coefficient
$\bar{C}_L$ ≡ time-filtered lift coefficient
i,j,k ≡ unit vectors along coordinate directions
m ≡ blade number
n,s ≡ normal and tangential coordinates
N ≡ number of vortices
p ≡ pressure field
p_0 ≡ reference surface pressure
P ≡ period of the array
r ≡ position vector
$\mathbf{r}_k$ ≡ position vector of the kth vortex
Re ≡ Reynolds number
S ≡ pitch
t ≡ time
T ≡ time interval of the filtering
Δt ≡ time step of the computation
x,y ≡ spatial coordinates
u,v ≡ x,y-components of velocity field **v**
U_0 ≡ free-stream velocity
V_p ≡ propagation velocity of stall
z ≡ complex variable $x+iy$
α ≡ angle of attack
β ≡ stagger angle
Γ_k ≡ strength of kth vortex
σ ≡ bounded support of vortex blobs
ψ ≡ stream function
ω ≡ vorticity

Special Notation

∇^2 ≡ Laplacian

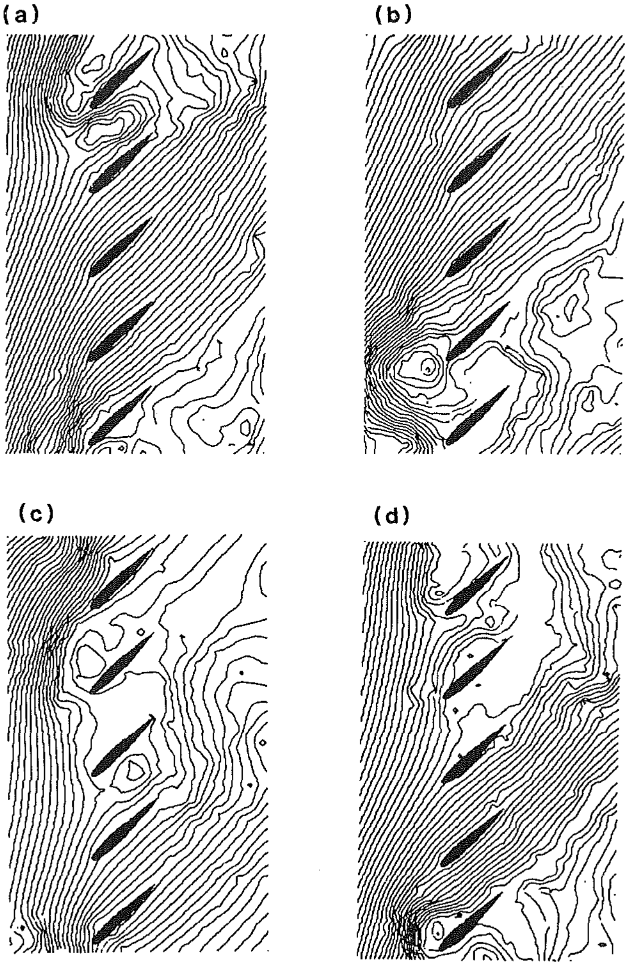

Fig. 2 Streamlines for flow in a linear cascade of NACA 0012 airfoils; Re = 10^7, α = 30°, β = 45°, S/C = 1; (*a*) t = 28, (*b*) t = 32, (*c*) t = 36, (*d*) t = 40

The vortices are moved in time using an approximate vortex tracing algorithm based on the Euler equation [2]. According to this algorithm, the kth vortex changes position, in some small time interval Δt, by the formula

$$\mathbf{r}_k(t+\Delta t)=\mathbf{r}_k(t)+\Delta t\left[\sum_{\substack{j=1\\ j\neq k}}^{N}\mathbf{v}_j(\mathbf{r}_k,t)+\mathbf{U}_0\right] \tag{11}$$

where

$$\mathbf{v}_j=\mathbf{k}\times\nabla\psi_j \tag{12}$$

is the velocity induced by the jth vortex and $\mathbf{U}_0$ is the free-stream velocity. In the limit as Δt, $U_0 \to 0$, equation (11) reduces to the form

$$\frac{d\mathbf{r}_k}{dt}=\sum_{\substack{j=1\\ j\neq k}}^{N}\mathbf{v}_j(\mathbf{r}_k,t) \tag{13}$$

which is the well-known result (for a collection of N vortices in an unbounded and otherwise stationary inviscid fluid) that a given vortex moves with the velocity induced by the remaining $N-1$ vortices [6].

The effects of viscosity near the boundaries of the airfoils are simulated by the creation of a chain of new vortices (i.e., a discrete vortex sheet) at each time step. These vortices of strength Γ_k are created at fixed intervals along the boundaries of the airfoils such that they produce the correct total circulation (i.e., satisfy the requirement of conservation of total vorticity [12]) and satisfy the no-slip condition [11]. The latter condition is satisfied in a weak sense. More specifically, the integral of the normal velocity over each wall interval is made zero by selecting the correct vortex strengths Γ_k obtained by solving a linear system of algebraic equations whose matrix coefficients a_{ij} are determined by the geometry of the cascade; hence, this "wall influence matrix" need only be inverted once [11]. Since a continuous flux of vorticity through the boundaries of the airfoils is maintained, it follows that the vorticity in the flow field is such that the sum of the velocity induced by it and the free-stream velocity is zero inside each airfoil – a result which must hold for a viscous fluid [6]. However, the velocity induced inside each body by the free-stream velocity and vorticity of the flow field is *incompressible and irrotational*. This guarantees that the tangential component of the velocity at the walls of the airfoils vanishes in a similar approximate sense [11]. For the calculations to be presented in the next section, the no-slip condition is satisfied to within an error of less than 1 percent. This is extremely good considering that all of the computed results that will be presented in the next section have an uncertainty which is of the order of 10 percent; see Spalart [7].

In order to more accurately predict the effects of flow separation, Spalart [7] allowed the vortices created at the walls of the airfoils to be released into the flow field *downstream* of the separation points. These separation points were predicted by using Head's method which is a semiempirical integral boundary-layer technique (c.f., Cebeci and Bradshaw [8]). The only parameters needed for the implementation of this boundary-layer routine are the Reynolds number, free-stream velocity, and pressure field. The latter quantity is obtained from the Navier-Stokes equation which, at a stationary solid boundary, can be written in the form [6]

$$\frac{dp}{ds}=-\frac{1}{\mathrm{Re}}\frac{\partial\omega}{\partial n} \tag{14}$$

where n and s are, respectively, intrinsic coordinates normal and tangential to the boundaries and Re is the Reynolds number. Equation (14) can be integrated directly to yield the result

$$p=p_0-\frac{1}{\mathrm{Re}}\int_{s_0}^{s}\frac{\partial\omega}{\partial n}\,ds \tag{15}$$

which determines the pressure, to within an additive constant, directly from the vorticity. This is easily accomplished since the quantity $-1/\mathrm{Re}\ \partial\omega/\partial n$ is the flux of vorticity through the boundary which is known at each time step. Furthermore, it should be noted that the drag and lift coefficients can be obtained directly from (15) by a simple integration. Some criticisms can be raised about the accuracy of the boundary-layer routine which is somewhat empirical. However, it will be argued in the next section that the computed results are relatively insensitive to its structure unless there is strong camber present.

Calculations will be conducted for a Reynolds number (based on the free-stream velocity and airfoil chord length) of 10^7. The ratio of pitch-to-chord length S/C (see Fig. 1) was chosen to be 1 thus giving a fairly low solidity in order to promote stall. Disturbance wavelengths of four and five blades were considered; one of the goals of this study was to examine the effect of imposing such a specified period. Calculations were conducted using a NACA 0012 airfoil and two cambered airfoils with a 10 percent thickness; one had a mild camber of 20° whereas the other had a strong camber of 45°. In this manner, the effects of camber on the structure of propagating stall could be studied in more detail. The boundary of each airfoil was discretized into 100 subintervals (for the creation of the "discrete vortex sheets") and the motion of approximately 1000 or 1500 vortices were tracked in time where the lower number corresponds to a wavelength of four blades per

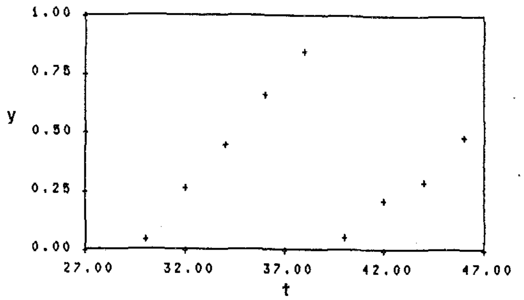

Fig. 3 Mass flow diagram denoting position of centroid of largest patch of reverse flow as a function of time (NACA 0012 airfoils, Re = 10^7, α = 30°, β = 45°, S/C = 1)

period. The number of vortices was kept at this approximate number by the same vortex merging device used by Spalart [7]. These calculations required 30-45 min of CPU time on a Cray XMP supercomputer to achieve statistically periodic flow characteristics for a given set of physical parameters. In order to accelerate the onset of this nonlinear instability of propagating stall, a finite amplitude disturbance (in the form of a dipole) was introduced at the initial iteration. A detailed discussion of the numerical results obtained will be presented in the next section.

3 Numerical Results

Computations for an uncambered NACA 0012 cascade with a wavelength of five blades will be presented initially. In Figs. 2(*a*-*d*), the streamlines of the computed flow are shown at equal time intervals for an angle of attack $\alpha = 30°$ and a stagger angle $\beta = 45°$. Consistent with the results obtained by Spalart [7] for a NACA 0009 airfoil, it is clear that a propagating stall is present. The intrinsic periodicity of this flow in time can be seen parametrically by the introduction of the mass flow diagram which is shown in Fig. 3 for this case. In this diagram, the position y of the centroid of the largest patch of reverse mass flow (normalized to one by the wavelength of the cascade) is plotted as a function of time. From this figure, the propagation velocity of the stall can be calculated directly (these results will be discussed in more detail in the latter part of this section). In Figs. 4(*a*, *b*), the time filtered drag and lift coefficients are shown as functions of time for each of the five airfoils. To be more specific, the quantities

$$\bar{C}_D(t) = \frac{1}{2T}\int_{-T}^{T} C_D(t+\tau)d\tau \tag{16}$$

$$\bar{C}_L(t) = \frac{1}{2T}\int_{-T}^{T} C_L(t+\tau)d\tau \tag{17}$$

(where C_D and C_L are, respectively, the drag and lift coefficients) are plotted for each blade $m = 1, 2, \ldots 5$.[1] In (16)-(17), the time interval $2T = 10\Delta t$: a value which is large compared with the time step of the computation but small compared with the period of the propagating stall which is of the order of $500\Delta t$. Hence, the high frequency Fourier components of C_D and C_L are filtered out which allows us to examine more clearly the fluctuations of C_D and C_L in the time scale of the propagating stall. It is clear that in Fig. 4(*a*) as well as Fig. 4(*b*) the time filtered drag and lift coefficients for each airfoil exhibit strong periodic peaks (as a result of the effects of stall) with a characteristic phase lag from airfoil to airfoil. This constitutes the type of "waterfall diagram" that one expects to encounter in the presence of propagating stall. Propagating stall was also encountered in this cascade of NACA 0012 airfoils (where $\beta = 45°$) for a band of angles of attack given by $27° \leq \alpha \leq 33°$. At substantially smaller angles of attack, the flow is attached and at other angles of attack, the flow separated structures have a more chaotic structure; it is well known that the N vortex problem exhibits chaos for $N > 3$; c.f., Aref [13]. The significance of these results will become clearer after examining computed results for cascades with cambered airfoils.

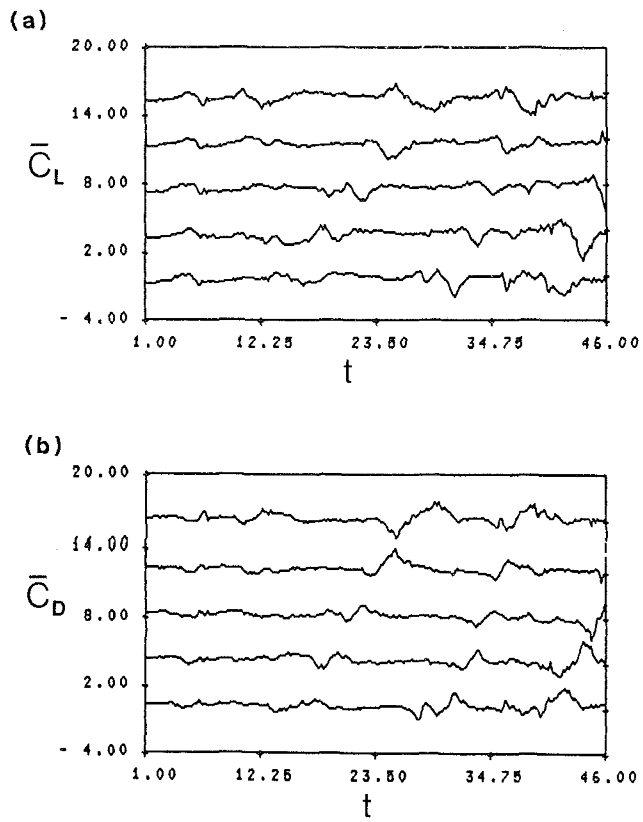

Fig. 4 Forces on a linear cascade of NACA 0012 airfoils, Re = 10^7, α = 30°, β = 45°, S/C = 1; (*a*) filtered lift coefficients as a function of time; (*b*) filtered drag coefficients as a function of time

The computed results obtained for a cascade of moderately cambered airfoils with a disturbance wavelength of five blades will now be discussed. Here, the camber is 20° and the maximum thickness is 10 percent for this double circular arc airfoil. The stagger angle was fixed at 20° for simplicity. The computations done by Spalart [7] tended to indicate that the inlet flow angle $\alpha + \beta$ was the parameter of key importance; thus β could be held fixed and α could be varied for simplicity. In Figs. 5(*a*-*d*), the computed streamlines of the flow are shown at various times for an angle of attack $\alpha = 50°$. It is clear that a propagating stall is present. However, it seems to have more of a chaotic structure in the somewhat smaller scales of the separated flow than that shown for the NACA 0012 airfoil in Fig. 2. The mass flow diagram shown in Fig. 6 has a smooth periodic structure and the time-filtered lift and drag coefficients, shown in Fig. 7, have the characteristic "waterfall" structure indicative of the presence of propagating stall.[2] It is interesting to note that for this cascade of cambered airfoils, the propagation speed is noticeably lower than for the noncambered case. Furthermore, the time-filtered lift and drag coefficients have more dramatic peaks than those obtained for the NACA 0012 airfoil. Hence, it would appear

---

[1] A constant of the amount $4(m-1)$, for each successive blade, was added to the time-filtered lift and drag coefficients in order to be able to clearly plot these results on a single scale.

[2] In Fig. 7, a constant of the amount $5(m-1)$, for each successive blade, was added to the time-filtered lift and drag coefficients in order to show these results on a single scale.

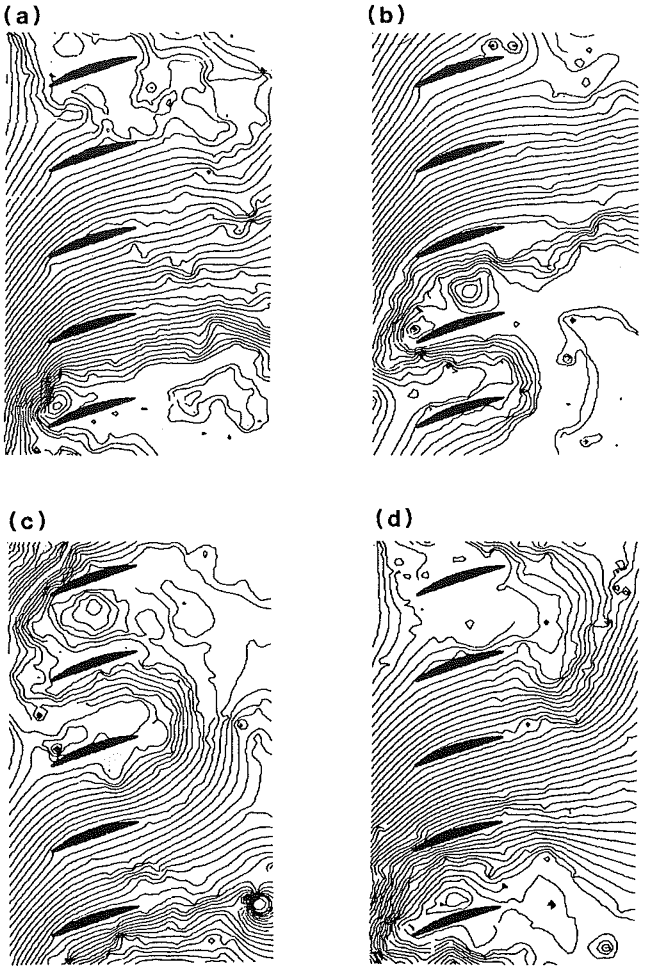

Fig. 5 Streamlines for flow in a linear cascade of cambered airfoils (20° camber, 10 percent thickness, Re = 10^7, α = 50°, β = 20°, S/C = 1); (*a*) t = 40, (*b*) t = 44, (*c*) t = 50, (*d*) t = 54

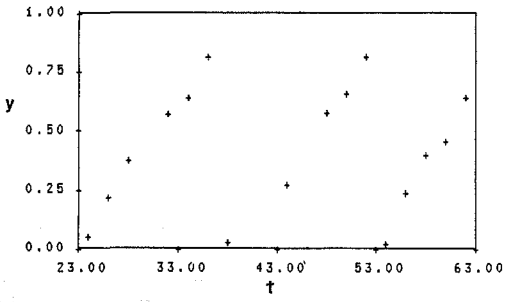

Fig. 6 Mass flow diagram for a cascade of cambered airfoils (20° camber, 10 percent maximum thickness, Re = 10^7, α = 50°, β = 20°, S/C = 1)

that this somewhat slower propagating stall has a more extreme influence on the lift and drag fluctuations, and thus can lead to more deleterious effects in the event of structural resonance.

If the same physical parameters (i.e., Re = 10^7, β = 20°, α = 50°) are used for a four-blade wavelength in this cascade of moderately cambered airfoils, decidedly different results are obtained. The computed streamlines of this flow are shown in Figs. 8(*a–d*) at various times. A propagating stall is *not* present for this case and the flow appears to exhibit a state of chaotic deep stall (i.e., there are separated flow patches in *every* blade passage which seem to change randomly with time). The fact that the mass flow diagram shown in Fig. 9 has a somewhat random structure is an additional indication of the lack of a propagating stall. Furthermore, when additional calculations were done for the five-blade wavelength in which the angle of attack was increased by a slight amount (i.e., the case where α = 52° instead of 50°) the propagating stall was lost. The computed streamlines for this latter case are shown in Figs. 10(*a–d*) at various times. Analogous to the four-blade case for α = 50°, these results indicate a chaotic deep stall configuration rather than the presence of a propagating stall. Similarly, the mass flow diagram shown in Fig. 11 has a more random structure indicating that a clearly delineated propagating stall is not present. These results have important physical consequences. To be more specific, these calculations demonstrate that for a given geometrical cascade of airfoils and inlet flow angle $\alpha + \beta$, propagating stall will only occur *for a narrow range of wavelengths*. In physical applications where there is an annular array of airfoils, propagating stall can occur for a variety of inlet flow angles since the flow is free to adjust itself to a physically consistent wavelength or number of stall patches in the flow annulus. However, in this numerical approach, the wavelength of the flow is assumed at the outset of the computation through the specification of the number of blades per period. Hence, one would only expect to obtain propagating stall for a narrow range of inlet flow angles; a conclusion which is consistent with the calculations of Spalart [7] who only found propagating stall in the cascade that he studied for inlet flow angles that differed by 5°–10°. The results just presented indicate that cambering the airfoils can substantially reduce the range of acceptable wavelengths where propagating stall can occur. In Figs. 12(*a–d*), the computed streamlines of the flow are shown at various times for the same cambered cascade (with a period of five blades) when the angle of attack α is reduced to a value of 48°. It is clear

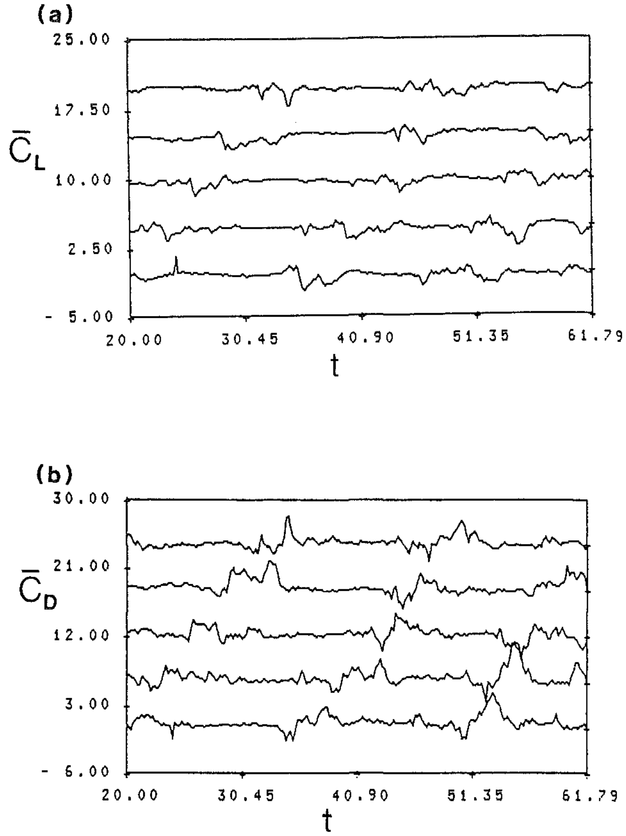

Fig. 7 Forces on a linear cascade of cambered airfoils (20° camber, 10 percent thickness, Re = 10^7, α = 50°, β = 20°, S/C = 1); (*a*) filtered lift coefficients as a function of time; (*b*) filtered drag coefficients as a function of time

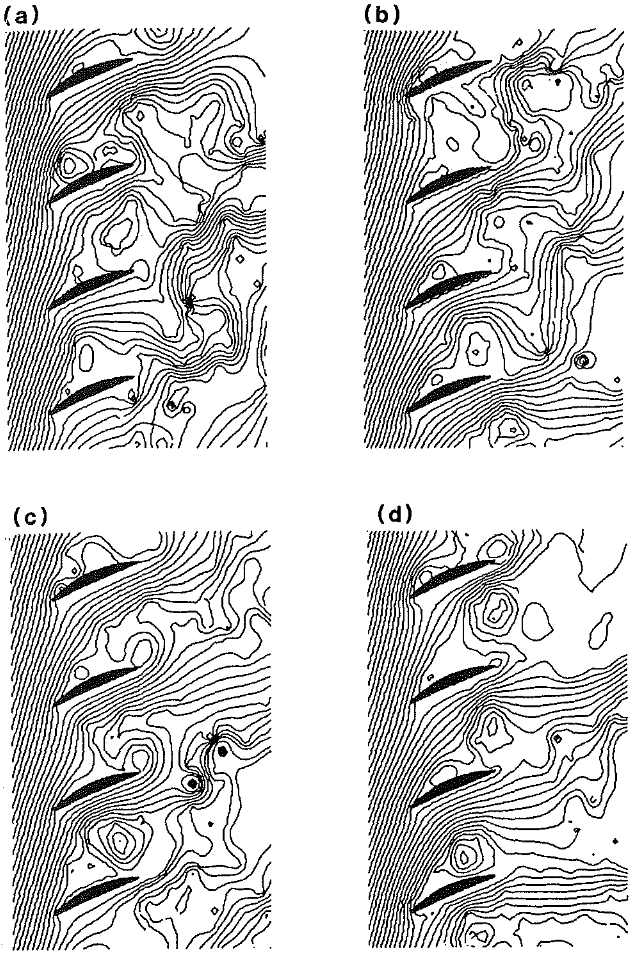

Fig. 8 Streamlines for flow in a linear cascade of cambered airfoils (20° camber, 10 percent maximum thickness, Re = 10^7, α = 50°, β = 20°, S/C = 1); (*a*) t = 28, (*b*) t = 32, (*c*) t = 36, (*d*) t = 40

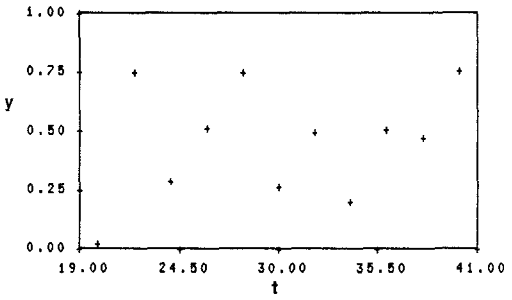

Fig. 9 Mass flow diagram for a cascade of cambered airfoils (20° camber, 10 percent maximum thickness, Re = 10^7, α = 50°, β = 20°, S/C = 1)

that no propagating stall is present; rather, the flow assumes a chaotic deep stall configuration somewhat similar (although less intense) to that which occurs when the critical angle of attack for propagating stall was exceeded. At significantly lower angles of attack the flow is, of course, attached. The computed streamlines for this cascade of airfoils with a wavelength of five blades is shown in Fig. 13 when $\alpha = 30°$ and $\beta = 20°$. Clearly, there is a fully developed attached flow. Thus, for a given cascade geometry, disturbance wavelength, and stagger angle we obtain the following computed results: Attached flow at lower angles of attack and a chaotic deep stall configuration at larger angles of attack with an intermediate range of such angles where propagating stall occurs.

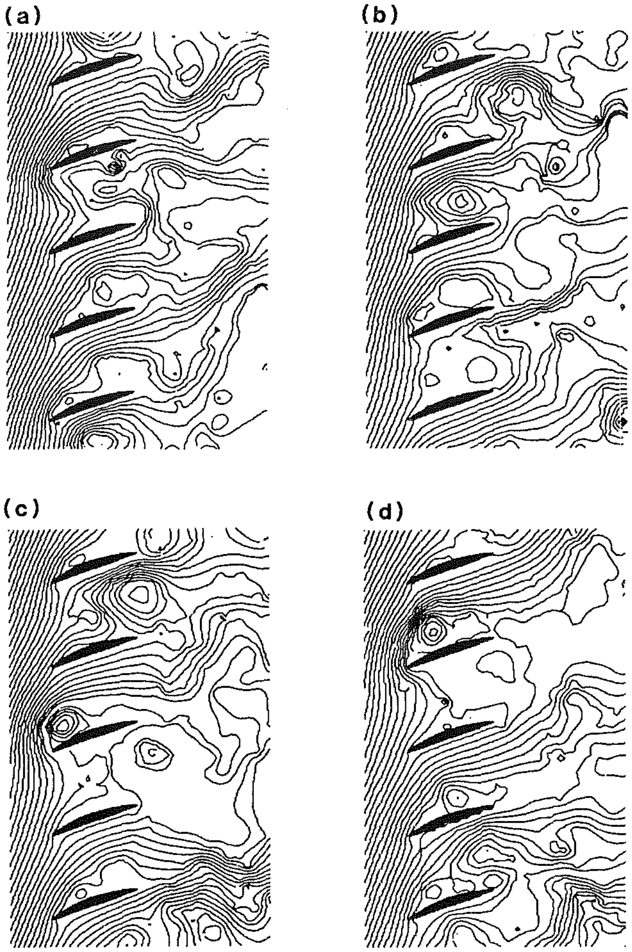

Fig. 10 Streamlines for flow in a linear cascade of airfoils (20° camber, 10 percent maximum thickness, Re = 10^7, α = 52°, β = 20°, S/C = 1); (*a*) t = 30, (*b*) t = 34, (*c*) t = 38, (*d*) t = 42

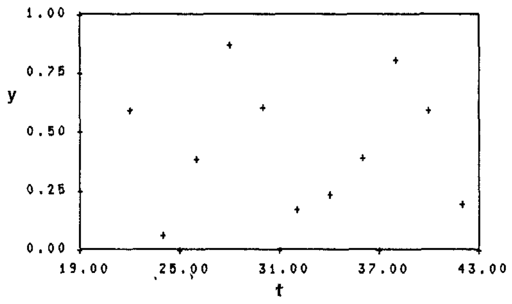

Fig. 11 Mass flow diagram for a cascade of cambered airfoils (20° camber, 10 percent maximum thickness, Re = 10^7, α = 52°, β = 20°, S/C = 1)

Now, we will present some computed results for a cascade, with a period of five blades, consisting of more strongly cambered airfoils. To be specific, we will consider double circular arc cambered airfoils with a camber of 45° and a maximum thickness of 10 percent. The computed streamlines are shown in Figs. 14(*a–d*) at various times for $\alpha = 52°$ and $\beta = 20°$. The mass flow diagram for this case is shown in Fig. 15. A propagating stall is present for this flow configuration as can be seen from the mass flow diagram which assumes a definite periodic structure; see Fig. 15. However, the streamline patterns shown in Figs. 14(*a–d*) have a decidedly more chaotic substructure than those obtained for the moderately cambered and uncambered airfoils shown

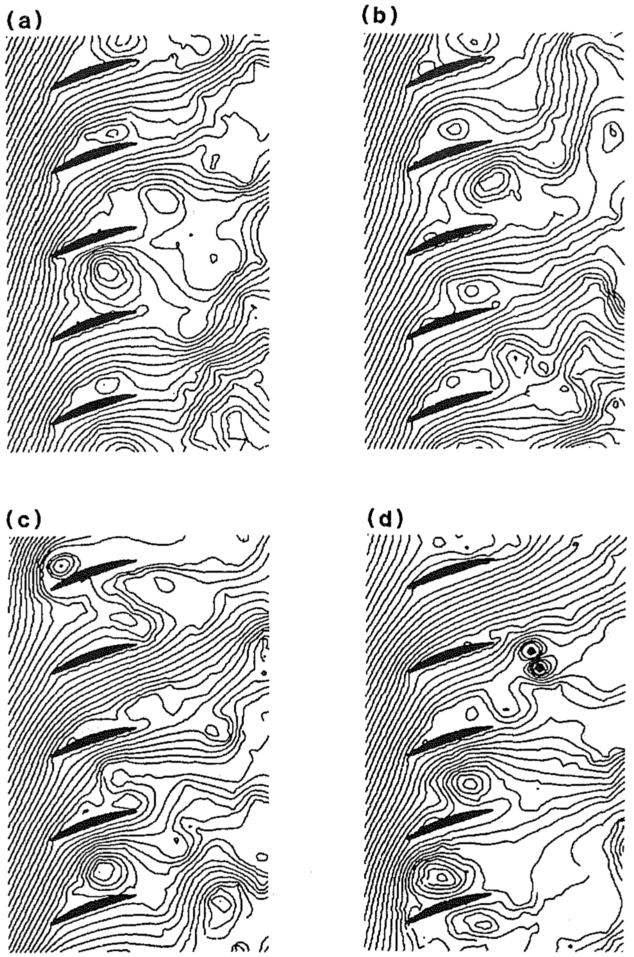

Fig. 12 Streamlines for flow in a linear cascade of cambered airfoils (20° camber, 10 percent maximum thickness, Re = 10^7, α = 48°, β = 20°, S/C = 1); (*a*) t = 28, (*b*) t = 32, (*c*) t = 36, (*d*) t = 40

previously. Hence, it would appear that an increase in camber gives rise to propagating stalls with a much more complex structure. It should be noted that for slightly lower and also slightly higher angles of attack, this propagating stall gets replaced with a chaotic deep stall configuration analogous to what occurs in cascades with more moderately cambered airfoils as previously discussed. However, for this more strongly cambered airfoil, the propagation velocity lies somewhere in between that which is obtained for the uncambered and moderately cambered cascade of airfoils. Furthermore, the peaks in the time-filtered drag and lift coefficients are, surprisingly, not as dramatic as those obtained for the more moderately cambered cascade. Hence, it would appear that these calculations do *not* establish a direct or monotonic correlation between the amount of camber and the speed of propagating stall or its physical effect on fluctuations in lift and drag. This point is illustrated in Table 1 where the propagation velocity of the stall V_P (nondimensionlized with respect to the free-stream velocity U_0) is tabulated for various amounts of camber. It should be noted that there is a range of such propagation velocities for each case (rather than a unique value) which is indicative of the fact that the least stable mode has not been reached. This would require that the values of α, β and the disturbance wavelength be in close proximity to their critical values. The fact that we have not reached this least stable mode is clear from an inspection of the mass flow diagrams shown in Figs. 3, 6, and 15 which have slopes (these are directly tied to the propagation velocity) that vary with time. It is, however, encouraging to note that these computed values of the propagation velocity are in the range of those obtained in previously conducted experiments. For instance, Montgomery and Braun [14] conducted experiments on propagating stall in a single-stage axial compressor and obtained a value of

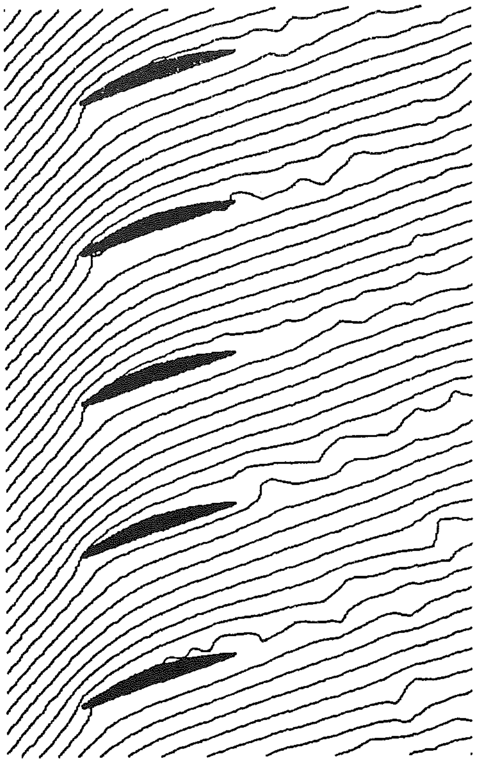

Fig. 13 Fully developed attached flow in a linear cascade of airfoils (20° camber, 10 percent maximum thickness, Re = 10^7, α = 30°, β = 20°, S/C = 1)

$$V_P/U_0 = 0.33 \qquad (18)$$

for an inlet flow angle of 72.5°. Similarly, Stenning, Seidel and Senoo [15] obtained a value of

$$V_P/U_0 = 0.376 \qquad (19)$$

for an inlet flow angle of 70° in a cascade of NACA 0010 airfoils.

4 Conclusion

A numerical simulation has been conducted on propagating stall in a linear cascade of airfoils using a vortex code that was initially developed for this problem by Spalart [7]. This vortex method has several unique features. The conditions of vanishing normal and tangential components of velocity at a solid boundary are simultaneously satisfied in an excellent approximate sense by the introduction of a chain of wall vortices (i.e., a discrete vortex sheet), of the appropriate strengths, at each time step. These wall vortices are only allowed to be released into the flow *downstream* of the predicted separation points which are obtained by a semiempirical integral boundary-layer routine. This is done in order to enhance the accuracy of the computations. Detailed computations were presented for a variety of cascades where the effects of camber and imposed wavelength were studied and an effort was made to parameterize the physical effects of propagating stall through the introduction of mass-flow and time-filtered lift and drag coefficient diagrams. The computed results obtained gave rise to a slightly different physical interpretation of this phenomenon than that presented earlier [7]. More specifically, it was found that this vortex method (for a given cascade

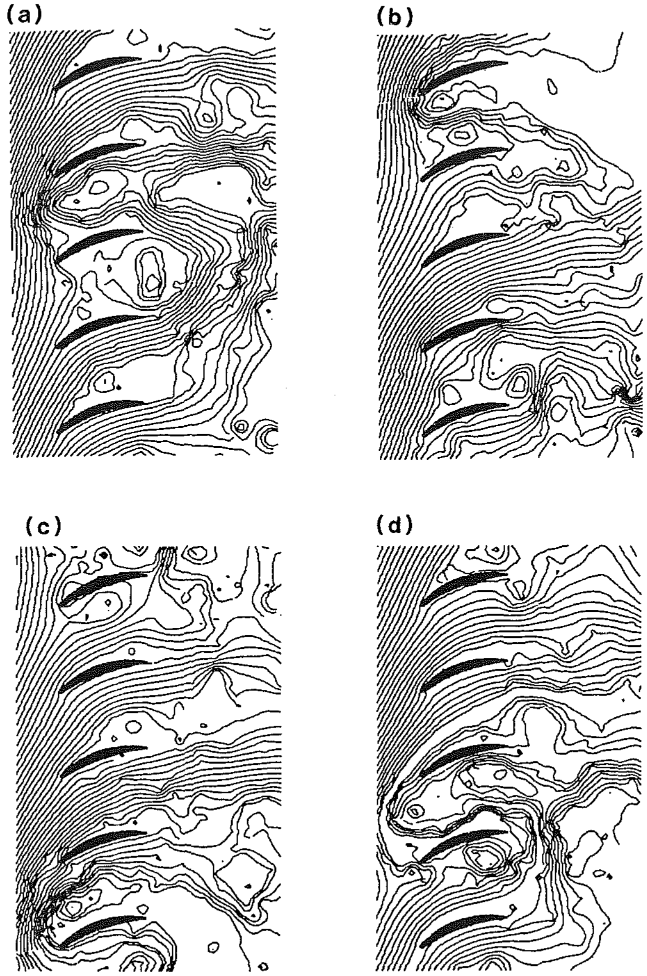

Fig. 14 Streamlines for flow in a linear cascade of cambered airfoils (45° camber, 10 percent maximum thickness, Re = 10^7, α = 52°, β = 20°, S/C = 1); (*a*) t = 32, (*b*) t = 36, (*c*) t = 40, (*d*) t = 44

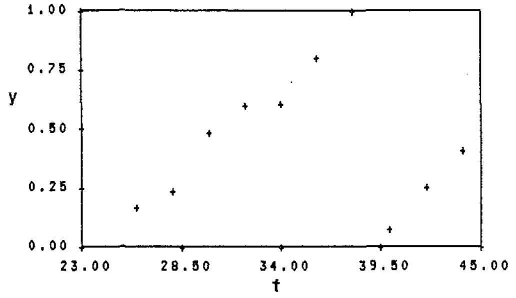

Fig. 15 Mass flow diagram for a cascade of cambered airfoils (45° camber, 10 percent maximum thickness, Re = 10^7, α = 52°, β = 20°, S/C = 1)

Table 1 Variation of the propagation velocity of the stall with camber for a disturbance wavelength of five blades (70° $\le \alpha + \beta \le$ 75°)

Camber	V_p/U_o
0°	0.37 - 0.49
20°	0.27 - 0.44
45°	0.36 - 0.43

geometry, wavelength, and stagger angle) yields attached flow at lower angles of attack and a chaotic deep stall configuration at larger angles of attack with a narrow intermediate range of angles where propagating stall occurs. The reason for this narrow range of propagating stall is tied to the fact that the period of the cascade (and, hence, the wavelength of the nonlinear disturbance) is imposed by the numerical method; thus a propagating stall in a particular cascade is only physically consistent with a few distinct values of inlet flow angles. In real physical systems, propagating stall can be observed for a wider range of such angles since the flow field is free to adjust itself to the appropriate wavelength which is physically consistent with the other flow parameters. This represents a somewhat more complete physical picture of the computer results obtained by this approach than that presented by Spalart [7] who only demonstrated the existence of three regimes: attached flow, propagating stall, and deep stall.

One of the major goals of this preliminary study was to determine the effect of camber on the structure of propagating stall. It was found that an increase in camber yielded a more narrow range of acceptable angles of attack (for a given disturbance wavelength) wherein propagating stall occurs and gave rise to propagating stalls which have a much more chaotic substructure. No direct correlation could be established between the amount of camber and the propagation speed of the stall or the intensity of its effect on the fluctuations in the lift and drag coefficients. However, it should be noted that no such correlations have been obtained in the limited experimental results that are available so it remains an open question as to what tie there is between these parameters. Furthermore, it is encouraging that the computed results for the propagation speeds of the stall were in the range of those obtained from previous experimental studies as demonstrated in Section 3.

Future research is needed along several different directions in order to improve the predictive value of this vortex method in the description of propagating stall. Modifications in the computer code are needed in order to allow the wavelength of the disturbance to be a noninteger number of blade passages. In addition, it would be preferable if the wavelength of the disturbance could be arrived at as part of the solution as opposed to being required as an input parameter; this would obviate the need for obtaining an "inverse solution" by the systematic variation of the flow parameters – a task which substantially raises the level of computation. A more detailed study along these lines, which makes use of the intrinsic periodicity of the velocity field when propagating stall is present, will be included in future work. Additional research is still needed to improve the performance of the boundary-layer routine. The results of this study tend to indicate that the critical computed results were only sensitive to the choice of the boundary-layer routine in the presence of strong camber which introduces increased streamwise curvature and boundary-layer loading. An optimization of this routine to deal better with the effects of strong camber is a complicated problem which must yield to future research. By incorporating such anticipated improvements along with further refinements in the numerical algorithm, there is an excellent prospect that this vortex method can provide useful information for the design engineer of the future.

Acknowledgments

The authors are indebted to Dr. P. R. Spalart for many helpful comments and for allowing us the use of his computer code. This study would not have been possible without the computer time made available on the Cray XMP supercomputer at the NASA Ames Research Center. This work was supported by the Office of Naval Research under Contract No. N00014-84-K-0741 for which Dr. R. P. Shreeve served as the project monitor.

References

1 Chorin, A. J., 1973, "Numerical Study of Slightly Viscous Flow," *Journal of Fluid Mechanics*, Vol. 57, pp. 785–796.

2 Chorin, A. J., 1980, "Vortex Models and Boundary-Layer Instability," *SIAM J. Sci. Stat. Comput.*, Vol. 1, pp. 1–21.

3 Ashurst, W. T., 1979, "Numerical Simulation of Turbulent Mixing Layers Via Vortex Dynamics," *Turbulent Shear Flows I*, F. Durst, et al., Eds., Springer, New York, pp. 402–413.

4 Leonard, A., 1980, "Vortex Methods for Flow Simulation," *J. Comput. Phys.*, Vol. 37, pp. 289–335.

5 Cheer, A. Y., 1979, "A Study of Incompressible 2-D Vortex Flow Past a Circular Cylinder," Technical Report LBL-6443, Lawrence-Berkeley Laboratory.

6 Batchelor, G. K., 1967, *An Introduction to Fluid Dynamics*, Cambridge University Press, London, England.

7 Spalart, P. R., 1984, "Two Recent Extensions of the Vortex Method," AIAA Paper 84-0343.

8 Cebeci, T., and Bradshaw, P., 1977, *Momentum Transfer in Boundary Layers*, McGraw-Hill, New York.

9 Lewis, R. I., and Porthouse, D. T. C., 1982, "A Generalized Numerical Method for Bluff Body Stalling Aerofoil Flow," ASME Paper 82-GT-70.

10 Lamb, H., 1945, *Hydrodynamics*, Dover, New York.

11 Spalart, P. R., and Leonard, A., 1981, "Computation of Separated Flows by a Vortex Tracing Algorithm," AIAA Paper 81-1246.

12 Wu, J. C., 1980, "Aerodynamic Force and Moment in Steady and Time-Dependent Viscous Flows," AIAA Paper 80-0011.

13 Aref, H., 1983, "Integrable, Chaotic and Turbulent Vortex Motion in Two-Dimensional Flows," *Ann. Rev. Fluid Mech.*, Vol. 15, pp. 345–389.

14 Montgomery, S. R., and Braun, J. J., 1957, "Investigation of Rotating Stall in a Single-Stage Axial Compressor," NACA Report TN 3823.

15 Stenning, A. H., Seidel, B. S., and Senoo, Y., 1959, "Effect of Cascade Parameters on Rotating Stall," NASA Memorandum 3-16-59W.

R. G. Williamson
Head,
Gas Dynamics Laboratory,
National Research Council,
Ottawa, Ontario, Canada K1A 0R6

S. H. Moustapha
Staff Aerodynamicist,
Pratt and Whitney Canada Inc.,
Longueuil, Quebec, Canada

Annular Cascade Testing of Turbine Nozzles at High Exit Mach Numbers

This paper presents detailed information on the three-dimensional flow field in a realistic low aspect ratio, high turning nozzle vane design which incorporates endwall contouring and which has been tested over a range of exit Mach number from subsonic up to the design value at mean section of 1.15. The experimental results, in the form of nozzle surface pressure distributions as well as surveys of pressure losses and flow angles at exit, are compared with those calculated by a three-dimensional flow analysis. The effects of exit Mach number on the measured nozzle performance are also presented.

Introduction

The requirements for compact, low cost and fuel efficient engines for small aircraft applications generally lead to gas generator turbines of the single stage axial type with low aspect ratio blading, large pressure ratio, and high inlet temperature. Selection of low rotor speed for such turbines, in order to realize mechanical and first cost advantages, implies high stage loading and probable adverse effects on aerodynamic efficiency. The investigation described here is a preliminary step in a comprehensive research program involving a representative highly loaded stage. Most of the work in this initial phase has been undertaken on the nozzle in the absence of the rotor. Subsequent work will deal with the performance of the complete stage.

One of the major causes of low stage efficiency in a highly loaded turbine design lies in the unfavorable nozzle characteristics. Such a nozzle design typically incorporates aerofoil twist, high angles of flow turning, low aspect ratio, high exit Mach number and relatively large trailing-edge thickness to permit effective cooling. The complexity of the resulting flow pattern leads to uncertainty in the application of established analytical procedures and requires experimental verification of prediction techniques under realistic operating conditions. The present work builds on several earlier investigations. Langston, et al. [1, 2] described three-dimensional subsonic flow in a large scale, low apsect ratio (1.0) planar cascade of turbine aerofoils with a turning angle of 70°. Biner and Romey [3] utilized an annular rather than a planar cascade of aspect ratio 0.56, turning angle 69°, and exit Mach number of 0.74. The investigations of Sieverding, et al. [4, 5] involved a low aspect ratio (0.6) annular nozzle of 68° turning angle, again at subsonic conditions. Camus, et al. [6] extended the exit Mach number range to 1.2 but utilized a planar cascade of blades with geometry similar to that of a turbine rotor (121° turning, 2.1 aspect ratio). Recent work reported by Haas [7] presented a comparison of analytical and experimental results from a relatively lightly loaded annular cascade operated at pressure ratios up to 2.1, and concluded that further work was desirable on cascades of increased loading.

The present series of tests was undertaken to provide detailed information on the performance of a representative annular nozzle arrangement designed as part of a highly loaded turbine stage of total pressure ratio 3.7. Aspect ratio (based on mean airfoil chord) was 0.6, nominal turning angle 76° and design exit Mach number 1.15 at the vane mean section.

Nozzle Design

The stator was designed to accomplish most of the flow turning in the upstream portion of the flow channel. Vane minimum trailing-edge thickness was dictated by cooling requirements of a typical engine application. Selection of number of aerofoils was based on a tradeoff between trailing-edge losses and aspect ratio (secondary) losses, leading to 14 vanes corresponding to a solidity of 1.2. Leading-edge diameter was compromised between stator cooling effectiveness, horseshoe vortex size, and local overspeed in the leading-edge region. Large leading-edge ramps were employed which were blended with a general fillet radius of 4.6 mm. Inlet metal angle was then selected to have −10° incidence in order to account for induced effects at design conditions. Vane sections were stacked such that the trailing edge was straight and radial in both meridional and axial views. Vane geometry is shown in Fig. 1.

Endwall contouring of turbine nozzles has been demonstrated in references [7–9] to offer potential for performance improvement. The larger vane height at nozzle entry in effect permits initial turning of the flow to be accomplished at lower velocities than would otherwise be the case, with subsequent additional acceleration available to help reduce exit flow nonuniformities. If endwall contouring is introduced only at the tip, then some local diminution of radial pressure gradients should be possible, with associated decrease of

---

Contributed by the Fluids Engineering Division of THE AMERICAN SOCIETY OF MECHANICAL ENGINEERS and presented at the Winter Annual Meeting, Miami Beach, FL, November 17–22, 1985. Manuscript received by the Fluids Engineering Division, September 4, 1985.

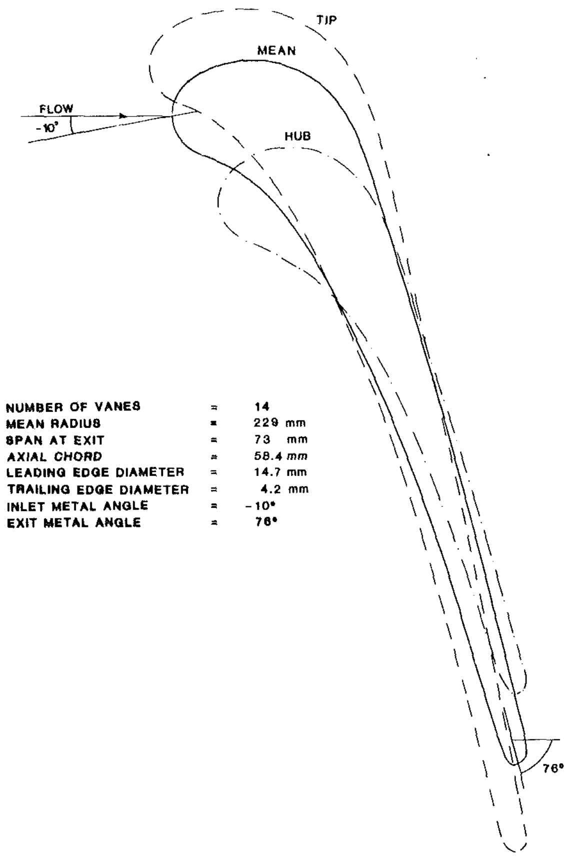

Fig. 1 Vane sections and midspan geometric parameters

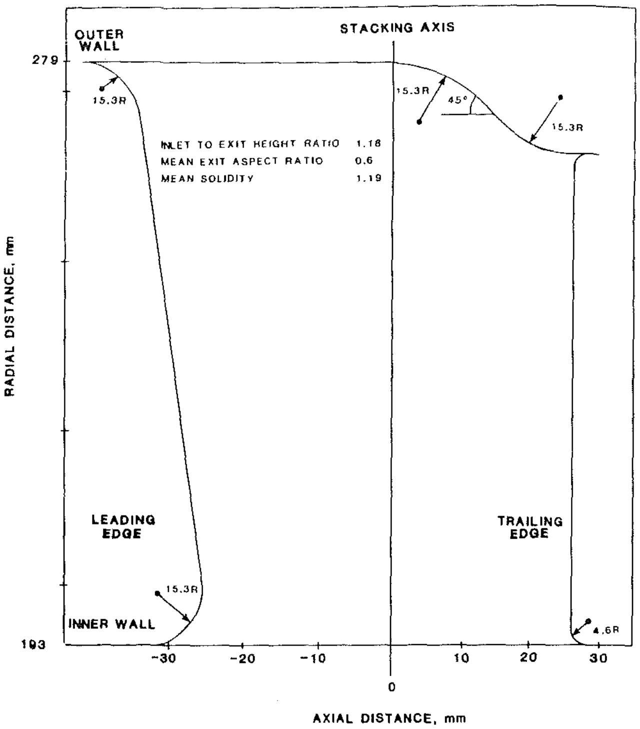

Fig. 2 Stator meridional view

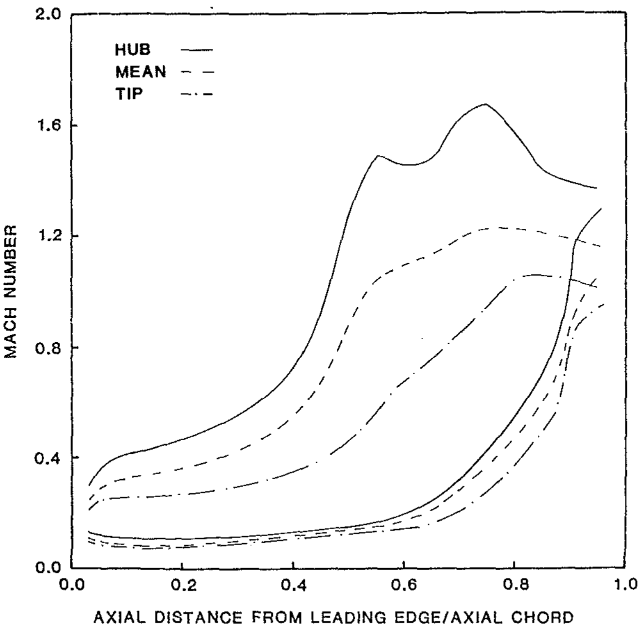

Fig. 3 Predicted vane surface Mach number distributions at design conditions

secondary flow development [10]. Figure 2 shows a stator meridional view which illustrates the endwall contour used in the present tests. For an aspect ratio of 0.6 (or 1.25 based on axial chord) an inlet-to-exit height ratio of 1.18 was selected, slightly less than the optimum of 1.24 suggested in reference [11].

Time-marching solutions of the Euler equations (e.g., [12]) have been widely used in calculating the three-dimensional inviscid flow field in a turbomachinery passage. The main advantage of such a method is the ability to compute subsonic and supersonic flows with automatic capturing of shock waves, although it is noted that the version of the calculation procedure used here (based on [12]) tends to smear the discontinuities associated with shock waves.

Analysis of the nozzle design, including the contoured endwall, resulted in hub, mean, and tip surface Mach number distributions shown in Fig. 3 for the design pressure ratio condition. Noteworthy is the strong diffusion on the hub suction surface at about 75 percent chord which might be expected to promote rapid boundary-layer growth and increase the possibility of flow separation in that region. Mach number

Nomenclature

Cp_0 = local total pressure loss coefficient, $Pom_1 - Po_2 / Pom_1 - Psm_2$
$\overline{Cp_0}$ = circumferential mean of Cp_0
$\overline{\overline{Cp_0}}$ = area weighted radial mean of $\overline{Cp_0}$
Cx = axial chord at midspan
Pom = mean total pressure
Po = local total pressure
PR = nozzle total-to-static pressure ratio, Pom_1/Psm_2
Psm = mean static pressure
Ps = local static pressure
q = area weighted mean of $Po_2 - Ps_2$
Yp = area weighted mean of $(Pom_1 - Po_2)/Pom_1$
Yq = area weighted mean of $(Pom_1 - Po_2)/q$
α = local exit yaw angle (from axial)
$\bar{\alpha}$ = circumferential mean of α
$\bar{\bar{\alpha}}$ = area weighted radial mean of $\bar{\alpha}$

Subscripts

1 = nozzle inlet plane
2 = nozzle exit plane, 0.14 Cx from nozzle trailing edge

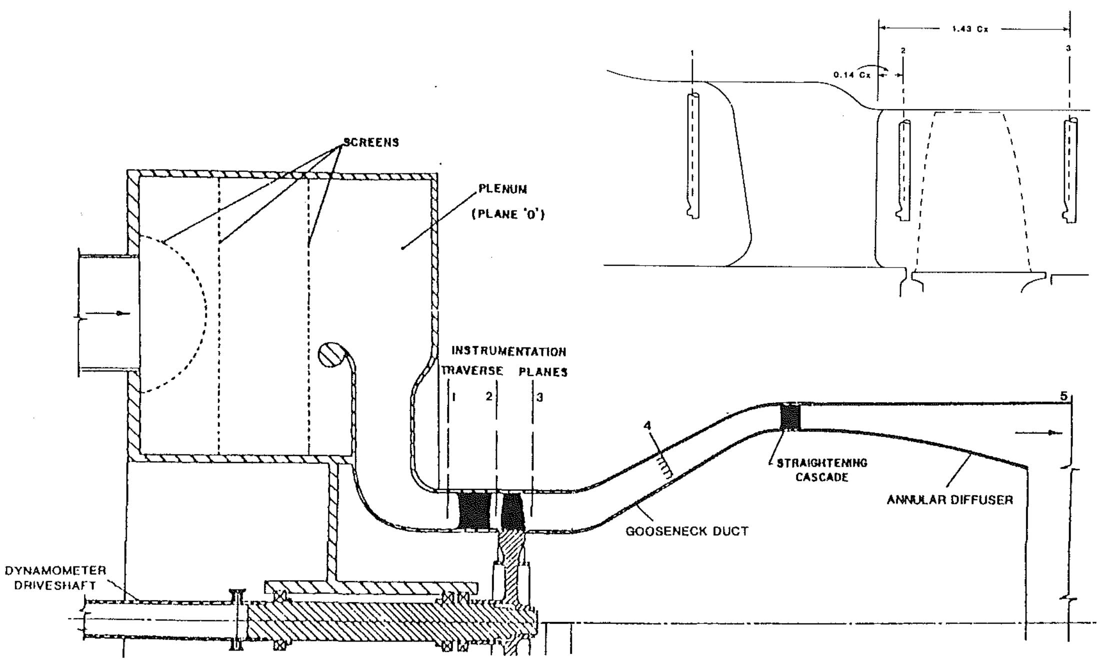

Fig. 4 Highly loaded turbine rig

distributions at mean height and tip indicate that peak Mach numbers reduce with increasing radius (reflecting radially increasing static pressure) and that shock-related effects should be correspondingly less severe. Also evident is a reduction of airfoil loading with increasing radius, resulting from vane design and stacking and also from wall contouring.

Experimental Arrangements

Test Details. The facility was designed to accommodate single turbine stages of about 53 cm o.d. with blade heights up to 7½ cm. Such dimensions are typically several times those of full-size small turbine engines and permit "cold" testing at representative Mach and Reynolds numbers, with ample space for comprehensive instrumentation. A sketch of the overall layout, which also shows instrumentation planes, is presented in Fig. 4.

Air was drawn through the rig by a separate exhauster plant. In tests on a complete stage, the inlet air can be prewarmed by mixing with the output of a propane combustor to maintain stage exit temperature near cell ambient conditions. The prewarming feature was used in the present series of tests on nozzles alone when ambient conditions of low temperature and/or high humidity would have led to freezing or condensation problems at nozzle exit. Inlet temperatures in these tests were limited to about 35°C.

During the preliminary tests described here, the rotor was replaced by a dummy ring of diameter equal to that of the rotor blade hub platform. It is noted that small steps were present in outer and inner walls, corresponding to actual design practice associated with cooling requirements. For these tests, conducted in the absence of a rotor, it was necessary to throttle the inlet slightly to permit the exhauster to operate within its power limitations. The plenum pressure was generally about 0.75 bar. Mass flow at design pressure ratio was 4.1 kg/s, corresponding to a mean inlet Mach number of 0.1. Vane Reynolds number based on mean chord and inlet conditions was about 1.8×10^6, and near 9×10^6 based on exit conditions.

Instrumentation. Instrumentation was designed to explore gas angles and pressures under steady-state conditions. Mass flow was measured by a calibrated bellmouth at entry to the mixing tank. Plenum conditions (plane "0") were sensed by 16 partially shielded thermocouples equispaced around the circumference and by four static pressure tappings. In view of the very low air velocities involved, the measurements were assumed to represent inlet stagnation conditions.

Nozzle inlet conditions (plane "1") were defined from the average of readings from three static pressure tappings at both hub and tip, and could be explored in more detail by radial traverses at three locations each circumferentially midway between adjacent vane leading edges at the tip surface. Two nozzle blades were equipped with a row of static pressure tappings at midheight, one covering the suction and the other the pressure surface. A further row of static pressure tappings midway between blades on hub and tip endwalls completed instrumentation on the four surfaces of one nozzle passage.

The test facility, designed for investigation of a complete stage, permitted radial and circumferential traversing at nominal nozzle and rotor exit planes (Fig. 4), the actual traverse positions being, respectively, 8.5 mm and 84.5 mm axially downstream of the nozzle trailing edge (corresponding to 0.14 and 1.43 nozzle axial mean chords). Traverses were performed using a 4.8-mm-dia wedge probe. (Some limited additional traverse work was carried out using a cobra probe with a thinner, lozenge-shaped stem, which permitted possible probe blockage effects to be investigated. The similarity of total pressure losses recorded with both probes suggests that probe blockage was not a major factor in the results.) Approach of the probe to the hub was limited by contact with the wall when the total pressure port was 4.8 mm from the surface. Considerable care was taken to ensure adequate sealing of the traverse slots, and final checks were made with smoke to ensure no detectable leaks were present.

The probe was operated under computer control, being automatically nulled for flow direction at each preselected point before total temperature and pressure data were recorded. For each circumferential position, data were secured at 12 radial immersions of the probe. A total of 11 circumferential increments, equispaced across a nozzle exit, was required to complete the mapping for each test condition. Experiments were conducted at three nominal pressure ratios ranging from subsonic to supersonic exit conditions.

No attempt was made to derive local static pressure from probe readings in the complex high Mach number flow field of wakes and secondary flows. Analysis indicated a near linear

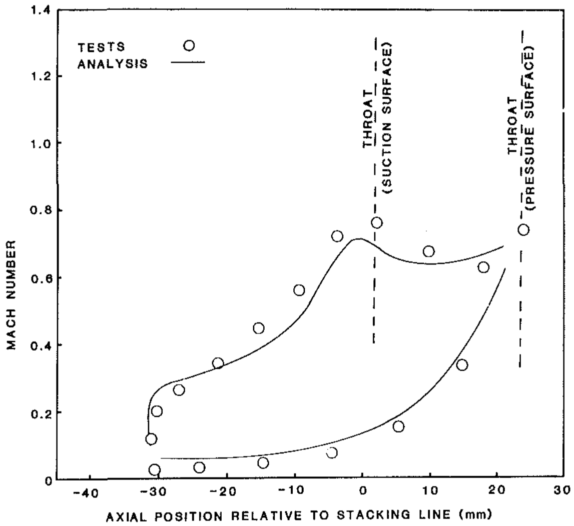

Fig. 5 Vane surface Mach number distribution at mean section (*PR* = 1.4)

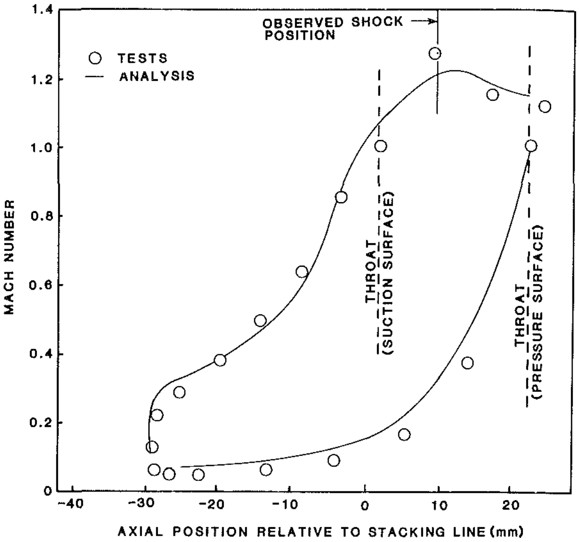

Fig. 7 Vane surface Mach number distribution at mean section (*PR* = 2.3)

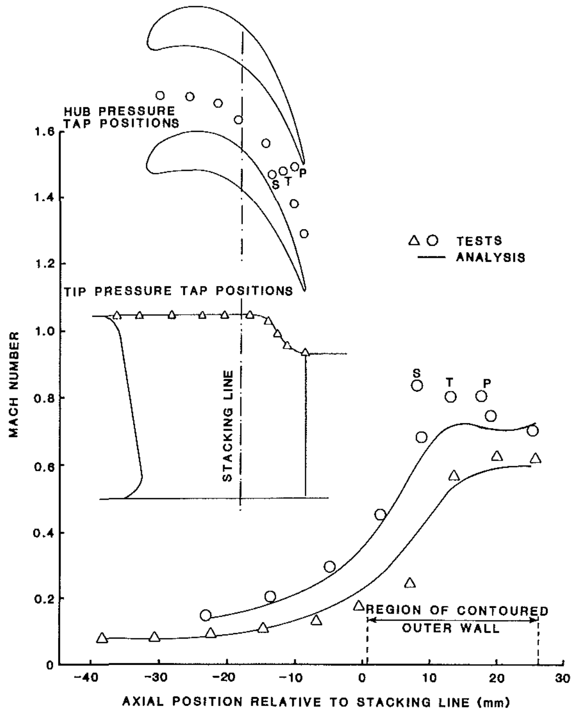

Fig. 6 Nozzle endwall Mach number distributions (*PR* = 1.4)

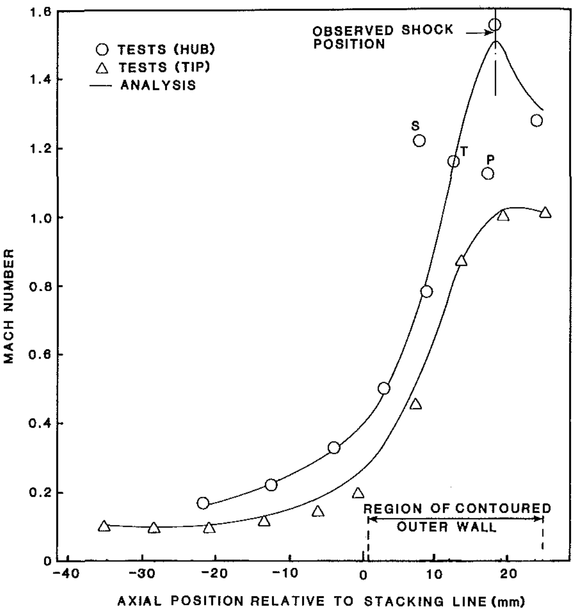

Fig. 8 Nozzle endwall Mach number distributions (*PR* = 2.3)

mean static pressure gradient from hub to tip could be expected, and accordingly linear interpolation from measured wall static pressures at the measurement planes was adopted in calculations of local Mach numbers, without regard for local circumferential variations from blade to blade or variations in wakes and secondary flows. Nozzle exit wall static pressures were averaged from blade to blade at hub and tip by using circumferential slits which extended over two nozzle exit passages and which connected to relatively large volume subsurface chambers in which the static pressures were measured.

Traverse positional accuracy is estimated as ±0.5 mm radially and ±2 mm circumferentially. Accuracy in yaw was a function of the flow conditions, more difficulty being experienced in nulling the probe in regions of unsteadiness associated with blade wakes and strong secondary flows. Although probe calibrations were repeatable to within ±0.2°, repeatability in the more difficult exit flow regions was no better than ±2°. It is noted, however, that the circumferentially averaged values of yaw angle were generally repeatable to within ±0.8°.

Accuracy of surface pressures is estimated at ±0.01 of total pressure. Values of Cp_0 are considered accurate to within ±.01 in areas of relatively low total pressure loss. Some practical confirmation of this is provided by examination of data from the areas of the nozzle exit plane indicating a nominal zero loss. The two independently measured pressures (Pom_1 and the probe total pressure corrected for normal shock loss when appropriate) agreed closely in these locations. Errors introduced by nulling the traverse probe in regions of large pressure gradients, and the fact that pitch angle error on probe total pressure measurement was neglected, were expected to cause additional uncertainties in a small proportion of the readings. Overall averages are affected by these errors and by the difficulties of interpolation when averaging discrete values in rapidly changing total pressure gradients, such as blade wakes.

Experimental Results

Inlet Conditions. Inlet turbulence level at midannulus height was assessed using a constant temperature hot-wire probe mounted at the inlet traverse location. The measured longitudinal intensity of 1.7 percent was independent of test Mach number and is probably low by actual turbine inlet standards. Increase of turbulence level by grids or screens was not attempted as it was felt that turbulence decay rates would be large, introducing additional uncertainties into experimental conditions.

Inlet traverses were conducted at the three circumferential positions using a cobra probe to permit total pressure and angularity readings to be obtained nearer to the hub wall. Typical inlet velocity profiles were seen to be essentially flat with thin boundary layers, particularly at the hub wall. Boundary-layer thicknesses in terms of annulus height are estimated as 2 percent at hub and 9 percent at tip. Measured flow angularity was less than 10° from axial and was clearly affected by nearby vane leading edges which were not radial (in either circumferential or meridional planes) and whose proximity was therefore a function of probe immersion.

Surface Mach Number Distributions. Measured static pressures along the vane surfaces at midspan and midway between vanes on both endwalls were converted isentropically to Mach number using the measured upstream stagnation pressure. The results are compared with analytical predictions based on the three-dimensional version of [12] in Figs. 5-8 at area weighted mean exit Mach numbers of 0.65 (nominal pressure ratio 1.4) and 1.04 (nominal pressure ratio 2.3).

Examination of the low Mach number data in Figs. 5 and 6 shows fairly good agreement between analysis and experiment, although it is apparent from Fig. 6 that extreme values of local pressure gradients on the walls are underpredicted. In particular, the measured adverse pressure gradient downstream of the throat on the hub endwall is more significant than the analysis suggests.

Figures 7 and 8, representing high exit Mach number conditions, display remarkable agreement between measurement and calculations, the only real differences arising in regions of decelerating supersonic flow just downstream of the throat, indicative of the impingement of an oblique shock wave emanating from the trailing edge of the adjacent vane. The smearing of the discontinuity by the calculation method has been noted earlier. Confirmation of the presence of the shock wave was provided by surface flow visualization (Fig. 9) which showed excellent agreement with the implications of the measured pressure distributions at midspan and on the endwall.

The calculation method required introduction of appropriate cusps at the relatively blunt vane leading and trailing edges to prevent the occurrence of a grid discontinuity at these locations. The soundness of the cusp modeling technique was confirmed by the generally good agreement between measured and predicted shock systems, although it is noted that leading-edge stagnation points are not predicted.

Radial Distribution of Losses at Plane 2. As mentioned earlier, traversing was conducted at 11 circumferential positions spanning one vane pitch. Circumferential area averaging of total pressure losses at each radial immersion led to the mean radial distributions presented in Fig. 10 for the three nozzle pressure ratios.

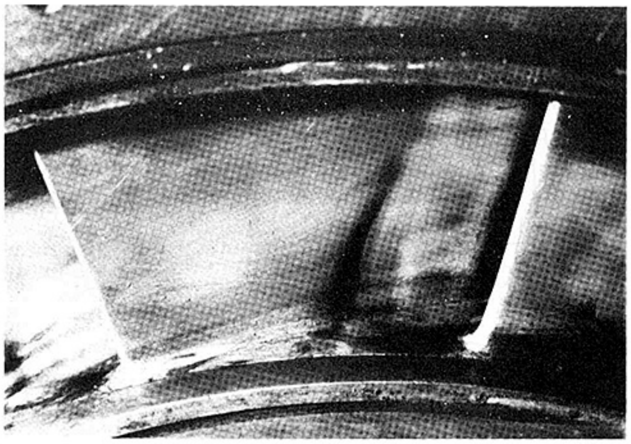

Fig. 9 Surface flow visualization of shock position on suction surface ($PR = 2.3$)

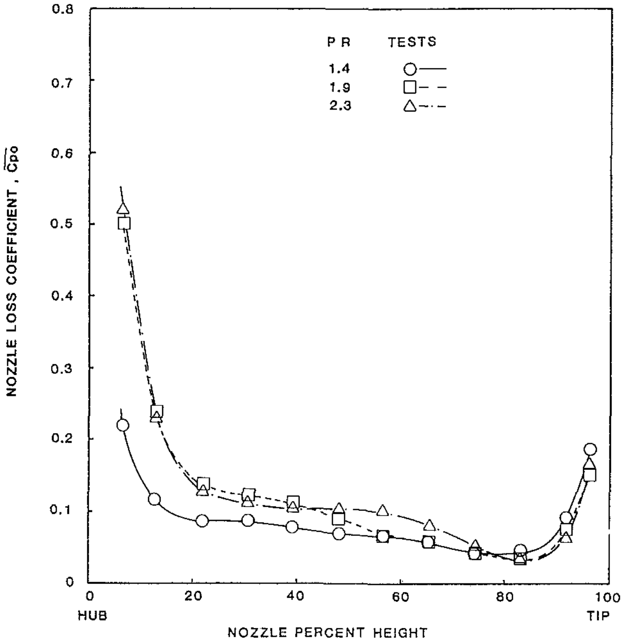

Fig. 10 Radial distribution of circumferentially averaged total pressure loss at plane 2

At all three test conditions, the hub wall has higher overall loss coefficients than the tip region, arising from increased boundary-layer growth in the adverse pressure gradient downstream of the throat as well as radial migration of vane surface boundary layers. It is interesting to note that near the hub the loss coefficients do not rise monotonically with increasing pressure ratio, the largest values being observed at the intermediate condition. This may stem from the fact that at low supersonic Mach numbers the shock wave from the trailing edge of the adjacent vane impinges on the uncovered suction surface farther upstream than is the case at higher Mach numbers when the shock is more oblique. Although the shock/boundary-layer interaction is a function of shock strength it may well be that the greater development distance of the disturbed boundary layer and the angle of the impinging shock wave play a significant role in determining the magnitude of the observed loss coefficients. Sonic conditions could also be expected to occur first in the free-stream near the hub suction surface where local static pressures are lowest, leading to maximum shock strength in that region under given conditions. As nozzle pressure ratio is increased to the design value, the shock/boundary-layer interaction region on the suction surface would extend farther toward the tip, leading to greater radial extent of the higher loss region.

Total Pressure Loss Contours at Plane 2. Further information can be gleaned from consideration of the individual total pressure loss measurements which are presented as contours of loss coefficients, Cp_0, in Fig. 11. As noted earlier, measurements were taken over a circumferential distance cor-

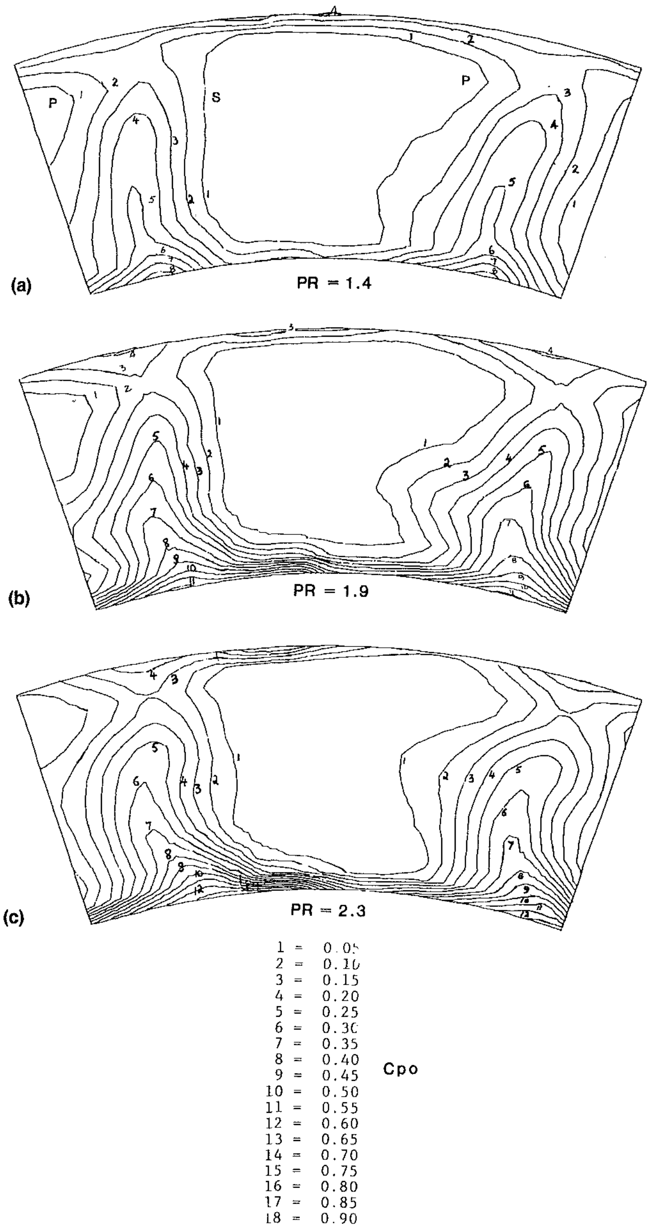

Fig. 11 Total pressure loss contours at plane 2

responding to one vane pitch. For clarity of presentation the pattern of measurements has been partially repeated to cover more than a single pitch and to show the repetitive wake effect. Essentially radial regions of loss corresponding to vane wakes are evident in the Figures, the magnitude and extent of the loss contours clearly increasing with pressure ratio. The shock/boundary-layer interaction at intermediate pressure ratio at the hub/suction surface intersection (referred to earlier) is clearly seen as a thickening of the loss region on the hub surface in Fig. 11(*b*). It is evident from Fig. 11(*c*) that at design pressure ratio the near-hub loss region has become somewhat smaller in radial extent, although more intense, as mentioned in the discussion of Fig. 10.

Radial Distribution of Exit Flow Angle at Plane 2. Radial distributions of flow angle at plane 2 are presented in Fig. 12. The low pressure ratio results clearly demonstrate the classical secondary flow pattern, with overturning near the endwalls and underturning in the passage center. (Oil flow visualization confirmed more extreme local overturning of the flow on the hub and tip endwalls.) The measured angle distribution shows the region of flow overturning to be more extensive near the vane tip than near the hub, probably reflecting the thicker inlet tip boundary layer.

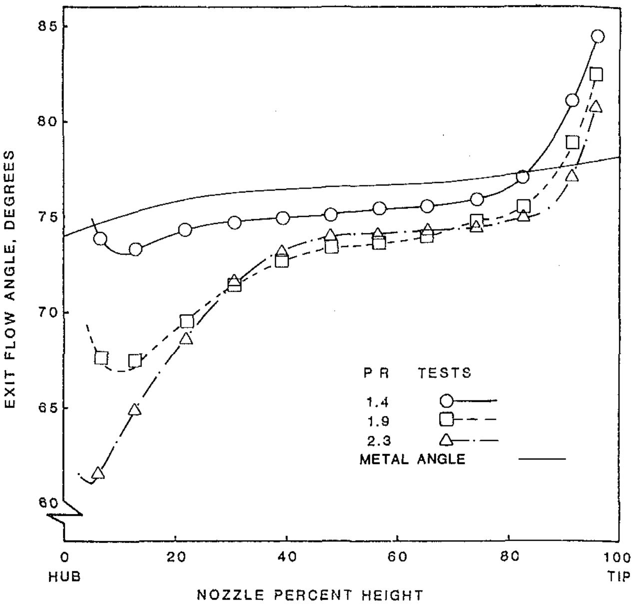

Fig. 12 Radial distribution of circumferentially averaged exit flow angle at plane 2

Increasing pressure ratio from the low to the intermediate value decreases the overall flow turning across the span and produces a marked change near the hub where the vortex action is significantly increased. This action near the hub is consistent with the modifications to the total pressure loss distribution presented earlier, and appears to be a manifestation of increased secondary flow in that growing low energy region associated with the shock/boundary-layer interaction. Further increase in pressure ratio drives the secondary vortex center closer to the hub wall as the high loss region diminishes in extent, and also reduces turning near the tip as the shock system continues to spread radially along the span. It appears from the present observations that the circumferentially averaged values of flow angle are consistent with the inferences from the total pressure measurements.

Comparison With Analysis – Plane 2. Comparison of the circumferentially averaged flow angle distributions with the predictions of the analytical method is afforded by Fig. 13. The mean flow angle agreement at low pressure ratio is excellent when viscous (secondary flow) effects at both endwalls are neglected. With increasing pressure ratio some discrepancy in level becomes evident, although radial trends outside the endwall regions are well reproduced. Bearing in mind the limitations of the inviscid calculation method and the experimental uncertainties, the extent of the agreement is encouraging.

For completeness experimentally derived radial distributions of Mach number are compared with predictions in Fig. 14. Local values of Mach number, calculated from measured total pressure and static pressure interpolated from mean wall values, have been averaged circumferentially over one vane pitch. Again, the general agreement away from wall boundary layers is good.

Assessment of Overall Performance. Area weighted averaging of the mean radial distributions of total pressure loss coefficients and flow angles measured at plane 2 (Figs. 10 and 12) permitted overall performance to be assessed for the three values of nozzle pressure ratio. As a point of interest an attempt was made to use mass flow weighted averaging, but

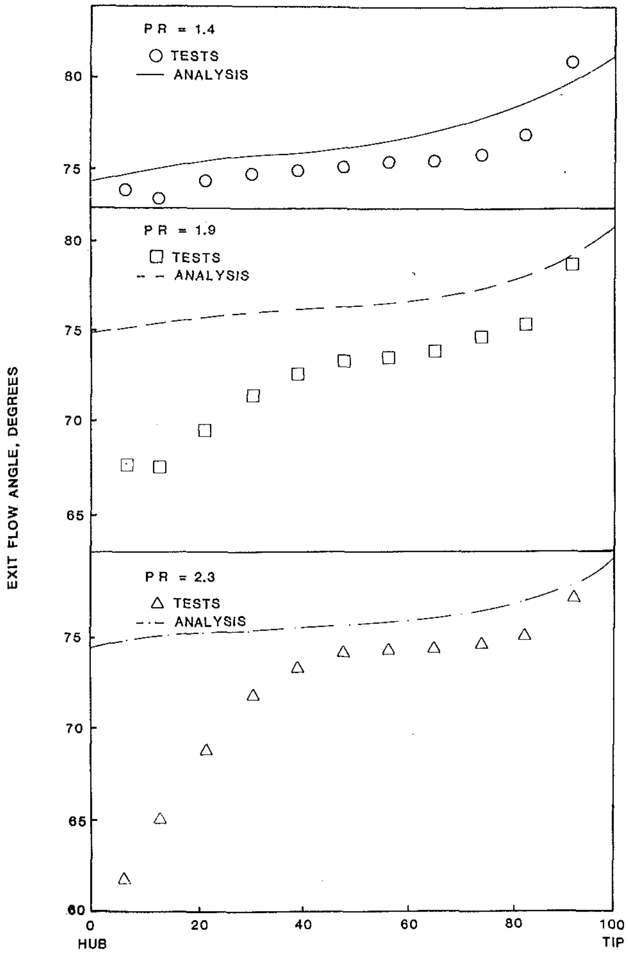

Fig. 13 Radial distribution of circumferentially averaged exit flow angle at plane 2 (comparison with analysis)

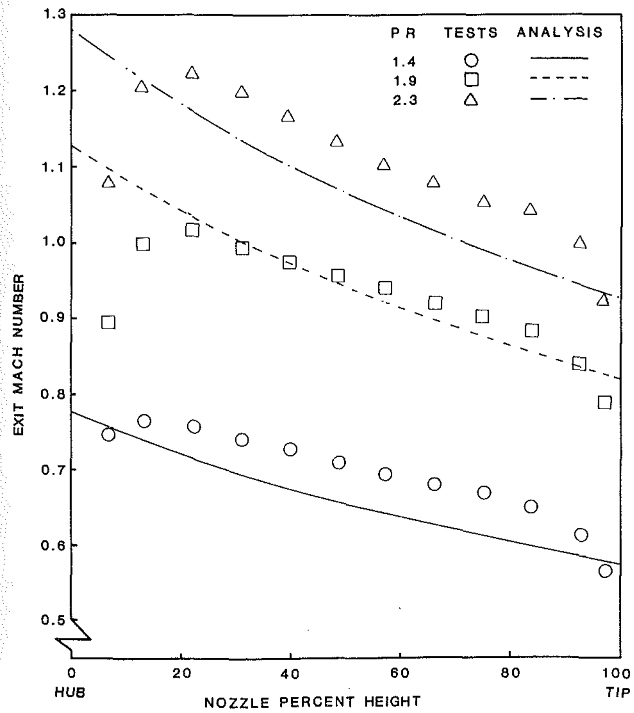

Fig. 14 Radial distribution of circumferentially averaged exit Mach number at plane 2 (comparison with analysis)

Table 1

Nominal PR		1.4	1.9	2.3 Design
Mean Exit Mach No.	Measured Parameters	0.67	0.89	1.05
$\bar{\alpha}$ (deg)		76.2	73.5	72.7
Yp		0.039	0.075	0.096
$\bar{\bar{C}}p_0$		0.129	0.161	0.168
Yq		0.150	0.195	0.204
Total loss, Yq	[13]	0.159	0.167	0.168
Profile loss	[13]	0.035	0.035	0.049
Secondary loss	[13]	0.083	0.083	0.083
Trailing-edge loss	[13]	0.041	0.049	0.054

check calculations against measured mass flow were unsatisfactory. Accuracy of mass flow weighting in flows such as these requires use of appropriate local values of static pressure, rather than overall mean interpolated values, and knowledge of local flow angles assumes considerable importance (1° error in a flow angle of 76° incurs a 7 percent error in mass flow).

Values of the overall measured performance parameters are summarized in Table 1, which also shows the values of Yq calculated for the nozzle using the method of Kacker and Okapuu [13]. The calculated values do not include transonic shock/boundary-layer interactions, and significantly underpredict the losses in these conditions. The general level at lower and higher exit Mach numbers is in fair agreement with the measurements.

It is noted that the present results apply to an isolated annular nozzle cascade, i.e., nozzles without a downstream rotor. Although Boletis and Sivereding [5] found essentially no effect of a downstream rotor on nozzle performance, their tests were conducted under incompressible flow conditions. The Highly Loaded Turbine facility is therefore currently being used to investigate possible rotor interaction effects at realistic nozzle exit Mach numbers. Initial results suggest that the nozzle hub separation stemming from shock/boundary-layer interaction can be significantly reduced by the rotor, the extent of the modification depending on the rotor design and operating conditions. Further tests are in progress to elucidate this effect and will be reported in [14].

Conclusion

Experimental data have been presented on the aerodynamic performance of a full annular cascade of highly loaded turbine nozzles incorporating a contoured endwall, tested over a range of pressure ratio (inlet total to mean exit static) from 1.4 to 2.3. These results have been compared with analytical predictions of an inviscid flow calculation procedure due to Denton [12].

Good agreement was obtained between measured data and calculation in terms of nozzle surface static pressure distributions, from which it was possible to predict a potential problem area at the hub/suction surface intersection.

Three-dimensionality of the flow was observed to increase with the onset of transonic conditions in the nozzle when a sharp rise in total pressure loss at the hub was observed. Implications of the changes in distribution of total pressure loss with increasing nozzle pressure ratio were correlated with observed modifications in radial distribution of exit flow angle. Trends in radial distribution of exit flow angle were reasonably well reproduced by the calculation procedure in midspan regions less susceptible to viscous effects.

Overall nozzle performance parameters in terms of area-weighted mean flow angle and mean total pressure losses (normalized in three standard fashions) have been presented for the test range of nozzle pressure ratio and suggest the largest changes are experienced under transonic conditions.

The results have demonstrated the ability of an inviscid flow calculation procedure to achieve remarkably close predictions of the surface Mach number distributions in a transonic low aspect ratio nozzle of complex geometry. The exit flow field from such nozzles is, however, strongly influenced by viscous effects as evidenced by the comparison of measured and predicted radial distributions of flow angle.

Work is currently in hand to assess the effects on nozzle performance of a downstream rotor. Preliminary data indicate that the hub separation found in the present tests under transonic and supersonic flow conditions may be significantly reduced by the presence of an operating rotor.

Acknowledgment

The work reported here is part of a joint research program carried out by the National Research Council of Canada and Pratt and Whitney Canada Inc. Contributions to the original design by numerous colleagues at P&WC are gratefully acknowledged, with particular recognition of the inputs and assistance of Ü. Okapuu (overall Program Manager), S. C. Kacker, and J. P. Huot. The unremitting efforts of B. J. Day and D. L. Logan of NRC in the experimental work are greatly appreciated.

References

1 Langston, L. S., Nice, M. L., and Hooper, R. M., March 1976,"Three-Dimensional Flow Within a Turbine Cascade Passage," ASME Paper No. 76-GT-50.

2 Langston, L. S., March 1980, "Crossflows in a Turbine Cascade Passage," ASME Paper No. 80-GT-5.

3 Binder, A., and Romey, R., April 1982, "Secondary Flow Effects and Mixing of the Wake Behind a Turbine Stator," ASME Paper No. 82-GT-46.

4 Sieverding, C. H., Van Hove, W., and Boletis, E., March 1983, "Experimental Study of the Three-Dimensional Flow Field in an Annular Turbine Nozzle Guidevane," ASME Paper No. 83-GT-120.

5 Boletis, E., and Sieverding, C. H., June 1984, "Experimental Study of the Flow Field Behind an Annular Turbine Nozzle Guide Vane With and Without Downwstream Rotor," ASME Paper No. 84-GT-15.

6 Camus, J-J., et al., March 1983, "An Experimental and Computational Study of Transonic Three-Dimensional Flow in a Turbine Cascade," ASME Paper No. 83-GT-12.

7 Haas, J. E., 1982, "Analytical and Experimental Investigation of Stator Endwall Contouring in a Small Axial-Flow Turbine. I—Stator Performance," NASA Techanical Paper 2023, AVRADCOM Technical Report 82-C-4.

8 Morris, A. W. H., and Hoar, R. G., November 1975, "Secondary Loss Measurements in a Cascade of Turbine Blades With Meridional Wall Profiling," ASME Paper No. 75-WA/GT-13.

9 Kopper, F. C., Milano, R., and Vanco, M., June 1980, "An Experimental Investigation of Endwalls Profiling in a Turbine Vane Cascade," AIAA Paper No. 80-1089.

10 Moustapha, S. H., and Williamson, R. G., July 1985, "Investigation of the Effect of Two Endwall Contours on the Performance of an Annular Nozzle Cascade," AIAA Paper No. 85-1218.

11 Ewen, J. S., Huber, F. W., and Mitchell, J. P., April 1973, "Investigation of the Aerodynamic Performance of Small Axial Turbines," ASME Paper No. 73-GT-3.

12 Denton, J. D., 1975, "A Time Marching Method for Two and Three-Dimensional Blade to Blade Flow," ARC R&M 3775.

13 Kacker, S. C., and Okapuu, Ü., 1981, "A Mean Line Prediction Method for Axial Flow Turbine Efficiency," ASME Paper No. 81-GT-58.

14 Williamson, R. G., Moustapha, S. H., and Huot, J. P., June 1986, "The Effect of a Downstream Rotor on the Measured Performance of a Transonic Turbine Nozzle," ASME Paper No. 86-GT-103.

H. J. Tucker
Associate Professor,
Department of Mechanical Engineering,
University of Windsor,
401 Sunset Avenue,
Windsor, Ontario N9B 3P4
Canada

S. M. N. Islam
Associate Professor,
Department of Mechanical Engineering,
University of Engineering and Technology,
Dacca, Bangledesh

Development of Axisymmetric Laminar to Turbulent Free Jets From Initially Parabolic Profiles

Experiments were carried out on air in air axisymmetric free jets having parabolic profiles at the nozzle exit. The range of Reynolds numbers investigated was from 2342 to 11,000 and transition from laminar to turbulent flow was observed. The development of the laminar mean velocity profiles agrees well with that predicted from solution of the continuity and momentum equations using an explicit finite-difference technique of the Dufort-Frankel type. Some observations are made of the transition from laminar to turbulent flow using hot-wire turbulence measurements, and an empirical equation for the location of the transition is given.

Introduction

Axisymmetric free jets have been studied extensively over a period of many years and from many perspectives. Visual observations made by A. J. Reynolds [1] and others, show many different types of flow phenomena which depend primarily on the jet Reynolds number based on the nozzle diameter and mean velocity. At high Reynolds numbers, jets are fully turbulent starting from the nozzle exit and are classified as turbulent jets. At lower Reynolds numbers, jets flow for some distance from the nozzle in a laminar state before developing a sinuous turbulent motion. The onset of turbulence takes place over a range of distances from the nozzle which vary from moment to moment, with the time average location of the transition moving downstream as the Reynolds number is decreased; these jets are classified here as laminar to turbulent. At lower Reynolds numbers, the breakdown of the laminar motion takes place at increasing distances from the nozzle with the formation of a variety of large regular patterns the character of which also depend on the Reynolds number. At still lower Reynolds numbers, free jets appear to remain laminar for considerable distances from the nozzle.

The present experiments on laminar to turbulent jets were carried out on air in air free jets for Reynolds numbers in the range 2342 to 11,000. The jets originated from a nozzle with a rounded entrance followed by a long straight tube which produced parabolic velocity profiles at the nozzle exit.

In the study of laminar to turbulent jets it would be convenient if existing calculation methods for laminar jets could be applied to the developing laminar portion of the flow. The classical method of treating laminar jets by Schlichting [2] and by Andrae and Tsein [3] and others is to assume that a laminar jet originates from a point source and that the jet has self-preserving profiles, i.e., remain similar in the downstream direction. For the jets presently studied, these assumptions are not valid since the initial velocity profiles are finite and parabolic and the similarity of profiles is not maintained.

The calculation method used here for the laminar portion of the jet is to solve the continuity and the momentum equations using a numerical finite difference method of the Dufort-Frankel type, starting from a parabolic velocity profile. However, the method is general in that an arbitrary axisymmetric profile may be used.

The experimental results presented are for jets having Reynolds numbers 2342 to 11,000. For the laminar portion of the jets these results are complementary to those of Du Plessis, et al. [4] for laminar jets with Reynolds numbers between 168 and 290; also developing from initially parabolic profiles. The numerical method used by the authors is considered to be easier to apply than the method used by Du Plessis, et al. [4].

Laminar Flow Equations

For steady, incompressible, axisymmetric laminar flow, the governing equations are as follows:

The Continuity Equation

$$\frac{\partial(ur)}{\partial x}+\frac{\partial(vr)}{\partial r}=0 \tag{1}$$

The Momentum Equation

$$u\frac{\partial u}{\partial x}+v\frac{\partial u}{\partial r}=\frac{\nu}{r}\frac{\partial}{\partial r}\left(r\frac{\partial u}{\partial r}\right) \tag{2}$$

In the momentum equation, it is assumed that there is no pressure gradient and that the boundary-layer approximations apply. The kinematic viscosity, ν, is assumed constant, x is the axial distance measured from the exit plane of the nozzle, r is the radial distance measured from the longitudinal centerline of the jet and u and v are the longitudinal and radial velocity components, respectively. The appropriate boundary conditions are

$$\frac{\partial u}{\partial r}(x,0)=0,\quad v(x,0)=0,\quad \lim_{r\to\infty} u(x,r)=0 \tag{3}$$

Contributed by the Fluids Engineering Division for publication in the JOURNAL OF FLUIDS ENGINEERING. Manuscript received by the Fluids Engineering Division April 1986.

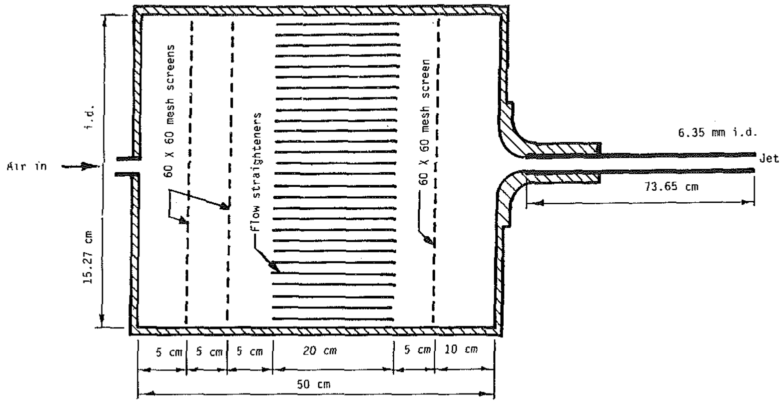

Fig. 1 Details of the settling chamber and nozzle

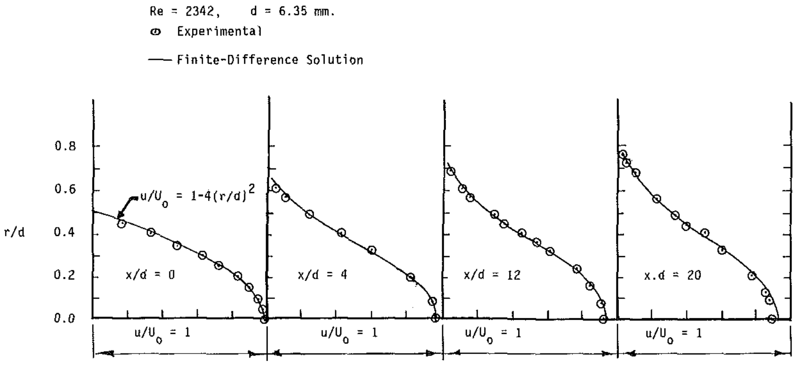

Fig. 2 Jet velocity profiles

In addition the initial parabolic distribution of the axial velocity, u, is

$$u(0,r) = U_0\left(1 - \frac{r^2}{R^2}\right) \tag{4}$$

where U_0 is the centerline velocity at $x=0$ and R is the inner radius of the nozzle at the exit.

Calculation Technique

An explicit finite-difference technique of the Dufort-Frankel type was used to solve equations (1) and (2) with boundary conditions (3) and (4). This method was originally developed for turbulent jets; the finite-difference equations and calculation procedures are given in reference [5] and are not repeated in this paper. Calculations for the laminar portions of the jets were carried out using the same equations and procedures but neglecting the turbulent diffusivity terms.

Experimental Facilities

Air from the laboratory supply was passed through filters, pressure regulator, needle valve and flowmeter before entering the settling chamber, the details of which are shown in Fig. 1. Air in the settling chamber passed through two screens, a set of flow straighteners of 6.35 mm hexagonal honeycomb and a third screen before entering the nozzle which was carefully constructed using a smooth bellmouth entrance followed by a tube of diameter 6.35 mm and length 736.5 mm, giving an l/d ratio of 116 which was considered sufficient to establish a developed parabolic laminar profile at the exit.

The probing mechanism allowed the jet to be traversed in the radial direction using a vernier with a micrometer gauge capable of measuring within 0.025 mm. The mounting was such that the probe could be rotated 90° about the jet axis so that the axial symmetry of the jet could be investigated. The probing mechanism also allowed measurements to be taken at any location in the longitudinal direction of the jet with a precision of 0.25 mm.

The longitudinal turbulence intensities and the mean velocity in the jet were measured using a DISA constant temperature hot-wire anemometer (Type 55A01). Although the anemometer contained its own rms meter and d-c voltmeter, greater accuracy was obtained by using a Bruel and Kjaer rms voltmeter (Type 2417) with an accuracy of 1 percent full-scale deflection, and a Hewlett-Packard digital voltmeter (Model 3340A) with an estimated accuracy of ±0.5 percent of the reading of the bridge d-c voltage. A DISA probe (Type 55A25) was used with a 5μ platinum-plated tungsten normal wire, approximately 1 mm long.

The hot wire was calibrated by locating the wire and a pitot tube side by side in a uniform velocity region of a variable speed wind tunnel and obtaining simultaneous readings of bridge voltage and velocity in steps. The pitot tube was connected to a Lambrecht inclined tube manometer, which in turn was calibrated using a Merian micromanometer having a precision of 0.025 mm. The velocity was varied in steps over the range of velocities encountered in the jet flows. The hot-wire equation was of the form, $E = A + Bu^C$ where E is the bridge d-c voltage and u is the stream velocity. The constants A, B, and C were obtained by curve fitting using the least rms deviation and varying C between 0.4 and 0.55.

Tests

Tests were carried out under steady-state conditions for Reynolds numbers in the range 2342 to 11,000 with the Reynolds number based on the inside diameter, d, and the mean velocity at the nozzle exit. Measurement, sufficient to

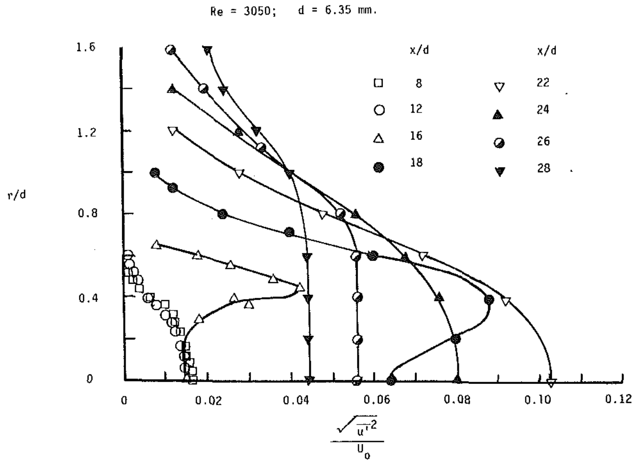

Fig. 3 Turbulence intensity profiles

determine time-averaged velocity profiles up to $x/d = 24$, were made for Reynolds numbers 2342 and 3050, also at Reynolds number 3050 longitudinal turbulence intensity profiles were measured up to $x/d = 28$. For Reynolds numbers 3920 to 11,000, time-averaged velocities and turbulence intensities were measured only along the jet longitudinal centerline.

Discussion of Results

It can be seen in Fig. 2, for Re = 2342, that the experimental velocity profile at the exit of the nozzle, $x/d = 0$, is close to the parabolic velocity profile associated with fully developed laminar flow in a circular tube. Although not shown, similar agreement with parabolic profiles were obtained for Reynolds numbers 2342 and 3820. In ordinary pipe flow, the transition to turbulent flow takes place at Reynolds numbers close to 2300. The existence of laminar flow at the high Reynolds numbers of the present experiments can be largely attributed to the settling chamber with its flow straighteners, fine mesh screens and high reduction ratio nozzle. Additional features which probably influenced the flow were the care taken in finishing the nozzle, mounting of the settling chamber to reduce vibrations and location of the apparatus in a low noise area.

The experimental velocity profiles obtained at increasing distances from the exit of the nozzle are compared with the results of the finite-difference solution for Reynolds number 2342 in Fig. 2. A parabolic profile was used to start the finite-difference calculations. The agreement of the experimental and theoretical results are satisfactory at sections $x/d = 4$, 12 and 20. It was observed during the experiment that the flow became turbulent near $x/d = 20$. The slight disagreement shown at $x/d = 20$ may be attributed to the initiation of turbulence near this location.

For the jets, the transition from laminar to turbulent flow takes place at some distance downstream from the nozzle. This can be seen more clearly by observing the turbulence intensity, $\sqrt{\overline{u'^2}}/U_0$, at increasing distances downstream as shown in Fig. 3 for Reynolds number 3050. Here $\sqrt{\overline{u'^2}}$ is the rms longitudinal fluctuating velocity and U_0 is the centerline velocity at the nozzle exit. At x/d of 8 and 12 the measured values of the turbulence intensities are less than 2 percent. At $x/d = 16$ peaks of intensity of magnitude near 4 percent exit in the region r/d near 0.5 which is in the region of high shear. Comparison of the intensity at x/d of 16, 18 and 22 show a gradual spread of turbulence from the high-intensity high-shear region. The maximum turbulence intensity of over 10 percent occurs at $x/d = 22$ on the jet centerline. Since production of turbulence by mean flow takes place in the high-shear region, the existence of the maximum at the centerline can only be attributed to large-scale mixing across the jet. Although the tests were run under steady-state conditions the turbulence in the region of $x/d = 16$ as indicated by the hot-wire signals was observed to be intermittent.

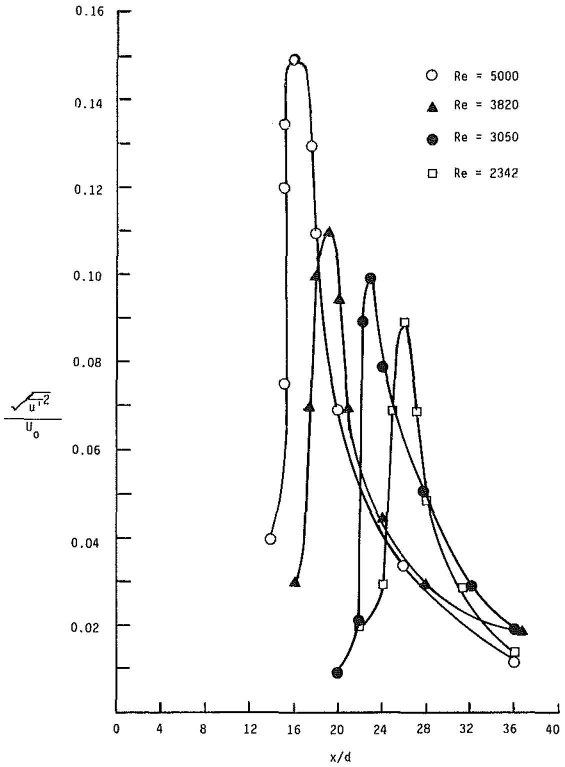

Fig. 4 Intensity of turbulence along the jet centerline

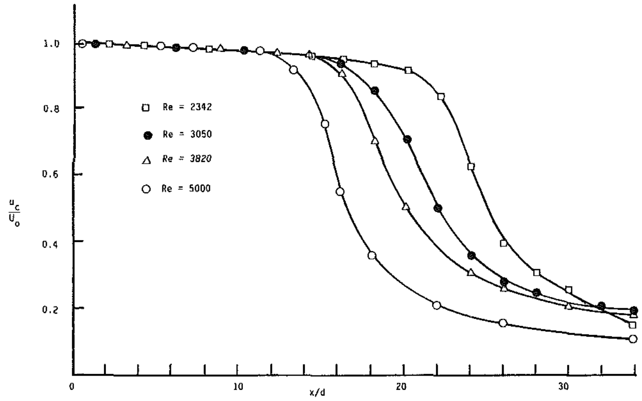

Fig. 5 Centerline mean velocity distribution

The turbulence intensity along the centerline of the jet is shown in Fig. 4. For each Reynolds number, the turbulence in the jet increases rapidly, reaches a maximum value and then decreases. The locations x/d of the maximum values decreases as the Reynolds number is increased; for Reynolds numbers 2342, 3050, 3820, and 5000, the peaks were near x/d, 25, 23, 19, and 16, respectively. Using the turbulence intensity along the centerline from Fig. 4, the location of the transition from laminar to turbulent flow was taken as the x/d corresponding to rapid rise in the $\sqrt{\overline{u'^2}}/U_0$-values.

Figure 5 shows the centerline axial velocities, u_c, in the jets for the four Reynolds numbers. Near the nozzle, the centerline velocity decreases only slightly with distance from the nozzle and in an approximately linear manner. Further downstream a location is reached where the centerline velocity decreases rapidly and this location as measured by x/d decreases with in-

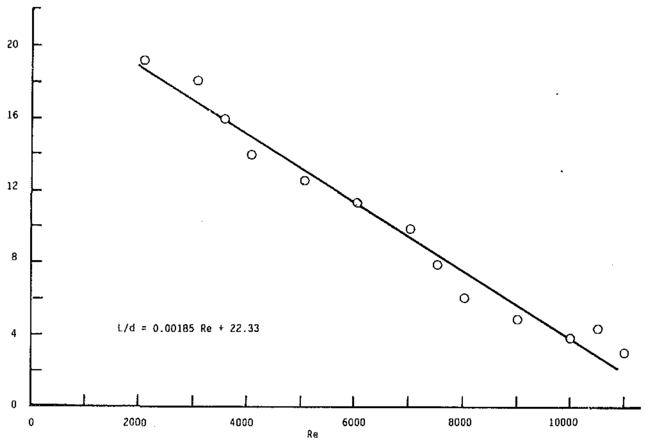

Fig. 6 Downstream distance of the transition from laminar to turbulent flow for different Re

creasing Reynolds number. The decrease in velocity is caused by the transition from laminar to turbulent flow with high transfer of momentum in the turbulent flow. The location of the change in slope of the centerline velocity may be used to indicate the transition from laminar to turbulent flow if turbulence intensity measurements are not available.

It is obvious from Figs. 4 and 5 that the transition from laminar to turbulent flow depends on the Reynolds number. For the jets investigated here the transition lengths versus Reynolds numbers are plotted in Fig. 6 and show good agreement with the empirical formula, $L/d = 0.00185$ Re + 22.33. To obtain Fig. 6, experiments were extended to cover a Re range up to 11,000, with turbulence intensities measured along the jet centerline.

It should be noted that the Reynolds number is only one of the variables influencing the transition from laminar to turbulent flow. A second variable is the small disturbances that exist even in the laminar flow as it issues from the nozzle. The magnitude and characteristics of these small disturbances will depend on the design of the settling chamber and the vibrations transmitted to the settling chamber and nozzle through connections and supports. One measure of these small disturbances in the laminar flow is the longitudinal intensity, $\sqrt{\overline{u'^2}}/U_0$, which in the present experiments measured approximately 1.5 percent on the centerline near the nozzle exit. Another variable which is known to influence the transition from laminar to turbulent flow in jets is small disturbances existing in the ambient fluid. These disturbances may be caused by noise or convection currents. In these experiments, although much care was taken, convection currents caused by movement of the operator, etc., most likely existed. The ambient noise level in the location of the experiments was approximately 70 db and no effort made to reduce this level. The empirical equation for transition to turbulence given here may not apply if small disturbances in the jet and ambient fluid are different from those which existed in the present experiments.

Summary and Conclusions

1 All the experimental jets, Reynolds numbers 2342 to 11,000, were originally laminar with profiles close to parabolic at the nozzle exit. Transition from laminar to turbulent flow occurred as the jets moved downstream.

2 The development of the laminar jet flow, from parabolic profile, can be predicted by solving the continuity and momentum equations using an explicit finite-different technique of the Durfort-Frankel type. This method could be used for axisymmetric jets with arbitrary initial profiles; however, only parabolic initial profiles have been treated here.

3 The initiation of turbulence in jets takes place in the region of high velocity gradient which corresponds to high turbulence production. In a short distance downstream, the maximum longitudinal turbulence intensity is near the jet centerline although the velocity gradient and expected production of turbulence at this location is close to zero.

4 Turbulence measurements along the centerline of the jet show that transition from laminar to turbulent flow takes place at a distance from the nozzle which bears the following linear relationship to the Reynolds number: $L/d = 0.00185$ Re + 22.33. This equation is not expected to apply if small disturbances in the jet and in the ambient fluid are very different from those existing in the present experiments.

Acknowledgments

The authors wish to thank Mr. T. Vaz, former graduate student of the University of Windsor for his careful measurements and the National Science and Engineering Council of Canada for its financial support.

References

1 Reynolds, A. J., 1962, "Observations of a Liquid-Into-Liquid Jet," *Journal of Fluid Mechanics*, Vol. 14, pp. 522–556.

2 Schlichting, H., 1933, "Laminar Strochlausbereitung," *ZAMM*, Bd. 13, pp. 260–263.

3 Andrae, E. N. DaC., and Tsein, L. C., 1937, "The Velocity-Distribution in a Liquid-Into-Liquid Jet," *Proceedings of the Physical Society*, Vol. 49, pp. 381–391.

4 Du Plessis, M. P., Wang, R. L., and Tsang, S., June 1973, "Development of a Submerged Round Laminar Jet From an Initially Parabolic Profile," ASME *Journal of Dynamic Systems, Measurement and Control*, pp. 148–154.

5 Islam, S. M. U., and Tucker, H. J., March 1980, "Flow in the Initial Region of Axisymmetric Turbulent Jets," ASME JOURNAL OF FLUIDS ENGINEERING, Vol. 102, No. 1, pp. 85–91.

Laminarization and Reversion to Turbulence of Low Reynolds Number Flow Through a Converging to Constant Area Duct

Hiroaki Tanaka
Professor.

Hirotaka Yabuki
Graduate Student.

Department of Mechanical Engineering,
University of Tokyo,
Bunkyo-ku, Tokyo, 113 Japan

Airflow in fully developed turbulent state between two parallel plates was accelerated through a linearly converging section, and then it flowed into a parallel-plate channel again. The Reynolds number $2hu_m/\nu$ *was 10,000 and the acceleration parameter* K *in the accelerating section was* 8×10^{-6}. *Fluctuations of streamwise velocity as well as time-mean velocity profiles were measured at ten traversing stations located along the test channel by a hot-wire anemometer. It was found that the flow, partly laminarized in the accelerating section, continued to laminarize in the first part of the downstream parallel-plate section and then the reversion to turbulence occurred in the way similar to the case of natural transition in a pipe, where the transition proceeds through a regime of the so-called turbulent slug flow.*

Introduction

The laminarization of turbulent gas flow subjected to strong heating is of primary importance in the thermal design of a high-temperature gas-cooled nuclear reactor. In this connection, probable reversion to turbulence of a partly laminarized flow in a downstream section where heating rate is moderated is of interest from theoretical as well as practical viewpoints. It is generally admitted that the main cause of the laminarization in a heated pipe is an acceleration of the mean flow velocity [1, 2]. In the experiment reported in the previous paper [3], in order to investigate the laminarization and the subsequent reversion to turbulence essentially under a constant property condition, a fully developed turbulent flow between two parallel plates was first accelerated through a passage between two converging flat plates, and then the flow was led into a second parallel-plate section. Here it should be noted that the Reynolds number defined by $2hu_m/\nu$ (h is the height of the channel, u_m the mean flow velocity and ν the kinematic viscosity) becomes constant along the channel irrespective of a change in the channel height h since hu_m is constant. In reference [3], the variation of the local heat-transfer coefficient along this parallel-converging-parallel plate system was measured by imposing a very small heating rate. The obtained results were compared with the predictions from the two-equation models of turbulence. The k-kL model by Kawamura [4] reproduced the experimental results acceptably well. This paper presents the results of measurements of the flow structure made subsequently to the previous report [3] using a hot-wire anemometer in the channel with the same geometry as that used in [3]. As a result, it revealed an unexpected mode of reversion to turbulence of a partly laminarized flow, which was concealed behind the superficial agreement between the experimental and theoretical heat-transfer coefficients.

Experiment

The test channel is shown in Fig. 1. It was made of acrylic resin. The width of the channel was 150 mm, and its total length was 2800 mm. The height of the channel over the first 1200-mm length was kept constant at $h_0 = 15 \pm 0.1$ mm so that the flow attained the fully developed turbulent state in this first parallel-plate section. In the succeeding section of $l = 200$ mm in length, the channel height was converged linearly from h_0 to $h_1 = 7 \pm 0.1$ mm. So the gradient of the upper plate in this accelerating section was $\beta = (h_0 - h_1)/l = 8/200$. In the last 1400-mm section, the channel height was again kept constant at h_1. The streamwise distance x was defined to be measured from the inlet of this second parallel-plate section.

Room air was sucked into the channel through an air filter by the turboblower which was placed near the outlet end of the duct system. The airflow rate was measured by means of an orifice located after the test channel and a manometer. The Reynolds number was defined on the assumption of two-dimensional flow as

$$\mathrm{Re} = 2hu_m/\nu \tag{1}$$

In the linearly converging section, the condition of continuity, $hu_m = \text{const.}$, results in a constant value of the acceleration parameter K

$$K = \frac{\nu}{u_m^2}\frac{du_m}{dx} = \frac{2\beta}{\mathrm{Re}} \tag{2}$$

In the present experiment, the Reynolds number was set con-

Contributed by the Fluids Engineering Division for publication in the JOURNAL OF FLUIDS ENGINEERING. Manuscript received by the Fluids Engineering Division October 10, 1984.

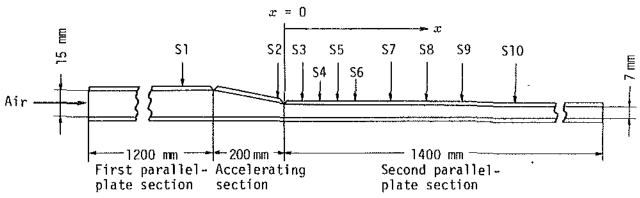

Fig. 1 Test section (height-to-length ratio is magnified by five times); ten traversing stations, S1, S2, · · · , and S10, are, respectively, located at $x = -290$, -20, 50, 100, 150, 200, 300, 400, 500 and 650 mm

stant at 10,000. Then $K = 2\times(8/200)/10{,}000 = 8\times10^{-6}$. This value exceeded the upper bound of $K_c = 3\times10^{-6}$ for a turbulent flow to be maintained [3].

Fluctuations of streamwise velocity component as well as time-mean velocity profiles were measured at ten traversing stations shown in Fig. 1. Boundary-layer type hot-wire probes were used together with the KANOMAX 7000 anemometer system. A sensing element was a tungsten wire of 5 μm in diameter and 1-mm long. The output signal from the anemometer was once stored by the TEAC R-210A magnetic tape recorder, and then processed by the MELCOM 70/30C computer system. Sampling rate of the analog-to-digital converter was 10 kHz.

Uncertainty estimations other than that of the hot-wire anemometry are given in the previous paper [3]. Prior to a one-day experiment the hot-wire probe was calibrated to a standard Pitot tube in a small wind tunnel at 8 velocities chosen in the range below 20 m/s. The corresponding outputs from the linearizer could be fitted to a straight line with an error of less than 2 percent. Each channel traverse started from the midplane of the channel and ended at the wall. Upon completion of every traverse, the probe was returned to the midplane and the anemometer output was checked. The drift of a sensor through any single traverse was within 2 percent. At the end of the one-day experiment the hot-wire probe was calibrated again. The drift of a sensor through any day was not greater than 5 percent. The mean characteristics of the two calibrations were used in processing the data of that day. The overall uncertainty in measuring the mean streamwise velocity component was 5.4 percent (odds of 20 to 1).

Since the channel wall was of a low thermal conductivity, thermal effect of the wall on a hot-wire sensor was considered to be small [5], but the measured mean velocity apparently deviated from $u^+ = y^+$ in the region $y^+ < 3$. Effects of imperfect spatial resolution due to a finite probe size on turbulent measurement [6] will be discussed later in the relevant section.

The absolute distance of the sensor from the wall was determined by virtue of the specially designed device for mounting a probe, which was capable of determining the initial position of the probe with an accuracy of 0.02 mm. The wall location determined in this way agreed with that obtained by the linear extrapolation to zero of the velocity distribution near the wall with an error of less than 0.05 mm.

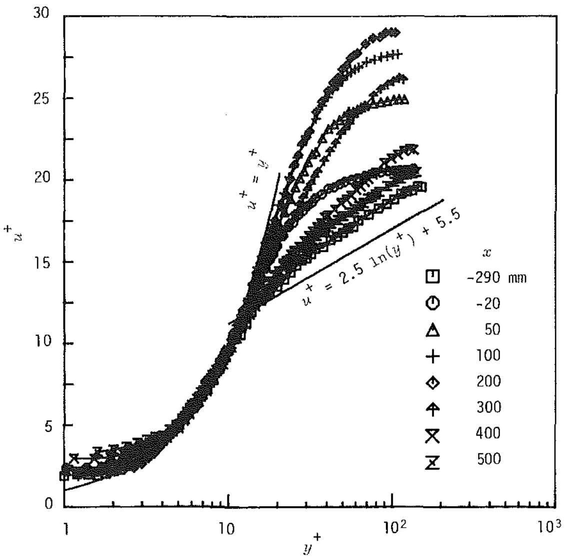

Fig. 2 Mean velocity profiles

Results and Discussions

Figure 2 shows the measured mean velocity profiles plotted in the form of u^+ $(=\bar{u}/\sqrt{\tau_w/\rho})$ against y^+ $(=y\sqrt{\tau_w/\rho}/\nu)$. Here, the shear stress at the wall, τ_w, was determined from the velocity gradient near the wall. The velocity distribution measured at the station near the end of the first parallel-plate section ($x = -290$ mm) is somewhat higher than the "universal" velocity profile in the log-region. Some authors [7, 8] have reported that in the case of pipe flow, the mean velocity distribution deviated upward from the universal profile when the Reynolds number was decreased to a few times the critical Reynolds number. Further, the critical Reynolds number for the channel flow is said to be appreciably higher than that for the pipe flow even if the Reynolds number is defined by equation (1) [9]. These observations seem to explain the tendency of the foregoing deviation.

At the measuring station near the end of the accelerating section ($x = -20$ mm), the mean velocity overshoots the universal profile near the wall and then shows a flat distribution in the core region, as has been well established by previous investigations [10–13].

After the flow enters the second parallel-plate section, the near-wall region where the velocity almost follows $u^+ = y^+$ grows thicker up to $x = 200$ mm. Henceforward, the velocity distribution gradually reverts to the turbulent profile. The reversion is almost completed at $x = 500$ mm.

Nomenclature

c_f = friction coefficient, $2\tau_w/(\rho u_m{}^2)$
E = power spectral density
f = frequency
h = channel height
K = acceleration parameter, $(\nu/u_m{}^2)(du_m/dx)$
l = length of the accelerating section
Nu = Nusselt number, $2\alpha h/\lambda$
Re = Reynolds number, $2hu_m/\nu$
t = time
u = streamwise velocity component
u_m = cross-sectional mean velocity
u' = fluctuating streamwise velocity component
u^+ = dimensionless velocity, $\bar{u}/\sqrt{\tau_w/\rho}$
x = streamwise distance from the inlet of the second parallel-plate section
y = distance from the wall
y^+ = dimensionless distance, $y\sqrt{\tau_w/\rho}/f$
α = heat-transfer coefficient
β = gradient of roof plate in the accelerating section, $(h_0 - h_1)/l$
λ = thermal conductivity of the fluid
ν = kinematic viscosity
ρ = density of the fluid
τ_w = shear stress at the wall
$\bar{\ }$ = time mean

Subscripts

0 = first parallel-plate section
1 = second parallel-plate section

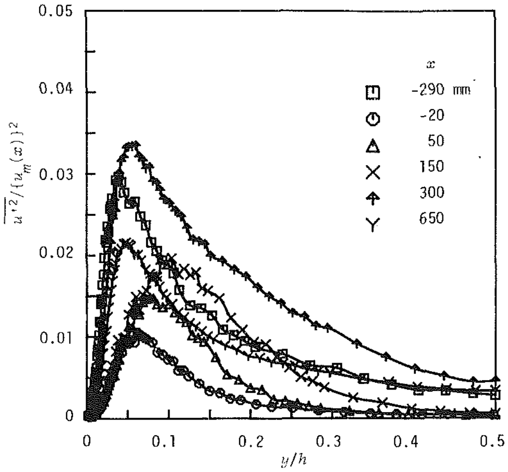

Fig. 3 Distributions of the variance of the streamwise velocity fluctuations

Figure 3 shows the distributions of the variance of the streamwise velocity fluctuations, $\overline{u'^2}$, normalized by the square of the mean velocity at each traversing station, $\{u_m(x)\}^2$. The distance from the wall y in the abscissa is normalized by the local channel height $h(x)$. Here we employed coordinates in Fig. 3 instead of $\sqrt{\overline{u'^2}}/\sqrt{\tau_w/\rho}$ versus y^+ because the absolute change of $\overline{u'^2}$ along the second parallel-plate section can be perceived directly from Fig. 3 since u_m is constant in the second parallel-plate section while $\sqrt{\tau_w/\rho}$ is not.

It must be noted that the fully developed turbulent-flow distributions in the first and the second parallel-plate sections should merge into a single curve in the coordinate system of Fig. 3. In Fig. 3, however, the distribution at $x=650$ mm is somewhat lower than that at $x=-290$ mm. This is attributable to the effects of imperfect spatial resolution due to a finite size of a hot-wire sensor. Johansson and Alfredsson [6] have shown that the maximum of $\sqrt{\overline{u'^2}}/\sqrt{\tau_w/\rho}$ decreases from about 2.9 for an ideally small probe to 2.1 for a probe with a length of 100 viscous length units $(\nu/\sqrt{\tau_w/\rho})$. In the present experiment, the sensing element length of 1.0 mm is equivalent to 20 and 41 viscous units for the conditions at $x=-290$ mm and at $x=650$ mm, respectively. And, when replotted in $\sqrt{\overline{u'^2}}/\sqrt{\tau_w/\rho}$ versus y^+ coordinates, the maximum of $\sqrt{\overline{u'^2}}/\sqrt{\tau_w/\rho}$ distribution measured at $x=-290$ mm occurs at around $y^+=13$ and amounts to 2.9, while that at $x=650$ mm occurs at the same y^+ and amounts to 2.6. Thus the rate of decrease in the maximum of $\sqrt{\overline{u'^2}}/\sqrt{\tau_w/\rho}$ agrees with that expected from [6]. Though the maximum values obtained here are a little higher than those given in [6], Blackwelder and Haritonidis [14] claimed that the maximum of $\sqrt{\overline{u'^2}}/\sqrt{\tau_w/\rho}$ attained 3.0 for a sensor with its length smaller than 20 viscous units.

The mean flow velocity in the second parallel-plate section, u_{m1}, as well as that at $x=-20$ mm, are approximately twice the value in the first parallel-plate section, u_{m0}. Then it can be seen from Fig. 3 that the relative intensity of the streamwise velocity fluctuations, $\sqrt{\overline{u'^2}}/u_m$, decreases through the accelerating section indeed, but that the absolute strength of fluctuations, $\sqrt{\overline{u'^2}}$, remains approximately unchanged except for the core region. This will be confirmed by comparison of the instantaneous velocity signals, in the following section.

In the first part of the second parallel-plate section, the velocity fluctuations begin gradually to increase in the region remote from the wall. Here it is noted as to the scaling of the distance from the wall that $y/h=0.1$ corresponds to $y^+=30$ for the fully developed turbulent condition that is almost attained at $x=-290$ mm and at $x=650$ mm. From $x=200$ mm, the level of velocity fluctuations starts a sharp increase in the whole cross section. It overshoots, and then tends gradually to, the fully developed turbulent profile.

Figure 4(a) shows instantaneous velocity signals obtained at six traversing stations by setting the hot-wire sensor at the midplane of the channel ($y/h=0.5$) in common with the six stations. The velocity fluctuation u' in the ordinate is normalized by the mean velocity at each traversing station, $u_m(x)$, and time t in the abscissa is nondimensionalized by the time scale $h(x)/u_m(x)$. In this coordinate system, the velocity signal of the fully developed turbulent flow in the second parallel-plate section will show the same pattern as that in the first parallel-plate section. Similarly, Figs. 4(b, c) show velocity signals obtained at the same six stations by setting the sensor at $y^+=30$ and at $y^+=10$, respectively. Figures 5(a–c) are power spectra E of the velocity fluctuations shown in Figs. 4(a–c), respectively. These spectra are again nondimensionalized by the local parameters, $h(x)$ and $u_m(x)$, so that integration of each profile results in $\overline{u'^2}/u_m{}^2$.

At the bottom of each part of Fig. 4, in order to make it easier to compare the signals at the inlet and at the outlet of the accelerating section, the signal at $x=-20$ mm is nondimensionalized and replotted by using the parameters at $x=-290$ mm, i.e., h_0 and u_{m0}. Though pointed out earlier regarding Fig. 3, it is revealed more clearly from comparison between the top and bottom traces in Fig. 4(b) (also in Fig. 4(c)) that the velocity fluctuations near the wall (typically at $y^+=30$) keep both amplitude and frequency characteristics almost unchanged through the accelerating section. This is reconfirmed from Figs. 5(b, c) by the fact that the profile representing $x=-20$ mm is obtained by parallel displacement of the profile showing $x=-290$ mm in the direction of the frequency axis by the amount of $-\log 4$, since $(h/u_m)_{x=-20}/(h_0/u_{m0})\cong 1/4$ and $hu_m=$ constant.

In the following discussion, we may refer to a frequency as "high" or "low" according to whether its value is over or below, say, $0.2u_m(x)/h(x)$. This boundary value is chosen because, in the core region of the fully developed turbulent flow [see $x=-290$ mm in Fig. 5(a)], the energy-containing eddies turn out to fall within a frequency band a little higher than this value, having sizes of roughly h and moving at velocities of approximately u_m. Further, it has been suggested by several investigators [15] that the bursting frequency f_b in turbulent boundary layers or in pipe and channel flows scales with the outer flow variables and is correlated approximately by $f_b\delta/u_\infty=0.2$, where δ is the boundary-layer thickness, the pipe radius or the half channel width and u_∞ is the free-stream or the centerline velocity; although the controversy has not yet been settled whether the bursting frequency should scale with the outer flow variables or with the wall layer variables [14]. Then $f_b\delta/u_\infty=0.2$ may be transformed to $f_bh/u_m\cong 0.5$. In fact this frequency seems to have considerable contribution to $\overline{u'^2}$ near the wall; see $x=-290$ mm in Figs. 5(b, c). In the end, it may be concluded that the frequency structures of the essentially turbulent flow in the present channel, irrespective of the position of a detector, should fall within the high frequency range.

At the station near the outlet end of the accelerating section, when measured with the local time scale $(h/u_m)_{x=-20}$, the velocity fluctuations are, of course, considerably elongated as compared with the developed turbulent flow; see the second trace in each part of Fig. 4. In the first part up to $x=100$ mm of the second parallel-plate section, fluctuation components with high frequencies are damped, whereas fluctuations with considerably low frequencies of about $0.03u_{m1}/h_1$ become conspicuous particularly at $y^+=30$; see Fig. 4(b) and Fig. 5(b). At this y position, the power spectral density corresponding to the low frequencies has attained its highest level

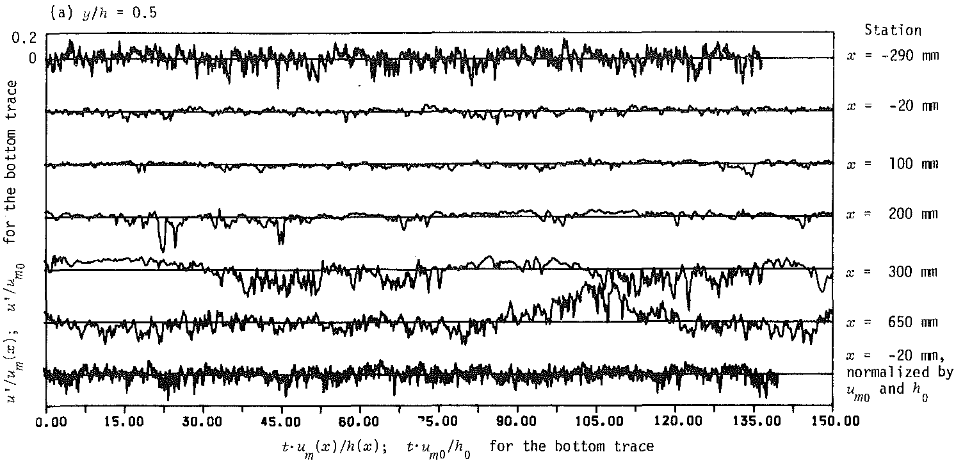

Fig. 4(*a*) At the midplane of the channel

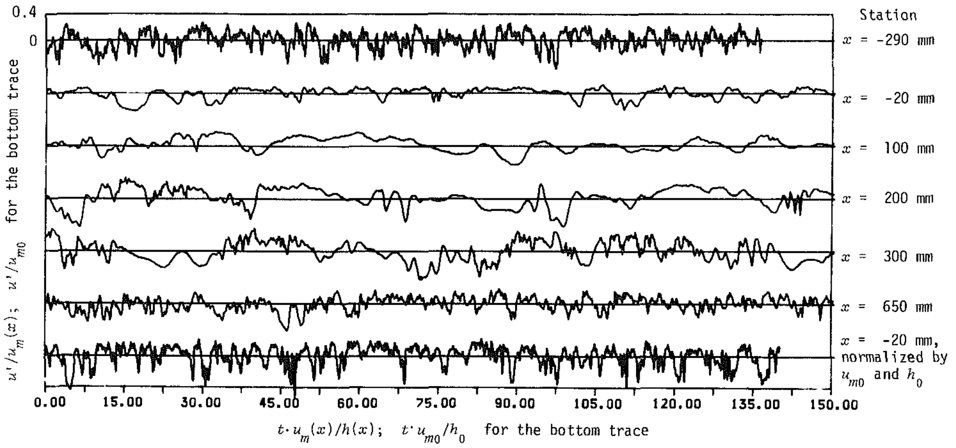

Fig. 4(*b*) At $y^+ = 30$

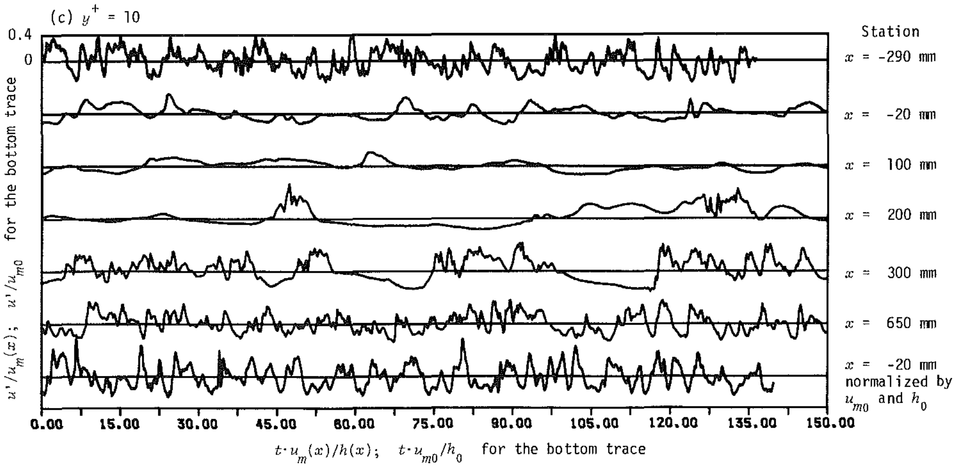

Fig. 4(*c*) At $y^+ = 10$

Fig. 4 Instantaneous velocity signals at six traversing stations obtained by setting the sensor

already at $x = 100$ mm, while at $y/h = 0.5$ as well as at $y^+ = 10$ its increase is delayed, with its maximum reached at $x = 300$ mm (see Fig. 5). Thus the low-frequency fluctuations are considered to originate in the neighborhood of $y^+ = 30$. At $x = 200$ mm, large positive spikes of an order of $u'/u_m = 0.4$ appear in the region close to the wall; and also in the core region spiky patters come out but here they are with negative signs and of an order of $u'/u_m = -0.2$; see Figs. 4(*a*, *c*). Until the flow comes up to $x = 300$ mm, the spikes increase in number. They are not distributed uniformly but make groups. The mean period $\bar{T}$ between neighboring groups of spikes corresponds approximately to that of the low-frequency fluctuations initially observed at $y^+ = 30$ and $x = 100$ mm, i.e., $\bar{T} \cong 30h/u_m$.

At this juncture, we become aware that the flow structure at $x = 300$ mm resembles the intermittently turbulent flow which was observed in previous experiments on transition to turbulence of pipe flow [16, 17]. Wygnanski and Champagne [17] first made distinction between turbulent "slugs" and "puffs" as follows:

(*i*) At any Re $\geqq$ 3200 and for smooth or only slightly disturbed inlets, transition occurred as a result of instabilities in the boundary layer. This type of transition gave rise to turbulent slugs which occupied the entire cross section of the pipe, and they grew in length as they proceeded downstream. The structure of the flow in the interior of a slug was identical to that in a fully developed turbulent pipe flow.

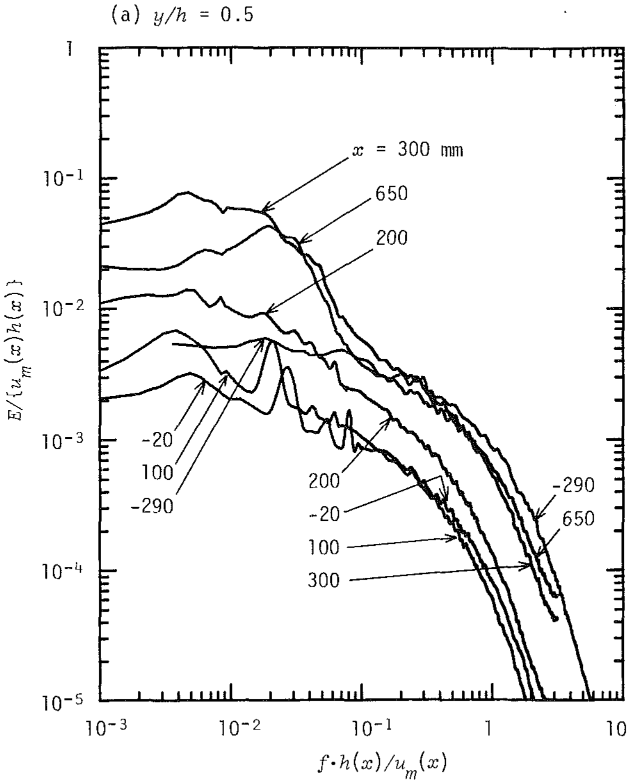

Fig. 5(*a*) At the midplane of the channel

(*ii*) At 2000 $\leqq$ Re $\leqq$ 2700, when a large disturbance was introduced into the inlet, mixed laminar and turbulent flows were observed far downstream. In this flow condition, the turbulent regions were referred to as puffs. Puffs were considered to represent an incomplete relaminarization process.

Direct comparison of the present experiment with [17] should be refrained, since not a pipe but a channel was used in the present experiment. We are, however, strongly tempted to consider the highly disturbed parts seen at $x = 300$ mm in the present experiment as turbulent slugs suggested in [17], even though the length of the individual disturbed regions is fairly short as compared with that of slugs reported in [17] and their spanwise extent is still unknown. In fact, the present Reynolds number is thought to be too high for puffs to occur. The disturbed regions are apparently growing in length downstream, until the whole flow field is filled with disturbances at $x = 650$ mm; see Fig. 4. Further, the velocity signals in the disturbed region are almost the same as that of the fully developed turbulent flow; see Fig. 4. In Fig. 5, in proportion to the increase in the fraction of the disturbed region, power spectrum in the high frequency region begins to increase from $x = 200$ mm at every y position and it eventually comes near the fully developed profile. At the same time, the difference between the regional-mean velocity profile in the disturbed parts and that in the nondisturbed parts (in the first approximation, the difference between the fully developed turbulent and the laminar profiles) causes the velocity fluctuations with the low frequencies to be amplified, both in the region next to the wall and in the core region; see Figs. 5(*a*, *c*). The overshoot of $\overline{u'^2}/u_m^2$ at $x = 300$ mm, mentioned previously regarding

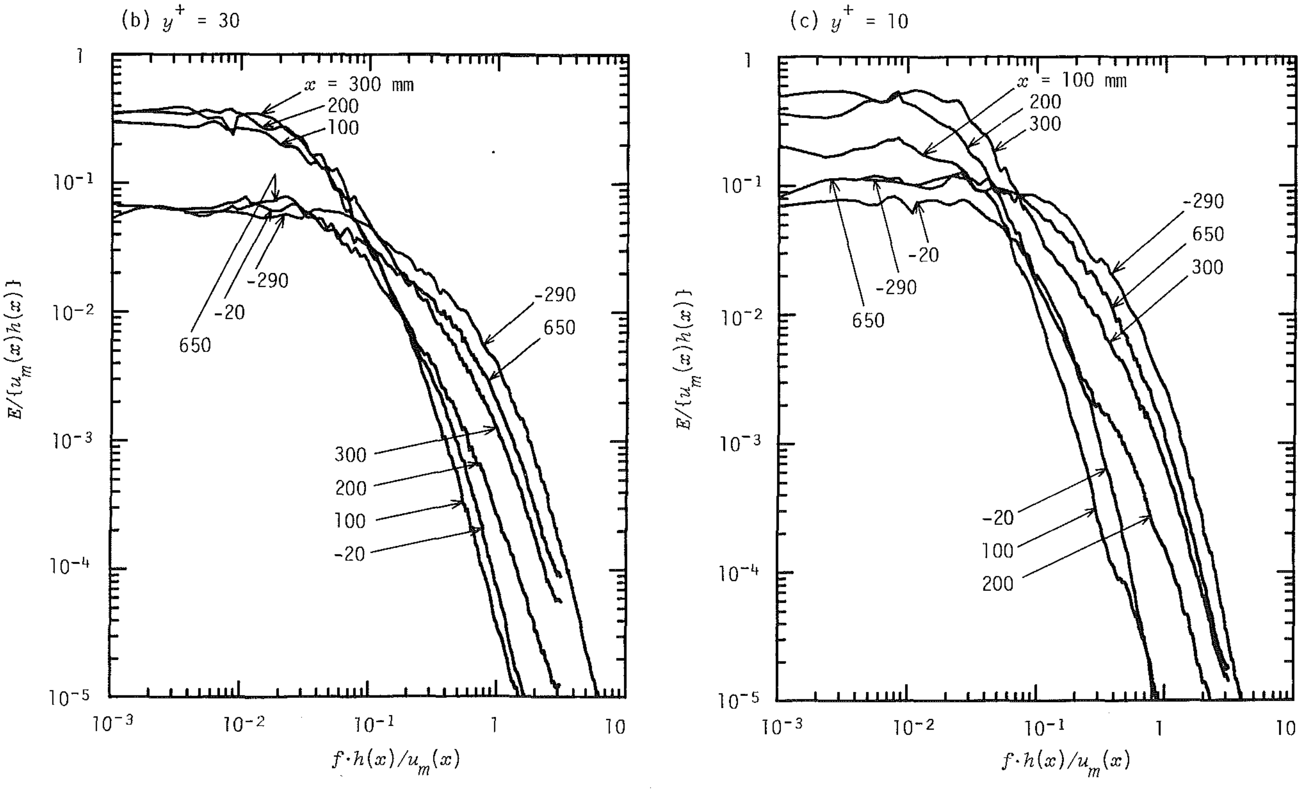

Fig. 5(*b*) At $y^+ = 30$

Fig. 5(*c*) At $y^+ = 10$

Fig. 5 Power spectra of the velocity fluctuations measured at six traversing stations by setting the sensor

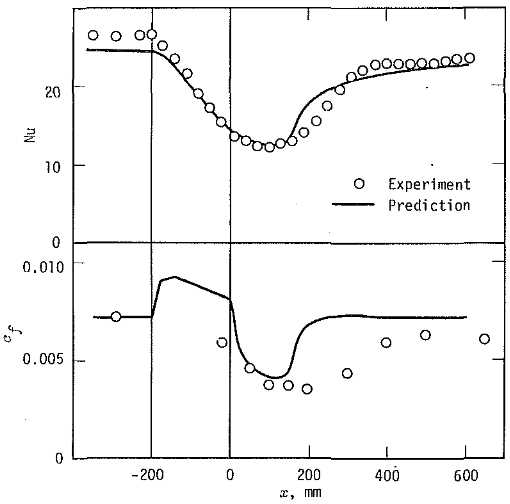

Fig. 6 Variations of the friction coefficient and the Nusselt number with the streamwise distance (uncertainty in Nu is ±9 percent and in c_f is ±6 percent)

Fig. 3, proves to be attributed to this amplification of the low-frequency fluctuations.

Figure 6 shows the variation with the streamwise distance of the friction coefficient, $c_f = 2\tau_w/(\rho u_m{}^2)$, measured in the present experiment and also that of the experimental Nusselt number replotted from the previous paper [3]. The Nusselt number is defined by $\mathrm{Nu} = 2\alpha(x)h(x)/\lambda$, where α is the heat-transfer coefficient and λ is the thermal conductivity of the fluid. Solid lines in the same figure are the predictions from the *k-kL* model of turbulence by Kawamura [4]. As far as the comparison between experiment and theory was restricted within the scope of the change in heat-transfer coefficient, the predictability of the theory seemed fairly satisfactory [3]. At the present juncture, however, we cannot but judge that the agreement in heat-transfer coefficient was only superficial. Turbulence models of this kind are thought not to expect such a large intermittency as revealed in the present experiment but to assume more uniform reversion of turbulence intensity. Further, it is noted in Fig. 6 that, in experiment, the friction coefficient recovers more gradually than the Nusselt number whereas the theory predicts the restoration of the friction coefficient faster than the Nusselt number. As a result there exists a considerable difference between the experimental and theoretical friction coefficients.

Conclusion

Even if velocity fluctuations are substantially preserved, once relaminarization destroys the so-called coherent structure in the wall-bounded turbulent flow which is considered to play an important role in producing the Reynolds stress, the reversion to turbulence seems to trace almost the whole stages, though shortened, of the natural transition from laminar to turbulent flow. The reversion in due course gives rise to intermittently turbulent flow, whose streamwise interval amounted to about 30 times the channel height in the present experimental conditions. In such cases, application of turbulence models to this kind of flow should be made carefully.

References

1 Coon, W. C., and Perkins, H. C., 1970, "Transition From the Turbulent to the Laminar Regime for Internal Convective Flow With Large Property Variations," ASME *Journal of Heat Transfer*, Vol. 92, pp. 506-512.

2 Bankston, C. A., 1970, "The Transition From Turbulent to Laminar Gas Flow in a Heated Pipe," ASME *Journal of Heat Transfer*, Vol. 92, pp. 569-579.

3 Tanaka, H., Kawamura, H., Tateno, A., and Hatamiya, S., 1982, "Effect of Laminarization and Retransition on Heat Transfer for Low Reynolds Number Flow Through a Converging to Constant Area Duct," ASME *Journal of Heat Transfer*, Vol. 104, pp. 363-371.

4 Kawamura, H., 1979, "Analysis on Laminarization of Heated Turbulent Gas Using a Two-Equation Model of Turbulence," *Proceedings of the 2nd Symposium on Turbulent Shear Flows*, London, pp. 18.16-18.21.

5 Bhatia, J. C., Durst, F., and Jovanovic, J., 1982, "Corrections of Hot-Wire Anemometer Measurements Near Walls," *Journal of Fluid Mechanics*, Vol. 122, pp. 411-431.

6 Johansson, A. V., and Alfredsson, P. H., 1983, "Effects of Imperfect Spatial Resolution on Measurements of Wall-Bounded Turbulent Shear Flows," *Journal of Fluid Mechanics*, Vol. 137, pp. 409-421.

7 Kudva, A. K., and Sesonske, A., 1972, "Structure of Turbulent Velocity and Temperature Fields in Ethylene Glycol Pipe Flow at Low Reynolds Number," *International Journal of Heat and Mass Transfer*, Vol. 15, pp. 127-145.

8 Pennell, W. T., Sparrow, E. M., and Eckert, E. R. G., 1972, "Turbulence Intensity and Time-Mean Velocity Distributions in Low Reynolds Number Turbulent Pipe Flows," *International Journal of Heat and Mass Transfer*, Vol. 15, pp. 1067-1074.

9 Patel, V. C., and Head, M. R., 1969, "Some Observations on Skin Friction and Velocity Profiles in Fully Developed Pipe and Channel Flows," *Journal of Fluid Mechanics*, Vol. 38, pp. 181-201.

10 Patel, V. C., and Head, M. R., 1968, "Reversion of Turbulent to Laminar Flow," *Journal of Fluid Mechanics*, Vol. 34, pp. 371-392.

11 Badri Narayanan, M. A., and Ramjee, V., 1969, "On the Criteria for Reverse Transition in a Two-Dimensional Boundary Layer Flow," *Journal of Fluid Mechanics*, Vol. 35, pp. 225-241.

12 Back, L. H., and Seban, R. A., 1967, "Flow and Heat Transfer in a Turbulent Boundary Layer With Large Acceleration Parameter," *Proceedings of the Heat Transfer and Fluid Mechanics Institute*, P. A. Libby, et al., Eds., pp. 410-426.

13 Back, L. H., Cuffel, R. F., and Massier, P. F., 1970, "Laminarization of a Turbulent Boundary Layer in Nozzle Flow – Boundary Layer and Heat Transfer Measurements With Wall Cooling," ASME *Journal of Heat Transfer*, Vol. 92, pp. 333-344.

14 Blackwelder, R. F., and Haritonidis, J. H., 1983, "Scaling of the Bursting Frequency in Turbulent Boundary Layers," *Journal of Fluid Mechanics*, Vol. 132, pp. 87-103.

15 Fleischmann, S. T., and Wallace, J. M., 1984, "Mean Streamwise Spacing of Organized Structures in Transitional and Developed Bounded Turbulent Flows," *American Institute of Aeronautics and Astronautics Journal*, Vol. 22, pp. 766-769.

16 Lindgren, E. R., 1957, "The Transition Process and Other Phenomena in Viscous Flow," *Arkiv för Fysik*, Band 12, pp. 1-169.

17 Wygnanski, I. J., and Champagne, F. H., 1973, "On Transition in a Pipe. Part 1: The Origin of Puffs and Slugs and the Flow in a Turbulent Slug," *Journal of Fluid Mechanics*, Vol. 59, pp. 281-335.

F. O. Thomas
School of Mechanical and
Aerospace Engineering,
Oklahoma State University,
Stillwater, OK

V. W. Goldschmidt
School of Mechanical Engineering,
Purdue University,
West Lafayette, IN

Acoustically Induced Enhancement of Widening and Fluctuation Intensity in a Two-Dimensional Turbulent Jet

The enhancement of widening rate and turbulence intensity in a turbulent plane jet, due to an acoustic disturbance are considered. Detailed data at a representative Strouhal number suggest a well organized symmetric structural array in the initial region of the flow. These highly organized flow structures act as efficient agents in the transport of energy to the fine-grained turbulence, leading to greater diffusivity, enhanced turbulence and an increase in widening. The data also suggest significant differences in the underlying structure of the natural and excited jet flows, hence putting in jeopardy any generalization of coherent motions especially excited to facilitate their study.

Introduction

Acoustic excitation of jet flows may lead to a premature transition [1-7] as well as an enhancement of spread and increase of turbulence intensity levels [8-17]. With the gradual recognition of the importance of large-scale coherent structures in free shear flow dynamics (see earlier contributions in [18-20]) acoustic excitation has often been applied to remove phase jitter and organize the structures so as to facilitate their study. (Examples are [21-26].) Conclusions concerning the dynamical behavior of coherent structures in the excited flow are often generalized to the corresponding natural flow.

The work now reported extends [17]. There, through correlations and energy spectra, restructuring in the initial region due to the acoustic forcing was documented. Extraordinary high widening rates and turbulence intensities were obtainable for excitation over a specific range of frequencies. Data suggested the corresponding structures were vertical and arranged symmetrically with respect to the centerline. Strong acoustically induced effects were also noted in the similarity region, and the inference was that these were related to those in the initial region. The earlier work is extended while addressing two fundamental questions: 1) What is the mechanism responsible for the enhanced widening and fluctuation intensities? 2) What role do the coherent structures play and how are the jet structural patterns influenced by the excitation?

Experimental Apparatus

The measurements to be reported were all obtained in a two-dimensional jet flowfield with an aspect ratio of 48 and an exit Reynolds number of 6000. The flowfield is shown schematically in Fig. 1. The near exit nozzle boundary layers were laminar with a momentum thickness of 86 μm (for $Re_D = 6000$), while the turbulence at the nozzle exit had an intensity lower than 0.2 percent.

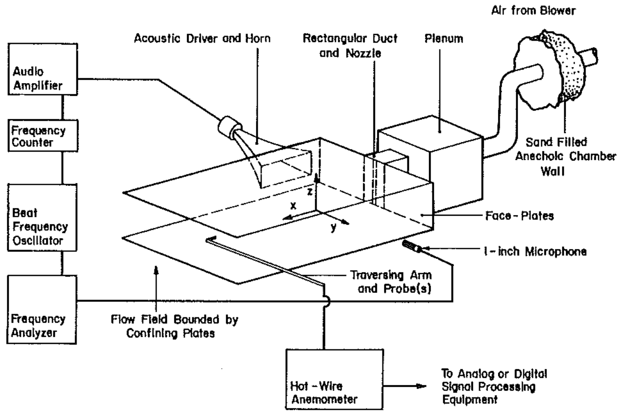

Fig. 1 Schematic of experimental apparatus

The entire flowfield was placed in a large cubic anechoic chamber with dimensions of 12 ft (3.7 m) on a side, completely isolating the flow from laboratory noise and room drafts.

Pure tone excitation was supplied by a beat frequency oscillator, an audio amplifier, and an acoustic driver and horn assembly. The acoustic wavelengths employed in this study were much greater than the nozzle width "D". Hence to good approximation the acoustic traveling waves propagating at right angles to the mean flow may be considered to form a symmetric pressure perturbation on the initial flow. Furthermore, frequencies that were used for excitation were well away from those producing resonant modes in the test section of plenum. Reflection of acoustic waves back into the flow-field was avoided by performing all experiments within the confines of the fiberglass wedge lined walls of the anechoic chamber.

All the experimental results to be reported were obtained at

Contributed by the Fluids Engineering Division for publication in the JOURNAL OF FLUIDS ENGINEERING. Manuscript received by the Fluids Engineering Division, April 22, 1985.

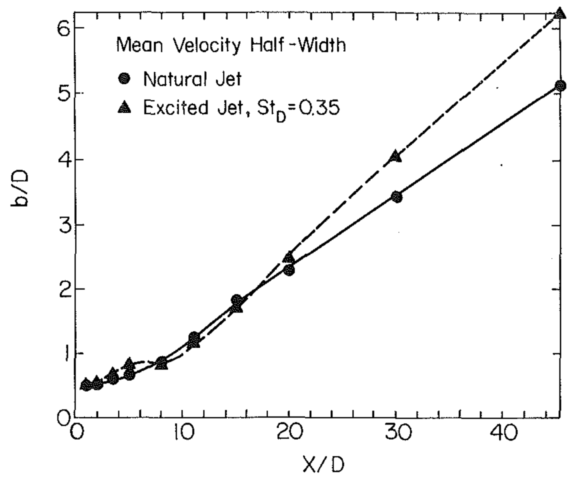

Fig. 2 Excited and natural jet widening (uncertainty in widening rate is in the order of 3.5 percent)

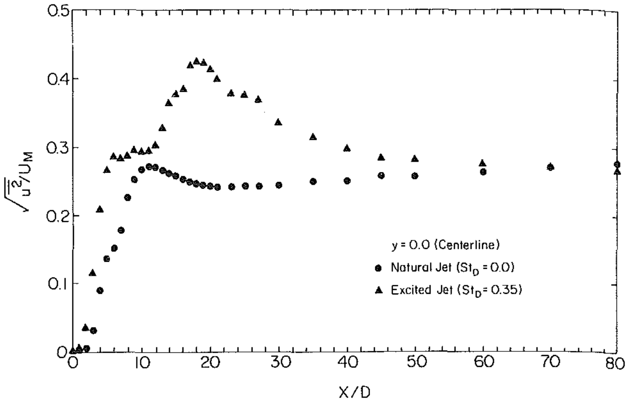

Fig. 3(*a*) Excited and natural jet centerline longitudinal fluctuation intensity variation with *x/D* (uncertainty in the order of 4 percent)

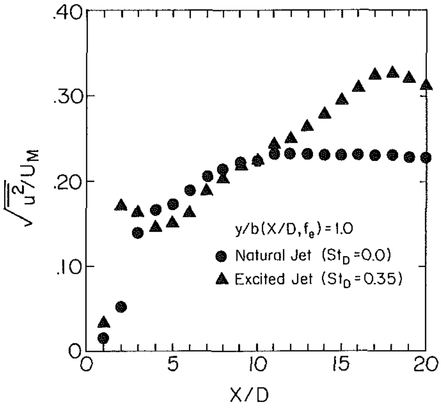

Fig. 3(*b*) Excited and natural jet shear layer longitudinal fluctuation intensity variation with *x/D* (uncertainty in the order of 4 percent)

a sound pressure level of 105 dB SPL re 20 $\mu N/m^2$. This corresponds to an excitation pressure fluctuation that is about 3.5 percent of the jet mean exit dynamic pressure. Experiments were performed to determine the effect of excitation amplitude on developing longitudinal velocity fluctuations. The results of these tests are presented in [27] and show that the excitation amplitude used in this study was close to that giving maximum effects on the flow field. Levels as low as 70 dB re 20 $\mu N/m^2$ were tested and showed their ability to excite the same basic modes as the higher levels, and hence give credence to the generality of the trends to be reported.

Basic Effect of the Excitation

An initial survey of the response of the planar jet to symmetric acoustic forcing over a wide frequency range is given in [17]. A range of excitation frequencies producing widening rate enhancement of up to 50 percent over no sound levels accompanied by corresponding increases in fluctuation intensities was found. This excitation range was, in terms of Strouhal number (based on excitation frequency, slot width, and exit velocity), roughly 0.25 to 0.50. In this study an excitation Strouhal number of $St_D = 0.35$ ($f_e = 850$ Hz) was selected as representative of this "sensitive" range and detailed measurements were made for this excitation condition. In the results to follow, the $St_D = 0.35$ excitation condition will be referred to as the "excited jet." "Natural jet" will be the term adopted to refer to the unexcited case.

The widening of the developing natural and excited jet are compared in Fig. 2. The streamwise fluctuation intensities (on both the centerline and at $y/b = 1.0$) are presented in Figs. 3(*a*) and 3(*b*).

The acoustic disturbance leads to substantial increase in turbulence intensities and widening rates. As one would expect, the initial growth rate of velocity fluctuations is most notable in the shear layer.

The lateral profiles of longitudinal fluctuation intensity are compared at selected *x/D* stations in Figs. 4(*a*) through 4(*c*). The natural jet profiles show the gradual formation of the characteristic saddle-shaped profile observed by a number of researchers (for example [28]) while the development of the intensity profiles for the excited jet are quite different. In particular, the profiles at $x/D = 3.5$ and 5.0 suggest the presence

Nomenclature

b = jet half width (lateral location where $U = U_M/2$)
D = nozzle width
f = frequency, Hz
f_c = correlation function frequency, defined by equation (3)
f_e = excitation frequency, Hz
f_p = peak or passage frequency
Δf = bandwidth, Hz
u = longitudinal fluctuating velocity component
x = longitudinal coordinates measured from the nozzle exit
y = lateral coordinates measured from the centerline
z = vertical coordinates, measured from the midplane
Re_D = Reynolds number based on exit nozzle width and velocity
$R_u(\tau)$ = correlation function defined by equation (2)
RF = randomization factor, defined by equation (1)
$S(f)$ = longitudinal velocity fluctuation energy spectrum
St_D = Strouhal Number $= fD/U_0$
U = local mean velocity
U_0 = nozzle exit velocity
U_M = local centerline mean velocity
τ = time delay
ϕ = phase angle, defined by equation (4)
Λ = integral macroscales (based on numerical integration to the point where the correlation reaches 0)

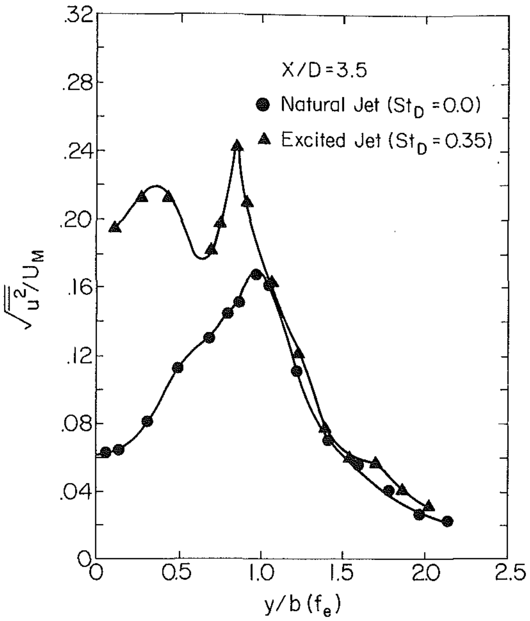

Fig. 4(*a*) **Excited and natural jet longitudinal fluctuation intensity profiles at x/D = 3.5 (uncertainty in the order of 4 percent)**

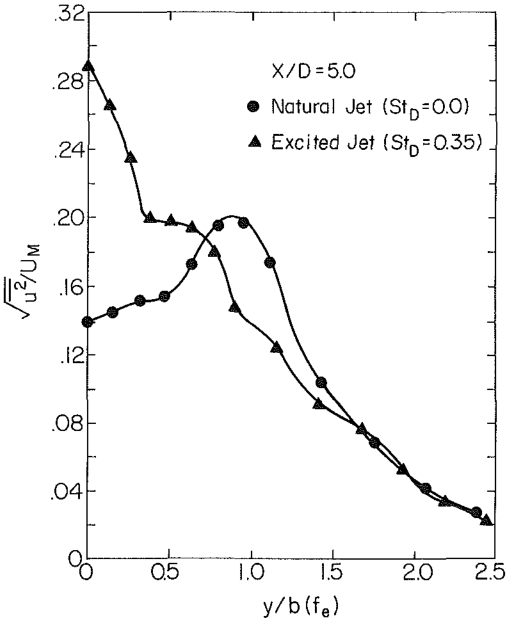

Fig. 4(*b*) **Excited and natural jet longitudinal fluctuation intensity profiles at x/D = 5.0 (uncertainty in the order of 4 percent)**

of a fundamentally different underlying flow structure. Farther downstream the profiles indicate that the elevated fluctuation intensities already noted on the centerline and shear layer exist across the entire jet.

Development of Structural Patterns in the Excited Jet

Structural patterns based upon measurements of spectral evolution, characteristic wavelength, phase angles and two-dimensionality of velocity fluctuations are seen as characteristics of the large-scale flow development and are now presented.

A) Spectral Measurements. Energy spectra of the longitudinal velocity fluctuations were measured on both the jet centerline and on the shear layer ($y/b(f_e)=1.0$) at several x/D stations ($1 \leq x/D \leq 40$).

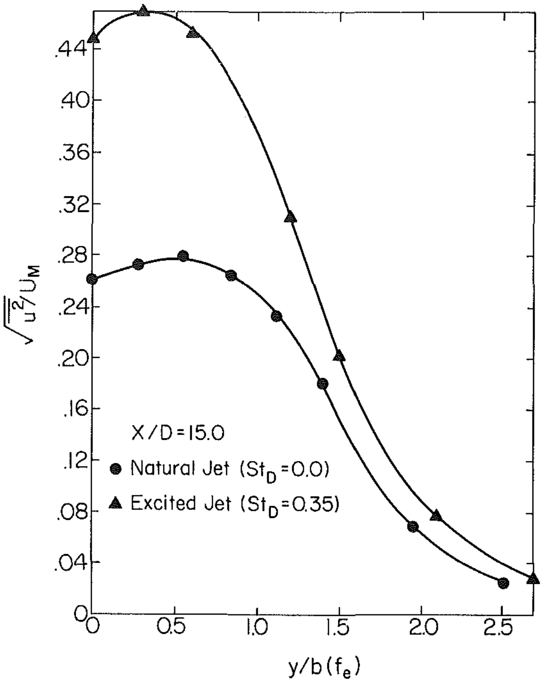

Fig. 4(c) **Excited and natural jet longitudinal fluctuation intensity profiles at x/D = 15.0 (uncertainty in the order of 4 percent)**

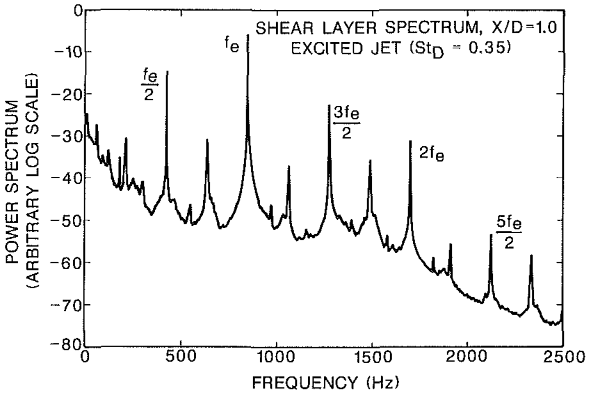

Fig. 5 **Excited jet shear layer spectrum at x/D = 1 (frequency resolution is of 2.4 Hz; ordinate scale is arbitrary)**

The ability of the excitation to organize the initial flow is apparent from Fig. 5 which shows the jet shear layer power spectrum as obtained at $x/D=1$. This is essentially a line spectrum with over 80 percent of the fluctuation energy contained in the spike at the excitation frequency $f_e=850$ Hz. Characteristics associated with the nonlinear interaction between velocity fluctuations (see [29]–[32]), such as subharmonic and harmonic formation are already apparent. It should be noted that the harmonics are at a much lower amplitude than the fundamental; the logarithmic ordinate used in presenting the spectrum visually overemphasizes the amplitude of these modes. The excited and natural jet shear layer spectra obtained at $x/D=2$ are compared in Fig. 6. The excited jet spectrum at this location demonstrates the continued growth of all modes, especially the subharmonic $f_e/2=425$ Hz which exhibits the largest increase in amplitude. It is important to note the suppression of the naturally occurring modes by the dominant acoustically induced modes which is clearly evident in this figure. The suppression of spectral modes due to the presence of a larger amplitude acoustically induced mode has also been noted in the plane wake [31]. The suppression was found most effective when the frequency dif-

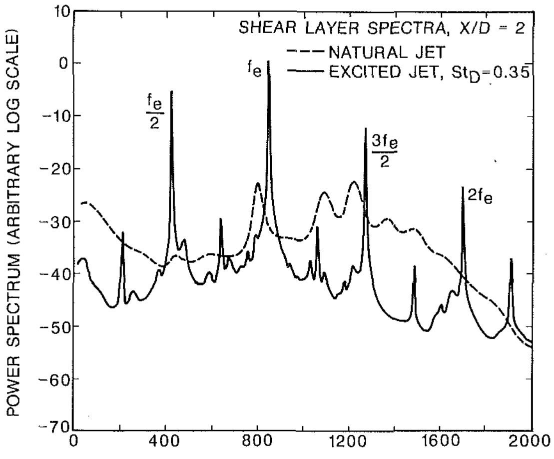

Fig. 6 Excited and natural jet shear layer spectra at $x/D = 2$, $y/b = 1$ (frequency resolution is of 2.4 Hz; ordinate scale is arbitrary)

ference between the dominant and suppressed mode was small but the amplitude disparity large.

Figure 7(*a*), which is derived from the shear layer spectral measurements, conveniently summarizes the primary features of the excited jet spectral evolution. This plot shows the variation with downstream distance of mean square amplitudes of velocity fluctuations contained in a 15 Hz bandwidth centered on each of the frequencies f_e, $f_e/2$, and $f_e/4$. The subharmonic mode is dominant by $x/D = 3$ and the fundamental is noted to undergo decay. The rapid decay of the primary mode f_e indicates that the coupling of the acoustic field and flowfield occurs in the nascent shear layers near the nozzle exit (as was suggested in [9]). The rapid formation of the subharmonic modes simultaneous with the decay of their respective fundamentals is striking. This sequential formation of first and second subharmonics occurs over a relatively short spatial distance - essentially 6 nozzle widths (corresponding to less than 4 original model wavelengths).

The second subharmonic mode continues to remain dominant over a range of subsequent downstream stations but ceases its growth at $x/D = 9$ and by $x/D = 10$ it begins to decay. The spectra demonstrate the increased randomization of the shear layer fluctuations associated with the demise of the line spectrum. This degree of randomization may be quantified by considering the ratio of energy in the continuous spectrum to that in the total spectrum. Hence a randomization factor *RF*, is defined as

$$RF = 1 - \frac{\sum_{i=1}^{N} \int_{(f_i-\Delta f/2)}^{(f_i+\Delta f/2)} S(f)df}{\int_0^{\infty} S(f)df} \qquad (1)$$

where $S(f)$ is the longitudinal velocity fluctuation spectrum and bandwidth $\Delta f = 15$ Hz. With this definition, $RF = 1$ corresponds to a broadband spectrum while $RF = 0$ indicates a line spectrum. Figure 7(*b*) presents *RF* derived from the shear layer spectra as a function of x/D. Note that initially nearly all of the energy is contained in discrete modes. An increase in the randomization occurs between $x/D = 4$ and 5. Figure 7(*a*) suggests that this is associated with the production of the second subharmonic mode (i.e., a pairing event). Once this mode has formed, the value of *RF* stabilizes with nearly 80 percent of the fluctuation energy still associated with discrete modes. The largest increase in randomization is associated with the decay of the $f_e/4$ mode. Increases in shear layer fluctuation intensity noted in Figs. 3(*a*) and 3(*b*) are apparently associated with this modal breakdown. The value of *RF* is noted to approach 1 near $x/D = 20$.

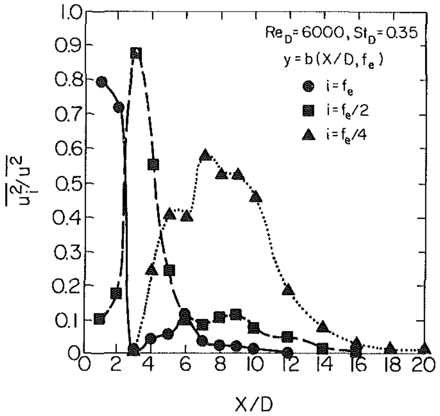

Fig. 7(*a*) Mean square amplitudes of shear layer modes f_e, $f_e/2$, and $f_e/4$ in the excited jet (uncertainty under 5 percent; results primarily qualitative)

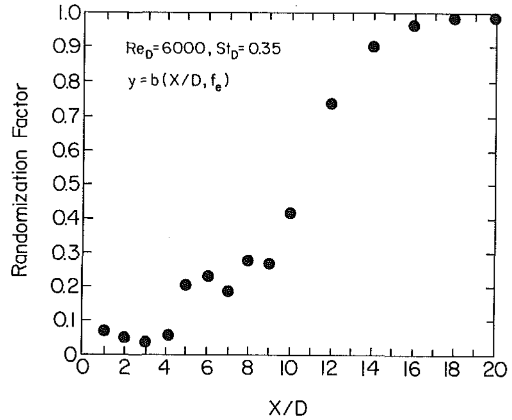

Fig. 7(*b*) Randomization factor for the excited jet shear layer spectra (randomization factor within 0.05)

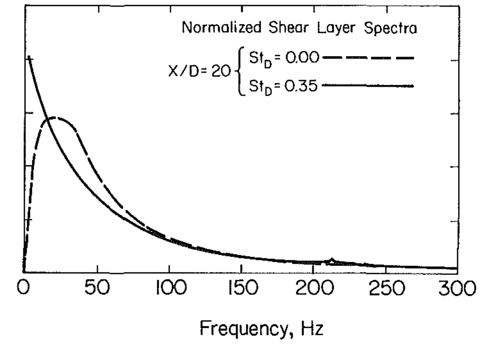

Fig. 8 Comparison of normalized broadbend spectra obtained in the natural and excited jet (frequency resolution is within 2.4 Hz; ordinate scale is arbitrary)

The basic trends discussed above for the shear layer spectra are similar to those for the centerline spectra except for a more gradual decay of the *fe*/2 mode with subsequent development of the second subharmonic. This difference is indicative of the fact that the subharmonic formation originates in the shear layer.

The longitudinal velocity fluctuation spectra for the $St_D = 0.35$ excitation condition have been shown to be initially discrete, and then to undergo a rather sudden breakdown to become continuous with increasing streamwise distance. Smoothed broadband shear layer spectra for the excited and natural jet taken at $x/D = 20$ are compared in Fig. 8. The natural jet spectrum is characterized by a maximum amplitude at peak frequency f_p which has been shown in [33] to be indicative of the passage of a self-preserving large-scale structural array past the fixed probe. This characteristic peak or passage frequency is absent in the excited jet spectra which decrease continuously from large to small scales. It would appear then that application of excitation has modified the transition of the jet in such a manner that similar structures have not yet formed or the structural passage frequency is not apparent due to the elevated background turbulence level.

B) Correlation Results. In order to gain insight into the frequency and phase development of structural patterns in the excited jet, use was made of space-time correlation measurements. Here consideration will be given to a lateral correlation function given by,

$$R_u(\tau)=\lim_{T\to\infty}\int_0^T u(x,-b,z,t)u(x,+b,z,t+\tau)dt \qquad (2)$$

The two probes are positioned at the same streamwise locations but are laterally separated a distance of $2b(f_e)$ (i.e., $y=\pm b(f_e)$). One unique feature of these correlation functions as they occur in the natural jet, is their exhibition of a decaying pseudo oscillatory component. This was first noted in [34] and explained in [33, 35].

It is expected that correlation function oscillations are related to the passage of large-scale structures past the probe pair [33, 36] (The probe separation $\Delta y=2b(f_e)$ is large compared to the length scales of fine-grained turbulence). A correlation function frequency based upon time delay $\Delta\tau_i$ between successive maxima is defined as,

$$f_c=\frac{1}{\Delta\tau_{\text{avg}}}=\left[\frac{\sum_{i=1}^{N}\Delta\tau_i}{N}\right]^{-1} \qquad (3)$$

where N is the number of time-delay intervals considered.

The lateral space-time correlation measurements also provide the phase relationship between fluctuations on the opposite sides of the jet. The phase angle ϕ between the fluctuations may be obtained from the time lag $\Delta\tau_\phi$ between zero time-delay and the first correlation function maximum. That is,

$$\phi=\frac{2\pi\ \Delta\tau_\phi}{\Delta\tau_{\text{avg}}}=2\pi f_c\Delta\tau_\phi \qquad (4)$$

The lateral correlation functions obtained for the excited jet are periodic over a significant streamwise distance. The correlation function frequencies resulting from measurements in the excited jet are shown in nondimensional form in Fig. 9(*a*). Corresponding phase data are presented in Fig. 9(*b*). The initial correlation frequency is equal to the excitation frequency and is halved at $x/D=3$, which coincides with the location of dominance of the first subharmonic mode in the spectral measurements (see also [17]). There is a sudden shift in phase angle associated with the formation of this mode, after which the fluctuations return to an in-phase arrangement. A second halving occurs by $x/D=4$ which leads to the presence of the second subharmonic which becomes the dominant dynamic feature of the developing jet and its presence may be traced to $x/D=16$. The phase data indicate zero phase angle in this region, suggesting the presence of organized flow structures arranged symmetrically with respect to the jet centerline. This is in marked contrast to measurements in natural two-dimensional jets which show the dominance of anti-symmetric structural patterns beyond the jet potential core ([17], [33]-[38]).

The dominance of the symmetric arrangement noticed in the excited jet is gradually lost over the region $12<x/D<16$. The correlation function frequency is reduced to one-quarter its previous value and there is a gradual shift in phase angle to $\phi\simeq\pi$, indicating the onset of an anti-symmetric arrangement as is seen in the natural flow [33].

C) Two-Dimensionality. In order to quantify the extent of two-dimensionality, the integral macroscales Λ_z and Λ_x (corresponding to the vertical and longitudinal correlation, respectively) were determined by numerically integrating

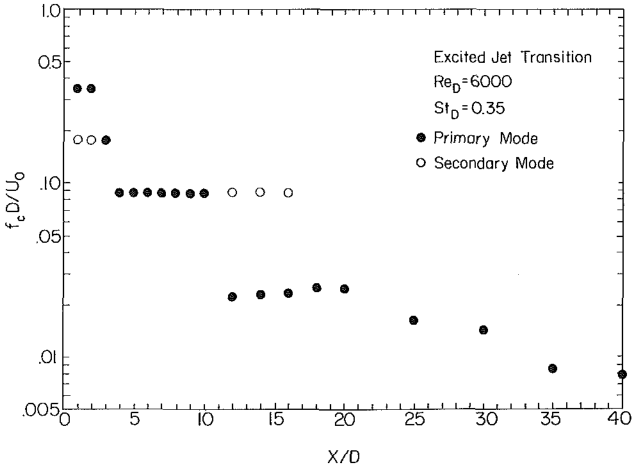

Fig. 9(*a*) **Excited jet correlation function frequencies (uncertainty of 5 Hz on the correlation function frequency)**

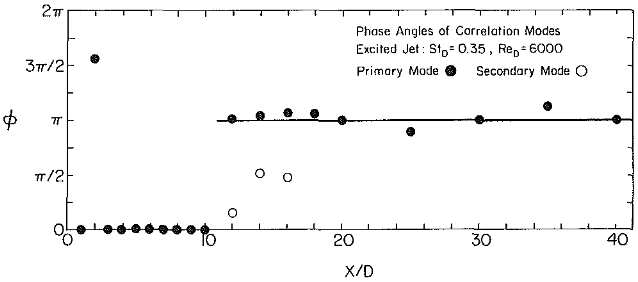

Fig. 9(*b*) **Excited jet phase angles (uncertainty in phase angles of 0.4 radians)**

Table 1 Measured Λ_z and Λ_x macroscales

x/D	$\Lambda_z/b(f_e)$	Λ_z/D	$\Lambda_x/b(f_e)$	Λ_x/D	Λ_z/Λ_x	$\frac{(\Lambda_z/\Lambda_x)_{\text{excited}}}{(\Lambda_z/\Lambda_x)_{\text{natural}}}$
4	*	*	0.56	0.38	*	*
8	4.00	3.26	0.95	0.78	4.21	7.52
12	0.49	0.60	1.07	1.31	0.46	1.48
20	0.35	0.86	0.88	2.15	0.40	0.85

*Vertical macroscale not defined for this case.
(uncertainty in the order of 5 percent)

measured correlation coefficients. The ratio Λ_z/Λ_x may be expected to provide an indication of the extent of the z-directed two-dimensionality exhibited by flow structures.

The excited jet exhibits very strong two-dimensionality initially. As Table 1 indicates, the vertical macroscale cannot be defined at $x/D=4$ since the correlation coefficient remains at elevated values even for large Δz probe separations. This suggests that at $x/D=4$, the structures possess a length scale in the z-direction that is on the same order of magnitude as the flow-field confining plate separation (about 70 $b(f_e)$). The enhanced two-dimensionality, though reduced at $x/D=8$, is still apparent. By $x/D=12$ the two-dimensionality of the flow is greatly reduced, as the vertical macroscale becomes similar in magnitude to that of the natural jet. This is likely to be related to the breakdown of the second subharmonic mode noted earlier. The longitudinal macroscales for downstream stations of 4, 8, and 12 are each noted to be similar to those corresponding to the unexcited jet. The longitudinal macroscale at $x/D=20$ is significantly larger than that occurring for the natural jet, however, while the vertical scale appears only slightly larger. The ratio Λ_z/Λ_x at this location is then somewhat lower than that occurring naturally and indicates a lack of any strong two-dimensionality.

Discussion and Conclusions

Spectral as well as correlation measurements indicate that the excitation produces strong organizational effects in the initial flow. Nonlinear behavior is already present at $x/D=1$ as measurements indicate the early formation of symmetrically distributed, highly organized flow structures in the initial jet shear layers. Naturally occurring disturbance modes are suppressed by the presence of the dominant coherent mode at the excitation frequency f_e. This is critically important in maintaining the organization of the developing flow. Nonlinear interactions between organized fluctuations all related to the periodic excitation can then only produce other periodic components (harmonics, subharmonics, sum and difference modes, etc.) thus sustaining the initial organization imposed upon the flow.

A subharmonic mode which is present at small amplitude even at $x/D=1$ grows rapidly and becomes dominant by $x/D=3$. Associated with the formation of this mode at $f_e/2=425$ Hz ($\mathrm{St}_D=0.177$) is the simultaneous and complete decay of the fluctuating component at the excitation frequency. The rapid loss of this mode indicates that the acoustic field-flow field coupling occurs very near the nozzle exit. Almost immediately after reaching maximum amplitude, the subharmonic mode $f_e/2$ begins to decay, leading to the formation of a second subharmonic mode at $f_e/4$. This process is complete by $x/D=5$. The lateral correlation measurements indicate that the resulting second subharmonic mode is also symmetrically distributed with respect to the jet centerline. Also, correlation measurements between z separated probes indicate the fluctuations in this region of the flow are highly two-dimensional exhibiting nearly complete homogeneity in the z-direction.

Correlation and spectral measurements suggest then that the result of the pairing event/events induced by this specific disturbance frequency is an ordered array of initially symmetrically distributed flow structures, possessing a remarkable degree of two-dimensionality in the direction of mean flow homogeneity. This symmetric structural arrangement is remarkably stable and propagates to $x/D\simeq 12$, well beyond the position of establishment of an anti-symmetric structure in natural planar jet flows [33]. Spectral measurements show that due to the continued dominance of this organized structure in the jet, establishment of turbulent flow conditions is much delayed. Nonlinear interaction between fluctuations occurs primarily among periodic modes and serves to produce only other organized modes resulting in a delay in turbulence transition. The elevated fluctuation intensities noted in Fig. 3(*a*) to occur over the range $4<x/D<12$ are thus not indicative of turbulent flow conditions. Rather they are due to fluctuations associated with the presence of organized symmetrically distributed structures in the flow. These orderly structures are responsible for the limited range of reduced jet widening shown in Fig. 2.

Correlation measurements indicate a fundamental change in the organization of the flow structures for $x/D\geq 12$. The characteristic passage frequency is quartered and there is a shift to an anti-symmetric structural arrangement which is maintained at all subsequent downstream stations. In addition, the spectra give evidence of a marked increase in randomization of the velocity fluctuations beginning near $x/D=10-12$. The vertical correlation measurements indicate a corresponding substantial loss in z-directed two-dimensionality of the flow structures as well. Associated with the above noted structural related changes are significant resulting effects on the mean and fluctuating flow quantities. The jet widening increases substantially as does the rate of decay of mean velocity. The longitudinal velocity fluctuation intensity (see Fig. 3) suddenly begins a climb to elevated values at $x/D=12$. These effects are obviously related to the structural "breakdown" that occurs near $x/D=12$. The elevated intensities observed for $x/D>12$ are then due primarily to enhanced turbulence rather than coherent fluctuations.

It was found that a range of frequencies below and up to the natural jet breakdown frequency (such as $\mathrm{St}_D=0.35$ presented) leads to a well organized, symmetric, two-dimensional structural array in the flow which is maintained well beyond the location corresponding to the formation of an anti-symmetric pattern in the natural jet. Of primary importance in the ability of the excitation to organize and hence modify the structural development of the flow is the effective initial suppression of naturally occurring jet shear layer modes.

The measurements performed in this study exhibit greatly enhanced turbulence intensities which are directly attributable to growth and subsequent decay of acoustically induced, highly organized flow structures. According to the theoretical work of Alper and Liu [39] such enhanced coherent modes are very effective in acting as an efficient intermediary in the transport of energy from the mean flow to the fine-grained turbulence. This transport was found in [39] to effectively supplement conventional Reynolds stress based turbulence production from the mean flow. The increase in jet widening is then a result of the greater diffusivity of the flow associated with the enhanced turbulence intensities.

The results of this study demonstrate significant difference in the underlying structure of the developing natural and excited jet flows in terms of characteristic phase angle and two-dimensionality. The greatest differences between the natural and excited jet structural pattern occur in the early flow where the organizational effects associated with the excitation are most pronounced. Naturally this is the same region where researchers are most likely to generalize excited jet results to the corresponding natural flow. That significant structural differences exist between natural and excited flows, especially with regard to phase angle, indicate that such generalizations must be viewed with caution. The results of this study also suggest that with sufficient distance downstream both natural and excited flows achieve a similar underlying anti-symmetric structure. However, this occurs only after the organizational effects of the excitation have essentially been lost. Thus the excitation has little practical value in aiding in the deduction of the nature of the coherent modes in the region. In effect, where excitation induced organization prevails, so too does a basic dissimilarity between the natural and excited jet structures.

Acknowledgments

The initial phases of part of this work were conduced under sponsorship of the National Science Foundation and the Office of Naval Research. Following phases were conducted under support of the Purdue Research Foundation. Their support is gratefully acknowledged.

References

1 Brown, G. B., "On Sensitive Flames," Phil. Mag., Vol. 13, 82, 1932, pp. 161-195.

2 Sato, H., "The Stability and Transition of a Two-Dimensional Jet," *J. Fluid Mech.*, Vol. 1, No. 1, 1960, pp. 53-80.

3 Chanaud, R. C., and Powell, A., "Experiments Concerning the Sound-Sensitive Jet," *J. Acoustical Soc. of Am.*, Vol. 34, No. 7, 1962, pp. 907-915.

4 Sato, H., and Sakao, F., "An Experimental Investigation of a Two-Dimensional Jet at Low Reynolds Numbers," *J. Fluids Mech.*, Vol. 20, No. 2, 1964, pp. 337-352.

5 Freymuth, P., "On Transition in a Separated Laminar Boundary Layer," *J. Fluid Mech.*, Vol. 25, No. 4, 1966, pp. 683-704.

6 Becker, H. A., and Massaro, T. A., "Vortex Evolution in a Round Jet," *J. Fluid Mech.*, Vol. 31, No. 3, 1968, pp. 435-448.

7 Rockwell, D. O., "The Macroscopic Nature of the Jet Flows Subjected to Small Amplitude Periodic Disturbances," *AIChE Chem. Engr. Progress Symposium Series*, Vol. 67, No. 109, 1971, pp. 99-107.

8 Vlasov, E. V., and Gineviskii, A. S., "Acoustic Modification of the Aerodynamic Characteristics of a Turbulent Jet," Izv. AN SSSR, Mekhanika Zhidkosti i Gaza, Vol. 2, No. 4, 1967, pp. 133-138.

9 Morkovin, M. V., and Paranjape, S. V., "On Acoustic Excitation of Shear Layers," *Z Flugwiss*, Vol. 19, No. 8/9, 1971, pp. 328-335.

10 Simcox, C. D., and Hoglund, R. F., "Acoustic Interactions with Turbulent Jets," ASME *Journal of Basic Energy*, Vol. 93, 1971, pp. 42-46.

11 Roffman, G. L., and Toda, K., "A Discussion of the Effects of Sound on Jets and Flueric Devices," ASME *Journal of Engineering for Industry*, Vol. 91, 1969, pp. 1161-1167.

12 Goldschmidt, V. W., and Kaiser, K. F., "Interaction of an Acoustic Field and a Turbulent Plane Jet: Mean Flow Measurements," *AIChE Chem. Eng. Prog. Symp. Series*, Vol. 67, No. 109, 1971, pp. 91-98.

13 Thompson, C. A., "Organized Motion in a Plane Turbulent Jet Under Controlled Excitation," Ph.D. thesis, University of Houston, 1975.

14 Thomas, F. O., "Effect of Nozzle Geometry on Acoustic Interaction with a Turbulent Plane Jet," M.S. thesis, School of Mechanical Engineering, Purdue University, 1980.

15 Chambers, F. W., and Goldschmidt, V. W., "Acoustic Interaction with a Turbulent Plane Jet – Effects on Mean Flow," AIAA-81-0057, 1981.

16 Chambers, F. W., and Goldschmidt, V. W., "Acoustic Interaction with a Turbulent Plane Jet – Effects on Turbulent Structure," AIAA 82-0048, 1982.

17 Thomas, F. O., and Goldschmidt, V. W., "Interaction of an Acoustic Disturbance and a Two-Dimensional Turbulent Jet: Experimental Data," ASME JOURNAL OF FLUIDS ENGINEERING, Vol. 105, No. 2, 1983, pp. 134-139.

18 Laufer, J., "New Trends in Experimental Turbulence Research," *Annual Review of Fluid Mechanics*, Vol. 7, 1975, pp. 307-326.

19 Roshko, A., "Structure of Turbulent Shear Flows: A New Look," *AIAA Journal*, Vol. 14, No. 10, 1976, pp. 1349-1357.

20 Kovasznay, L. S. G., "The Role of Large Scale Coherent Structures in Turbulent Shear Flows," *Proceedings: Fifth Biennial Symposium on Turbulence*, 1977, pp. 379-389.

21 Crow, S. C., and Champagne, F. H., "Orderly Structure in Jet Turbulence," *J. Fluid Mech.*, Vol. 48, No. 3, 1971, pp. 547-591.

22 Rockwell, D. O., "External Excitation of Planar Jets," ASME *Journal of Applied Mechanics*, Vol. 39, No. 4, 1972, pp. 883-890.

23 Moore, C. J., "The Role of Shear Layer Instability Waves in Jet Exhaust Noise," *J. Fluid Mech.*, Vol. 80, No. 2, 1977, pp. 321-367.

24 Kibens, V., "Discrete Noise Spectrum Generated by an Acoustically Excited Jet," *presented at the 5th Aero-acoustics Conference of the American In*stitute of Aeronautics and Astronautics, Seattle, Wash., 1979.

25 Zaman, K. B. M. Q., and Hussain, A. K. M. F., "Vortex Pairing in a Circular Jet Under Controlled Excitation. Part 1. General Jet Response," Vol. 101 3, 1980, pp. 449-491.

26 Hussain, A. K. M. F., and Zaman, K. B. M. Q., "Vortex Pairing in a Circular Jet Under Controlled Excitation. Part 2. Coherent Structure Dynamics, Vol. 101, No. 3, 1980, pp.493-544.

27 Thomas, F. O., "Development of a Two-Dimensional Turbulent Jet Under Natural and Excited Conditions," Ph.D. thesis, School of Mechanical Engineering, Purdue University, 1983.

28 Gutmark, E., and Wygnanski, I., "The Planar Turbulent Jet," *J. Fluid Mech.*, Vol. 73, 1976, pp. 465-495.

29 Miksad, R. W., "Experiments on Nonlinear Stages of Free-Shear-Transition," *J. Fluid Mech.*, Vol. 56, No. 4, 1972, pp. 695-719.

30 Miksad, R. W., "Experiments on Nonlinear Interactions in the Transition of a Free Shear Layer," *J. Fluid Mech.*, Vol. 59, No. 1, 1973, pp. 1-21.

31 Sato, H., "An Experimental Study of Non-Linear Interaction of Velocity Fluctuations in the Transition Region of a Two-Dimensionality Wake," *J. Fluid Mech.*, Vol. 44, No. 4, 1970, pp. 741-765.

32 Sato, H., and Saito, H., "Fine-Structure of Energy Spectra of Velocity Fluctuations in the Transition Region of a Two-Dimensional Wake," *J. Fluid Mech.*, Vol. 67, No. 3, 1975, pp. 539-559.

33 Thomas, F. O., and Goldschmidt, V. W., "Structural Characteristics of a Developing Turbulent Planar Jet," *J. Fluid Mech.*, Vol. 163, 1986, pp. 227-256.

34 Goldschmidt, V. W., and Bradshaw, P., "Flapping of a Plane Jet," *Phys. Fluids*, Vol. 16, No. 3, 1973, pp. 354-355.

35 Cervantes de Gortari, J., and Goldschmidt, V. W., "The Apparent Flapping Motion of a Turbulent Plane Jet – Further Experimental Results," ASME JOURNAL OF FLUIDS ENGINEERING, Vol. 103, 1981, pp. 119-126.

36 Oler, J. W., and Goldschmidt, V. W., "A Vortex-Street Model of the Flow in the Similarity Region of a Two-Dimensional Free Turbulent Jet," *J. Fluid Mech.*, Vol. 123, 1982, pp. 523-535.

37 Moallemi, K., and Goldschmidt, V. W., "Smoke Wire Visualization of the External Region of a Two-Dimensional Jet," *Proceedings: Seventh Biennial Symposium on Turbulence*, University of Missouri-Rolla, 1981.

38 Weir, A. D., and Bradshaw, P., "Resonance and Other Oscillations in the Initial Region of a Plane Turbulent Jet," I. C. Aero Report 75-07, Imperial College of Science and Technology, Department of Aeronautics, 1975.

39 Alper, A., and Liu, J. T. C., "On the Interactions Between Large-Scale Structure and Fine Grained Turbulence in Free Shear Flow II. The Development of Spatial Interactions in the Mean," *Proc. R. Soc. Lond.*, Vol. 359, 1978. pp. 497-523.

Self-Excited Shear-Layer Oscillations in a Multi-Cavity Channel With a Steady Mean Velocity

K. D. Stephanoff
Assistant Professor,
Department of Mechanical Engineering
and Mechanics,
Lehigh University,
Bethlehem, PA 18015

Self-excited shear-layer oscillations are observed in the cavity flows of a multi-cavity channel when the mean velocity through the channel exceeds a critical value. These coherent shear-layer oscillations appear as one or sometimes two selectively-amplified frequencies in the Fourier-analyzed signals of hot-film gauges that are sintered into the channel walls. At a constant velocity above the critical velocity, the self-excited oscillations are present in only a few cavities. Downstream from these cavities there are oscillations in the cavity flows but one or two selectively-amplified frequencies are not observed. The self-excited oscillations move upstream and the selectively-amplified frequency increases as the mean velocity through the channel is increased.

1 Introduction

The results from an experimental study on shear-layer oscillations in a multi-cavity channel are presented in this paper. This work is an extension of earlier numerical [1] and experimental [2] investigations on the same channel which is a model of a membrane oxygenator [3]. In the earlier investigations it was found that, when the mean velocity is steady, a vortex forms in each cavity in the channel at a Reynolds number R_h of about 5.0, where R_h is based on the mean velocity through the channel and half the minimum channel gap. Photographs of particle pathlines showed that the volume of fluid in the vortex and the rate of rotation of the vortex in each cavity increase with increasing Reynolds number for $5.0 \leq R_h \leq 30.0$. For increasing Reynolds number from $R_h = 30.0$ to $R_h = 55.0$, it was observed that the size of the vortex remains constant in each cavity and the rate of rotation of the vortex increases weakly.

In the present investigation the transition to turbulent flow in the multi-cavity channel is examined. It is found that, when the mean velocity is steady, the multiple cavity geometry allows a disturbance frequency to be selectively-amplified in a cavity shear layer. Hot-film gauges, which are sintered into one of the channel walls, are used to measure, noninvasively and indirectly, these cavity shear-layer oscillations. The output from the hot-films show that the selective amplification of a single frequency occurs only in a few cavities when the mean velocity is held constant. The location of the cavities where a frequency is selectively-amplified and the values of the selectively-amplified frequencies are measured as a function of the mean velocity. The manner in which the selectively-amplified frequencies depend on the mean velocity through the channel is compared with the results of studies on shear-layer oscillations in single cavity flows.

2 Experimental System and Data Analysis

The experiments were conducted in a recirculating Plexiglas flow channel which can be disassembled into three commponent parts, two settling chambers and the test section (Fig. 1). It is the channel used by Stephanoff et al. [2] except that one Plexiglas wall of the test section has been replaced by a machinable glass-ceramic wall. There are nineteen cavities machined into the ceramic and Plexiglas walls (Fig. 2); each cavity in these walls is 0.40 cm long and 0.10 cm deep and the minimum gap 2h between the two walls is 0.10 cm. A schematic drawing of a pair of typical cavities is shown in Fig. 3. Distilled water was used in all the experiments and the temperature was kept constant so that the kinematic viscosity remained at 0.010 cm^2/s.

Seventeen hot-film gauges, which are sintered into the glass-ceramic wall (Fig. 4), were used to measure qualitatively the

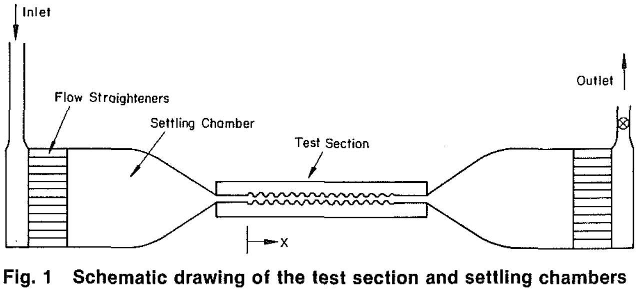

Fig. 1 Schematic drawing of the test section and settling chambers

---

Contributed by the Fluids Engineering Division for publication in the JOURNAL OF FLUIDS ENGINEERING. Manuscript received by the Fluids Engineering Division, August 7, 1985.

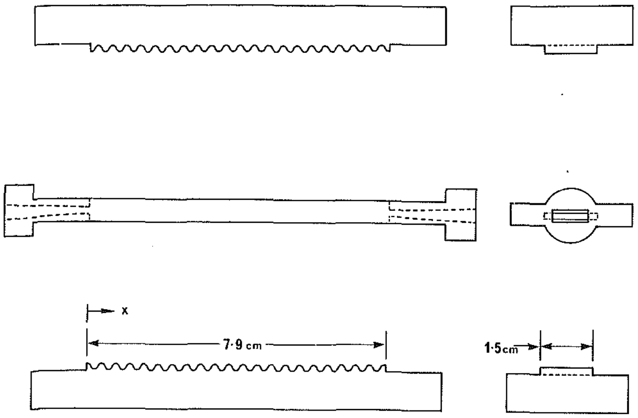

Fig. 2 Drawing of the test section showing the X coordinate

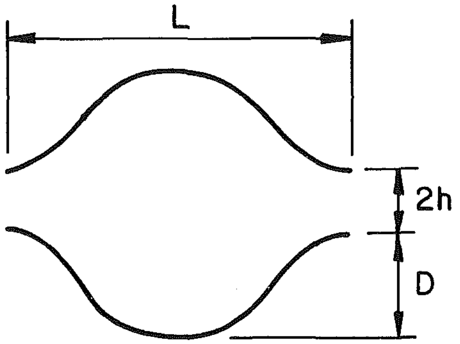

Fig. 3 Schematic drawing of a pair of cavities in the test section. D = 0.10 ± 0.01 cm, h = 0.05 ± 0.01 cm, and L = 0.40 ± 0.01 cm

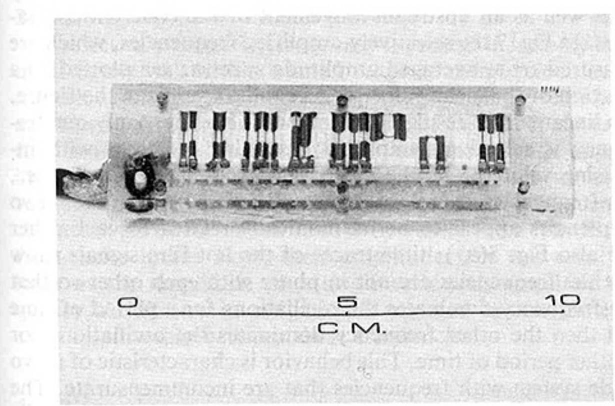

Fig. 4 Photograph of the glass-ceramic substrate with the hot-film gauges

shear fluctuations along the channel. The output from the hot-films was digitized by a mini-computer and stored on floppy discs. The frequency resolution for the experiments was 0.25 Hz and the Nyquist frequency was 256 Hz. Before sampling, each hot-film signal was band-passed filtered with a low frequency cut-off of 0.3 Hz and a high frequency cut-off of 45 Hz. The low frequency cut-off eliminated the mean signal so that the oscillating signal could be amplified. The high frequency cut-off eliminated 50 Hz noise (the experiments were done in the U.K.) and ensured that aliasing did not occur. Only one hot-film was used at a time and each run consisted of taking 30 records of data. The data analysis was performed by converting each record of data into a form proportional to the shear at the wall [4, 5, 6] and then Fourier-analyzing the result. In the frequency domain, an averaged amplitude spectrum of the 30 records in a run was obtained by forming an amplitude spectrum of each record and ensemble averaging identical frequency components.

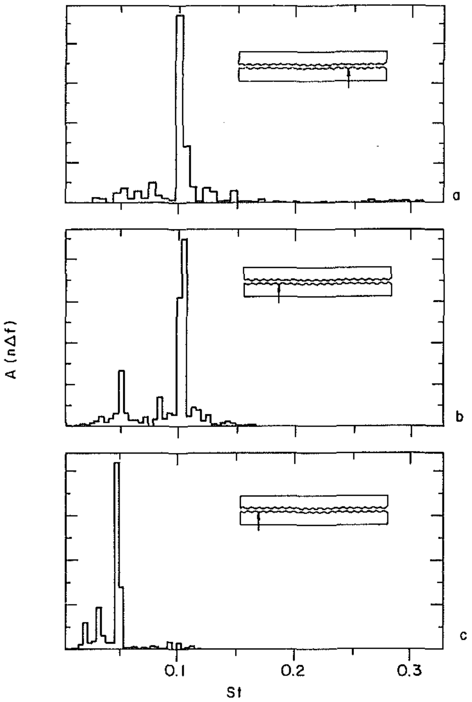

Fig. 5 The average amplitude spectra from three hot-film gauges showing the nondimensional selectively-amplified frequencies. The vertical arrows in the schematics of the channel point to the cavities where the amplitude spectra have been taken. (*a*) x = 5.35 ± 0.01 cm, $\bar{U}$ = 16.9 ± 0.1 cm/s; (*b*) x = 2.05 ± 0.01 cm, $\bar{U}$ = 24.2 ± 0.1 cm/s; and (*c*) x = 1.25 ± 0.01 cm, $\bar{U}$ = 26.2 ± 0.1 cm/s.

3 Experimental Results

The selectively-amplified oscillations were observed to occur only within a small range of mean velocities for a particular cavity in the channel. The procedure to determine the velocity at which the oscillations in a cavity had their maximum amplitude was as follows: 1) a hot-film in a cavity was turned on; 2) the velocity was increased until large amplitude oscillations were observed; 3) the velocity was tuned to get the maximum oscillations; and 4) 30 records of data were recorded. When the mean velocity was tuned to get the maximum amplitude of the selectively-amplified frequency, it was varied only slightly; it is this velocity that is used in Figs. 5, 7, 8, and 9. The maximum amplitude appeared almost as soon as oscillations were observed in a hot-film gauge output.

The amplitude of the selectively-amplified frequency or frequencies varies within a cavity. A selectively-amplified frequency is easily visible in the waveforms and spectra of gauges sintered into the downstream wall of a cavity whereas it is dif-

Nomenclature

f = frequency (Hz)
h = half the minimum gap between the channel walls (cm)
L = length of a cavity (cm)
x = distance from the upstream edge of the first cavity in the channel (cm)
x^* = x + 5.77 cm
ν = kinematic viscosity (cm^2/s)
l = length scale in equation (3)
λ = wavelength for Tollmein-Schlichting wave

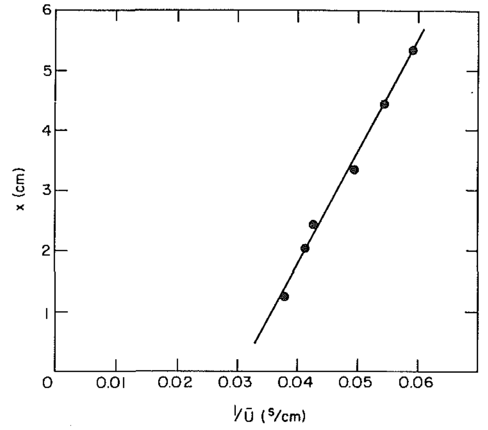

Fig. 6 The position of the self-excited oscillations in the channel as a function of the inverse of the mean velocity

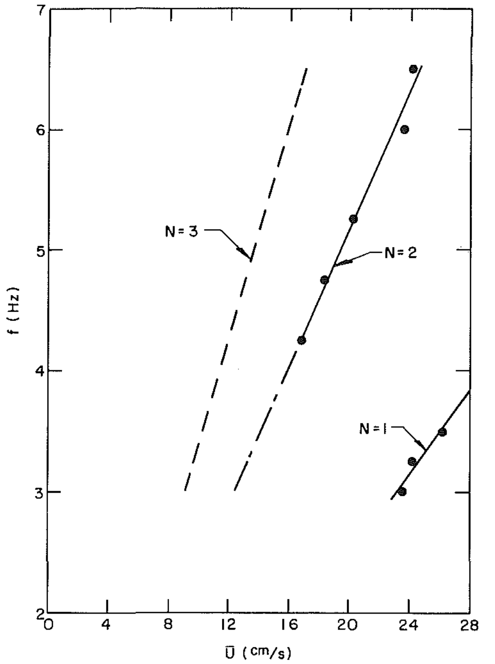

Fig. 7 The values of the selectively-amplified frequencies as a function of the mean velocity. The solid lines are the best fit lines through the data points for modes $N = 2$ (upper line) and $N = 1$ (lower line). The dashed line shows the location of the predicted $N = 3$ mode.

ficult to detect or is absent in the waveforms of the gauges sintered into the upstream wall of a cavity. Consequently, all the results reported in this paper are from spectra of gauges located along downstream cavity walls.

The amplitude of a selectively-amplified frequency is much larger than the amplitude of the other frequencies in a typical average amplitude spectrum from a hot-film gauge; Figs. 5, 8, and 9 show examples of typical amplitude spectra with either one or two selectively-amplified frequencies. The frequencies in these figures, expressed in cycles per second, have been nondimensionalized by the ratio of the cavity length to the mean velocity $L/\bar{U}$ so that a Strouhal number $\mathrm{St} = fL/\bar{U}$ is defined. As can be seen from Fig. 5 the position in the channel where a selectively-amplified frequency is present moves upstream as the mean velocity through the channel increases; the upstream edge of each cavity x is measured from the upstream edge of the first cavity in the channel (see Fig. 2). By plotting the location where a selectively-amplified frequency is first observed in the streamwise direction as a function of the inverse of the mean velocity (see Fig. 6), a linear relation is obtained which gives

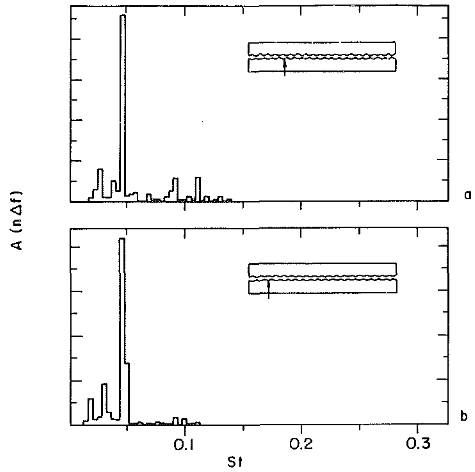

Fig. 8 The average amplitude spectra from two hot-film gauges in cavities separated by one cavity at $\bar{U} = 26.2 \pm 0.1$ cm/s. The vertical arrows in the schematics of the channel point to the cavities where the amplitude spectra have been taken. The streamwise position of the cavities are: (*a*) $x = 2.05 \pm 0.01$ cm and (*b*) $x = 1.25 \pm 0.01$ cm.

$$188/\bar{U} = (x + 5.77)\text{cm}. \qquad (1)$$

A constant Reynolds number can be defined, which separates the laminar flow regime from the flow regime with a selectively-amplified frequency, if the length scale for the Reynolds number, x^*, is chosen to be $x^* = x + 5.77$ cm; this Reynolds number is

$$\mathrm{R}_{x^*} = \bar{U}x^*/\nu = 18{,}800.$$

As the mean velocity through the channel is increased, there is an increase in the value of the selectively-amplified frequency as well as an upstream movement of the coherent oscillations. In Fig. 7 the selectively-amplified frequencies, which are measured from averaged amplitude spectra, are plotted as a function of the mean velocity. As can be seen from the figure, two linear curves result. For the lower velocities, only one frequency is selectively-amplified; its value increases with increasing velocity. As the mean velocity is increased further, two frequencies are selectively-amplified. Although these two frequencies appear to be harmonically related to each other (see also Fig. 5(*b*)), time traces of the hot-film signals show that the frequencies are not in phase with each other so that one frequency dominates the oscillations for a period of time and then the other frequency dominates the oscillations for another period of time. This behavior is characteristic of a two mode system with frequencies that are incommensurate. The higher frequency disappears with a continued increase in the mean velocity so that only the lower frequency is present in the averaged amplitude spectra (see Fig. 5(*c*)). The selectively-amplified frequencies which lie on the upper curve in Fig. 7 are expressed by $\mathrm{St} \approx 0.10$ in the spectra of Figs. 5 and 9 the frequencies which lie on the lower curve of Fig. 7 are expressed by $\mathrm{St} \approx 0.053$ in the spectra of Figs. 5 and 8. The Strouhal numbers vary from $\mathrm{St} = 0.101$ to $\mathrm{St} = 0.107$ for the higher mode of oscillation and from $\mathrm{St} = 0.051$ to $\mathrm{St} = 0.054$ for the lower mode of oscillation.

A selectively-amplified frequency can be observed in up to three consecutive cavities at a given mean velocity. Averaged amplitude spectra from gauges located in cavities that are separated by a cavity illustrate this point in Fig. 8. Because the coherent oscillations are not confined to a single cavity at a given velocity, they are observed over a small range of velocities at a given cavity. At a given cavity, the maximum amplitude of the selectively amplified frequency occurs at the low velocity end of the range of velocities in which it exists. In the two or three cavities where it is possible for two frequencies to be selectively-amplified, the relative amplitude of the

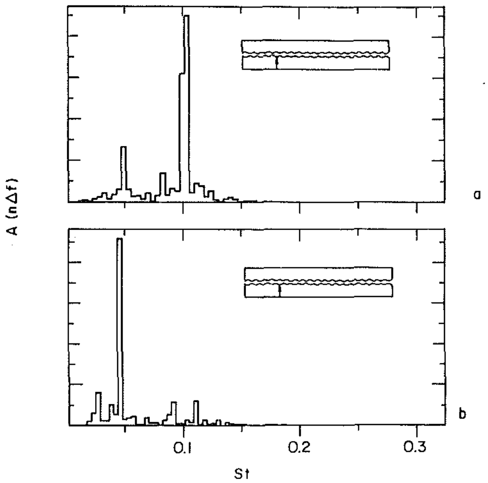

Fig. 9 The average amplitude spectra from a hot-film gauge in the middle section of the channel. At this location the disturbance frequencies that are selectively-amplified depend on $\bar{U}$. The vertical arrows in the schematics of the channel point to the cavity where the amplitude spetra have been taken. In (*a*) $\bar{U} = 24.2 \pm 0.1$ cm/s and in (*b*) $\bar{U} = 26.2 \pm 0.1$ cm/s.

two frequencies depends on the value of the velocity within the range of velocities in which selective amplification occurs. In the lower half of the range, St $\approx$ 0.10 predominates, in the middle St $\approx$ 0.10 and St $\approx$ 0.053 have comparable amplitudes and in the upper half St $\approx$ 0.053 predominates. As an illustration of this point, Fig. 9 shows averaged amplitude spectra from a gauge located in a cavity in the channel midsection. As can be seen, for $\bar{U}$ = 24.2 cm/s, St $\approx$ 0.10 and St $\approx$ 0.053 are present with the higher frequency predominating and for $\bar{U}$ = 26.2 cm/s only St $\approx$ 0.053 is present.

A selectively-amplified frequency is present in a cavity in the multi-cavity wall within a small range of mean velocities. As the velocity is increased above this range, a single selectively-amplified frequency is no longer visible. Instead there are at first a finite number of multiple frequencies with approximately equal amplitudes of oscillation and then at higher velocities there are broadband spectra of frequencies characteristic of turbulent flow. When there are a few distinct frequencies in the flow, their amplitudes are not nearly as large as the amplitude of a single selectively-amplified frequency. Additional investigation is required to determine the exact relationship between these frequencies.

4 Discussion

The experiments described in this paper have shown that there is a critical Reynolds number for the multi-cavity flow which separates a laminar flow regime from a flow regime where at least one disturbance frequency is selectively-amplified. At the critical Reynolds number, a finite band of frequencies is observed to be selectively-amplified. These results are interpreted in the following manner. A broadband of stable infinitesimal disturbances is present in the developing boundary layer in the channel. These disturbances are probably introduced into the flow from the settling chamber upstream of the channel. (Amplitude spectra and oscilloscope traces from the hot-films in and between the first couple of cavities in the channel show that there are no finite amplitude disturbances entering the channel in the mean velocity range of this study.) As the disturbances are convected downstream, there is a critical Reynolds number for the flow at which a finite band of disturbances is unstable if there is an inflection point in the velocity profile. The cavities along the channel walls allow this criterion to be satisfied. Their finite length, however, impose an additional constraint, the cavity phase constraint, so that usually only a single frequency from the band of unstable frequencies is selectively-amplified. Sometimes, though, two frequencies are selectively-amplified; this phenomenon occurs when a mode jump is in progress. When two frequencies are selectively-amplified, both frequencies satisfy the cavity phase constraint and are approximately equally unstable. The selective-amplification of one and sometimes two frequencies has also been observed in unstable single cavity flows. In addition, harmonics due to nonlinear shear-layer oscillations and subharmonics due to vortex clipping at the downstream cavity corner have been observed [7-11].

There is one major difference between the selective-amplification of disturbance frequencies in a multi-cavity flow and the selective-amplification of disturbance frequencies in a single cavity flow. In a multi-cavity geometry, usually one frequency (but sometimes two frequencies) is selectively-amplified in a cavity and only within a small range of Reynolds numbers, whereas in the flow past a single cavity the selective-amplification of one or two (when a mode jump is occurring) frequencies exists over a much wider range of Reynolds numbers and frequencies. In the multi-cavity flow, a selectively-amplified frequency appears in a cavity only when R_{x^*} at the upstream edge of the cavity is approximately 18,800. By increasing the mean velocity, the position where R_{x^*} = 18,800 moves upstream and, as long as a frequency jump does not occur, the selectively-amplified frequency increases. Therefore, for a given geometry, the mean velocity determines where along the multi-cavity wall self-excited oscillations will occur and the value of the selectively-amplified frequency. In contrast, in single cavity flows selectively-amplified frequencies appear over a range of Reynolds numbers. By increasing the mean velocity the Reynolds number and the value of the selectively-amplified frequency are increased. Since the band of unstable frequencies at the upstream edge of a single cavity flow depends on the Reynolds number there, an increase in the mean velocity changes the band of unstable frequencies. Therefore, the band of unstable frequencies at a constant Reynolds number is determined by varying the length of the cavity. For long cavities, though, the shear-layer oscillations can be nonlinear and it is much more difficult to interpret the flow spectra.

A third mode of oscillation may exist in a longer multi-cavity channel than the present channel, if the flow is not fully developed at the greater distance from the inlet and at lower velocities. By assuming that the band of unstable frequencies at R_{x_*} = 18,800 is approximately equal to the band of unstable frequencies that have been selectively-amplified in the present experiments (3.00 to 6.25 Hz) and by assuming that the upper curve in Fig. 7 corresponds to an N = 2 mode and the lower curve corresponds to an N = 1 mode, an N = 3 mode will appear within the range of velocities as shown by the dashed line in Fig. 7. The curve for the N = 3 mode has been calculated in the following manner. The data in Fig. 7 collapses onto a single curve if the selectively-amplified frequencies are divided by their mode number. The equation for the resulting linear relation is

$$f/N = 0.145\bar{U} - 0.316\ \text{Hz}. \tag{2}$$

By substituting into the above equation the values of the selectively-amplified frequencies and the mode number N = 3, the velocity range for the N = 3 mode can be estimated. In the region where modes N = 2 and N = 3 overlap (see Fig. 7), two frequencies will be selectively-amplified only during a mode jump; otherwise one frequency will be selectively-amplified. At a given velocity, this frequency will be the frequency with the higher amplification rate and, according to linear stability theory, it will be the frequency which is closer to the center of the band of unstable frequencies.

The phase velocity U_p of the selectively-amplified disturbance frequencies could be estimated from equation (2) if the correct length scale l for the flow is known since

$$fl/U_p = N = 1,2,3,4, \ldots . \quad (3)$$

At present this information cannot be determined from the experiments. It appears, however, as though the length scale for the multiple cavity geometry may be equal to the distance between the shear layer separation point of one caivty and the shear layer reattachment point of another cavity further downstream. This suggestion is based on observations from hot-film spectra which show that three and maybe more cavities selectively amplify the same frequency at a given mean velocity. It is possible that the shear layer oscillations are exciting a Tollmein-Schlichting wave in the boundary layer above the cavities [12]. A coupling between the Tollmein-Schlichting wave and the cavity oscillations would imply that the length scale for the oscillations should be, λ, the wavelength of the Tollmein-Schlichting wave and not, L, the length of a single cavity. Since the wavelength of a Tollmein-Schlichting wave is long when compared with the boundary layer thickness of a flow [13], λ should span many cavities in the multi-cavity channel. The correct length scale in equation (3), therefore, may be $l = \lambda = ML$, where M is a integer. Additional experiments using flow visualization and multiple transducers, which could measure simultaneously the phases of the oscillations in adjacent cavities, are required to verify this hypothesis.

5 Concluding Remarks

The self-excited oscillations that develop in the membrane oxygenator model, when the mean velocity through the model is steady, may cause fluid to enter and leave a cavity flow in the region of the shear-layer reattachment point. This exchange of fluid between the cavity flow and the mainstream can be increased by making the downstream cavity corner sharper and by lengthening the cavity. In the membrane oxygenator, the cavity walls are a semi-porous membrane through which oxygen diffuses into the blood (water in this study). An oxygen rich boundary layer is prevented from forming along the membrane surface by pulsating the blood through the device [1-3]. The results from the present study show that the cavity shear layer oscillations should also inhibit the formation of an oxygen rich boundary layer. It is possible, therefore, that good mass transfer rates can be obtained in the oxygenator without having to use oscillatory flow, as is now the case. The shear layer oscillations in the multi-cavity channel should also prevent a stable thermal boundary layer from forming and additional research should be done to study the effectiveness of the multicavity geometry on heat transfer rate enhancement.

Acknowledgments

Financial support for this research was provided by a Thouron Award from the University of Pennsylvania. I am grateful to Ian J. Sobey for guidance during the course of this research and to James W. Rottman for helpful criticism of a draft of this paper. Special appreciation is extended to John Allen for instruction in the art of making hot-film gauges.

References

1 Sobey, I. J., "On Flow Through Furrowed Channels. Part 1. Calculated Flow Patterns," *J. Fluid Mech.*, Vol. 95, 1980, pp. 1-26.

2 Stephanoff, K. D., Sobey, I. J., and Bellhouse, B. J., "On Flow Through Furrowed Channels. Part 2. Observed Flow Patterns," *J. Fluid Mech.*, Vol. 95, 1980, pp. 27-32.

3 Bellhouse, B. J., Bellhouse, F. H., Curl, C. M., MacMillan, T. I., Gunning, A. J., Spratt, E. H., MacMurray, S. B., and Nelems, J. M., "A High Efficiency Membrane Oxygenator and Pulsatile Pumping System, and Its Application to Animal Trials," *Trans. Amer. Soc. Artif. Int. Organs*, Vol. 19, 1973, pp. 72-79.

4 Fage, A., and Falkner, V. M., "Relation Between Heat Transfer and Surface Friction for Laminar Flow," *British A.R.C. R & M.*, 1931, p. 1408.

5 Ludwieg, H., "Instrument for Measuring the Wall Shearing Stress of Turbulent Boundary Layers," *N.A.C.A. Tech. Mem.*, 1950, p. 1284.

6 Liepmann, H. W., and Skinner, G. T., "Shearing Stress Measurements by Use of a Heated Element," *N.A.C.A. Tech. Note*, 1954, p. 3268.

7 Sarohia, Y., "Experimental Investigations of Oscillations in Flows Over Shallow Cavities," *A.I.A.A.J.*, Vol. 15, 1977, pp. 984-991.

8 Rockwell, D., and Naudascher, E., "Review---Self-Sustaining Oscillations of Flow Past Cavities," ASME JOURNAL OF FLUID ENGNG., Vol. 100, 1978, pp. 152-165.

9 Rockwell, D., and Naudascher, E., "Self-Sustained Oscillations of Impinging Free Shear Layers," *Ann. Rev. Fluid Mech.*, Vol. 11, 1979, pp. 67-94.

10 Rockwell, D., and Knisely, C., "Vortex-Interaction: Mechanisms for Generating Low Frequency Components," *Phys. Fluids*, Vol. 23, 1980, pp. 239-240.

11 Rockwell, D., "Oscillations of Impinging Shear Layers," *A.I.A.A.J.*, Vol. 21, 1983, pp. 645-664.

12 Ghaddar, N. K., Korczak, K. Z., Mikic, B. B., and Patera, A. T., "Numerical Investigation of Incompressible Flow in Grooved Channels. Part 1: Stability and Self-Sustained Oscillations," *J. Fluid Mech.*, Vol. 163, 1986, pp. 99-127.

13 Schlichting, H., *Boundary-Layer Theory*, 1968, McGraw-Hill, New York.

The Influence of Surface Roughness on Resistance to Flow Through Packed Beds

C. W. Crawford
Graduate Student,
Department of Mechanical Engineering.

O. A. Plumb
Associate Dean,
College of Engineering and Architecture.

Washington State University,
Pullman, WA 99164-2714

Experiments were performed to determine the effect of roughness on flow through randomly packed beds of spheres. Three different packings were investigated, one of smooth spheres, and two others composed of spheres with roughness elements added to the surface. The relative roughness, defined as the height of the added elements divided by the diameter of the smooth spheres, was .012 and .026 for these two cases. The experiments covered a range of Reynolds numbers based on the sphere diameter from near unity where the flow is dominated by viscosity to 1600 where the flow is dominated by inertia. It was found that the pressure drop is substantially increased by the presence of surface roughness over the entire range of Reynolds numbers studied. The observed behavior is quite different from that which has been proposed previously by drawing analogy with flow in rough pipes, since the flow at low Reynolds number as well as high Reynolds number was affected by roughness.

Introduction

Flow through porous or packed beds is of interest in many areas of science and engineering including groundwater hydrology, petroleum reservoir engineering, food processing, and number of chemical processes such as filtration and catalytic reactors. Packed beds are particularly well suited to applications where surface area is an important factor as in the case of a catalytic reactor or adsorption bed. Many of these applications involve flow through rough or irregularly shaped particles, however, the effect of roughness on the important flow parameters, namely pressure drop, has not been well established through either experimental or theoretical works.

Ideally one would like to relate pressure drop across a packed bed to flow rate through consideration of macroscopically measurable properties of the packing material. These properties include the porosity, the length of the bed in the flow direction, and the characteristics of the packing material which might include shape, mean diameter, aspect ratio and surface roughness. Additional parameters which are more difficult to measure but commonly used in characterizing porous media are the tortuosity and specific surface area. The latter of which is strongly influenced by surface roughness.

Unfortunately the complex shape of flow channels renders impractical the solution of the continuum equations. Hence, such flows are universally treated using empirical or quasi-empirical theories. A review of the various theories and correlations which have been established for predicting the relationship between pressure and velocity can be found in Bear [1]. Most of these models are a simple extension of Darcy's law to include inertial effects. The simplest example is that first proposed by Forchheimer [2].

$$-\nabla P = \alpha \mu v + \beta \rho v^2 \tag{1}$$

It is generally accepted that the term which is first order in velocity represents the effect of viscosity while the second order term accounts for inertial losses.

If the wealth of experimental data for pressure drop versus velocity is examined [3, 4] it can be shown that models of general form of equation (1) are qualitatively correct. However, the experimental data demonstrates a significant amount of scatter. It has been proposed by some researchers [3, 4] that surface roughness is responsible for this scatter yet experimental results delineating the effect of surface roughness are not available. The objective of this study was to determine experimentally the effect of surface roughness on the relationship between velocity and pressure drop for flow through packed beds and to develop and improved model which would be of utility in predicting such flows.

Theoretical Considerations

Theoretical models for flow in porous media or packed beds generally fall into two categories – those based upon analogies between flow through porous media and flow through a bundle of capillary tubes and those based upon the analogies between flow over a single particle and a packed bed of similar particles. The most widely used model is probably that due to Ergun [5] which is based upon the analogy between flow in porous media and flow in pipes. The details of the derivation are given in [6].

$$\rho \frac{\Delta P D_p \epsilon^3}{G_0^2 L(1-\epsilon)} = \frac{A_e(1-\epsilon)\mu}{G_0 D_p} + B_e \tag{2}$$

Contributed by the Fluids Engineering Division for publication in the JOURNAL OF FLUIDS ENGINEERING. Manuscript received by the Fluids Engineering Division, March 19, 1985.

Ergun proposed that if the empirical constants were set as $A_e = 150$ and $B_e = 1.75$ good agreement existed between the prediction of equation (2) and experimental results. The development of Ergun's equation assumes that all porous materials have similar roughness characteristics so that a unique friction factor can be assumed in developing the model. Thus, Ergun's equation can account for roughness only through the influence of roughness on surface area since for a packed bed the mean particle diameter can be related to the surface area per unit bed volume

$$D_p = \frac{6(1-\epsilon)}{S} \tag{3}$$

MacDonald et al. [3] reviewed existing experimental data for both consolidated (monolithic) and unconsolidated (granular) porous media and classified the particles composing the media as either smooth or rough. They recommend that the Ergun equation be modified by setting $A_e = 180$ with $B_e = 1.8$ or 4.0 depending upon whether the particles composing the media are smooth or rough. This recommendation is based on the analogy to flow in rough pipes, hence, only the inertial term is affected by surface roughness. One would expect that the applicability of this result might be limited since the effect of roughness is not dependent on a parameter indicative of the degree of roughness.

The earlier approach of Brownell and Katz [4] is similar to that of MacDonald et al. In an effort to better correlate the experimental data they attempted to relate friction factor to Reynolds number while modifying the porosity to account for surface roughness. Their results resembled the Moody diagram, however, the underlying correlation was found to be valid over only a limited range of porosity.

At low Reynolds number or in the viscous dominated flow regime Rumpf and Gupte [7] performed a comprehensive series of tests on packed beds composed of uniform sized smooth spherical particles covering a broad range of porosities. They conclude that the experimental data can be fit much more accurately with the Ergun equation if the porosity dependence given by $\epsilon^3/(1-\epsilon)^2$ is replaced with $\epsilon^{5.5}$. However, their results do not extend far enough into the inertially dominated flow regime to allow for an assessment of the applicability of this result at high Reynolds numbers.

The only proposed correlation which is available which includes the effect of surface roughness is that of Meyer and Smith [8]. Again, by applying the analogy to turbulent pipe flow they propose, for compressible flow, the following relationship:

$$\frac{\bar{\rho}\Delta P Z \epsilon^3}{G_0^2 Z_e L S} = \tau\left[\frac{2\bar{\mu} S}{G_0} + C_1 + \frac{C_2}{2}\left(\frac{q}{D_h}\right)^n\right] \tag{4}$$

In equation (4) τ is the tortuosity, Z the compressibility factor, S the specific surface area (total particle surface area/unit volume) and q/D_h is the parameter indicating the degree of roughness (roughness height/particle hydraulic diameter). Meyer and Smith suggest values for the coefficients which appear in equation (4) based on flow studies for sintered stainless steel power compacts. The studies involved specimens of a single assumed value for the roughness parameter, q/D_h, thus the general applicability of equation (4) with the recommended coefficients is not conclusively confirmed.

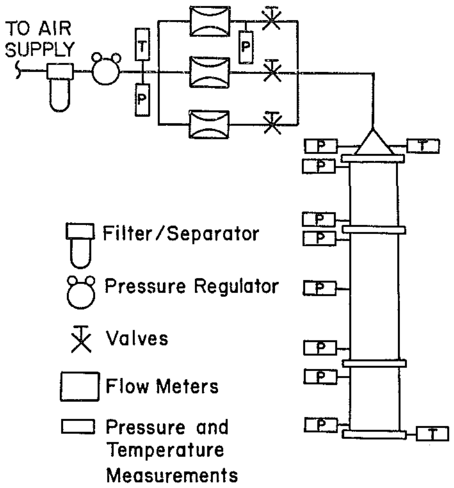

Fig. 1 Schematic of flow apparatus and test section

Since our objective was in part to develop an empirical model for use in predicting flows involving rough particles the above correlations form the basis for comparison with the experimental results.

Description of the Experiment

The investigation of the characteristics of three packed beds was performed in the open-loop fluid flow facility pictured schematically in Fig. 1. The working fluid was compressed atmospheric air delivered to the test facility at a pressure of 6200 kPa (90 psig). The air was first passed through a filter/separation unit before being throttled to system pressure by a regulator. The air then entered one of three flow meters necessitated by the wide range of Reynolds numbers covered. A positive displacement Wet Test meter was used for the lowest flow rates, a tapered tube rotameter for the intermediate, and an ASME square-edged concentric orifice for the highest flow rates. The meters were calibrated and displayed agreement in the overlapping flow ranges. The test section consisted of a 61 cm (2 ft) and two 30.5 cm (1 ft) sections of 15.24 (6 in) inside diameter plexiglass pipe. The ends of these sections were flanged and could be assembled to a total length of 1.22 m (4 ft). The diameter of the pipe was

Nomenclature

A_e = viscous coefficient in Ergun's equation
B_e = inertial coefficient in Ergun's equation
B_0 = inertial coefficient for packed beds of smooth spheres
C_1 = constant in equation (4)
C_2 = constant in equation (4)
C_d = drag coefficient
D_h = hydraulic diameter
D_1 = diameter of smooth spheres
D_p = mean particle diameter
G_0 = superficial mass flow rate
L = length of test section in flow direction
L_i = length from bed entrance to ith pressure probe
n = exponent of relative roughness in equation (4)
P = pressure
q = measured roughness height
Re_p = Reynolds number based on mean particle diameter
Re_s = Reynollds number based on S
S = surface area per unit bed volume
v = superficial (filtration) velocity
Z = average fluid compressibility factor
Z_e = effective fluid compressibility factor
α = viscous coefficient in Forchheimer's equation
β = inertial coefficient in Forchheimer's equation
ϵ = void fraction (porosity)
ρ = fluid density
$\bar{\rho}$ = average fluid density
τ = tortuosity
μ = fluid viscosity
$\bar{\mu}$ = average fluid viscosity

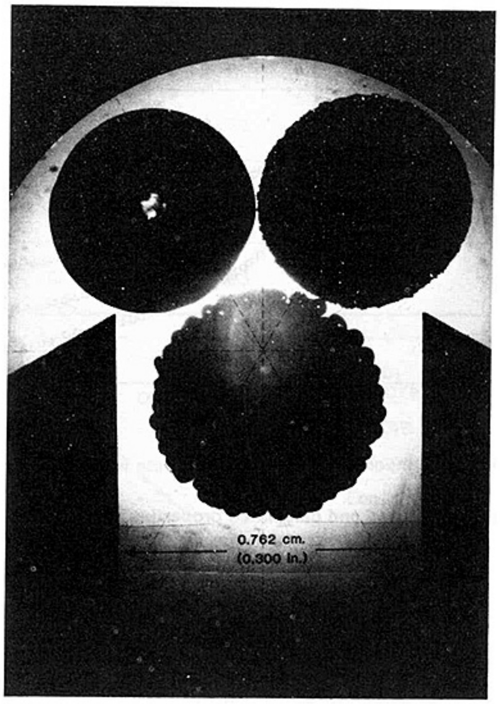

Fig. 2 Representative particles of the three packings

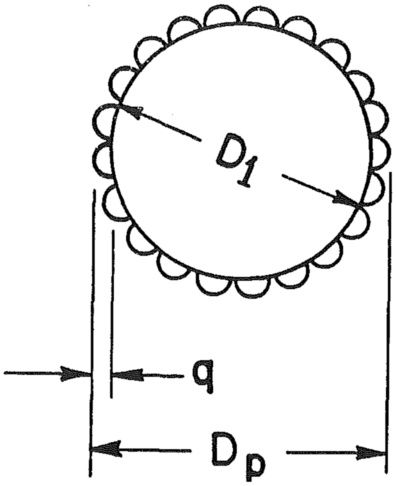

Fig. 3 Illustration of the effective particle diameter and relative roughness

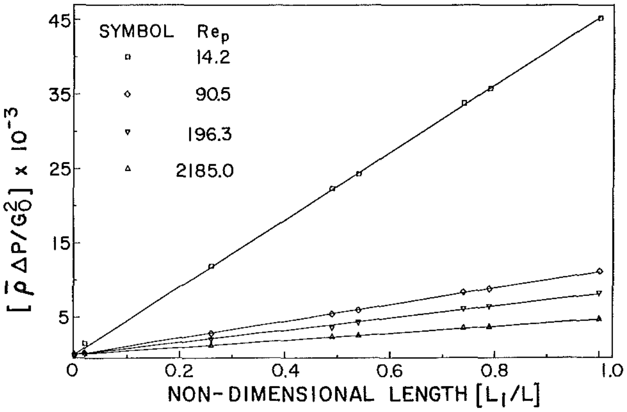

Fig. 4 Non-dimensional axial pressure distribution for bed of smooth spheres

carefully selected in order that the wall effects would be negligible. The resulting diameter ratio D_t/D_p for the three packings was approximately 30. Beavers, Sparrow, and Rodenz [9] tested packed beds of spheres over a range of equivalent diameter ratios. Their results indicate the permeability is unaffected by the presence of the walls for diameter ratios greater than 12, while the inertial coefficient may be affected for diameter ratios as high as 40.

The packings in the test section were supported from below by a fine mesh wire screen at the exit. Pressure probes made of 0.48 cm (0.188 in.) tubing were mounted at intervals along the length and protruded into the center of the pipe. Two small radial holes prevented erroneous pressure readings caused by the ends of the probes becoming plugged by the packings. The last pressure probe was located 2.2 cm (0.875 in) from the exit and eliminated the inclusion of the supporting screen in the pressure drop measurements.

Copper-constantan thermocouples measured the temperature of the air in the flow meters and at the entrance and exit of the packed bed. Flow through the bed was essentially isothermal even for the highest pressure drops investigated. Pressure differentials less than 5.1 cm (2 in) of water were measured with a micromanometer capable of discerning to 0.005 cm (.002 in) of water. Higher pressure measurements were made with a bank of U-tube manometers. When required these were read with a cathometer which provided a measurement accuracy of 0.01 cm (.004 in) of manometer fluid.

To obtain packings of known roughness two sizes of glass microspheres were glued to the surface of smooth 5 mm (0.2 in) diameter glass spheres with an epoxy based paint. The microspheres were sized by the manufacturer as 100 μm (0.004 in) and 350 μm (0.014 in). Details of the application procedure as well as other aspects of the experiment can be found in [10]. Figure 2 is a photograph of representative particles of the three packings investigated.

An optical comparator was used in determining the mean diameter and relative roughness of a statistically representative sample of the roughened particles. The particle diameter D_p used in the definitions of the friction factor and Reynolds number was the mean outside diameter of the roughened particles or the diameter of a sphere that would circumscribe the particle. The relative roughness parameter, q/D_1, is defined as the ratio of the diameter of the roughness elements, q, divided by the diameter of the smooth spheres, D_1, as shown in Fig. 3. This definition was selected to be consistent with that used in characterizing particles [11]. The combinations of spheres used in this study resulted in measured relative roughness values of 0.012 and 0.026.

Experimental measurements on the smooth spheres were conducted in a test section of 1.22 m (4 ft) overall length. In order to minimize the quantity of spheres that needed to be roughened the measurements on the rough spheres were conducted in a 30.5 cm (1 ft) test section. For the results to be comparable the flow must have been fully developed throughout the length of the test section with no appreciable entrance or exit effects. To determine the developing length for the experimental apparatus pressure drop measurements were made between the pressure probe at the entrance and each consecutive probe along the length of the bed of smooth spheres. The first probe was located only 2.22 cm (0.875 in) from the entrance to the bed. These measurements were nondimensionalized and plotted against length in Fig. 4. The nondimensional pressure drop parameter is linear with distance from the entrance, and decreases with increasing Reynolds number as a result of the pressure drop becoming increasingly proportional to the flow velocity squared. Figure 4 emphasizes

Table 1 Results of uncertainty analysis of data fit to equation [2]

$\frac{G_o D_p}{(1-\varepsilon)}$	1.9	7.2	103.1	525.9	1645.1
$\frac{\bar{\rho}\Delta P D_p\,\varepsilon^3}{G_o^2\,L(1-\varepsilon)}$	88.9	24.3	3.2	1.9	1.5
% uncertainty $\frac{G_o D_p}{(1-\varepsilon)}$	1.6	1.6	2.1	2.1	2.2
% uncertainty $\frac{\bar{\rho}\Delta P D_p\varepsilon^3}{G_o^2\,L(1-\varepsilon)}$	9.7	4.2	5.3	5.4	5.5

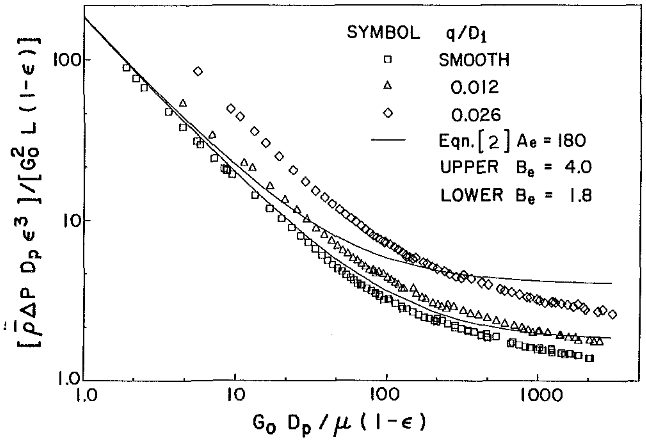

Fig. 5 Comparison of experimental data with Ergun's equation

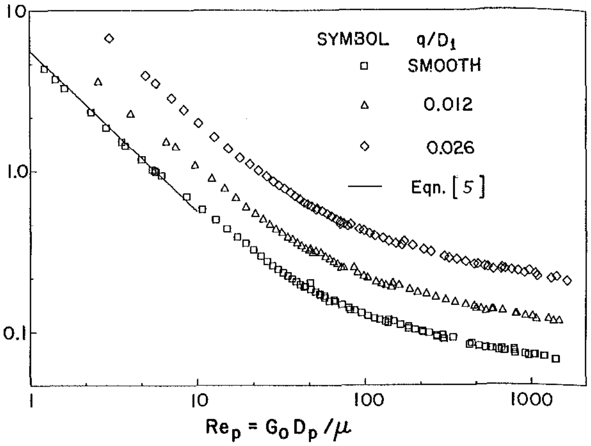

Fig. 6 Comparison of experimental data with equation (5)

Table 2 Measured and calculated properties of the packed beds

D_p (cm)	ε	q/D_i	A_e	B_e
0.503	0.356	"Smooth"	166.1	1.50
0.539	0.442	0.012	230.4	1.93
0.592	0.467	0.026	447.0	2.64
Ergun equation		Ref [5]	150	1.75
Modified Ergun equation [Ref 3]		"Smooth"	180	1.8
Modified Ergun equation [Ref 3]		"Rough"	180	4.0

how quickly the flow becomes fully developed at least as far as the pressure drop is concerned and justifies the use of a 30.5 cm long test section for the rough spheres.

Porosity of each of the packings was calculated from three measurements. The weight of spheres loaded into the test section, the volume of the test section, and the density of the spheres. The latter parameter was obtained by measuring the volume displacement of water by a known weight of the particles. This method resulted in an estimated uncertainty for the porosity calculation of less than 3.5 percent. The porosity for the smooth spheres was 35.6 percent. The bed of .012 relative roughness spheres packed to a porosity of 42.2 percent while the roughest spheres packed to a porosity of 46.7 percent.

Table 1 contains the results of an uncertainty analysis for those parameters in equation (2) which are calculated from the experimental data. These estimates of uncertainty were calculated using the method proposed by Kline and McClintock [12]. At low Reynolds numbers the greatest contribution to the uncertainty was measurement of the small pressure differentials across the bed. At high Reynolds number the measurement of the air flow rate dominated the uncertainty.

Results and Discussion

Figure 5 is a plot of the data in terms of a modified friction factor and Reynolds number consistent with the Ergun equation. Table 2 contains the values of the coefficients of Ergun's equation determined for the data from a least squares curve fit routine. The viscous coefficient A_e increased substantially due to the surface roughness, displaying a 169 percent increase for the roughest spheres when compared to the value for the smooth spheres of this study.

As indicated earlier, the porosity of the beds of roughened spheres was significantly greater than that for the smooth spheres. Therefore, an error in the porosity dependence of Ergun's equation could account for some of the upward shift in the rough bed data shown in Fig. 5. If the porosity dependence of Ergun's equation is modified as suggested by Rumpf and Gupte for the viscous dominated regime the following equation results:

$$\frac{\rho\Delta P D_p \epsilon^{5.5}}{G_0^2 L} = \frac{5.6\mu}{G_0 D_p} + \frac{B}{(1-\epsilon)} \tag{5}$$

Figure 6 plots the experimental data according to equation (5). Again the data for the beds of rough spheres display a substantial deviation from the smooth sphere result in the viscous region and equation (5) appears to offer little improvement over the original correlation. These results indicate than an equation obtained from a direct analogy to flow in rough pipes is inadequate in characterizing the flow through porous beds of rough packing materials. The demonstrated effect of roughness is different for the two flows, possibly due to the large change in surface area caused by the roughness. One would expect roughness to effect the wetted surface area in a packed bed by much more than that in a conduit.

The mean diameters of the spheres were changed very little by the addition of the roughness elements, however, the surface area was increased substantially. This suggests that a correlation like equation (4) which includes a specific surface area as a parameter may be necessary to correlate the low Reynolds

Table 3 Drag coefficient data of the spheres

q/D_i	Re_p	C_d
Smooth	1.72	11.97
0.012	1.81	12.94
0.026	2.03	13.39

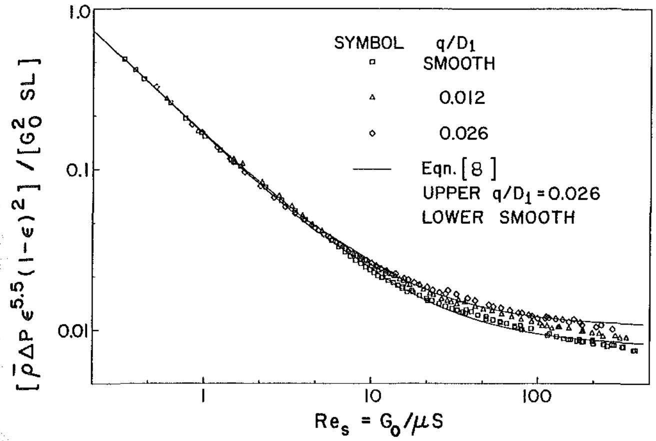

Fig. 7 Comparison of experimental data with equation (8) using characteristic length calculated from equation (6)

number data. Substituting equation (3) into equation (5) allows for the determination of what will be termed the "effective" surface area per unit bed volume from the experimental data in the viscous dominated flow regime.

$$S^2 = \frac{36\bar{\rho}\Delta P(1-\epsilon)^2\epsilon^{5.5}}{5.6G_0L\mu} \tag{6}$$

Using the Carmen-Kozeny relation for permeability it is easily seen that S is inversely proportional to the square root of the permeability. Ward [13], Beavers, Sparrow and Rodenz [9], and others have proposed this as the proper characteristic length to be used in the definitions of the friction factor and Reynolds number for flow through permeable material. The data of this study reduced by using the calculated "effective" suface area per unit bed volume are presented in Fig. 7. This method of calculating S ensures that the three data sets converge to a single curve for low values of the Reynolds number based on S. Figure 7 also emphasizes that surface roughness has a different effect in the inertial dominated regime of flow than it does in the viscous regime. Using equation (4) as an example of correlation for B in terms of the relative roughness was determined from the experimental data.

$$B = B_0 + C_2(q/D_1)^n \tag{7}$$

Here, B_0 is taken as a universal constant with a value of 0.0471 obtained from the smooth sphere data. For the data of this study C_2 was found to have a value of 0.5825 and n a value of 0.992. Thus, for both smooth and rough particles of spherical shape the following correlation resulted:

$$\frac{\bar{\rho}\Delta P\epsilon^{5.5}(1-\epsilon)^2}{G_0^2 SL} = \frac{5.6\mu S}{36G_0} + \frac{0.0471}{6} + \frac{0.5825}{6}(q/D_1)^{0.992} \tag{8}$$

Equation (8) for relative roughness values of zero and 0.026 is compared to the experimental data in Fig. 7.

The above discussion has indicated that models developed using analogies with turbulent flow in conduits do not adequately describe the effect of roughness on flow in packed beds. The other approach which was alluded to earlier is to consider the packed bed to be a collection of discrete submerged particles. This second type of analogy was explored very superficially by measuring the drag coefficients of the three particles used in the study. Table III lists drag coefficients determined for single particles using terminal velocity measurements. The measurements were taken close to the Stokes flow regime so that an analogy could be drawn with the viscous dominated regime of the packed beds. The results do indicate an increase in drag coefficient with surface roughness. However, the increase in drag coefficient is much smaller than the measured increase in the friction factor for flow through packed beds of the same spheres.

Conclusions

The data of this experimental study indicates that surface roughness can have a substantial effect on the resistance of fluid flow through packed beds of spherical particles. Specifically both the viscous dominated and inertial dominated regimes of flow are affected. Therefore a direct analogy to rough pipe flow in prediction of the effect of surface roughness in packed beds is not possible. Based on the experimental measurements of this study an equation is proposed that adequately describes the flow through beds of rough and smooth particles provided the effective surface area per unit bed volume is used as the characteristic length. This parameter must be obtained from low Reynolds number permeability measurements. The result has some limitations due to the fact that only two values of the relative roughness parameter were studied.

References

1 Bear, J., *Dynamics of Fluids* in Porous Media, Elsevier, New York, 1972.

2 Forchheimer, P., "Wasserbewegung durch Boden," *Forschtlft Ver. D. Ing.*, Vol. 45, 1901, pp. 1782–1788.

3 MacDonald, I. F., et al., "Flow Through Porous Media–The Ergun Equation Revisited," *I & EC Fund.*, Vol. 18, No. 3, 1979, pp. 199–208.

4 Brownell, L. E., and Katz, D. L., "Flow of Fluids through Porous Media," *Chemical Engineering Progress*, Vol. 43, No. 10, 1947, pp. 537–548.

5 Ergun, S., "Fluid Flow through Packed Columns," *Chemical Engineering Progress*, Vol. 43, No. 2, 1952, pp. 89–94.

6 Bird, R. B., Stewart, W. E., and Lightfoot, E. N., *Transport Phenomena*, Wiley, New York, 1960.

7 Rumpf, H., and Gupte, A. R., "Einflusse der Porositat und KorngroBenverteilung im Widerstandsgesetz der Porenstromun," *Chemie Ingenieur Technik*, Vol. 43 No. 6, 1971, pp. 367–375.

8 Meyer, B. A., and Smith, D. W., "Flow Through Porous Media: Comparison of Consolidated and Unconsolidated Materials," SAND 83-8788, Sandia National Laboratories, Livermore, Ca., 1983.

9 Beavers, G. S., Sparrow, E. M., and Rodenz, D. E., "Influence of Bed Size on the Flow Characteristics and Porosity of Randomly Packed Beds of Spheres," ASME *Journal of Applied Mechanics*, Vol. 40, 1973, pp. 655–660.

10 Crawford, C. W., "Surface Roughness and its Influence on Resistance to Flow Through Packed Beds," MS Project Report, Department of Mechanical Engineering, Washington State University, Pullman, Wa., 1984.

11 Clift, R., Grace, J. R., and Weber, W. E., *Bubbles, Drops, and Particles*, Academic Press, New York, 1978.

12 Kline, S. J. and McClintock, F. A., "Describing Uncertainties in Single-Sample Experiments," *Mechanical Engineering*, 1953, p. 3.

13 Ward, J. C., "Turbulent Flow in Porous Media," *J. Hydr. Div. Proc. of the ASCE*, 90:HY5, 1964, pp. 1-12.

A. Hamed
Department of Aerospace Engineering
and Engineering Mechanics,
University of Cincinnati,
Cincinnati, Ohio 45221

S. Abdallah
Applied Research Laboratory,
Pennsylvania State University,
State College, Pa. 16801

Internal Three-Dimensional Viscous Flow Solution Using the Streamlike Function

This paper presents a new method for the three-dimensional elliptic solution of the Navier-Stokes equations. It is based on the streamlike-function vorticity formulation which was developed by the authors to study the development of secondary velocities and streamwise vorticity for inviscid flows in curved ducts. This formulation is generalized for viscous flows and used to predict the development of internal three dimensional flow fields. The computed results are presented and compared with experimental measurements for the three-dimensional viscous flow in a straight duct.

Introduction

A large number of numerical methods have been developed over the years for the solution of internal viscous flow fields. The earliest solutions [1-3] were obtained for the parabolized Navier-Stokes equations. Several successful implicit iterative solution procedures [4-8] have since been developed for the numerical solution of the parabolized Navier-Stokes equations in primitive variables for incompressible [8], compressible [4-7], supersonic [4], laminar [4, 5, 8] and turbulent [6, 7] internal flows. The only elliptic influence which is accounted for in the parabolized solution is that due to the potential pressure field. Partially parabolized solution procedures [5-7] were subsequently developed for the numerical solution of viscous flow fields in which pressure is the dominant transmitter of influences in the upstream direction [5]. These flows are still characterized by the absence of recirculation in the primary flow direction and by high Reynolds number, so that the viscous diffusion and thermal conduction are significant only in the lateral direction. The solution procedure remains unchanged for the main and lateral momentum equations, but the pressure correction equation at each marching step contains terms that link the pressure correction in a given lateral plane to upstream and downstream pressure corrections. In both methods, the velocity components are obtained from the momentum equations, and the continuity equation is only satisfied indirectly by the pressure field. This indirect approach to satisfying the continuity equation is common to all parabolized [1-4] and partially parabolized [5-7] methods.

The full Navier-Stokes equations are required to model flows with significant separation or shear layers not aligned with one of the coordinates. In addition, the parabolized and partially parabolized methods are not suitable for obtaining solutions to flow fields in which viscous phenomena significantly affect pressure distribution. Several methods have been developed for the solution of the time dependent form the governing equations [8-10]. These methods can be very expensive, when used in the solution of viscous three dimensional flow fields [10], but have been demonstrated to predict complex three dimensional phenomena such as the horseshoe vortex in turbine blade passages. The numerical solution to the full steady state Navier-Stokes equations in primitive variables was reported in reference [11] for natural convection and reference [12] for laminar flow in curved ducts. The results of the through flow computations [12] were shown to be dependent on the difference scheme for the continuity equation, especially in the prediction of the secondary flow development. The numerical solution fluttered on the inside of the bend, suffered a loss of mass and failed to fully converge [11], and the author suggested that more attention to the nonlinearities of the flow may possibly alleviate the last two problems. Other methods developed for the elliptic solutions of the steady state full Navier-Stokes equations are based on the extension of the well-known 2-D stream function vorticity formulation to three dimensions [13, 14]. Aziz and Hellums [13] defined a vector potential to identically satisfy the equation of conservation of mass in three dimensional flow fields. The vector potential vorticity formulation has been used to solve the problem of laminar natural convection [13, 14]. In this formulation, the resulting governing equations consist of three 3-D Poisson equations for the vector potential and three vorticity transport equations. The main advantage of this formulation, in two dimensions, namely the smaller size of the governing equations is actually reversed in three dimensions, since three-dimensional differential equations have to be solved for the three components of the vector potential.

One can conclude from the preceding discussions that existing space-elliptic solvers of the 3-D Navier-Stokes equations are very costly in terms of CPU time and storage requirements. In addition, some of these methods which were developed for simple convection problems have not been very successful in through flow calculations. The presented work

---

Contributed by the Fluids Engineering Division for publication in the JOURNAL OF FLUIDS ENGINEERING. Manuscript received by the Fluids Engineering Division, November 19, 1984.

represents a new formulation for the 3-D Navier-Stokes equations that leads to an elliptic solution. The formulation is based on the use of the 2-D streamlike functions [15] to identically satisfy the equation of conservation of mass for 3-D rotational flows [16, 17]. The governing equations consist of the vorticity transport equation and 2-D Poisson equations for the streamlike functions. The present method is very general, in that inviscid flow solutions can be obtained in the limit when Re → ∞. In fact, numerical solutions have been obtained for inviscid rotational incompressible [16] and compressible [17] flows in curved ducts and it was demonstrated that the method can predict significant secondary flow and streamwise vorticity development due to inlet vorticity. The following work represents the generalization of this formulation to internal three-dimensional viscous flow problems.

Analysis

The governing equations consist of the vorticity transport equation and the equation of conservation of mass, which are written in the following dimensionless form, for incompressible viscous flow:

$$(\bar{V}\cdot\nabla)\bar{\Omega}=(\bar{\Omega}\cdot\nabla)\bar{V}-\frac{1}{\mathrm{Re}}\nabla^2\bar{\Omega} \tag{1}$$

and

$$\nabla\cdot\bar{V}=0 \tag{2}$$

In the above equations $\mathrm{Re} = V^*D/\nu$ when the velocities are normalized by V^*, the space dimensions by D and the vorticity by V^*/D.

The solution to the three dimensional viscous flow is obtained in terms of the three vorticity components and three streamlike functions [15] which are defined to identically satisfy the equation of conservation of mass for general three-dimensional rotational flow fields. Unlike the traditional stream function solutions which must be obtained on stream surfaces, the following streamlike function velocity relations permit the definitions of these two dimensional functions $\chi_1(x, y)$, $\chi_2(y, z)$, $\chi_3(x, z)$ on fixed non-stream surfaces in the flow field.

Streamlike Functions Velocity Relations. The streamlike function formulation was developed by the authors [15] to model internal three dimensional flow fields [16]. More details and general definitions in curvilinear coordinates of the streamlike function can be found in reference [17]. For the sake of simplicity, the equations will be presented here for incompressible flow using Cartesian coordinates.

Definition of χ_1

$$\frac{\partial\chi_1}{\partial y}=u_1+\int_{x_0}^{x}\frac{\partial w_2}{\partial z}\,dx, \tag{3a}$$

$$\frac{\partial\chi_1}{\partial x}=-v_1 \tag{3b}$$

Definition of χ_2

$$\frac{\partial\chi_2}{\partial y}=-w_2-\int_{z_0}^{x}\frac{\partial u_1}{\partial z}\,dz, \tag{4a}$$

$$\frac{\partial\chi_2}{\partial z}=v_2 \tag{4b}$$

Definition of χ_3

$$\frac{\partial\chi_3}{\partial z}=-u_3-\int_{x_0}^{x}\frac{\partial w_2}{\partial z}\,dx, \tag{5a}$$

$$\frac{\partial\chi_3}{\partial x}=w_3-\int_{z_0}^{z}\frac{\partial u_1}{\partial x}\,dz\ \pi \tag{5b}$$

where the flow velocity components u, v, and w in the x, y, and z directions are given by:

$$u=u_1+u_3,\quad v=v_1+v_2\quad\text{and}\quad w=w_2+w_3 \tag{6}$$

It can be easily verified that equations (3)-(6) satisfy the equation of conservation of mass identically. One can see from the definition of the streamlike functions (equations (3-5)) that they contain integral terms of the gradient of the flux due to the velocity components from the other streamlike functions. The lower limit of these integrals can be chosen arbitrarily to simplify the boundary conditions, in the case of complex boundary configurations as was demonstrated by the authors in [15].

It is important to point out that the streamlike function definitions in equations (3), (4), and (5) on the fixed surfaces reduce to the classical two dimensional stream function definitions only if the surfaces coincide with the stream surfaces since the integrands become zero in this case. Generally, however, the integral terms in the streamlike function definitions are not zero if the equation of conservation of mass is to be satisfied for three dimensional flow. The presence of the integral terms, representing the normal derivative of the velocity component perpendicular to the surface, can be interpreted as a source or sink. Consequently, the contours representing constant values of the streamlike functions are not streamlines. In fact, the streamlike contours can intersect the solid boundaries [15] and the no flux condition is satisfied. Also the presence of loops in the streamlike contours do not necessarily indicate recirculating flow.

While equations (2), (4), and (5) are given in Cartesian coordinates, the present method is generally valid for both orthogonal and nonorthogonal coordinates. The equation of conservation of mass, can be written as follows:

$$\frac{\partial}{\partial\eta}\left(\frac{U}{\mathrm{J}}\right)+\frac{\partial}{\partial\xi}\left(\frac{V}{\mathrm{J}}\right)+\frac{\partial}{\partial\zeta}\left(\frac{W}{\mathrm{J}}\right)=0$$

where (U, V, W) are the contravariant velocity components in the direction of the coordinates (η, ξ, ζ) and J is the Jacobian. Subsequently, the streamlike function definitions easily follow the outlined steps.

Governing Equations. The governing equations consist of the vorticity transport equations and the differential equations for the streamlike functions. The vorticity transport equations in cartesian coordinates are given by:

$$\bar{V}\cdot\nabla\eta=\bar{\Omega}\cdot\nabla u+\frac{1}{\mathrm{Re}}\nabla^2\eta \tag{7}$$

$$\bar{V}\cdot\nabla\xi=\bar{\Omega}\cdot\nabla v+\frac{1}{\mathrm{Re}}\nabla^2\xi \tag{8}$$

Nomenclature

D = duct height
L = duct length
Re = Reynolds number
t = time
u,v,w = velocity components in x, y, and z directions

$\bar{V}$ = velocity vector
V^* = normalizing velocity at inlet
x,y,z = Cartesian coordinates
χ_1,χ_2,χ_3 = streamlike functions

ν = kinematic viscosity
$\bar{\Omega}$ = vorticity vector
η,ξ,ζ = vorticity components in x, y, and z directions

$$\bar{V}\cdot\nabla\zeta=\bar{\Omega}\cdot\nabla w+\frac{1}{\mathrm{Re}}\nabla^2\zeta \tag{9}$$

where η, ξ, ζ are the components of the vorticity vector, $\bar{\Omega}$, in the x, y, and z directions, respectively. The differential equations for the streamlike functions are obtained from the substitution of equations (3)-(5) into the following vorticity velocity relations:

$$\eta=\frac{\partial w}{\partial y}-\frac{\partial v}{\partial z} \tag{10}$$

$$\xi=\frac{\partial u}{\partial z}-\frac{\partial w}{\partial x} \tag{11}$$

$$\zeta=\frac{\partial v}{\partial x}-\frac{\partial u}{\partial y} \tag{12}$$

This results in the following two dimensional Poissons equations:

$$\frac{\partial^2\chi_1}{\partial x^2}+\frac{\partial^2\chi_1}{\partial y^2}=\zeta^*-\zeta+\frac{\partial}{\partial y}\int_{x_0}^{x}\frac{\partial w_2}{\partial z}\,dx \tag{13}$$

$$\frac{\partial^2\chi_2}{\partial z^2}+\frac{\partial^2\chi_2}{\partial y^2}=\eta^*-\eta+\frac{\partial}{\partial y}\int_{z_0}^{z}\frac{\partial u_2}{\partial x}\,dx \tag{14}$$

$$\frac{\partial^2\chi_3}{\partial x^2}+\frac{\partial^2\chi_3}{\partial z^2}=\xi^*-\xi+\frac{\partial}{\partial z}\int_{x_0}^{x}\frac{\partial w_2}{\partial z}\,dx$$

$$-\frac{\partial}{\partial x}\int_{z_0}^{z}\frac{\partial u_1}{\partial x}\,dz \tag{15}$$

where

$$\eta^*=\frac{\partial w_3}{\partial y}-\frac{\partial v_1}{\partial z} \tag{16}$$

$$\xi^*=\frac{\partial u_1}{\partial z}-\frac{\partial w_2}{\partial x} \tag{17}$$

$$\zeta^*=\frac{\partial v_2}{\partial x}-\frac{\partial u_3}{\partial y} \tag{18}$$

The governing equations (7)-(9) and (13)-(15) are solved for the vorticity components η, ξ, ζ and the streamlike functions χ_1, χ_2, and χ_3, respectively. The present elliptic formulation leads to three dimensional elliptic equations for the three vorticity components and two dimensional elliptic equations for the three streamlike functions. Other elliptic methods [18], whether they are based on the vector potential-vorticity or the velocity-vorticity formulations lead to three dimensional elliptic equations for all of the six dependent variables and hence require more computer time and storage. The boundary conditions used for the solution of these equations are given for the viscous flow in a square duct. Because of symmetry, only one quarter of the square duct is considered in the following derivations. The coordinate y along the straight duct is measured from the duct entrance, while x and z represent the coordinates in the cross sectional planes measured from the duct centerline as shown in Fig. 1.

Boundary Conditions. At the inlet station which extends far upstream of the duct entrance, the flow velocity is taken to be uniform ($v = v_I$, $u = w = 0$), leading to the following boundary conditions:

$$\eta=\zeta=\xi=0$$

and

$$\frac{\partial\chi_1}{\partial y}=\frac{\partial\chi_2}{\partial y}=0.$$

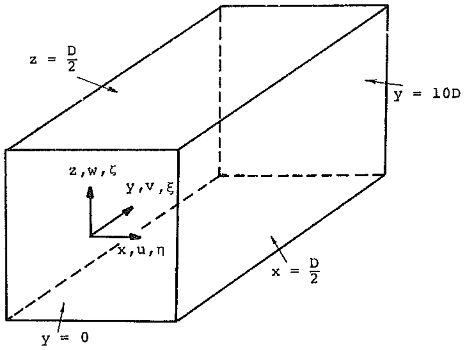

Fig. 1 Coordinate system in the duct

At the duct boundaries, the no slip condition is used to obtain the boundary conditions for the vorticity components, while the zero flux condition is used to obtain the boundary conditions for the streamlike functions.

The streamlike function boundary conditions are simplified through the appropriate choice of the reference coordinates x_0, z_0 in the lower limit of the integrals in equations (3)-(5). The following boundary conditions result when $x_0 = z_0 = 0$.

At $x = \dfrac{1}{2}$,

$$\eta=0$$

$$\xi=-\frac{\partial w}{\partial x},$$

$$\zeta=\frac{\partial v}{\partial x}$$

$$\chi_1=-\int_{x=0}^{x=1/2}V^*dx$$

and

$$\chi_3=0.$$

At $z = \dfrac{1}{2}$

$$\eta=-\frac{\partial v}{\partial z},$$

$$\xi=\frac{\partial u}{\partial \zeta}\pi$$

$$\zeta=0$$

$$\chi_2=\int_{z=0}^{z=1/2}V^*dz,$$

and

$$\chi_3=0.$$

The rest of the boundary conditions are due to symmetry at the planes $x = 0$ and $z = 0$.

At $x = 0$

$$\frac{\partial\eta}{\partial x}=0,$$

$$\xi=\zeta=0$$

and

$$\chi_1=\chi_3=0.$$

At $z = 0$

$$\eta=\xi=0$$

$$\frac{\partial\zeta}{\partial z}=0$$

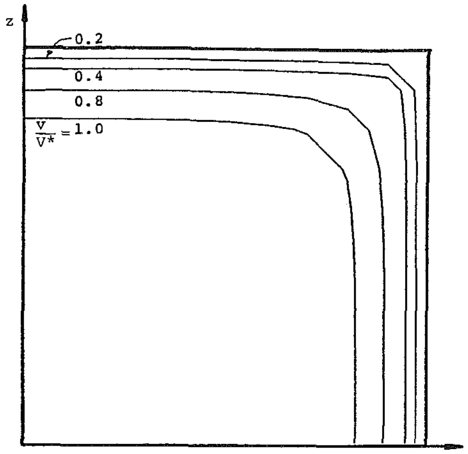

Fig. 2 Through flow velocity contours at the duct inlet ($Y/D\mathrm{Re}$ = 0.00)

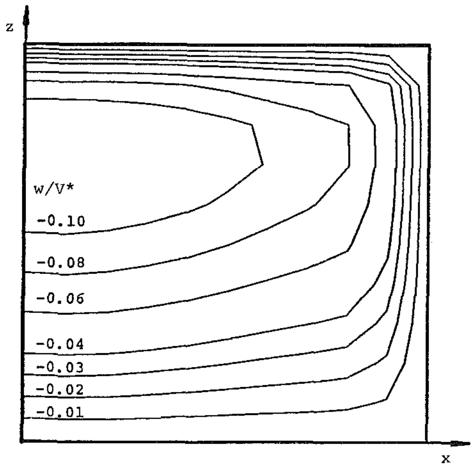

Fig. 3 Secondary velocity contours at the duct inlet ($y/D\mathrm{Re}$ = 0.00)

and

$$\chi_2 = \chi_3 = 0.$$

Fully developed flow conditions are applied at the duct exit.

$$\frac{\partial \eta}{\partial y} = \frac{\partial \zeta}{\partial y} = 0$$

$$\xi = 0$$

and

$$\frac{\partial \chi_1}{\partial y} = \frac{\partial \chi_2}{\partial y} = 0.$$

Results and Discussion

The elliptic system of equations are solved using an iterative procedure. At each global iteration, the linear equations were solved by successive over-relaxation method. The numerical results are presented for Re = 100 based on the inlet velocity, V^*, and the square duct width, D. Fully developed flow conditions were reported by Friedmann et al. [19] at $L/D\mathrm{Re}$ = 0.113 − 0.112 for Reynolds number ranging between 100 and 500. Based on this, numerical computations in a straight duct with $L/D\mathrm{Re} = 0.1$ were performed using a uniform grid with $\Delta x/D\mathrm{Re} = \Delta z/D\mathrm{Re} = 0.001$ and $\Delta y/D\mathrm{Re} = 0.0033$. Due to symmetry, the computations were only carried out in one quarter of the duct for χ_1, χ_3, ζ, and ξ since $\zeta(x, y, z) = -\eta(z, y, x)$ and $\chi_1(x, y) = -\chi_2(z, y)$. Relaxation parameters of 1.6 for χ_1, 1.9 for χ_3 and 0.4 for ζ and ξ were used in the inner iterations with a convergence criteria of $\epsilon_\zeta = 1 \times 10^{-4}$, $\epsilon_\xi = 1 \times 10^{-5}$, $\epsilon_{\chi_1} = 1 \times 10^{-5}$, $\epsilon_{\chi_3} = 5 \times 10^{-6}$ according to the following equation:

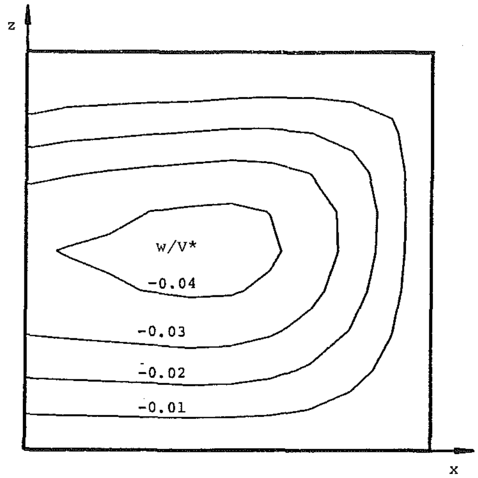

Fig. 4 Secondary velocity contours at $y/D\mathrm{Re}$ = 0.01

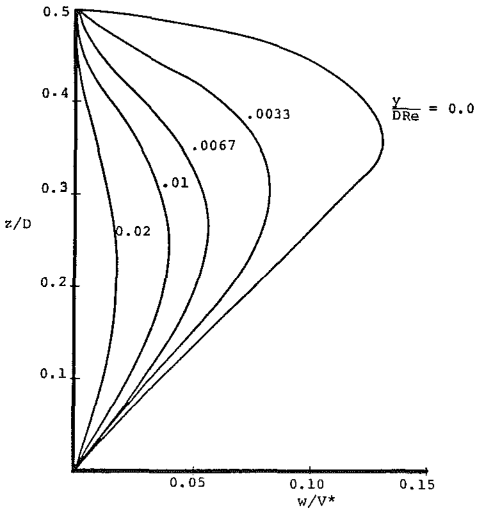

Fig. 5 The development of secondary flow velocity profile at the central plane, x = 0.0

$$\frac{1}{N}\sum_{1}^{N}(|\omega_{i,j}^{m+1} - \omega_{i,j}^{m}|) \le \epsilon_\omega.$$

The numerical solutions required 50 global iterations and a CPU time of 2 minutes and 13 seconds on AMDAHL 370 using an 11 × 11 × 14 uniform grid. The overall number of iterations was 357 for the vorticity equations and 179 for the streamlike function equations. The numerical solution domain extended 1.67 diameters upstream of the duct inlet, where the flow velocity was taken to be uniform and equal to one. The results of the numerical computations are presented at $y/D\mathrm{Re}$ = 0, 0.01 and 0.10. The through flow contours at the duct inlet are presented in Fig. 2. The flow development from a uniform through velocity to the profile of Fig. 2 at the duct inlet is accompanied by lateral flow displacements due to the secondary velocities. The secondary velocity contours at the duct inlet are shown in Fig. 3 for the vertical velocity component w. The ellipticity of the numerical solution is demonstrated in the velocity contours at the duct inlet, and in the velocity fields up to 0.83 diameters upstream of the duct inlet. Figure 4 shows the contours for the secondary velocity component, w, at $y/D\mathrm{Re}$ = 0.01. A comparison of Figs. 3 and 4 reveals the change in both the magnitude and the location of the maximum secondary velocities along the duct. The

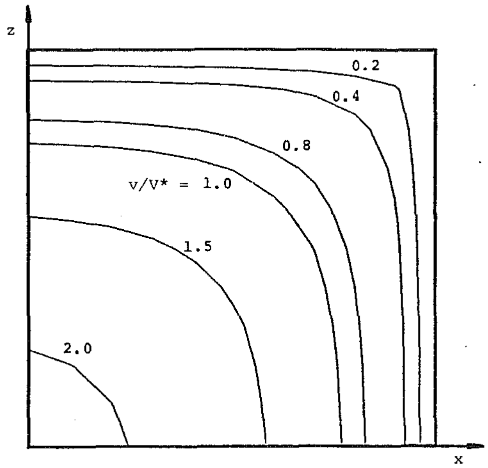

Fig. 6 Through flow velocity contours at $y/D\mathrm{Re} = 0.1$

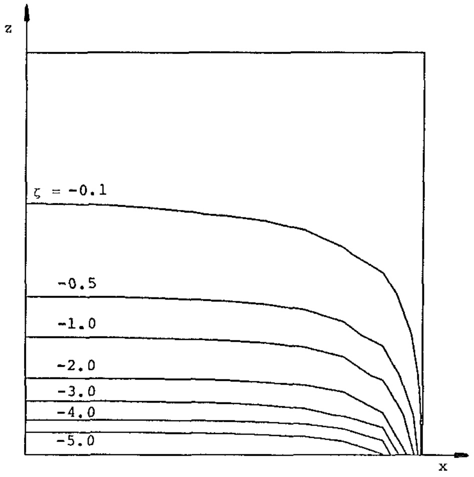

Fig. 7 Vorticity, ζ contours at the duct entrance ($y/D\mathrm{Re} = 0.0$)

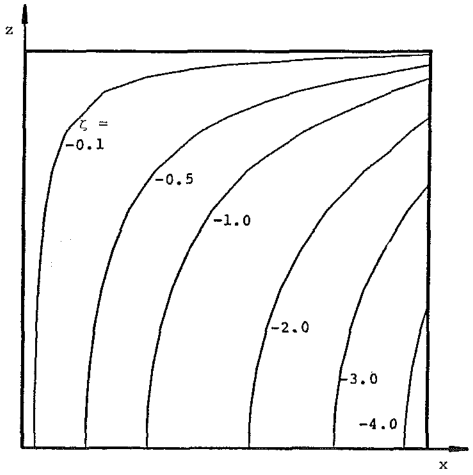

Fig. 8 Vorticity, ζ contours at $y/D\mathrm{Re} = 0.1$

development of the secondary velocity component, w, along the plane of symmetry, $x = 0$, is presented in Fig. 5. One can see that the maximum secondary velocities are found near the solid boundaries at the duct inlet. As the flow proceeds towards fully developed conditions, the secondary velocities decrease and the location of the maximum values moves toward the center of the duct. The results of the numerical computations at the duct exit are shown in Fig. 6 for the through flow velocity contours.

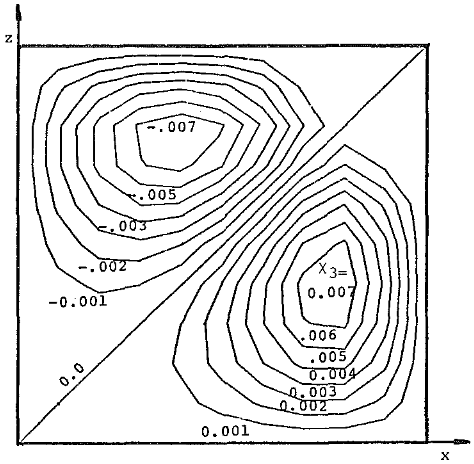

Fig. 9 Streamlike function, χ_3 contours at the duct inlet ($y/D\mathrm{Re} = 0.0$)

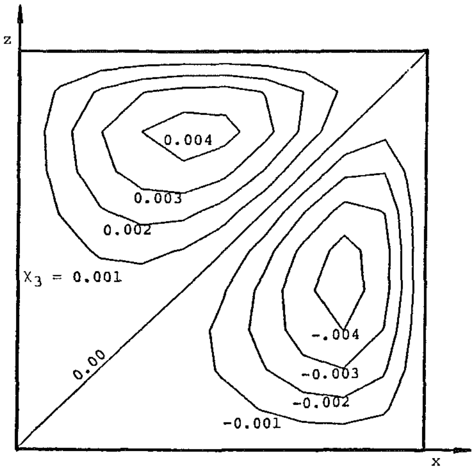

Fig. 10 Streamlike function, χ_3 contours at $y/D\mathrm{Re} = 0.01$

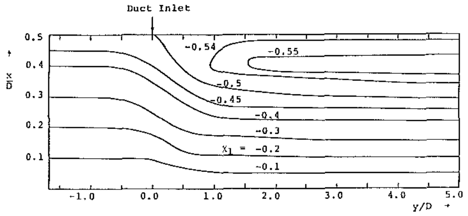

Fig. 11 Streamlike function, χ_1 contours at $z = 0$

The vorticity and streamlike function contours are shown in Figs. 7 through 11. The contours for the vorticity component ζ are shown at $y/D\mathrm{Re} = 0.0$ and 0.1 in Figs. 7 and 8. Figures 9 and 10 show the contours of the streamlike function χ_3 at $y/D\mathrm{Re} = 0.0$ and 0.01. The figures show a change in the sign of the streamlike function between these two sections. The contours for the streamlike function χ_1 at $z/D\mathrm{Re} = 0.0$ are shown in Fig. 11. One can see that χ_1 reaches values less than -0.5 inside the duct near the walls.

The computed through flow velocity profile along the plane of symmetry, $x = 0$, are compared with the experimental measurements of reference [20] in Fig. 12. One can see that the computed results are in good agreement with the experimental measurements. The computed through flow velocity develop-

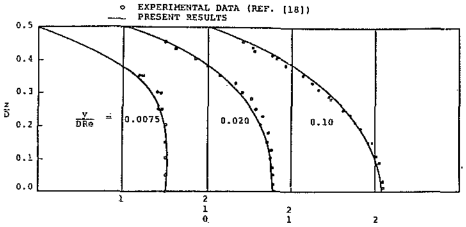

Fig. 12 Development of the through flow velocity profile at the central plane $x = 0$. $v/V^* \rightarrow$

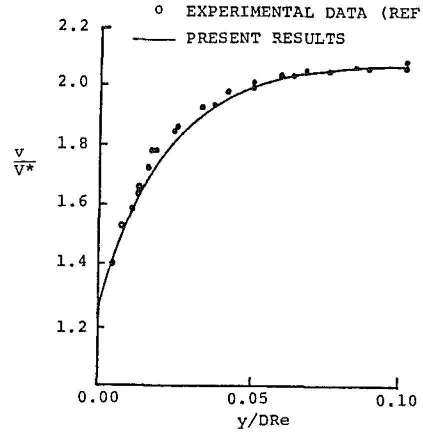

Fig. 13 Through flow velocity development along the duct centerline

ment along the duct centerline are compared with the experimental measurements of reference [20] in Fig. 13. The agreement between the computed results and the experimental data as shown in Figs. 12 and 13 is very satisfactory, in view of the uniform coarse grid used in the numerical calculations.

Conclusions

This paper presents a new method for the three-dimensional elliptic solution of the Navier-Stokes equations which is based on the streamlike-function vorticity formulation. The computed results for the three-dimensional viscous flow in a square duct are presented and compared with experimental measurements. The results demonstrate that the streamlike function can successfully model viscous effects in the three dimensional flow field computations. Since the same formulation has been successfully used in inviscid rotational flows, to model secondary flow development due to inlet shear velocity under the effect of curvature, one can conclude that the present method can be effectively developed to obtain efficient numerical elliptic solutions of internal viscous flow in curved passages.

Acknowledgment

This work was sponsored by U.S. Air Force Office of Scientific Research under Contract No. 80-0242.

The authors wish to express their appreciation to Mr. M. Mansour for his help in performing the numerical computations.

References

1 Patankar, S. V., and Spalding, D. B., "A Calculation Procedure for Heat, Mass and Momentum Transfer in Three-Dimensional Parabolic Flows," *Int. Journal of Heat and Mass Transfer*, Vol. 15, 1972, p. 1787.

2 Caretto, L. S., Curr, R. M., and Spalding, D. B., "Two Numerical Methods for Three-Dimensional Boundary Layers," *Computer Methods in Applied Mechanics and Engineering*, Vol. 1, 1973, p. 39.

3 Briley, W. R., "Numerical Method for Predicting Three-Dimensional Steady Viscous Flow in Ducts," *Journal of Computational Physics*, Vol. 14, 1974, pp. 8-28.

4 Buggeln, R. C., McDonald, H., Kreskovsky, J. P., and Levy, R., "Computation of Three-Dimensional Viscous Supersonic Flow in Inlets," AIAA Paper No. 80-0194, 1980.

5 Pratap, V. S., and Spalding, D. B., "Fluid Flow and Heat Transfer in Three Dimensional Duct Flows," *International Journal of Heat and Mass Transfer*, Vol. 19, 1976, pp. 1183-1188.

6 Roberts, D. W., and Forester, C. K., "A Parabolic Computational Procedure for Three-Dimensional Flows in Ducts with Arbitrary Cross-Sections," AIAA Paper No. 78-143, 1978.

7 Moore, J., and Moore, J. G., "A Calculation Procedure for Three-Dimensional Viscous, Compressible Duct Flow. Part II – Stagnation Pressure Losses in a Rectangular Elbow," ASME JOURNAL OF FLUIDS ENGINEERING, Vol. 101, Dec. 1979, pp. 423-428.

8 Briley, W. R., and McDonald, H., "Solution of the Multi-Dimensional Compressible Navier-Stokes Equations by a Generalized Method," *Journal of Computational Physics*, Vol. 24, 1977, p. 372.

9 Beam, R. M., and Warming, R. F., "An Implicit Factored Scheme for the Compressible Navier-Stokes Equations," *AIAA Journal*, Vol. 16, 1978, p. 393.

10 Hah, C., "A Navier-Stokes Analysis of Three-Dimensional Turbulent Flows Inside Turbine Blade Rows at Design and Off-Design Conditions," ASME Paper No. 83-GT-40, 1983.

11 Williams, G. P., "Numerical Integration of the Three-Dimensional Navier-Stokes Equations for Incompressible Flow," *Journal of Fluid Mechanics*, Vol. 37, Part 4, 1969, pp. 227-250.

12 Roscoe, D. F., "The Numerical Solution of the Navier-Stokes Equations for a Three-Dimensional Laminar Flow in Curved Pipes Using Finite Difference Methods," *Journal of Engineering Mathematics*, Vol. 12, No. 4, Oct. 1978, pp. 303-323.

13 Aziz, A., and Hellums, J. D., "Numerical Solution of the Three-Dimensional Equations of Motion for Laminar Natural Convection," *The Physics of Fluids*, Vol. 10, No. 2, 1967, pp. 314-324.

14 Mallinson, G. D., and Davis, G. DeVahl, "Three-Dimensional Natural Convection in a Box. A Numerical Study," *Journal of Fluid Mechanics*, Vol. 83, Part 1, 1977, pp. 1-31.

15 Hamed, A., and Abdallah, S., "Streamlike Function: A New Concept in Flow Problems Formulation," *Journal of Aircraft*, Vol. 16, No. 12, Dec. 1979, pp. 801-802.

16 Abdallah, S., and Hamed, A., "The Elliptic Solution of the Secondary Flow Problem," ASME *Journal of Engineering for Power*, Vol. 105, No. 3, 1983, pp. 530-535.

17 Hamed, A., and Liu, C., "Three Dimensional Rotational Compressible Flow Solution in Variable Area Channels," AIAA Paper No. 83-0259, 1983.

18 Roache, P. J., *Computational Fluid Dynamics*, Hermosa Publishers, 1976.

19 Friedmann, M., Gillis, J., and Liren, N., "Laminar Flow in a Pipe at Low and Moderate Reynolds Numbers," *Appl. Sci. Res.*, Vol. 19, No. 6, 1968, pp. 426-438.

20 Goldstein, R. J., and Kried, D. K., "Measurement of Laminar Flow Development in a Square Duct Using a Laser-Doppler Flow Meter," *Journal of Applied Mechanics*, Dec. 1967, pp. 813-818.

I. Elperin

O. Igra

G. Ben-Dor

The Pearlstone Center for Aeronautical
Engineering Studies,
Department of Mechanical Engineering,
Ben-Gurion University of the Negev,
Beer Sheva, Israel

Analysis of Normal Shock Waves in a Carbon Particle-Laden Oxygen Gas

The propagation of a normal shock wave into a quiescent oxygen gas seeded with carbon particles is studied. Due to the elevated postshock temperature the carbon particles ignite and burn until they disappear. For evaluating the effect of the burning carbon particles on the postshock-wave flow field, i.e., the relaxation zone, the conservation equations for a steady one-dimensional reactive suspension flow are formulated and solved numerically. The solution was repeated for a similar inert suspension flow. Comparing the two solutions revealed that the carbon burning has a major effect on the suspension properties in the relaxation zone and on the eventually reached postshock equilibrium state. For example, much higher temperatures and velocities are obtained in the reactive suspension while the pressure is lower than in a similar inert case. Longer relaxation zones are obtained for the reactive suspension.

Introduction

There is a growing interest in the flow field which develops behind shock waves propagating into a dusty gas. Such flows appear in many engineering applications, e.g., explosion generated shock waves above ground, supersonic flow in a rocket nozzle and explosions in coal mines. The first investigators to treat dusty shock waves were Carrier [1], Kriebel [2] and Rudinger [3]. They treated the gaseous phase of the suspension as an ideal gas and the solid phase (dust) was assumed to be inert. Their solutions were extended to cover monatomic (argon) reacting gases (nonideal) by Ben-Dor and Igra [4] and diatomic reacting gases (nitrogen) by Igra and Ben-Dor [5]. However, in both cases the solid phase (dust) was considered to be inert in spite of the fairly high postshock temperature. The main reason for treating the dust as an inert phase is the difficulty in formulating the dust chemical behavior at high temperatures. In order to overcome this difficulty several "simple-dust-models" have been proposed and solved. For example, Rakib, Igra, and Ben-Dor [6] replaced the dust with water droplets. The behavior of water droplets at high temperatures is well known – this enabled them to present a numerical solution for the relaxation zone which develops behind a strong normal shock wave propagating into an argon-water droplet suspension. In their solution both the argon and the water droplets were treated as reactive phases. Krier and Mozaffarian [7] treated a case of normal shock wave propagation into a suspension composed of air and reactive dust. In order to simulate the dust chemistry at relatively high temperatures they defined the dust to be a black powder. This definition enabled them to describe the response of the dust to the relatively high postshock temperatures (dust-burning) by a simple pressure controlled burning rate. In essence, Krier and Mozaffarian [7] overcome the difficulty of describing the dust chemical reactions, stimulated by the hot environment, by a prescribed fast burning in which a significant amount of energy is released. This formulation simplified the inclusion of the dust chemistry in the conservation equations and their subsequent solution.

The purpose of the present paper is to study the effect of a reacting dust on the postshock flow field. Unlike previous attempts a realistic burning-model will be used for a specified dust. The suspension to be treated in the present model is composed of carbon dust and pure oxygen. It is noted that the use of air would be more practical regarding engineering applications; however, this would have caused the model to be too complicated. The shock wave Mach number will be limited to $M = 5$. Although the oxygen can be treated as a perfect gas at $M = 5$ [15], real gas effect must be accounted for the combustion product CO_2. However, in order to reduce the complexity of the present model, all the components of the gaseous phase are assumed to be perfect. The postshock temperature is high enough to initiate burning of the carbon particles. As will be shown, this burning has a major effect on the relaxation zone.

Theoretical Background

When a normal shock wave propagates with a constant velocity into a quiescent suspension, the flow field can easily be transformed into a steady flow field using Galilean's transformation. In this transformation, a constant velocity, equal to the shock velocity, is subtracted from the entire flow field. The resulting steady flow field is shown schematically in Fig. 1. Now the normal shock wave is stationary and the suspension velocity ahead of the shock wave front is equal to the original shock wave velocity.

While crossing the shock front, the gaseous phase of the

Contributed by the Fluids Engineering Division and presented at the 10th International Colloquium on Dynamics of Explosion and Reactive Systems, San Francisco, CA, August 4-9, 1985 of THE AMERICAN SOCIETY OF MECHANICAL ENGINEERS. Manuscript received by the Fluids Engineering Division, September 24, 1984.

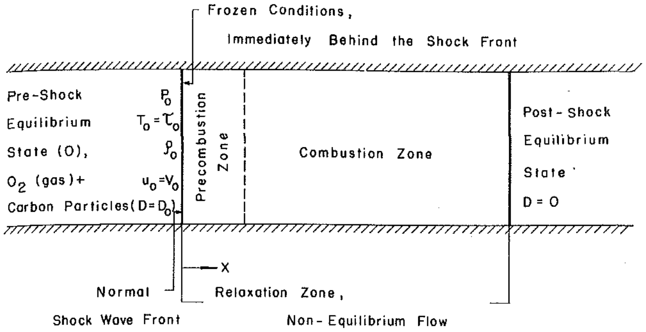

Fig. 1 Schematic description of the considered flow field

suspension experiences a sudden increase in its pressure, density and temperature and a sudden decrease in its velocity. The magnitude of these changes can be evaluated using the well-known Rankine-Hugoniot shock relations.

Unlike the gaseous phase, the solid phase of the suspension crosses the shock front unaffected because the diameter of the carbon particles (used in the present study) is 100 μm while the width of the shock front is of the order of a few mean free path (for the present study about 0.1 μm) and the characteristic response time of the solid phase is much longer than that of the gaseous phase. As a result, immediately behind the shock front the two phases of the suspension are no longer in a state of equilibrium. The gaseous phase is relatively hot and is moving relatively slowly while the carbon particles are relatively cold (they are at the preshock temperature, $T =$ 300K) and are moving relatively quickly (they move with the shock wave velocity, v_0). This difference in temperature and velocity between the two phases of the suspension will stimulate an intense heat and momentum transfer between the two phases. Once the carbon particle temperature reaches the ignition point a combustion process starts. It continues until the carbon particles disappear. The flow region where these processes take place is called the relaxation zone. It starts immediately behind the shock front and ends with the carbon disappearance via burning. At the end of the relaxation zone the gas mixture, composed of oxygen and the combustion products, is in a new state of equilibrium.

In the following, the conservation equations describing the flow field in the relaxation zone are listed. Their detailed derivation is given in reference [8]. The assumptions upon which their derivation was based are:

1 The flow is steady and one-dimensional.

2 The gas mixture (resulting from the carbon burning) can be treated as a mixture of perfect gases (see foregoing remark).

3 Heat transfer and viscous effects within the gaseous phase can be neglected. (These mechanisms are important only in the interaction between the two phases.)

4 All the components of the gaseous phase have the same velocity.

5 The carbon particles are small, rigid spheres of equal diameter, uniformly distributed in the gaseous phase.

6 The volume occupied by the carbon particles is negligibly small in comparison with the suspension volume.

7 There is no temperature distribution within the carbon particle. (This is a reasonable assumption considering the small size of the carbon particles and their relatively high heat conductivity.)

8 Interactions between carbon particles can be ignored.

9 The carbon particle weight and the buoyancy force it experiences are negligibly small in comparison with the drag force.

10 Heat transfer between the two phases is via heat convection only; see reference [9].

11 The thermal motion (Brownian motion) of the carbon particles can be ignored.

12 Ahead of the shock wave the suspension is in a state of complete equilibrium.

13 The carbon burning can be described by the following reaction only, $C(s) + O_2(g) \rightarrow CO_2(g) + h_b$ where h_b, the heat of formation of CO_2, is 3.937×10^5 KJ/Kg mole. A justification for this assumption is given subsequently.

14 The heat released by the burning carbon particles is independent of the suspension temperature and/or pressure.

15 The CO_2 gas generated in the combustion process is instantly mixed with oxygen to form a homogeneous gas mixture.

16 During the chemical reaction the CO_2 heat of forma-

Nomenclature

a = speed of sound
C = specific heat capacity of the carbon particles; concentration
C_D = drag coefficient
C_{P,CO_2} = specific heat capacity at constant pressure of the carbon-dioxide gas
C_{P,O_2} = specific heat capacity at constant pressure of the oxygen gas
$C_{p,g}$ = specific heat capacity at constant pressure of the gaseous phase
D = diameter
D_d = coefficient of molecular diffusivity
F = drag force
h = forced convection heat transfer coefficient
h_b = heat of formation
K = coefficient of thermal conductivity
k_d = diffusion coefficient [Kg/(m^2•s•Pa)]
k_s = rate of chemical reaction [Kg/(m^2•s•Pa)]
M = mass
M_A,M_B = molecular weights of gas A and B, respectively
M_C = molecular weight of carbon
m = particle or molecular mass
Nu = Nusselt number
P = pressure
Pr = Prandtl number
Q = heat transferred per unit time
R = gas constant
R_0 = universal gas constant
Re = Reynolds number
r_c = carbon particle rate of burning [Kg mole/s]
T = gas temperature
T_m = average temperature in the carbon particle boundary layer
u = gas velocity
v = carbon particle velocity
V_A,V_B = molar volume of gas A and B at their normal boiling points, respectively
v_0 = shock wave velocity
x = distance coordinate
η = initial mass ratio of carbon particles to oxygen gas
μ = viscosity
ρ = special density (mass per unit volume of the gas)
σ_c = carbon density
τ = temperature of the dust particle
ϕ = nondimensional parameter describing the carbon burning process

Subscripts

C = carbon
CO_2 = carbon dioxide
g = gaseous phase
O_2 = oxygen gas
0 = preshock equilibrium state

tion is released into the surrounding gas only, i.e., it cannot escape outside the flow field.

The conservation equations are as follows:

Continuity – Carbon Particles

$$\frac{d}{dx}(\rho_C v) = -\frac{M_C \rho_C r_c}{m_C} \tag{1}$$

Continuity – Oxygen Gas

$$\frac{d}{dx}(\rho_{O_2} u) = -\frac{M_{O_2} \rho_C r_c}{m_C} \tag{2}$$

Continuity – CO_2 *Gas*

$$\frac{d}{dx}(\rho_{CO_2} u) = +\frac{M_{CO_2} \rho_C r_c}{m_C} \tag{3}$$

Momentum – Carbon Particles

$$\frac{d}{dx}(\rho_C v^2) = -\frac{\rho_C}{m_C}(F + M_C r_c v) \tag{4}$$

Momentum – Gaseous Phase

$$\frac{d}{dx}[(\rho_{O_2} + \rho_{CO_2})u^2] + \frac{dP}{dx} = \frac{\rho_C}{m_C}(F + M_C r_c v) \tag{5}$$

Energy – Carbon Particles

$$\frac{d}{dx}[\rho_C v(C\tau + v^2/2)] = \frac{\rho_C}{m_C}[Q - Fv - M_C r_c (C\tau + v^2/2)] \tag{6}$$

Energy – Gaseous Phase

$$\frac{d}{dx}[\rho_{O_2} u(C_{p,O_2} T + u^2/2) + \rho_{CO_2} u(C_{p,CO_2} T + u^2/2)] = -\frac{\rho_C}{m_C}[Q - Fv - M_C r_c (C\tau + v^2/2 + h_b)] \tag{7}$$

Equation of State

$$P = (\rho_{O_2} R_{O_2} + \rho_{CO_2} R_{CO_2})T \tag{8}$$

Carbon Particle Diameter

$$\frac{dD}{dx} = -\frac{2}{\pi}\frac{M_C r_c}{\sigma_C D^2 v} \tag{9}$$

Equations (1)–(9) contain nine variables: The carbon dust spacial density ρ_C, oxygen density ρ_{O_2}, carbon dioxide density ρ_{CO_2}, carbon velocity v, gas velocity u, carbon temperature τ, gas temperature T, particle diameter D and the suspension pressure P. For solving equations (1)–(9) the parameters F, r_c and Q (the drag force on the carbon particle, the carbon burning rate and the amount of heat transferred from the gas to the carbon particles, respectively) must be expressed in terms of the aforementioned nine variables.

The drag force can be expressed as (see references [3, 9]):

$$F = \rho_g C_D |v - u|(v - u)\pi D^2/8 \tag{10}$$

where ρ_g is the gas density, C_D the carbon particle drag coefficient and D is its diameter. Many correlations relating C_D to the flow Reynolds number Re were proposed. Igra and Ben-Dor [9] showed that the following simple correlation is appropriate for describing the solid particles deceleration in the relaxation zone

$$C_D = 0.48 + 28\,\mathrm{Re}^{-0.85} \tag{11}$$

where $\mathrm{Re} = \rho_g |v - u| D/\mu_g$. μ_g, the viscosity of the gaseous phase, can be obtained from the viscosities of the individual components of the suspension (oxygen and carbon-dioxide); for details see reference [8].

The amount of heat transferred between the two phases of suspension is given by

$$Q = h\pi D^2(T - \tau) \tag{12}$$

where h is the coefficient of forced convection. This coefficient can be expressed in terms of the flow Nusselt number Nu, and the gas thermal conductivity K_g as follows

$$h = k_g \mathrm{Nu}/D \tag{13}$$

The thermal conductivity of the gaseous phase K_g, can be obtained from the thermal conductivities of the individual components of the suspension, $K_g = (\rho_{O_2} K_{O_2} + \rho_{CO_2} K_{CO_2}) / (\rho_{O_2} + \rho_{CO_2})$, for details see reference [8]. For spheres immersed in a gaseous phase the following correlation for Nu is generally used [10]

$$\mathrm{Nu} = 2 + 0.459\mathrm{Pr}^{1/3}\mathrm{Re}^{0.55} \tag{14}$$

The Prandtl number Pr can be expressed in terms of the gas viscosity μ_g, heat conductivity K_g and its specific heat capacity at constant pressure $C_{p,g}$, i.e.

$$\mathrm{Pr} = \mu_g C_{p,g}/K_g \tag{15}$$

K_g and $C_{p,g}$ can be obtained from the appropriate values of the components of the gas mixture; for details see reference [8].

For completing the supplementary equations necessary for the solution of equations (1)–(9), a correlation relating the carbon burning rate to the suspension parameters is required. The carbon burning is a fast oxidation process which starts at a relatively high temperature ($T \sim$ 1000K). This temperature is called the ignition temperature. At the burning region a depletion in the reactant concentration (O_2 and C) and an increase in the product concentration (CO and CO_2) is evident. The primary reactions describing the carbon oxidation are [11]

$$C(s) + O_2(g) \rightarrow CO_2(g) + 3.937 \times 10^5 \mathrm{KJ/Kg\ mole} \tag{16}$$

$$C(s) + \frac{1}{2}O_2(g) \rightarrow CO(g) + 1.115 \times 10^5 \mathrm{KJ/Kg\ mole} \tag{17}$$

The products mass (or concentration) ratio CO/CO_2, depends on the burning temperature and the availability of oxygen in the burning region. Increasing the burning temperature and/or decreasing the oxygen concentration results in an increase of this ratio [11]. The variations in the concentration of the various species involved in the carbon burning, as a function of the distance measured from the surface of the burning carbon (for air) is shown schematically in Fig. 2. Far away from the burning carbon, the oxygen concentration is about 21 percent (which is the oxygen concentration in air) and the amounts of CO and CO_2 are negligibly small. On the other hand, close to the burning carbon, the oxygen concentration depletes (due to the carbon burning) while the CO concentration increases. On the surface of the burning carbon the oxygen concentration is reduced to zero while the CO concentra-

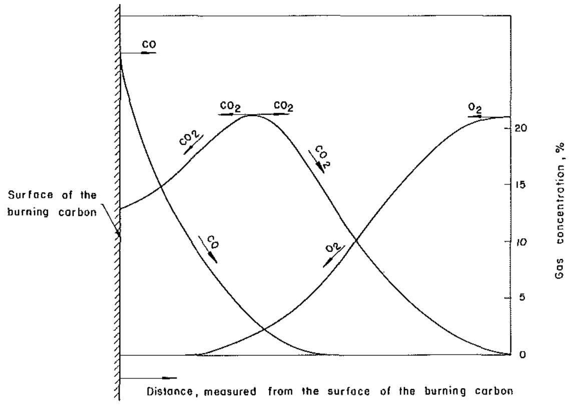

Fig. 2 **Schematic description of the reactant and product concentrations near the surface of burning carbon in air**

tion reaches a maximum. This antisymmetry in the oxygen and the CO concentrations produces opposite fluxes (via diffusion) of O_2 and CO. The interaction between these fluxes generates an additional product – CO_2. Its production can be described by

$$CO + \frac{1}{2} O_2 \rightarrow CO_2 + 2.822 \times 10^5 \text{KJ/Kg mole} \tag{18}$$

Obviously, the maximum concentration of CO_2 is found where the opposing fluxes of O_2 and CO are of similar strength, as is shown in Fig. 2. Moving away from this point, either toward or away from the surface of the burning carbon results in a decrease in the CO_2 concentration. As a result there will be a diffusive flux of CO_2 in two directions, away and toward the burning carbon. Due to the very low oxygen concentration close to the surface of the burning carbon and the availability of CO_2 molecules there, the following reaction takes place close to the burning carbon surface

$$C(s) + CO_2(g) \rightarrow 2CO(g) - 1.707 \times 10^5 \text{KJ/Kg mole} \tag{19}$$

This reaction will enhance the CO concentration close to the surface of the burning carbon (see Fig. 2). As we move away from this surface a depletion in the CO concentration takes place due to reaction (18). The carbon disappearance rate (rate of burning) depends on the rates of reactions (16)–(19) and the diffusion fluxes of O_2, CO, and CO_2.

In the considered work, the carbon burning takes place in a pure oxygen environment and not in air as was shown in Fig. 2. Furthermore, the initial amount of carbon is much smaller than that of oxygen (the carbon to oxygen mass ratio in the following solution is $\eta = 0.05$). It is reasonable, therefore, to assume that eventually the carbon is fully oxidized to CO_2, i.e., the reaction shown in equation (16) is sufficient for describing the carbon burning. (Recall that the present model assumes a perfect gas behavior and hence the CO_2 molecules cannot dissociate.)

The carbon burning rate, r_c, can be expressed in terms of the burning particle diameter D and the oxygen concentration C_{O_2} as follows [12]:

$$r_c = \pi D^2 k_C C_{O_2} \text{(Kg mole/s)} \tag{20}$$

where k_C is a constant which characterizes the burning rate of the carbon particles, k_C is expressed in m/s. Field, et al. [12] proposed the following expression for k_C

$$k_C = \frac{R_0 T_m / M_C}{1/k_s + 1/k_d} \tag{21}$$

where R_0 is the universal gas constant, T_m is the average temperature in the thermal boundary layer which surrounds the burning carbon sphere and k_s and k_d are the chemical reaction rate constant and the gas diffusion rate constant, respectively. For the present work, we used the following: $T_m = (T+\tau)/2$ and for k_s and k_d the expression proposed by Field, et al. [12] were adopted, i.e.,

$$k_s = 0.86 \exp(-1.4947 \times 10^8 / R_0 \tau) \tag{22}$$

$$k_d = 2.43 \times 10^{-2} \phi D_d / (D R_0 T_m) \tag{23}$$

Both k_s and k_d are expresesd in Kg/($m^2 \cdot s \cdot$Pa). In equation (23) D_d is the coefficient molecular diffusivity and ϕ is a parameter describing the relative amounts of CO and CO_2 produced during the carbon burning. ϕ is within the range $1 \leq \phi \leq 2$, see reference [12]. When most of the burning products are CO_2, $\phi \rightarrow 1$, this value ($\phi = 1$) was used for the present solution. For the coefficient of molecular diffusivity D_d, the expression proposed by Perry [13] was used, i.e.

$$D_d = \frac{4.24 \times 10^{-5} T^{3/2} (1/M_A + 1/M_B)^{1/2}}{(V_A{}^{1/3} + V_B{}^{1/3}) P} \tag{25}$$

where M_A and M_B are the molecular weight of gases A and B, respectively, V_A and V_B are the molal volumes of gases A and B at their normal boiling points, respectively, and P and T are the gas mixture pressure and temperature, respectively. In the present case we are concerned with self-diffusion of oxygen. This diffusion is generated by the severe gradients in the oxygen concentration near the burning particles.

Strictly speaking, the burning rate of the carbon spheres as expressed in equation (20) is applicable to cases where the relative velocity between the carbon particles and the gaseous phase is very small and thereby it is safe to assume that there exists a spherical symmetry in the oxygen concentration around the burning carbon particle. It is true that immediately behind the shock front the relative velocity between the two phases is quite high. However, as will be shown subsequently, due to the viscous interaction this velocity is reduced very rapidly. Furthermore, at the region where the relative velocity between the two phases of the suspension is relatively large, the carbon particles are still below their ignition temperature (they enter the relaxation zone having the preshock temperature, i.e., 300K). As will be shown in the following results, throughout most of the burning zone $(v-u)$ is fairly low and the usage of equation (20) is therefore justified.

Numerical Method

The numerical solution of equations (1)–(9) was conducted in two steps. First, the derivatives of the flow variables (du/dx, dv/dx, dT/dx, $d\tau/dx$, $d\rho_C/dx$, $d\rho_{O_2}/dx$, $d\rho_{CO_2}/dx$, dD/dx and dP/dx) were evaluated. Thereafter, the flow variable (u, v, T, τ, ρ_C, ρ_{O_2}, ρ_{CO_2}, D and P) were calculated by numerical integration. As a starting value for this integration the appropriate frozen values (as predicted by the Rankine-Hugoniot shock relations) were used. The integration was terminated at the end of the relaxation zone which was defined numerically as the distance at which $D \leq 1$ μm (the carbon particle disappeared). Details regarding the numerical solution of equations (1)–(9) as well as a printout of the computer program can be found in reference [8].

Results and Discussion

In order to demonstrate the effect of the burning carbon particles on the flow properties in the relaxation zone, equations (1)–(9) were solved numerically for the following conditions: shock wave Mach number M = 5, preshock pressure P_0 = 50 torr, preshock temperature T_0 = 300K, initial carbon particle diameter D_0 = 100 μm and carbon loading (mass ratio carbon-oxygen) η = 0.05. The solution was repeated for a similar inert particle (no burning) and the results obtained for both cases are shown in Figs. 3–7. The value of M = 5 is used in order to cover typical shock wave velocities at early stages of explosions. Since in most laboratories a shock wave of strength of M = 5 can be produced in shock tubes only when P_0 is subatmospheric, a value of P_0 = 50 torr was used for the present numerical study. In the parametric study of this problem, the more practical value of P_0 = 760 torr was also investigated [16]. Similarly a range of initial diameters D was also investigated to cover both small and large particles.

The variations in the gas (T) and dust (τ) temperatures in the relaxation zone are shown in Fig. 3. The results are normalized by the preshock suspension temperature (T_0 = 300K). Immediately behind the shock front the gas temperature experiences a sudden raise (according to the Rankin-Hugoniot shock relations) while the carbon particles pass through the shock front unaffected. Because of this large temperature difference, between the two phases, an intense heat transfer from the gas to the carbon particles takes place and as a result the carbon particles are heated and the gas is cooled; see Fig. 3 for $0 < x < 8$ m. As could be expected, until the carbon ignition identical temperature variations are obtained for the two cases

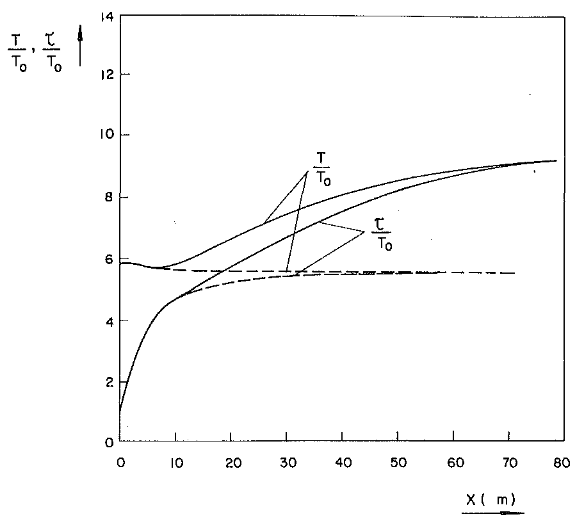

Fig. 3 Variations in the gas (T) and the carbon particles (τ) temperatures in the relaxation zone; ——— reactive suspension, --- inert suspension

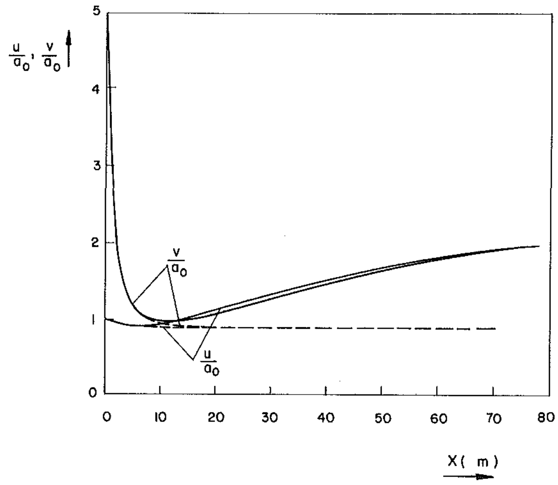

Fig. 4 Variation in the gas (u) and the carbon (v) velocities in the relaxation zone; ——— reactive suspension, --- inert suspension

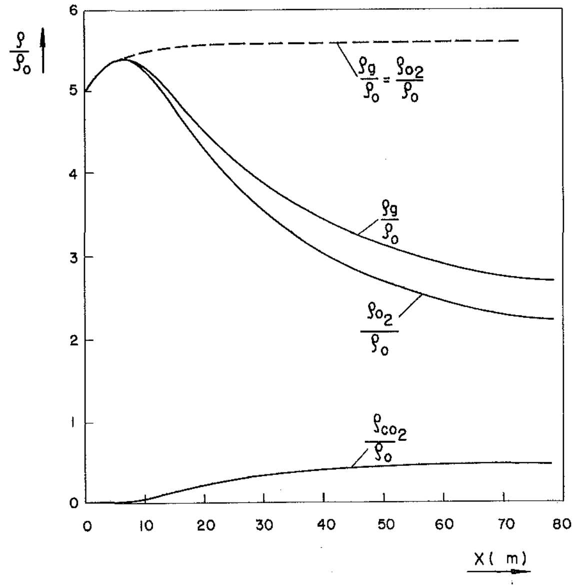

Fig. 5 Density variations in the relaxation zone; ——— reactive suspension, --- inert suspension

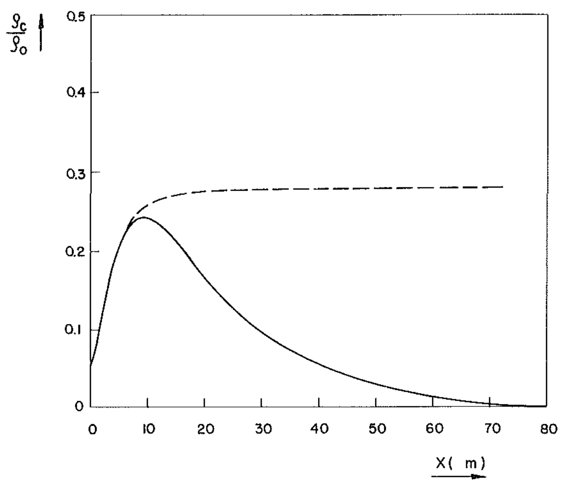

Fig. 6 Variations in the carbon space density in the relaxation zone; ——— reactive suspension, --- inert suspension

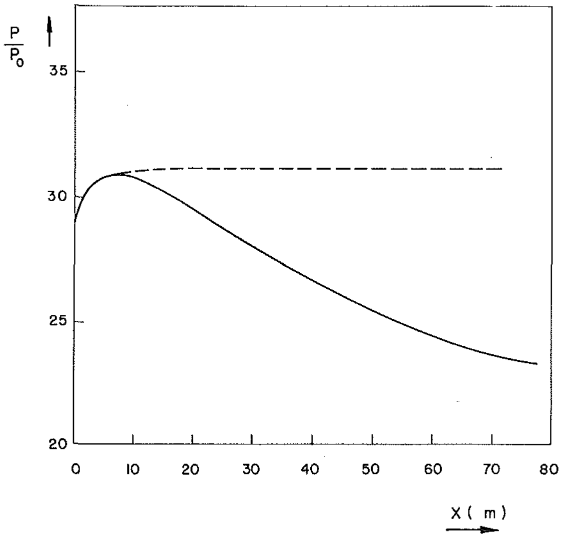

Fig. 7 Pressure variations in the relaxation zone; ——— reactive suspension, --- inert suspension

(active and inert particles). This is no longer the case after the carbon starts burning ($x \simeq 8$ m). From that point on, the gas and dust temperatures in the suspension containing the burning carbon particles are higher than those obtained for a similar inert case. The reason for this is quite simple; during the carbon oxidation the heat of formation is absorbed by the gaseous and solid phases of the suspension to result in higher values for T and τ in comparison with a similar inert suspension. Since larger amounts of heat have to be transferred between the two phases in the reactive case, the extent of the relaxation zone is longer than that obtained for a similar inert suspension (see Fig. 3). In the reactive case, the postshock equilibrium suspension temperature is 60 percent higher than the temperature of the inert case.

The kinematical behavior of the suspensions (reactive and inert) is shown in Fig. 4. The gas (u) and carbon (v) velocities are normalized by the preshock speed of sound (a_0 = 330 m/s). The carbon particles enter the relaxation zone with the preshock suspension velocity (in the present case it is five times the speed of sound), while the gaseous phase experiences a sudden decrease in its velocity when it crosses the shock front. The relative velocity between the two phases which is initially quite high, is reduced rapidly due to momentum exchange between the carbon particles and the gas. As in the temperature variations, here, too, until the carbon ignition both suspensions (reactive and inert) follow identical patterns; see Fig. 4

for $0 < x < 8$ m. After the carbon ignition, the velocity profiles differ significantly. In the reactive suspension, part of the released thermal energy is converted to kinetic energy resulting in an increase in both the gas and the carbon velocities; see Fig. 4. In the reactive case, the postshock equilibrium velocity is 100 percent higher than that obtained in the similar inert suspension. Furthermore, while the inert suspension reaches uniform and constant velocity fairly quickly (at $x \simeq 20$ m), it takes about 80 m for the reactive suspension to reach an equilibrium velocity.

In the inert suspension, the only mechanism through which equilibrium suspension velocity is reached is the viscous interaction between the two phases manifested as a drag force which acts on the carbon particles. This force is strongly dependent upon the relative velocity $v-u$; see equation (10). As a result, for the inert suspension the gas and dust velocities approach each other asymptotically and each behaves monotonically; see Fig. 4. In the reactive suspension, two forces are acting on the carbon particles – the drag force F, and a force generated by momentum transfer due to burning which is equal to $M_C r_c v$; see equation (4). As the two velocities, u and v, approach each other, the drag force becomes of secondary importance and the momentum exchange due to burning becomes the dominant one. The latter causes the carbon particles to be decelerated to velocities lower than the gas velocity, $v < u$. Now the drag force changes its direction (since $v < u$) and it causes the dust to be accelerated to the gas velocity; see Fig. 4.

Variations in the gas density, ρ_g, the oxygen gas density, ρ_{O_2}, and the carbon dioxide gas density, ρ_{CO_2}, in the relaxation zone are shown in Fig. 5. All values are normalized by the preshock gas density, $\rho_0 = 0.085$ kg/m^3. As could be expected, until the start of carbon ignition identical variations are observed in ρ_g for the two suspensions (reactive and inert). Furthermore, ρ_g is equal to ρ_{O_2} and $\rho_{CO_2} = 0$ until the carbon burning starts. Up to this point ρ_g increases monotonically with distance. This increase is expected because of the monotonic decrease in the gas velocity, u (see Fig. 4). For a steady, inert one-dimensional flow, the continuity equation is $\rho_g u =$ constant. Obviously when u decreases ρ_g must increase. Once the burning starts the variations in ρ_g differs from that observed for the inert suspension. Now, due to the carbon oxidation, a new species is generated – CO_2. Its production depletes the amount of O_2 molecules in the suspension. It is therefore expected that after ignition ρ_{CO_2} will increase while ρ_{O_2} will decrease and this pattern should persist as long as the carbon burning continues. This, indeed, is the case as is evident from Fig. 5. It is also apparent from Fig. 5 that in the reactive suspension ρ_g decreases with increasing distance, as long as the carbon particles burn. This behavior should be expected from observing the continuity equation for the suspension which is $\rho_g u + \rho_C v =$ constant. Excluding the early part of the relaxation zone $u \simeq v$; see for $x \geq 10$ in Fig. 4. Therefore, the foregoing continuity equation can be approximated by $(\rho_g + \rho_C)\, u =$ constant. It was shown in Fig. 4 that due to the carbon burning, the gas velocity, u, increases in the relaxation zone in comparison with a similar inert suspension case. Therefore $(\rho_g + \rho_C)$ must decrease. In the present solution, the mass ratio, carbon to oxygen gas η, is equal to 0.05; therefore $\rho_g >> \rho_C$ throughout the relaxation zone. As a result, in spite of the fact that ρ_C decreases in the relaxation zone (see Fig. 6), the reduction in ρ_C is too small to ensure a decrease in $(\rho_g + \rho_C)$ without having a meaningful reduction in ρ_g, as is shown in Fig. 5.

The behavior of the carbon spacial density, ρ_C, in the relaxation zone, is shown in Fig. 6. In the inert suspension case ρ_C reaches a plateau; when the carbon particles burn a maximum in ρ_C is reached at the ignition point, thereafter ρ_C decreases monotonically until the carbon particles disappear via burning. Like the changes in the other suspension properties, identical variations in ρ_C are observed for both suspensions (reactive and inert) up to the carbon ignition.

Initially, before combustion, the gas is cooled by the loss of heat to the carbon particles. Hence, the gas pressure and density increase and the gas velocity decreases. Once burning starts, due to heat addition (to the steady subsonic flow) the suspension pressure must decrease [14]. This indeed is the case as is evident from Fig. 7.

Summary and Conclusions

The conservation equations for a suspension composed of oxygen gas and solid carbon particles through which a normal shock wave is passing with a constant velocity, were formulated and solved numerically. It was shown that the carbon particle burning caused by the relatively high postshock wave gas temperature has a major effect on the suspension properties in the relaxation zone and on the eventually reached postshock equilibrium state. For example, it was shown that higher temperatures and velocities are obtained in the relaxation zone of the burning suspension as compared with a similar inert case. On the other hand, the static pressure and gas density of the burning suspension are lower than the values obtained for a similar inert case. In the considered case ($M = 5$, $P_0 = 50$ torr, $D_0 = 100$ μm and $\eta = 0.05$) the postshock equilibrium suspension temperature is 60 percent higher than that obtained in a similar inert case, the equilibrium velocity is almost double that of the inert case and the postshock equilibrium suspension pressure is 20 percent below the inert suspension value. In addition to its effect on the suspension properties, burning of the carbon particles significantly extends the relaxation zone. The ratio between the lengths of the kinetic relaxation zones for active and inert suspensions is about four.

References

1 Carrier, G. F., 1958, "Shock Waves in a Dusty Gas," *Journal of Fluid Mechanics*, Vol. 4, pp. 376–382.

2 Kriebel, A. R., 1964, "Analysis of Normal Shock Waves in a Particle-Laden Gas," ASME *Journal of Basic Engineering*, Vol. 86, pp. 655–665.

3 Rudinger, G., 1964, "Some Properties of Shock Relaxation in Gas Flows Carrying Small Particles," *Physics of Fluids*, Vol. 7, pp. 658–663.

4 Ben-Dor, G., and Igra, O., 1982, "The Relaxation Zone Behind Normal Shock Waves in a Reacting Dusty Gas. Part 1: Monatomic Gases," *Journal of Plasma Physics*, Vol. 27, pp. 377–395.

5 Igra, O., and Ben-Dor, G., 1984, "The Relaxation Zone Behind Normal Shock Waves in a Dusty Reacting Gas. Part 2: Diatomic Gases," *Journal of Plasma Physics*, Vol. 31, pp. 115–140.

6 Rakib, Z., Igra, O., and Ben-Dor, G., 1984, "The Effect of Water Droplets on the Relaxation Zone Developed Behind Strong Normal Shock Waves," ASME JOURNAL OF FLUIDS ENGINEERING, Vol. 106, pp. 154–159.

7 Krier, M., and Mozaffarian, A., 1977, "Two-Phase Reactive Particle Flow Through Normal Shock Waves," *International Journal of Multiphase Flow*, Vol. 4, pp. 65–79.

8 Elperin, I., 1984, "The Effect of Carbon Particles on the Flow Field Developed Behind a Normal Shock Wave in Oxygen," MSc Thesis, Department of Mechanical Engineering, Ben-Gurion University of the Negev, (in Hebrew).

9 Igra, O., and Ben-Dor, G., 1980, "Parameters Affecting the Relaxation Zone Behind Normal Shock Waves in a Dusty Gas," *Israel Journal of Technology*, Vol. 18, pp. 159–168.

10 Hoglund, R. F., 1962, "Recent Advances in Gas-Particle Nozzle Flows," *American Rocket Society Journal*, Vol. 32, pp. 662–671.

11 Timnat, Y. M., 1982, "Problems of Carbon Oxidation," *Israel Journal of Technology*, Vol. 20, pp. 31–36.

12 Field, M. A., Gill, D. W., Morgan, B. B., and Hawksley, P. G. W., 1976, "Combustion of Pulverized Coal," BCURA.

13 Perry, J. H., 1963, *Chemical Engineering Handbook*, McGraw-Hill, New York.

14 Shapiro, A. M., 1954, *The Dynamics and Thermodynamics of Compressible Fluid Flow*, Ronald Press Co., New York, Vol. I, pp. 190–200.

15 Law, C. K., and Bristow, M., 1969, "Tables of Normal Shock Wave Properties for Oxygen and Nitrogen in Dissociation Equilibrium," UTIAS TN 148.

16 Igra, O., Ben-Dor, G., and Elperin, I., 1986, "Parameters Affecting the Postshock Relaxation Zone in an Oxygen Carbon Particle Suspension," ASME JOURNAL OF FLUIDS ENGINEERING, Vol. 108, No. 3, pp. 360–365.

Parameters Affecting the Postshock Wave Relaxation Zone in an Oxygen Carbon Particle Suspension

O. Igra

G. Ben-Dor

I. Elperin

Pearlstone Center for Aeronautical
Engineering Studies,
Ben-Gurion University of the Negev,
Department of Mechanical Engineering,
Beer Sheva, Israel

A parametric study was conducted regarding the effects of the initial carbon concentration, the initial carbon particle diameter, the shock wave Mach number and the preshock suspension pressure on the suspension behavior in the relaxation zone. The suspension was composed of oxygen gas seeded with small carbon particles. It was found that changing either the initial carbon concentration or the shock wave Mach number has a marked effect on the suspension behavior in the relaxation zone and on the eventually reached postshock equilibrium state. Changes in the initial carbon particle diameter (at a constant shock wave Mach number and carbon concentration) has no effect on the postshock equilibrium state, but it does affect the way in which the suspension reaches this equilibrium state. Changes in the preshock suspension pressure has only minor effects on the suspension behavior in the relaxation zone.

Introduction

In an earlier paper, Elperin, Igra and Ben-Dor [1] analyzed the problem of a normal shock wave propagating into a carbon particle laden gas. In particular, the effect of the carbon particle combustion on the postshock wave flow field was studied. In that paper [1], the conservation equations for a suspension subjected to normal shock waves were formulated and solved numerically. The effect of the carbon particle combustion was assessed by comparing the obtained numerical results with results obtained for a similar inert suspension case. It was shown that the carbon combustion has a major effect on the postshock suspension flow, e.g., it causes an increase in both the gas and the carbon temperatures and velocities and a decrease in the suspension pressure. In addition, it significantly extends the relaxation zone in comparison with a similar inert suspension.

The purpose of the present paper is to study the effects associated with changes in the initial carbon particle mass concentration η, the initial diameter of the carbon particles D_0, the shock wave Mach number M, and the preshock suspension pressure P_0 on the suspension behavior in the relaxation zone.

The theoretical background given in reference [1] is valid for the present study; for the sake of brevity it is not repeated here. In the following, numerical results obtained from the solution of [1, equation (1)-(9)] are given and discussed. A complete set of all the obtained results are given in reference [2].

Results and Discussion

In order to assess the effects on the suspension flow in the relaxation zone associated with changes in η, D_0, M, and P_0, [1, equations (1)-(9)] were solved numerically for the following initial values:

Initial carbon particle to gas mass ratio: $\eta = 0.001$, 0.01, 0.05;
initial particle diameter: $D_0 = 50$, 100, 200 μm;
incident shock wave Mach number: M = 2, 5, 8;
preshock wave suspension pressure: $P_0 = 50$, 380, 760 torr;
preshock wave suspension temperature of $T_0 = 300$ K.

The obtained results are shown in Figs. 1-14 in a nondimensional form, i.e, the temperatures were normalized by the preshock suspension temperature ($T_0 = 300$ K), the velocities by the preshock speed of sound ($a_0 = 330$ m/s), the densities by the preshock gas density ($\rho_0 = 0.086$ kg/m^3) and the pressures by the preshock suspension pressure ($P_0 = 50$ torr). In the following, the effects associated with each individual change are shown an discussed separately.

Changes in the Initial Carbon Particle Concentration. The effects that changes in the initial carbon particle concentration have on the gaseous (T) and solid (τ) phase temperatures are shown in Fig. 1. Large η's mean large initial carbon content in the suspension. This in turn results in a release of relatively large amounts of heat during the carbon combustion. Obviously, the availability of large amounts of heat will affect the thermal and the kinematic state of the suspension. It is clear from Fig. 1 that this indeed is the case. For the smallest initial carbon concentration ($\eta = 0.001$), the temperature variations in the relaxation zone are similar to that observed in a similar

---

Contributed by the Fluids Engineering Division and presented at the 10th International Colloquium on Dynamics of Explosion and Reactive Systems, San Francisco, CA, August 4-9, 1985 of THE AMERICAN SOCIETY OF MECHANICAL ENGINEERS. Manuscript received by the Fluids Engineering Division, September 24, 1984.

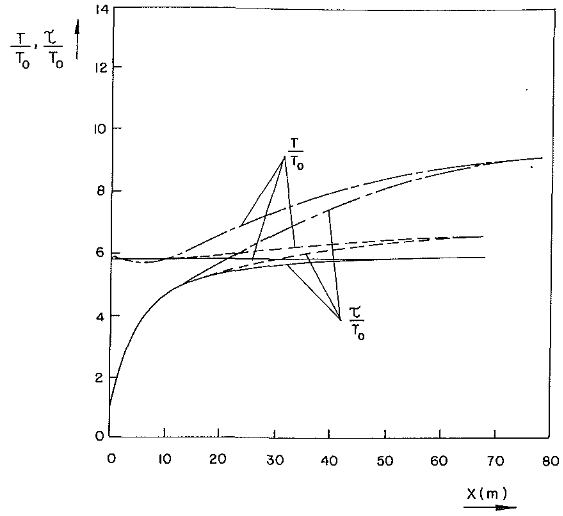

Fig. 1 Gas temperature (T) and carbon temperature (τ) variations in the relaxation zone for $M=5$, $D_0=100$ μm and $P_0=50$ torr; ———— $\eta=0.001$, — — — $\eta=0.01$, —— —— $\eta=0.05$

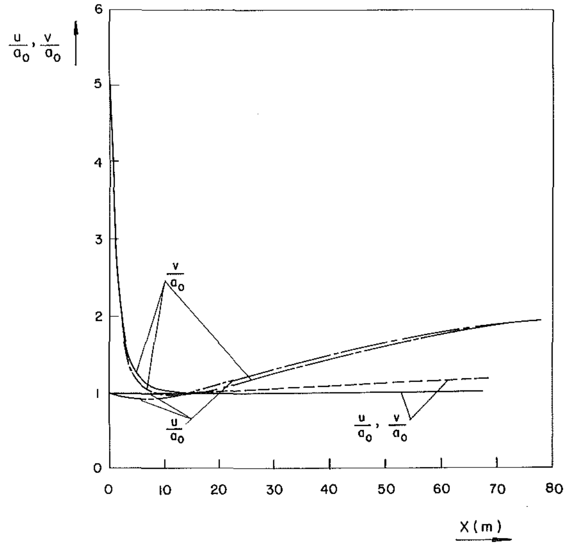

Fig. 2 Gas velocity (u) and carbon velocity (v) variations in the relaxation zone for $M=5$, $D_0=100$ μm and $P_0=50$ torr; ———— $\eta=0.001$, — — — $\eta=0.01$, —— —— $\eta=0.05$

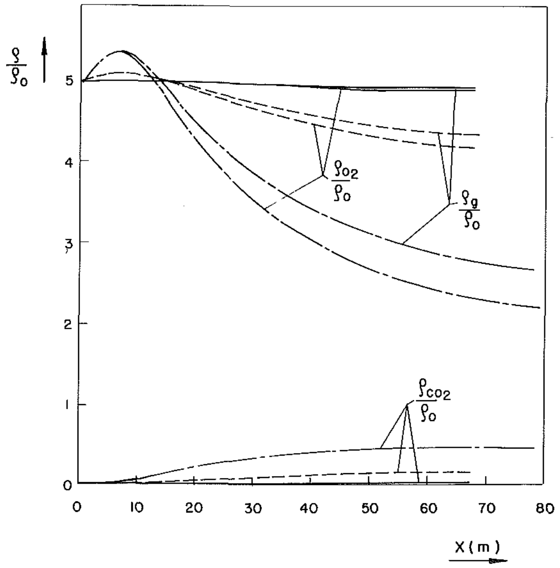

Fig. 3 Density variations of the suspension gases in the relaxation zone for $M=5$, $D_0=100$ μm and $P_0=50$ torr; ———— $\eta=0.001$, — — — $\eta=0.01$, —— —— $\eta=0.05$

inert suspension (shown in [1, Fig. 3]). As η increases, the amount of heat released during the carbon combustion also increases. This results in an increase in the temperature of the gaseous phase of the suspension (see Fig. 1). Forced heat convection from the gaseous phase to the carbon particles causes the carbon particle temperature to rise as well, until an equilibrium state is reached at the end of the relaxation zone. The larger is η, the higher both T and τ become (see Fig. 1). Since greater amounts of heat are being transferred between the two phases as η increases, it is expected that longer relaxation zones will be associated with increasing η's. It is apparent from Fig. 1 that when $\eta=0.05$, the thermal relaxation zone is about 70 m long; it is reduced to about 45 m for $\eta=0.001$. The effects of changing η on the gas (u) and the carbon particles (v) velocities in the relaxation zone are shown in Fig. 2. Some of the thermal energy released during the carbon combustion manifests itself as an increase in the suspension kinetic energy, as is evident from Fig. 2. The larger η is, the higher the postshock wave equilibrium suspension velocity becomes. For $\eta=0.001$, a postshock wave equilibrium suspension velocity is reached relatively rapidly (at $x \simeq 13$ m) and it is about 2 percent higher than that obtained for a similar inert case. When the carbon particle concentration is raised to $\eta=0.05$, the postshock equilibrium velocity is doubled and the extent of the relaxation zone is almost quadruplicated in comparison with a similar inert suspension case (shown in [1, Fig. 4]).

Increasing the initial carbon concentration in the suspension decreases the density of the gaseous phase ρ_g in the relaxation zone, as is evident from Fig. 3. This should be expected from observing the continuity equation for a steady, one-dimensional suspension flow, i.e., $\rho_g u + \rho_C v = \text{constant}$. After the carbon ignition $u \simeq v$ (see Fig. 2) and the continuity equation can be approximated by $(\rho_g + \rho_C)u = \text{constant}$. It was shown that increasing η results in higher u's; therefore $(\rho_g + \rho_C)$ must decrease. The largest value of η is 0.05 in-

Nomenclature

D = diameter of the carbon particle
M = shock wave Mach number; mass
N = number of carbon particles
P = pressure
R = gas constant
T = temperature of the gaseous phase
u = velocity of the gaseous phase
v = velocity of the solid phase (carbon particles)
γ = ratio of specific heat capacities of the gas
η = preshock wave carbon dust to oxygen gas mass ratio
ρ = density
ρ_C = spacial density of the carbon particles
ρ_{CO_2} = density of the CO_2 gas
ρ_g = density of the gaseous phase
ρ_{O_2} = density of the oxygen gas
σ_C = carbon density
τ = temperature of the solid phase (carbon particles)

Subscripts

0 = preshock wave conditions
f = frozen conditions reached immediately behind the shock front

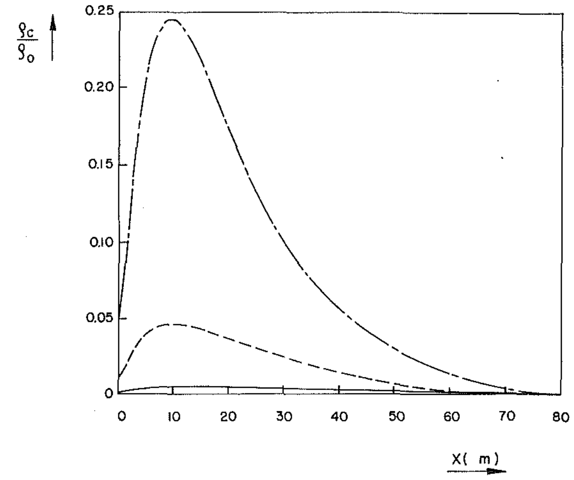

Fig. 4 *Carbon density variations in the relaxation zone for M = 5, $D_0 = 100$ μm and $P_0 = 50$ torr; ________ $\eta = 0.001$, _ _ _ _ $\eta = 0.01$, __ __ __ $\eta = 0.05$*

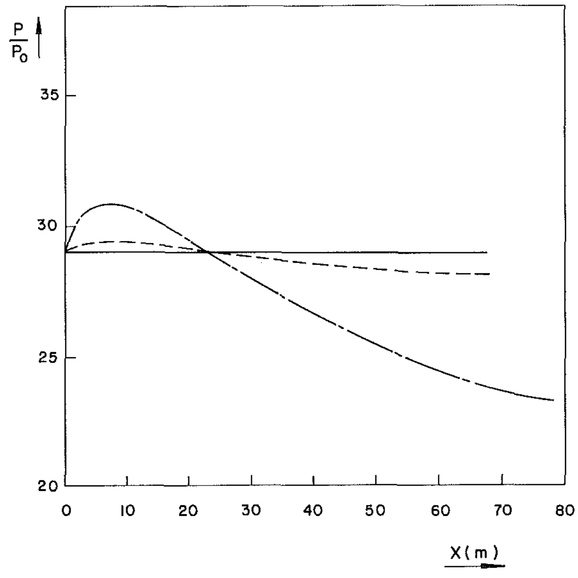

Fig. 5 **Pressure variations in the relaxation zone for M = 5, $D_0 = 100$ μm and $P_0 = 50$ torr; ________ $\eta = 0.001$, _ _ _ _ $\eta = 0.01$, __ __ __ $\eta = 0.05$**

dicating that $\rho_g >> \rho_C$. Therefore, in order to ensure the decrease of $(\rho_g + \rho_C)$, ρ_g must decrease as shown in Fig. 3. On the other hand, the larger η is, the more carbon is present in the suspension; this results in larger values for ρ_{CO_2}, see Fig. 3.

The variations in the carbon spatial density ρ_C in the relaxation zone are shown in Fig. 4. Obviously, at the end of the relaxation zone $\rho_C = 0$ (end of combustion) for all three cases. However, the larger η is, the larger ρ_C becomes, as could be expected.

The effect that changes in the initial carbon concentration have on the suspension pressure is shown in Fig. 5. It is evident that the highest postshock wave equilibrium suspension pressure is associated with the smallest η ($\eta = 0.001$), while the lowest postshock equilibrium suspension pressure is obtained for the largest η ($\eta = 0.05$). This behavior can easily be explained by observing the momentum conservation equation for a steady, one-dimensional suspension flow, i.e., $P + \rho_g u^2 + \rho_C v^2 = C_3$. The continuity equations for the gaseous and solid phases are: $\rho_g u = C_1$ and $\rho_C v = C_2$, respectively. Combining these with the momentum conservation equation yields, $P + C_1 u + C_2 v = C_3$ where C_1, C_2, and C_3 are constants. It was shown (in Fig. 2) that the higher η is, the higher u and v become. It is therefore expected that increasing the carbon concentration will reduce the suspension pressure. The fact that P decreases with increasing η's should be expected since for a one-dimensional, steady subsonic flow, heat addition results in a decrease in static pressure. As the amount of heat addition increases (larger η's), the static pressure further reduces; as is evident from Fig. 5.

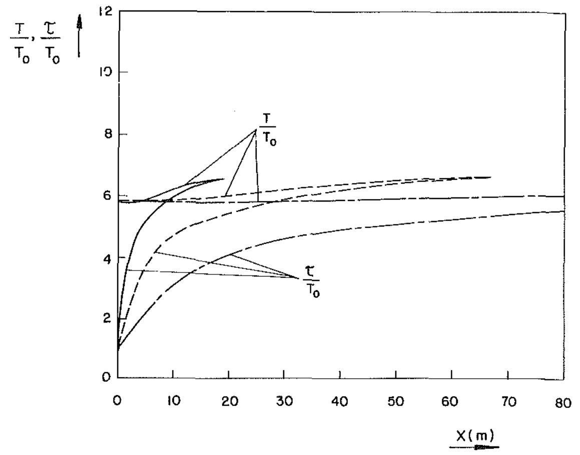

Fig. 6 **Gas temperature (*T*) and carbon temperature (τ) variations in the relaxation zone for M = 5, $\eta = 0.01$ and $P_0 = 50$ torr; ________ $D_0 = 50$ μm, _ _ _ _ $D_0 = 100$ μm, __ __ __ $D_0 = 200$ μm**

Changes in the Initial Diameter of the Carbon Particles. The effects that changes in the initial diameter of the carbon particles have on the suspension properties in the relaxation zone are shown in Figs. 6 to 11. Three different initial diameters were examined: $D_0 = 50$ μm, 100 μm, and 200 μm. For all three cases $\eta = 0.01$, M = 5, $P_0 = 50$ torr, and $T_0 = 300$ K. The three cases have the same initial carbon content, $\eta \equiv M_C / M_{O_2} = 0.01$ and the initial oxygen mass M_{O_2} is identical for the three cases (it depends solely upon T_0 and P_0 via the equation of state). Therefore, changing the initial carbon particle diameter affects the number of carbon particles present in the suspension, but not their initial mass ($M_C = 4\pi D_0^3 \sigma_C N/3$, where D_0 and σ_C are the carbon particle initial diameter and density, respectively, M_C and N are the initial total carbon mass in the suspension and the number of carbon particles, respectively). Since all cases have the same value of M_C, it is expected that the carbon combustion will release the same amount of thermal energy. However, it will take different times (and lengths) until this energy is released since the number of carbon particles and their size is different in each case.

The variations in the gas (T) and the carbon particles (τ) temperatures in the relaxation zone are shown in Fig. 6. As could be expected, the smaller the particle is, the faster it disappears via burning. However, since the same carbon content appears in all three cases and so does their initial temperature, it is expected that the same postshock wave equilibrium suspension temperature will be reached in the three cases. This is indeed the case as can be seen from Fig. 6. (For $D_0 = 200$ μm a postshock wave equilibrium suspension temperature is reached only after 194.8 m behind the shock front; not shown in Fig. 6.)

The initial carbon particle diameter has a direct effect on the particle volume and its mass; it will, therefore, influence the drag and inertia forces. These forces affect the particle velocity in the relaxation zone, as is evident from Fig. 7. However, while the inertia force is proportional to D^3, the drag force is approximately proportional to D^2. Therefore, the smaller particles will experience a relatively larger drag force while their inertia force will be relatively small. As a result, the smaller

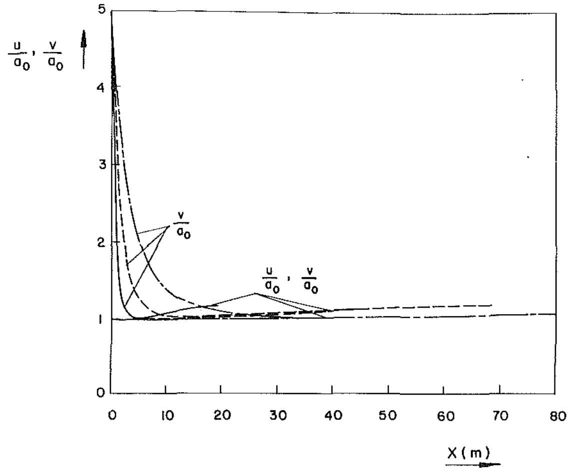

Fig. 7 Gas velocity (u) and carbon velocity (v) variations in the relaxation zone for $M = 5$, $\eta = 0.01$ and $P_0 = 50$ torr; ________ $D_0 = 50$ µm, — — — $D_0 = 100$µm, — — — — $D_0 = 200$ µm

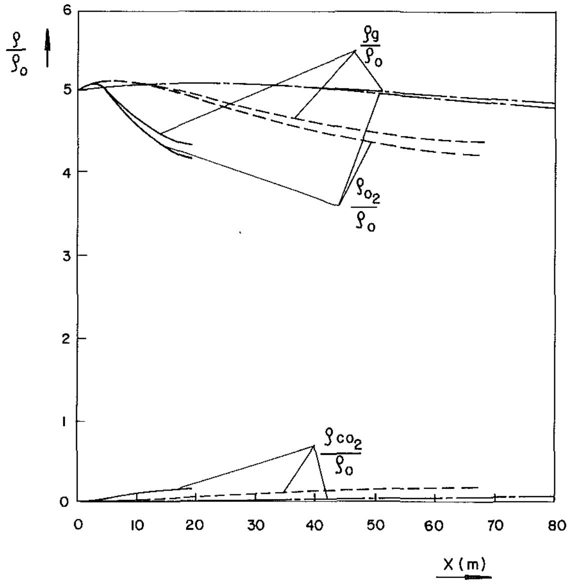

Fig. 8 Density variations of the suspension gases in the relaxation zone for $M = 5$, $\eta = 0.01$ and $P_0 = 50$ torr; ________ $D_0 = 50$ µm, — — — $D_0 = 100$ µm, — — — — $D_0 = 200$ µm

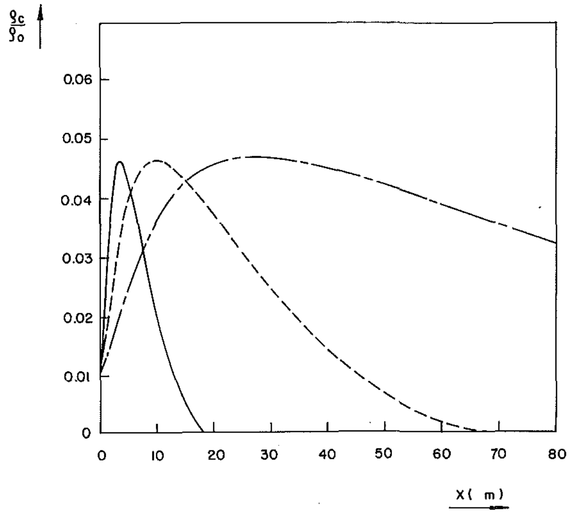

Fig. 9 Carbon density variations in the relaxation zone for $M = 5$, $\eta = 0.01$ and $P_0 = 50$ torr; ________ $D_0 = 50$ µm, — — — $D_0 = 100$ µm, — — — — $D_0 = 200$ µm

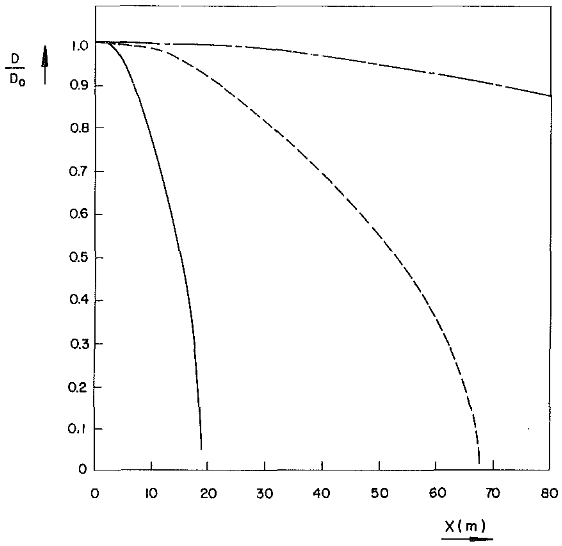

Fig. 10 Variations in the carbon particle diameter in the relaxation zone for $M = 5$, $\eta = 0.01$ and $P_0 = 50$ torr; ________ $D_0 = 50$ µm, — — — $D_0 = 100$ µm, — — — — $D_0 = 200$ µm

the particle is, the greater its deceleration becomes to result in a relatively short kinematic relaxation zone (see Fig. 7). Since the total carbon mass is the same for all three cases, they all reach the same postshock wave equilibrium suspension velocity (the equilibrium state for $D_0 = 200$ µm is not shown in Fig. 7).

The density variations experienced by the various suspension components are shown in Figs. 8 and 9. As could be expected, the smaller carbon particles ($D_0 = 50$ µm) burn faster to result in a relatively short relaxation zone. For $D_0 = 50$ µm the carbon particles disappear (via burning) after less than 20 m (see Fig. 9); at this distance ρ_{O_2} and ρ_{CO_2} reach their postshock wave equilibrium values (see Fig. 8). On the other hand, it takes close to 200 m, measured downstream of the shock front, for the larger carbon particles ($D_0 = 200$ µm) to burn out completely (out of scale in Fig. 9). As previously observed, for velocities and temperatures, here, too, the same postshock wave equilibrium densities (ρ_g, ρ_{O_2}, and ρ_{CO_2}) will be reached for all three cases since all have the same initial carbon mass in the suspension. (The postshock wave equilibrium value for ρ_C is, of course, zero since the carbon particles are completely burnt out at the end of the relaxation zone.) The variations in the carbon particle diameter in the relaxation zone are shown for the three different initial particle diameters in Fig. 10. As already observed in Fig. 9, the smaller particles disappear faster than the larger ones.

The effect of the initial particle size on the pressure variations in the relaxation zone is shown in Fig. 11. Again, the smaller the particle is, the faster a postshock wave equilibrium suspension pressure is reached. However, the same equilibrium pressure is reached eventually for the three cases. In summary, changes in D_0 mainly affect the suspension behavior inside the relaxation zone; they especially affect the extent of this zone. The smaller D_0 is, the shorter the relaxation zone becomes. However, changes in D_0 do not affect the eventually reached postshock wave equilibrium state (for constant values of η and M).

Changes in the Shock Wave Mach Number. Changes in the shock wave Mach number have a marked effect on the suspension properties in the relaxation zone. This is due to the fact that the frozen temperature (reached immediately behind the shock front) strongly depends upon M; see the Rankine-Hugoniot shock relations [3]. The carbon combustion will take place in the relaxation zone only if the postshock wave

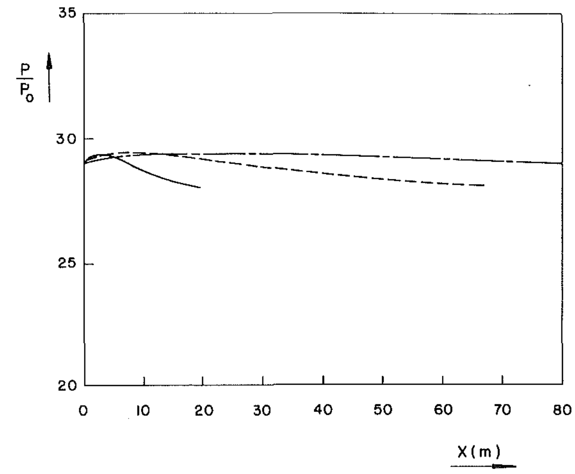

Fig. 11 Pressure variations in the relaxation zone for M = 5, $\eta = 0.01$ and $P_0 = 50$ torr; ________ $D_0 = 50$ μm, _ _ _ _ $D_0 = 100$ μm, __ __ __ $D_0 = 200$ μm

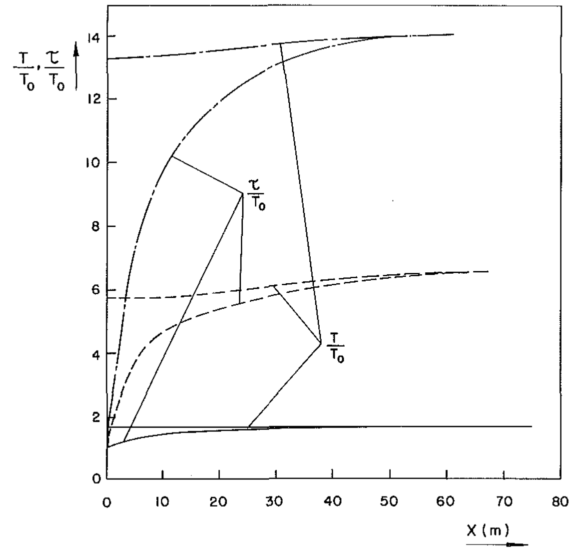

Fig. 12 Gas temperature (T) and carbon temperature (τ) variations in the relaxation zone for $\eta = 0.01$, $P_0 = 50$ torr and $D_0 = 100$ μm; ________ M = 2, _ _ _ _ M = 5, __ __ __ M = 8

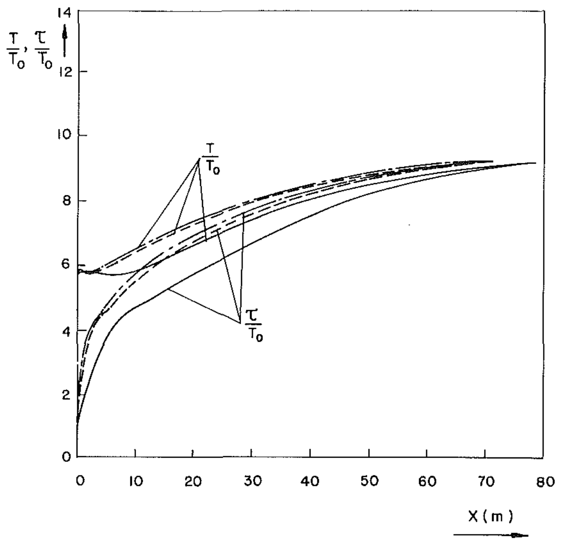

Fig. 13 Gas temperature (T) and carbon temperature (τ) variations in the relaxation zone for M = 5, $D_0 = 100$ μm and $\eta = 0.01$; ________ $P_0 = 50$ torr, _ _ _ _ $P_0 = 380$ torr, __ __ __ $P_0 = 760$ torr

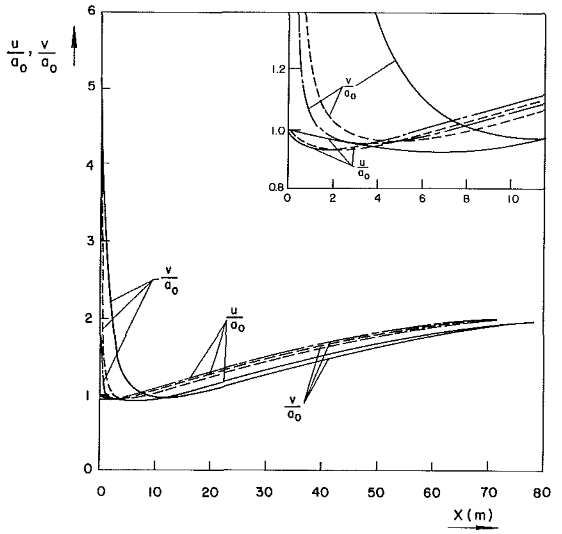

Fig. 14 Gas velocity (u) and carbon velocity (v) variations in the relaxation zone for M = 5, $D_0 = 100$ μm and $\eta = 0.01$; ________ $P_0 = 50$ torr, _ _ _ _ $P_0 = 380$ torr, __ __ __ $P_0 = 760$ torr

gas temperature reaches the carbon ignition temperature. It should therefore be expected that a critical shock wave Mach number exists. Below this value, the suspension remains inert (no carbon combustion) while above it the carbon burns throughout the relaxation zone. For the combustion model used [1], the critical shock wave Mach number was found to be equal to 2.75 (provided that $T_0 = 300$ K).

The temperature variations in the relaxation zone are shown in Fig. 12 for three different shock wave Mach numbers – M = 2, 5, and 8. (Eight was chosen as the upper limit for M since the present work treats the gaseous phase as an ideal gas.) It is clear from this figure that for M = 2, the suspension behaves as an inert one since the postshock wave gas temperature does not reach the carbon ignition temperature. For M = 5 and 8, the carbon particles burn in the relaxation zone to result in an increase in both T and τ in comparison with the inert case, see Fig. 12. The larger M is, the higher both T and τ becomes. This is expected since larger values of M mean higher postshock wave frozen gas temperatures [3]. The carbon burning further increases the temperature of the suspension components.

The variations in the other flow properties, in the relaxation zone, will have similar patterns, i.e., for M = 2 the suspension will behave like an inert one while for M = 5 or 8 the carbon burning will significantly affect the suspension properties in the relaxation zone. Detailed results for the variations in velocity, density, pressure, and the carbon particle diameter can be found in reference [2].

Changes in the Preshock Suspension Pressure. In the last set of numerical results, the dependence of the suspension properties in the relaxation zone on the preshock suspension pressure are shown. The Rankine-Hugoniot shock relations relate the pressures across the shock front [3],

$$\frac{P_f}{P_0}=\frac{2\gamma}{\gamma+1}\mathrm{M}^2-\frac{\gamma-1}{\gamma+1}$$

where P_0 and P_f are the pressures ahead and immediately behind the shock wave front, respectively; γ and M are the ratio of specific heat capacities and the shock wave Mach number, respectively. It is apparent from this expression that the higher P_0 is the larger P_f becomes, provided that all other parameters are kept constant. The temperature ratio across the shock front is given by [3].

$$\frac{T_f}{T_0} = 1 + \frac{2(\gamma - 1)}{(\gamma + 1)^2}(M^2 - 1)\left(\gamma + \frac{1}{M^2}\right)$$

Since T_0 is kept constant ($T_0 = 300$ K) in the present study, it is clear that T_f depends solely upon M. As a result, for a given M, the equation of state for an ideal oxygen gas ($P = \rho_{O_2} R_{O_2} T$) indicates that increasing P_0 will cause an increase in ρ_{O_2} (on both sides of the shock front). However, the carbon burning rate increases with increasing oxygen density [1]. Therefore, it should be expected that increasing P_0 should shorten the extent of the relaxation zone. This is indeed the case as is evident from Figs. 13 and 14 where the temperature and velocity variations in the relaxation zone are shown. The more intense burning, caused by higher oxygen content in the suspension (associated with increasing P_0), will cause higher gas (T) and carbon (τ) temperatures and velocities in the relaxation zone (see Figs. 13 and 14). However, the postshock wave equilibrium suspension temperature and velocity are practically independent of P_0. The more intense burning caused by higher oxygen density immediately behind the shock front (associated with higher P_0's) will cause a faster depletion in the combustion reactants. On the other hand, intense carbon burning will produce CO_2 faster, to result in higher values of ρ_{CO_2} in the relaxation zone. Detailed descriptions of the variations in ρ_g, ρ_{O_2}, ρ_C, and ρ_{CO_2} can be found in reference [2]. It is also shown there [2] that changes in P_0 mildly affects the pressure variations in the relaxation zone, i.e., the higher P_0 is, the lower the suspension pressure becomes. However, the eventually reached postshock wave equilibrium pressure is practically independent of P_0.

Conclusions

In the preceding parametric study, the dependence of the flow properties of the suspension in the relaxation zone on the initial carbon concentration, the initial carbon particle diameter, the shock wave Mach number and the preshock wave suspension pressure were evaluated. it was found that changes in the initial carbon concentration and/or the shock wave Mach number have a marked effect on the suspension properties, while changes in the initial carbon particle diameter and/or the preshock suspension pressure have only a minor effect on the suspension behavior in the relaxation zone. Specifically, increasing the initial carbon concentration (at $M = 5$) significantly increases the thermal energy released during combustion and thereby markedly affects the temperature and velocity variations in the relaxation zone. When η is changed from $\eta = 0.001$ to $\eta = 0.05$ the postshock equilibrium suspension temperature increases by 50 percent and the equilibrium suspension velocity by 100 percent.

Changing the carbon particle initial diameter (at constant M and η) does not affect the postshock equilibrium suspension state. However, it does affect the way in which the suspension approaches this equilibrium state. The smaller the carbon particle is, the shorter the relaxation zone becomes. For $D_0 = 50$ μm it takes about 20 m to reach the postshock equilibrium state; it takes almost 200 m when $D_0 = 200$ μm.

The shock wave Mach number plays a key role in the kinematic and thermodynamic behavior of the postshock wave suspension flow. For a relatively low shock wave Mach number, the gas temperature reached immediately behind the shock front is too low for carbon ignition, and the suspension remains inert. For the carbon burning model used, the critical shock wave Mach number was found to be $M = 2.75$ (provided that $T_0 = 300$ K). Above this value, combustion takes place and the suspension behavior is strongly dependent upon the specific value of M. For example, when M is increased from five to eight, the postshock wave equilibrium suspension temperature is more than doubled and so is the postshock equilibrium suspension pressure. Changes in the preshock suspension pressure will mildly affect the suspension behavior in the relaxation zone. Increasing P_0 increases the oxygen density immediately behind the shock front and thereby intensifies the carbon burning. It does not affect the postshock equilibrium suspension temperature and velocity.

It should be noted here, that the present model assumes a perfect gas behavior of all the gaseous components. In reality, at the temperatures obtained in this study CO_2 and O_2 will partially dissociate. This dissocation processes will be associated with reduction of the postshock temperatures.

References

1 Elperin, I., Igra, O., and Ben-Dor, G., "Analysis of Normal Shock Waves in a Carbon Particle Laden Oxygen Gas," ASME JOURNAL OF FLUIDS ENGINEERING, Vol. 108, No. 3, 1986, pp. 354-359.

2 Elperin, I., "The Effect of Carbon Particles on the Flow Field Developed Behind a Normal Shock Wave in Oxygen," M.Sc. Thesis, Department of Mechanical Engineering, Ben-Gurion University of the Negev, 1964.

3 Owczarek, J. A., *Fundamentals of Gasdynamics*, International Textbook Co., Scranton, PA, 1984, pp. 174-180.

Cavitation Nuclei Measurements With an Optical System

M. L. Billet
Senior Scientist,
Applied Research Laboratory,
The Pennsylvania State University,
State College, PA 16804

Many recent experiments have shown the significance of cavitation nuclei, i.e., gas bubbles and/or particulate; however, progress in making quantitative predictions of cavitation depends upon some knowledge of cavitation nuclei properties such as shape, size distribution and concentration. Thus, research has also been concerned with developing measuring systems that give the statistics of the cavitation nuclei distribution. There are many different systems currently being developed; however, only the accuracy and application of the light-scattering technique initially developed by Keller is addressed in this paper. A model is formulated based on appropriate statistical analysis that defines the accuracy for a given sample size. Very good agreement has been found between microbubble distributions measured with the light-scattering system and with holography. Microbubble distribution data were obtained in the 305 mm water tunnel for different air content levels, tunnel static pressures and several tunnel velocities. These data are compared to nuclei distributions obtained at other facilities.

Introduction

Cavitation nuclei is a general term used to refer to the impurities that cause weak spots in liquid and thus prevent the liquid from supporting higher liquid tensions. Various forms of cavitation nuclei have been theorized; however, they can be considered in one of two groups, i.e., stream nuclei and surface nuclei. Stream nuclei exist in the liquid in such forms as solid particulates or microbubbles. Surface nuclei originate in the surface of the fluid boundary, by means of cracks and crevices in the boundary. Many experimental investigations (i.e., see references [1] and [2]) have shown that stream nuclei are a more important source of cavitation nuclei. An excellent review of cavitation nuclei and its qualitative relationship to cavitation inception is given by Holl [3].

An evaluation of the cavitation inception characteristics of a body was determined by conducting "standard" cavitation tests at many facilities for the ITTC [4]. Results show that the fluid dynamics, i.e., boundary layer, turbulence, etc., and the bubble dynamics, i.e., stream nuclei, do significantly influence cavitation inception. As a direct result, many subsequent experiments have been conducted in order to establish the relative importance of the fluid dynamics and bubble dynamics. The work of Arakeri and Acosta [5] and Van der Meulen [6] clearly demonstrates the role of boundary layer separation on cavitation inception. In other work of Kuiper [7], Billet and Gates [8], Ooi [9], and Katz [10] the importance of stream nuclei has been established. A recent interview of cavitation inception is given by Shen and Peterson [11].

During this same period, work has begun on developing techniques to measure cavitation nuclei. Two significantly different approaches have been developed. One is to measure the particulate/microbubble distributions by utilizing acoustical [12, 13], electrical [14, 15], or optical techniques [16–19]. The other approach measures a rate of cavitation events for a liquid under various tensions and establishes a cavitation susceptibility [20–22].

The two most popular techniques applied to particulate/microbubble measurements are the optical technique such as holography, light-scattering, phase detection, photography, etc. and the acoustic technique. A review of some of these methods is given by Morgan [23] and Peterson, et al. [24]. Several good comparisons of optical techniques have been made by Peterson et al. [24], Billet and Gates [25], and Katz, et al. [26]. Another recent comparison that includes both approaches is given by Godefroy et al. [27].

From a review of the comparisons, it becomes evident that each technique has some disadvantages which lead to inaccuracies in measurements. It is not the intent here to discuss these advantages/disadvantages but to address the question of how accurate measurements can be made of a statistical process. This of course brings up the question of accuracy required to correlate cavitation inception data.

An analysis has been developed for the light-scattering technique in order to estimate measurement accuracy. This technique is one of the more popular techniques and has been utilized in a system developed at ARL/PSU [28, 29] to discriminate between particulate and microbubbles.

Light-Scattering System

System Configuration. A light-scattering system has been developed that utilizes the laser light-scattering technique introduced by Landa and Tebay [37] and Keller [16] and is shown schematically in Fig. 1. This system is based on the relationship between the radius of a scattering sphere and the scattered intensity. A comparison between experimental data and

---

Contributed by the Fluids Engineering Division for publication in the JOURNAL OF FLUIDS ENGINEERING. Manuscript received by the Fluids Engineering Division, November 27, 1984.

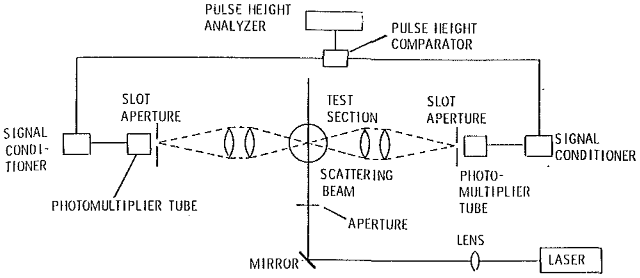

Fig. 1 Schematic of light-scattering system

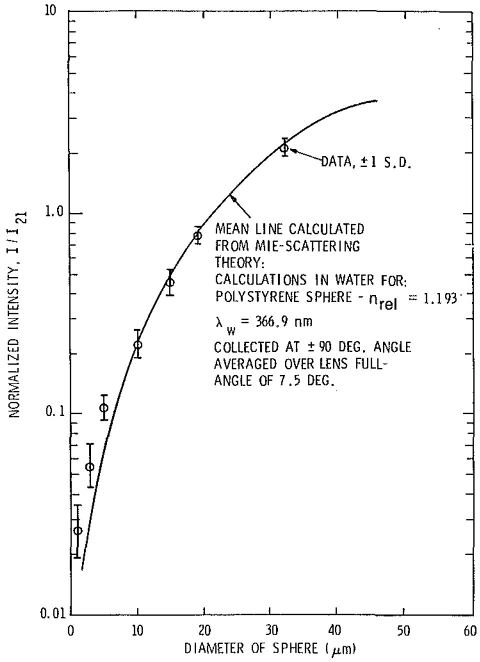

Fig. 2 Comparison between calculated and measured scattered intensities for spheres in water

Mie theory [30, 31] is given in Fig. 2. In this figure, the experimental data were obtained by injecting polystyrene spheres into the center of the probe volume in a tank of water and measuring the maximum intensity at a position 90 deg to the beam axis. Because the collection efficiency of the scattered light is unknown, a comparison can only be made by normalizing the data by the appropriate measured/calculated intensity of a 21 μm sphere (I_{21}). The calculations were made for the polystyrene sphere in water for the parameters listed in Fig. 2. Some deviation can be noted between theory and data as the diameter approaches the wavelength of the incident light.

An on-line method was developed to discriminate between the light scattered from microbubbles and particulates. An analytical investigation [28] showed that using the asymmetry of the particulate relative to the postulated spherical symmetry of the microbubbles discrimination can be accomplished by comparing intensities scattered at opposing angles. Experimental results [32] obtained in a water tunnel environment confirm that discrimination can be obtained when the results were compared to holographic data. This comparison was only done in the 20 to 100 μm diameter size range. However, discrimination is only necessary when the particulate population is significant when compared to the microbubble population.

The system is based on the principle that the measured maximum scattered intensity of a microbubble as it passes through a light beam can be uniquely related to the size of the microbubble and thus, the light-scattering system operates in the following manner. The light scattered by a microbubble as it passes through the probe volume is collected by a lens and is focused on a photomultiplier tube (PM). The PM has an aperture which restricts one dimension of the probe volume. The output of the PM goes through a signal conditioner. The pulse height processor now accepts the conditioned pulse, assesses the amplitude of each detected pulse and sorts the pulses into programmable classification channels until a predetermined total number of pulses is achieved. A display then gives the number of pulses in each classification channel. Each classification channel corresponds to a microbubble size range which is determined by a calibration procedure. The number per unit volume is obtained from the reference velocity, measuring time and dimensions of the probe volume as defined for each classification channel.

The calibration procedure consists of injecting polystyrene spheres having a nominal diameter of 21 μm through the center of the probe volume and measuring the maximum detected amplitude in situ. Because of a difference in scattering characteristics, the amplifier gain is adjusted so that the amplitude for the 21 μm polystyrene sphere corresponds to the higher amplitude of a 21 μm air bubble on the predetermined calibration curve for air bubbles. This air bubble curve was obtained in a similar manner as shown in Fig. 2 for polystyrene spheres in water. Comparisons were made between experimental data with air bubbles in water and Mie theory using a relative refractive index of 0.750 by normalizing the data curves with the appropriate measured/calculated intensity of a 21 μm bubble. It is important to note that the normalized Mie curve for the polystyrene spheres is different than that for the air bubbles. The probe volume is determined by

Nomenclature

A = voltage amplitude
B = constant
C = column matrix of detected count rates
D = sphere diameter
G = gain of the photomultiplier and associated electronics
$I(x,y)$ = intensity of the light beam in the control volume
$F(\alpha,\Omega,\eta_{rel})$ = scattering response function
n = index of refraction
N = column matrix of detected count rates
$\bar{N}$ = number density function (see equation (6))
n = index of refraction
r = effective optical distance from particle to photomultiplier
R = radius of bubble
ΔS_{ij} = equivalent cross-sectional area of the measuring volume which yields amplitudes in the range A_i to $A_i + \Delta A_i$ for microbubbles having normalized response functions in the range F_j to $F_j + \Delta F_j$
U = bulk velocity of the flow
x,y = coordinates
α = particle size parameter ($\pi D/\lambda$)
λ = light wavelength
i, j = indices referring to the channel number
Ω = solid angle into which light is scattered

Subscripts

a = air
w = water
rel = relative

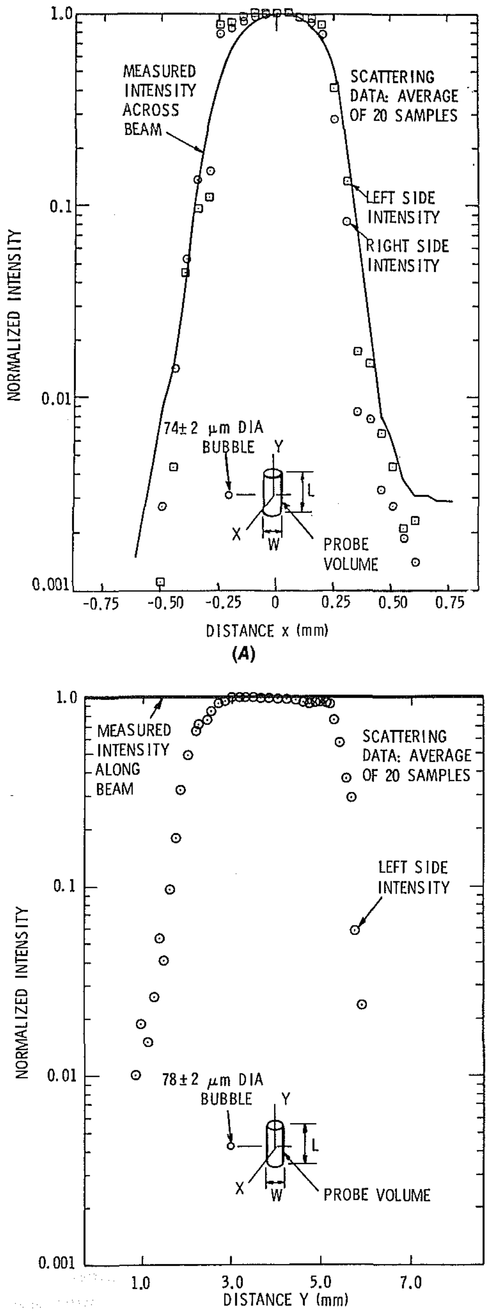

Fig. 3 Normalized maximum scattered intensity of a bubble along (A) the axis normal to the light beam and (B) the axis of the light beam

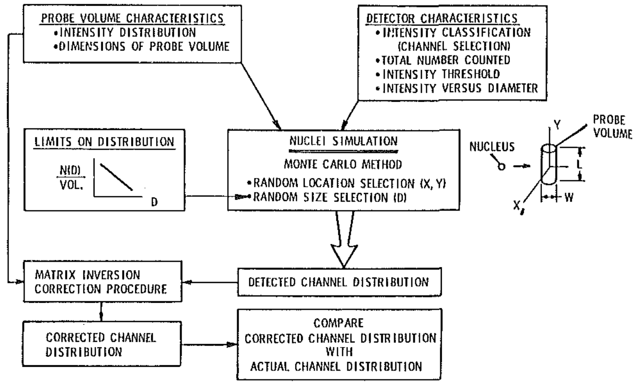

Fig. 4 Schematic of probe volume statistical analysis

measuring the intensity distribution by a detector with a 10 μm diameter aperature in situ.

The largest measurement inaccuracy in the light-scattering system is caused by the threshold determined by the electronics. Small changes in the amplitude near the threshold give rise to large size variations in the region below 10 μm. In order to minimize this problem, a minimum size of approximately 6 μm diameter was imposed which results in a dynamic range of 80 to 6 μm for the system.

Accuracy Analysis. The largest classifying error of the light-scattering technique is the tendency for spherical microbubbles of a given size to register numbers in not only the classification channel corresponding to that size but also in all channels lower than that size. This is due to the probe volume having a nonuniform light intensity. Figure 3A shows the normalized intensity of a mean 74 μm diameter bubble as it passes along an axis normal to the light beam and Fig. 3B shows a bubble as it passes along the axis of the light beam. The intensity of the light beam was measured by traversing a detector with a 10 μm aperature in the water. The bubble was generated by electrolysis and its size was verified by holography. The effect of the aperature located on the PM tube on the effective probe volume can be clearly noted.

The net effect of the nonuniform light beam is that the count histogram does not reflect directly the actual distribution of size measured so that microbubble distributions cannot be measured with confidence. The amplitude of the voltage pulse produced by a photomultiplier as a result of a microbubble entering the measuring volume of the light can be expressed as

$$A = G\frac{\lambda^2}{4\pi^2 r^2} I(x,y)F(\alpha,\Omega,n_{\rm rel}). \tag{1}$$

To correct for this, an inversion scheme that accounts for the nonuniformity of the light intensity in the probe volume has been applied to the technique. This mathematical method of evaluation was adapted from an analysis proposed by Holve and Self [33] and is documented in Yungkurth and Billet [29].

Thus, equation (1) can be generalized in terms of discrete classification channels as

$$C_i = U\Delta S_{ij} N_j. \tag{2}$$

It is important to note that the S_{ij} elements are simply probabilities.

The actual data received in a microbubble-counting experiment are the C_i collected in the channels of the pulse height analyzer. The information desired is the microbubble density, N_j, thus equation (2) can be written as

$$N_j = \frac{1}{U} C_i \Delta S_{ij}^{-1} \tag{3}$$

where ΔS_{ij}^{-1} is the inverse of the matrix ΔS_{ij} in equation (2). Thus it can be noted from equation (3) that the nuclei number density in one channel is actually a weighted sum of the count rates from every channel. The matrix coefficients of equation (3) can be easily determined from measurement of the light intensity distribution of the probe volume and the specification of the classification channel amplitudes.

Even utilizing an inversion procedure to account for the nonuniformity of the light intensity, the question of system accuracy cannot be answered. The system requires an appropriate statistical sample of the microbubbles before the inversion procedure can account for the nonuniformity of the light intensity distribution and the sample size must be addressed before the determination of the system accuracy can be made.

A computer model of the probe volume – microbubble

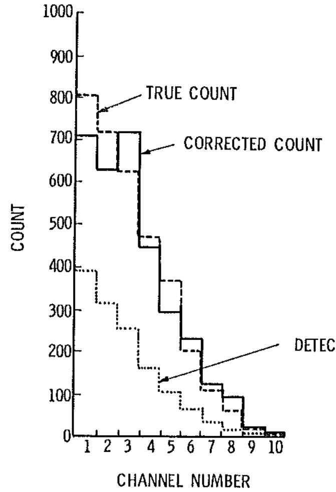

Fig. 5 Gaussian intensity distribution data for 1323 count sample

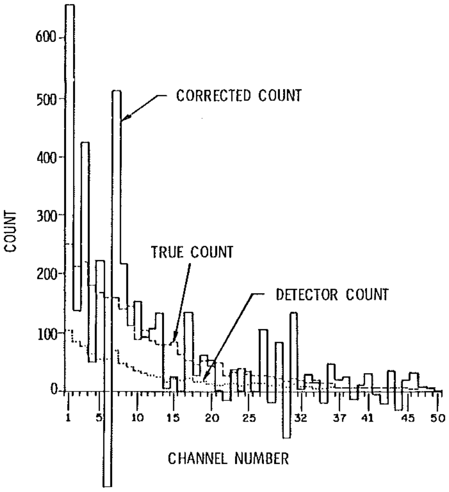

Fig. 6 Gaussian intensity distribution data for 50 classification channels and 5000 count sample

distribution – inversion procedure interaction has been developed in reference [34]. A schematic of the simulation program is shown in Fig. 4. The inputs to the program are the probe volume criteria and detector criteria. The output is the corrected channel distribution and actual distribution of the nuclei. The detector criteria involve specifying the size range of nuclei to be classified, the number of classification channels in which the nuclei are to be counted, the threshold level at which the nuclei will be detected and the calibration curve for intensity versus diameter.

The nuclei similation is a Monte Carlo type program in which the size (diameter) and the location within the probe volume (x, y coordinates) are randomly determined. In addition, limits can be imposed on the size distribution so that numbers for a specific size can be maintained.

The output of the program is the detected channel distribution, the corrected channel distribution and the actual size distribution. The inversion procedure is used to correct the detected distribution for the probe volume intensity distribution.

Results clearly demonstrate the importance of probe volume intensity distribution and the channel resolution on sizing nuclei correctly. In addition, the accuracy of the light-scattering system also depends upon the sample size. Several different probe volume intensity distribution such as Gaussian, triangular and logarithmic were used in the simulation model. The Gaussian intensity distribution gave the best correlation and Fig. 5 shows the correlation of the true nuclei distribution with the detector and the corrected count. For this result a sample size of only 1000 counts was used and only ten channels were utilized. The corresponding nuclei sizes are as follows:

Channel No.	Size, μm-Maximum Diameter
1	8
2	10
3	13
4	17
5	22
6	29
7	37
8	48
9	62
10	80

The relative widths of the channel were scaled logarithmically; that is, the upper limit amplitude, A_i, of a given channel i was related to the upper limit voltage amplitude of the next channel, A_{i+1}, according to

$$\frac{A_{i+1}-A_i}{A_i}=B \tag{4}$$

where $B=0.6$ for this model. By relating the channel widths logarithmically, only ten elements of the inversion matrix had to be determined. The Gaussian intensity distribution gave the best correlation because the S_{10} matrix element had a higher probability than any other single element. Thus, the nuclei had a highest probability of being sized correctly.

The importance of channel width on the matrix procedure can be noted by comparing Fig. 6 to Fig. 5. In Fig. 6 the correlation is given for 50 channels over the same size range shown in Fig. 5 (10 channels). Obviously, the best correlation can be obtained using only one channel. As channel number increases the matrix procedure has more errors. This is due to the fact that the probability of sizing a microbubble in the correct channel becomes smaller and smaller. More results of the nuclei simulation model are given in reference [34].

Clearly, the accuracy of any channel number depends, because of the matrix method, on the accuracy of the channels above it as well as its own inherent error. While the uncertainty in S_i is dependent upon the accuracy of the measurement of the laser beam cross-section intensity distribution, it might be agreed that the measurement of the intensity distribution should be less than approximately ±2 percent. Thus, the errors are mostly due to the counting statistics in the form of the number counted (C_i) and the probabilities (S_j).

It is difficult to define the random counting errors of this complex process; however, assuming that Poisson statistics can be used for desired confidence levels, an approximate expression for a 95 percent level is given as

$$\frac{\Delta C_i}{C_i}=\frac{2}{\sqrt{C_i}}. \tag{5}$$

Using equation (5) an error analysis [34] shows possible large counting error when a channel has only a few counts. If the next lower channel has a larger number of counts, the effect of the error of the higher channel will be reduced. Since typical microbubble populations in water have very few large microbubbles and many small microbubbles, the propagation of errors through the matrix inversion method is minimized. However, equation (5) can only be utilized with a large sample size, i.e., channel counts in the order of 1000 or greater.

One cannot insure a minimum sample size in a channel in order to satisfy the criteria for equation (5). Thus, a number of computer runs was done with the model in which only the sample size was varied in order to address the accuracy question for small sample sizes. Four groups of 30 runs each were

Table 1 Nuclei simulation data in terms of percent error with 1000 count samples

					Channel No.					
Run No.	1	2	3	4	5	6	7	8	9	10
1	-15.3	21.4	13.5	-14.8	-11.5	13.3	-100.0	-27.3	100.0	-100.0
2	10.5	-29.1	19.3	9.9	14.0	-37.8	-2.8	-40.9	50.0	-100.0
3	4.8	15.8	-22.1	1.0	13.8	-50.6	28.9	40.0	50.0	-100.0
4	17.0	-15.6	-6.1	19.8	-67.2	-9.5	13.5	-31.6	-66.7	50.0
5	-0.8	1.3	-0.5	-18.9	14.2	-29.0	-90.4	30.0	-50.0	-100.0
6	6.3	-16.3	14.5	6.3	-48.2	43.0	-51.5	-23.5	50.0	-100.0
7	4.1	-8.8	-17.1	32.5	-23.3	-30.0	29.7	-36.0	125.0	-100.0
8	-0.5	2.3	-0.8	3.1	-34.0	-37.2	37.0	106.7	-100.0	-100.0
9	11.3	-0.1	-5.3	-10.7	-8.82	18.3	-18.4	17.4	20.0	-100.0
10	13.6	-20.2	3.6	13.7	13.0	-88.5	57.7	-43.5	-25.0	-100.0
11	3.9	-21.8	10.8	-21.6	9.15	12.2	-33.3	-3.7	-25.0	-100.0
12	-13.4	-3.0	6.0	8.8	-12.3	9.9	-46.2	-46.2	20.0	-100.0
13	-0.4	12.2	-18.4	10.7	-29.2	-40.7	102.5	-100.0	-76.5	350.0
14	1.3	-16.2	-10.8	10.6	2.2	-6.2	-22.6	20.0	-100.0	-100.0
15	2.1	3.6	4.3	-48.8	40.1	-34.9	-7.3	-100.0	362.0	-100.0
16	-3.3	9.9	-6.9	-20.7	10.6	-52.3	91.3	-93.3	-25.0	-100.0
17	-5.9	2.1	-8.4	2.4	-13.6	16.3	-16.7	-12.5	50.0	-100.0
18	-6.6	13.2	-0.3	14.7	-45.1	-27.3	53.8	30.0	-14.3	-100.0
19	6.4	-19.1	16.8	-21.6	-9.7	-22.0	44.4	-56.3	-91.7	20.0
20	1.0	-21.0	-26.6	27.6	34.8	-1.3	-16.7	16.7	71.4	-100.0
21	-12.1	-3.8	15.5	-28.5	25.1	40.5	-44.8	-13.3	-90.0	200.0
22	-2.1	-0.5	-8.2	-4.3	-3.6	-4.3	-18.6	11.1	-14.3	-100.0
23	4.2	0.4	-14.4	-28.1	41.2	20.5	-51.2	100.0	287.0	-100.0
24	-1.3	-10.3	-16.7	-5.4	9.0	-9.4	-5.7	-63.6	125.0	-100.0
25	7.8	16.0	-25.4	35.8	-15.8	-80.3	-35.0	75.0	38.5	-100.0
26	-8.0	6.9	-14.4	5.9	9.8	-73.2	2.5	5.3	-40.0	0.0
27	23.4	2.7	-38.8	19.9	-2.3	-26.9	-23.3	5.3	-50.0	-100.0
28	20.7	8.5	-0.2	-17.6	-34.8	11.8	-30.6	52.4	-85.7	-25.0
29	-3.3	-18.0	7.1	10.7	-37.1	21.7	-30.6	92.9	0.0	-100.0
30	10.9	-19.3	-14.2	-4.8	0.6	-61.9	57.9	0.0	50.0	-100.0
Total Counts										
Actual Distribution	38530	22722	17266	9485	4914	2558	1115	547	254	103
Predicted Distribution	39483	21929	16421	9455	4673	2118	1070	489	286	42

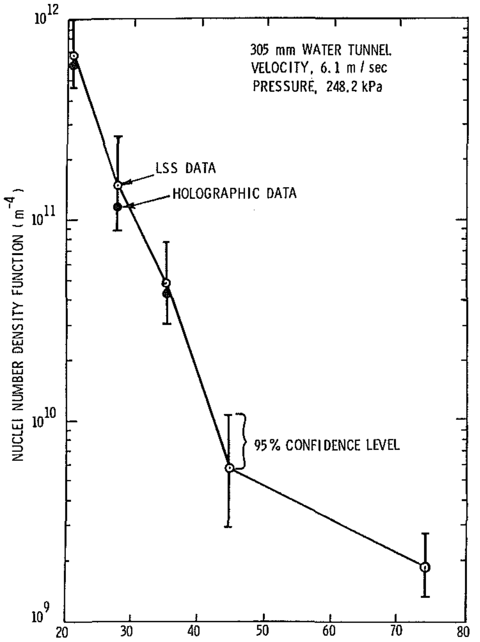

Fig. 7 Nuclei number density data for $V = 6.1$ m/s, $P = 248.2$ kPa in 305 mm water tunnel

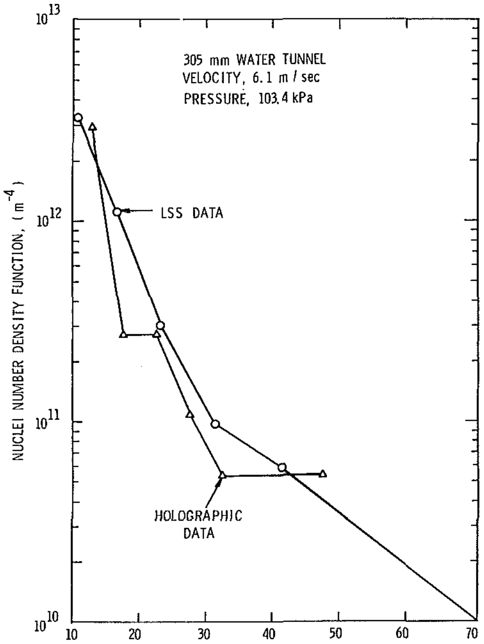

Fig. 8 Nuclei number density data for $V = 6.1$ m/s, $P \simeq 103.4$ kPa in 305 mm water tunnel

made for sample sizes of 1000, 5000, 10,000, and 20,000. The data for the 1000 count cases are given in Table 1 in terms of percent error. As can be noted the random counting errors are very significant with small sample sizes. For larger sizes, the errors were smaller and some agreement was found with equation (5).

Water Tunnel Nuclei Distributions. Measurements of microbubble/particulate distributions were made in the 305 mm water tunnel of the Applied Research Laboratory at The Pennsylvania State University. This facility is described in detail in Reference [35]; however, it is important to note that the air content level in the tunnel is controlled by a degassing system. During these tests the air content level was varied from 1.6 ppm to 8.9 ppm. At this level of air content, very few macroscopic gas bubbles were visible. In addition, the velocity range was 6.1 m/s to 19.3 m/s and the test section static pressure was varied from 68.9 kPa to 206.8 kPa. These conditions approximate the normal operating conditions for this tunnel.

Two of the 18 nuclei distributions measured in the tunnel are shown in Figs. 7 and 8. These nuclei distributions are expressed in terms of a number density function which is defined as

$$\bar{N}\left\{\frac{R_1 - R_2}{2}\right\} = \frac{\text{number of particles per unit volume with radii between } R_1 \text{ and } R_2}{R_2 - R_1} \qquad (6)$$

and are plotted versus nuclei diameter.

It can be noted that a very good comparison was found between measurements obtained with the light-scattering system and holography. These holographic data were obtained with a Korad holocamera utilizing an in-line Fraunhofer technique which was similar to that discussed in reference [11]. The bar lines shown on the light-scattering data in Fig. 7 indicate the 95 percent confidence level using the model given in equation (5). In addition, the sample size for the light-scattering data was approximately 3,000 counts per sample. It is important to note that the light-scattering data were obtained using only one detector because the dirt concentration was very low due to filtering.

The correlation shown in Fig. 8 is very good. It is important to note that at these conditions very few microbubbles were observed on the hologram and only 3000 counts were obtained by the light-scattering system. However, the accuracy of the light-scattering system is clearly a function of the number of counts in each classification channel. These data at $D \simeq 21\ \mu m$ show that the accuracy of the system is ±45 percent and at $D \simeq 45\ \mu m$ the accuracy is ±100 percent. The nuclei concentration at $D \simeq 45\ \mu m$ is only $0.05/cm^3$.

A summary of water tunnel microbubble/particulate data is given in Table 3 where numbers of nuclei/cc are listed. It can be noted that in this water tunnel environment some trends can be observed. For a given velocity and air content level, the number of microbubbles changed little with static pressure. For a given air content level the microbubble concentration is almost independent of velocity and pressure. The largest variation in microbubble concentration was obtained by changing air content level.

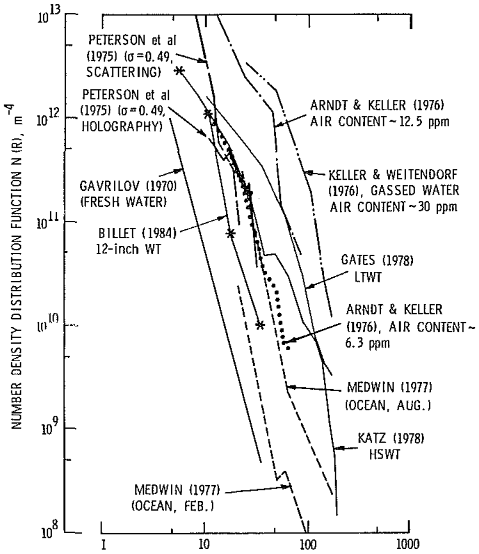

Fig. 9 Comparison of number density distribution data

These data indicate that within this water tunnel environment these bubbles do not appear to be in equilibrium with the test section static pressure. This is not surprising because higher pressures exist in other parts of the tunnel and because of the pump, turning vanes, etc. The air content was varied by continuously degassing some of the tunnel water in a vacuum tank. In addition, this by-pass system has filters which will change the dirt concentration.

A comparison of number densities with other data obtained from Katz [36] is shown in Fig. 9. Only the maximum number data of bubbles obtained with the holographic system are plotted.

Summary

Many experimental investigations at laboratories worldwide have attempted to correlate cavitation nuclei data obtained with various measurement systems with cavitation inception data. The bulk of this literature demonstrates that this is a very difficult problem due to not only the statistical nature of cavitation but also to the complex interaction of bubble dynamics and fluid mechanics. For example, the sensitivity to nuclei determined for a hemispherical nosed body will be different than that found for a jet. It is extremely difficult to correlate a small change in nuclei distributions to a change in cavitation inception. Therefore, it is equally difficult to determine the significance of the error in nuclei measurements on the observed variation in cavitation inception.

The accuracy or confidence level of the data as measured by a light-scattering system is a complex interaction between random counting errors and sizing errors (matrix element). An at-

Table 2 Summary of error data for log-normal bubble distribution

Classification Channel Number:

1	2	3	4	5	6	7	8	9	10	
$\frac{1316}{7.4}$	$\frac{731}{11.6}$	$\frac{547}{12.2}$	$\frac{315}{16.0}$	$\frac{156}{21.1}$	$\frac{71}{31.0}$	$\frac{36}{38.8}$	$\frac{16.3}{43.1}$	$\frac{9.5}{75.1}$	$\frac{1.4}{101.5}$	Average Number* / Mean Error - %
$\frac{4010}{6.0}$	$\frac{2218}{8.2}$	$\frac{1705}{6.9}$	$\frac{881}{11.5}$	$\frac{453}{13.5}$	$\frac{217}{22.0}$	$\frac{99}{27.4}$	$\frac{54.2}{31.4}$	$\frac{21.2}{46.7}$	$\frac{8.0}{63.0}$	
$\frac{6567}{4.5}$	$\frac{3787}{5.3}$	$\frac{2741}{6.2}$	$\frac{1506}{8.4}$	$\frac{755}{10.4}$	$\frac{392}{16.1}$	$\frac{165}{20.7}$	$\frac{81.6}{24.9}$	$\frac{32.3}{36.9}$	$\frac{15.9}{41.2}$	
$\frac{12949}{2.6}$	$\frac{7568}{3.6}$	$\frac{5635}{4.7}$	$\frac{3016}{6.9}$	$\frac{1496}{8.9}$	$\frac{758}{12.7}$	$\frac{300}{17.6}$	$\frac{180.1}{17.8}$	$\frac{71.5}{25.3}$	$\frac{26.9}{35.7}$	
$\frac{26449}{2.6}$	$\frac{14960}{3.4}$	$\frac{11285}{3.7}$	$\frac{5829}{6.8}$	$\frac{3054}{7.0}$	$\frac{1483}{12.3}$	$\frac{671}{12.4}$	$\frac{342.5}{14.2}$	$\frac{152.6}{18.1}$	$\frac{55.6}{28.0}$	

*Average Corrected Count Based on 30 Cases

Table 3 Nuclei data obtained in 305 mm water tunnel

			Number of Bubbles/cc						Dirt/cc
Velocity m/sec	Pressure kPa	Air Content Level ppm	10 - 20 μm Holo	10 - 20 μm LSS	20 - 40 μm Holo	20 - 40 μm LSS	40 - 80 μm Holo	40 - 80 μm LSS	10 - 80 μm Holo
6.1	68.9	8.9	12.0	7.5	0.8	1.5	-	0.3	1.9
6.1	103.4	8.9	11.5	20.0	2.2	2.5	0.8	0.4	3.5
6.1	206.8	8.9	11.5	16.0	1.9	1.5	-	0.2	2.7
12.2	103.4	8.9	10.1	19.0	2.4	3.5	0.5	0.5	3.2
12.2	137.9	8.9	11.5	20.0	3.2	3.5	0.5	0.5	2.3
12.2	206.8	8.9	19.2	19.0	2.9	2.8	-	0.4	-
6.1	68.9	5.1	1.1	0.7	-	0.1	-	-	2.1
6.1	103.4	5.1	1.1	0.7	-	0.1	-	-	-
6.1	206.8	5.1	1.1	0.6	-	0.1	-	-	-
12.2	68.9	5.1	7.2	15.0	0.5	0.9	-	-	1.5
12.2	103.4	5.1	5.4	15.0	0.8	0.7	0.5	-	-
12.2	206.8	5.1	8.9	12.0	1.9	0.6	0.3	-	-
18.3	103.4	5.1	7.8	10.1	2.7	5.2	0.5	0.4	2.3
18.3	206.8	5.1	6.4	5.0	1.3	0.4	-	-	0.9
12.2	68.9	1.6	2.5	3.0	1.6	0.4	-	0.1	-
12.2	103.4	1.6	2.0	4.5	-	0.5	-	0.1	-
12.2	206.8	1.6	2.4	4.0	0.5	0.6	-	0.1	-

tempt has been made to establish this relationship so that the number of counts and size resolution can be established in order to obtain an accuracy in experiments.

The accuracy of a nuclei measurement system that determines the number density of microbubbles/particulate is a complex function of not only the problem of errors in sizing but also of random counting errors. The number density function is formed from a finite number of classification channels as well as a finite number of samples. In most cases, the random counting errors are much larger than errors in sizing. Thus, it is very difficult to obtain the accuracy in numbers and size distribution required to correlate cavitation variations without very large samples and reducing the number of classification channels. Decreasing the number of classification channels improves the count accuracy; however, size resolution is lost. Large samples require long measurement times that are in most cases prohibited because of flow variations.

An analytical model of the light-scattering system has been developed in order to investigate the complex relationship between sizing errors and random counting errors. Results show that accurate sizing of microbubbles can be accomplished with the probe volume having a Gaussian intensity distribution. The inversion procedure does account for probe volume intensity variations; however, small size range resolution cannot be obtained with any acceptable accuracy. Errors are minimized by using larger classification channels whose channel widths are related logarithmically.

Acknowledgments

This paper is part of a continuing investigation of nuclei effects on cavitation inception at the Garfield Thomas Water Tunnel of the Applied Research Laboratory of The Pennsylvania State University. This work is sponsored by the Naval Sea Systems Command, Code NSEA-63R31. The author wishes to acknowledge William Moyer who designed the electronics for the light-scattering system and Robert Davis and Tim Davis who helped greatly in the development of the statistical model.

References

1 Treaster, A. L., "Cavitation Hysteresis," M.S. thesis, Department of Aerospace Engineering, The Pennsylvania State University, June 1964.

2 Gupta, S. K., "The Influence of Porosity and Contact Angle on Incipient and Desinent Cavitation," M.S. thesis, Department of Aerospace Engineering, The Pennsylvania State University, December 1969.

3 Holl, J. W., "Nuclei and Cavitation," ASME *Journal of Basic Engineering*, Dec. 1970, pp. 681-688.

4 Lindgren, H., and Johnson, C. A., "Cavitation Inception on Head Forms ITTC Comparative Experiments," Pub. of the Swedish State Shipbuilding Exper. Tank, No. 58, 1966.

5 Arakeri, V. H., and Acosta, A. J., "Viscous Effects in Inception of Cavitation on Axisymmetric Bodies," ASME JOURNAL OF FLUIDS ENGINEERING, Dec. 1973, pp. 519-526.

6 Van der Meulen, J. H. J., "A Holographic Study of Cavitation on Axisymmetric Bodies and the Influence of Polymer Additives," Publication No. 509, Netherlands Ship Model Basin, Wageningen, The Netherlands, 1976.

7 Kuiper, G., "Cavitation Inception on Ship Propeller Models," Ph.D. dissertation, Netherlands Ship Model Basin, 1981.

8 Gates, E. M., and Billet, M. L., "Cavitation Nuclei and Inception," *Proceedings of IAHR Symposium*, Tokyo, Japan, 1980, pp. 3-25.

9 Ooi, K. K., "Scale Effects on Cavitation Inception in Submerged Jets," California Institute of Technology, Report No. Eng. 183-6, December 1981.

10 Katz, J., "Cavitation Inception in Separated Flows," California Institute of Technology, Report No. Eng. 183-5, Dec. 1981.

11 Shen, Y. T. and Peterson, F. B., "Cavitation Inception," *Proceedings of 20th American Towing Tank Conference*, Stevens Institute of Technology, Hoboken, N.J., 2-4 Aug. 1983.

12 Schiebe, F. R., and Killen, J. M., "An Evaluation of Acoustic Techniques for Measuring Gas Bubble Size Distributions in Cavitation Research," St. Anthony Falls Hydraulic Laboratory, Report No. 120, May 1971.

13 Medwin, H., "Acoustical Determination of Bubble Size Spectra," *J. of Acoust. Soc. Am.*, Vol. 62, 1977, pp. 1041-1044.

14 Yilmaz, E., Hammitt, F. G., and Keller, A., "Cavitation Inception Thresholds in Water and Nuclei Spectra by Light-Scattering Technique," *J. Acoust. Soc. Am.*, Vol. 59, 1976, pp. 329-338.

15 Oba, R., "Cavitation Nuclei Measurements by a Newly Made Coulter Counter Without Adding Salt in Water," *Rep. Inst. High Speed Mech.*, Tohoku University, Vol. 43, No. 340, 1981.

16 Keller, A. P., "The Influence of the Cavitation Nucleus Spectrum on Cavitation Inception, Investigated With a Scattered Light Counting Method," ASME *Journal of Basic Engineering*, Dec. 1972, pp. 917-925.

17 Gates, E. M., and Bacon, J., "Determination of Cavitation Nuclei Distributions by Holography," *J. Ship Res.*, Vol. 22, No. 1, Mar. 1978, pp. 29-31.

18 Gowing, S. and Ling, S. C., "Measurements of Microbubbles in a Water Tunnel," *Proceedings of the 19th American Towing Tank Conference*, University of Michigan, Ann Arbor, Mich., July 1980, pp. 1023-1048.

19 Farmer, W. M., "Sample Space for Particle Size and Velocity Measuring Interferometers," *Applied Optics*, Vol. 15, No. 8, 1976, pp. 1984-1989.

20 Oldenziel, D. M., "New Instrument in Cavitation Research," *International Symposium on Cavitation Inception*, ASME, New York, N.Y., Dec. 1979, pp. 111-124.

21 Lecoffre, Y. and Bonnin, J., "Cavitation Tests and Nucleation Control," *International Symposium on Cavitation Inception*, ASME, New York, N.Y., 2-7 Dec. 1979, pp. 141-146.

22 d'Agostino, L., and Acosta, A. J., "On the Design of Cavitation Susceptibility Meters (C.S.M.'s)," *Proceedings of the 20th American Towing Tank Conference*, Stevens Institute of Technology, Hoboken, N.J., 2-4 Aug. 1983.

23 Morgan, W. B., "Air Content and Nuclei Measurements," 13th ITTC Report of Cavitation Committee, 1972.

24 Peterson, F. B., Danel, F., Keller, A. P., and Lecoffre, Y., "Comparative Measurements of Bubble and Particulate Spectra by Three Optical Methods," 14th ITTC Report of Cavitation Committee, 1975.

25 Billet, M. L., and Gates, "A Comparison of Two Optical Techniques for Measuring Cavitation Nuclei," ASME JOURNAL OF FLUIDS ENGINEERING, Vol. 103, Mar. 1981, pp. 8-13.

26 Katz, J., Gowing, S., O'Hern, T., and Acosta, A., "A Comparative Study Between Holographic and Light Scattering Techniques of Microbubble Detection," *Proceedings of I.U.T.A.M. Symposium on Measuring Techniques in Gas-Liquid Two-Phase Flows*, Nancy, France, July 1983.

27 Godefray, H. W. H. E., Jansen, R. H. J., Keller, A. P., Lecoffre, Y., Oldenziel, D. M., and van Renesse, R. L., "Comparison of Measuring and Control Methods of the Water Quality With Respect to Cavitation Behavior," Delft Hydraulics Laboratory, Jan. 1981.

28 Kohler, R. A., and Billet, M. L., "Light Scattering by a Nonspherical Particle," Cavitation and Polyphase Flow Forum – 1981, ASME, Boulder, Colo., June 1981.

29 Yungkurth, C. B., and Billet, M. L., "A Calibration Procedure for a Light-Scattering System," Cavitation and Polyphase Flow Forum – 1981, ASME, Boulder, Colo., June 1981.

30 Van de Hulst, H. C., *Light Scattering by Small Particles*, New York, Wiley, 1957.

31 Kerker, M., *Scattering of Light*, New York, Academic Press, 1969.

32 Yungkurth, C. B., "A Light-Scattering System to Measure Cavitation Nuclei: Analysis and Calibration," Master thesis, Dept. of Aerospace Engr., The Pennsylvania State University, Mar. 1983.

33 Holve, D., and Self, S. A., "An Optical Particle-Sizing Counter for In-Situ Measurements," Technical Report for Project SQUID, Office of Naval Research, Subcontract 8960-7, Jan. 1978.

34 Davis, R. J., and Billet, M. L., "Light-Scattering System: Probe Volume Statistical Analysis," Cavitation and Multiphase Flow Forum – 1983, Houston, Texas, June 1983.

35 Holl, J. W., "Cavitation Research Facilities at The Ordnance Research Laboratory of The Pennsylvania State University," *Proceedings of the ASME Symposium on Cavitation Research Facilities and Techniques*, 1964, pp. 11-18.

36 Katz, J., "Determination of Solid Nuclei and Bubble Distribution in Water by Holography," Report No. Eng. 183-3, California Institute of Technology, June 1978.

37 Landa, I. and Tebay, E. S., "The Measurement and Instantaneous Displays of Bubble Size Distribution, Using Scattered Light," Cavitation Forum – 1970, ASME, Detroit, Mich., May 1970.

Cavitation in Large Scale Shear Flows

J. Katz
Department of Civil Engineering,
Purdue University,
West Lafayette, IN 47907

T. J. O'Hern
Department of Mechanical Engineering,
California Institute of Technology,
Pasadena, CA 91125

Cavitation phenomena were studied in the shear layer behind a two-dimensional sharp-edged plate. Observations were made under stroboscopic light and by flash photography. The first traces of cavitation appear as a series of narrow long axial "strings" suggesting that the major contributor to cavitation inception is the longitudinal (axial) secondary shear layer eddy structure. In a more developed state the cavitation takes the form of a spanwise large eddy structure but the axial "strings" are still evident. The local cavitation inception indices based on the local velocity and pressure scatter between 1.0 and 1.4 when the water is saturated with dissolved air and vary between 0.8 and 1.2 when the air content is reduced to about 30 percent of saturation. These results are in good agreement with a collection of other measurements behind sharp-edged disks that display a consistent increase of the inception index with the Reynolds number.

Introduction

The close relation between the turbulent flow field and cavitation phenomena around bodies with large separation regions has been observed by several investigators. Kermeen and Parkin (1957) and Arndt (1978), for example, in studies of cavitating flow behind sharp-edged disks found that inception of cavitation occurred in the free shear layer downstream of separation, and that the cavitation inception indices increased with the body Reynolds number. They also observed a spanwise coherent eddy structure in the mixing layer and suggested that the onset of cavitation occurred in the low pressure region at the core of the vortices.

A similar increase of cavitation inception index with the Reynolds number was observed by Arakeri (1979), who studied the flow around an axisymmetric body with a downstream facing step, by van der Muelen (1980) on hydrofoils at large angles of attack, and by Katz (1981), who studied the cavitating flow around blunt circular cylinders.

Arndt (1976) attempted to explain this scaling trend of the inception indices by assuming that the onset of cavitation occurred in the core of the large shear layer eddies and that the size of these eddies depended on the boundary layer upstream of separation. His model led to a semiempirical relation in which the cavitation index was proportional to the square root of the Reynolds number. However, numerous studies of plane shear flows by Brown and Roshko (1974), Konrad (1976), Breidenthal (1978), and Bernal (1981) have demonstrated that the size and strength of the large mixing layer eddies does not depend on the velocity above the shear layer, but only on axial distance from separation. The transition zone affected by the separating boundary layer is limited to a small region, at most approximately 1000 times the momentum thickness at separation (see Hussain and Zedan (1978) for details). Thus, the scaling trend of the cavitation inception indices remains to be fully explained.

The preceding investigations form a background for the present study of cavitation phenomena in the two-dimensional shear layer behind a sharp-edged plate. The preliminary objectives are to determine the scaling trend of the inception index at high Reynolds number ($> 10^6$), and to carefully observe the relation between flow field characteristics, such as the structure of the turbulent shear layer, and cavitation phenomena.

Experimental Setup and Procedures

A schematic description of the experimental setup is presented in Fig. 1. The system consists of a vertical sharp-edged plate that extends completely across the 12 in. span of the test section of the Caltech Low Turbulence Water Tunnel. This plate is elevated 1 in. above the floor of the test section, and a 20 in. long horizontal plate separates the two regions of the flow. This bypass is installed in order to eliminate the effect of the turbulent boundary layer of the bottom wall. A series of 5 vertical holes are drilled inside the sharp-edged plate. Each hold can be connected either to a pressure tap on the front (upstream facing) surface or to a 100 micron pinhole orifice injector located in the oblique section behind the plate. The pinholes will later be used for injection of small bubbles and can be replaced with pressure taps. A series of delrin plugs are used for sealing either injectors or the pressure taps (or both) when not in use.

The present cavitation observations were made under stroboscopic light. The tests were carried out by maintaining the tunnel at a constant velocity and gradually reducing the pressure until the first traces of cavitation appeared. At that moment the pressure transducer reading was frozen and recorded together with the tunnel velocity. The water was recirculated for at least 10 minutes at atmospheric pressure before repeating the experiment, to reduce and maintain a steady population of free stream bubbles (see Katz (1981), for details). During the tests at high velocities it was necessary to pressurize the tunnel before each test since the flow was

---

Contributed by the Fluids Engineering Division for publication in the JOURNAL OF FLUIDS ENGINEERING. Manuscript received by the Fluids Engineering Division, March 28, 1985.

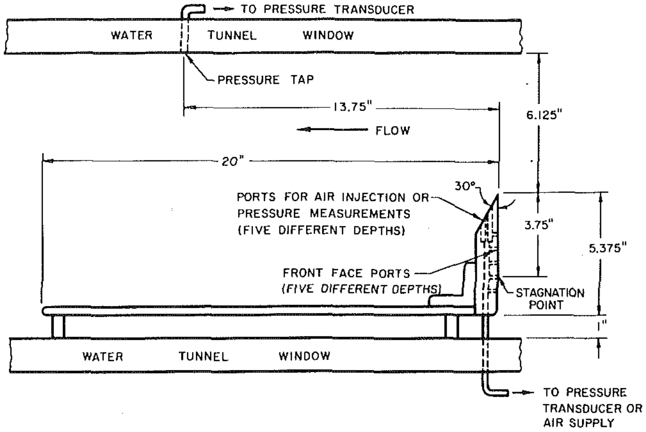

Fig. 1 A schematic description of the experimental setup

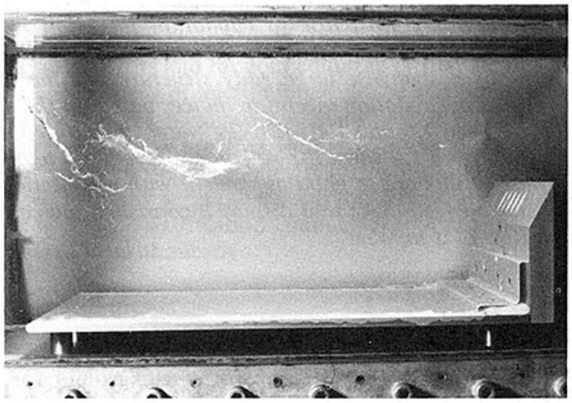

Fig. 2 Side view of cavitation behind the sharp-edged plate, $Re_S = 2.17 \times 10^6$, $\sigma_L = 0.762$

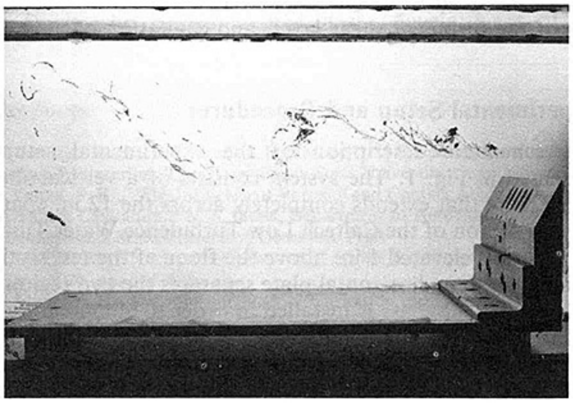

Fig. 3 Side view of cavitation behind the sharp-edged plate, $Re_S = 2.25 \times 10^6$, $\sigma_L = 0.628$

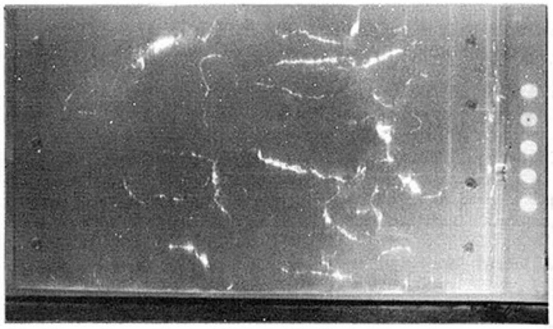

Fig. 4 Top view of cavitation behind the sharp-edged plate, $Re_S = 2.28 \times 10^6$, $\sigma_L = 0.601$

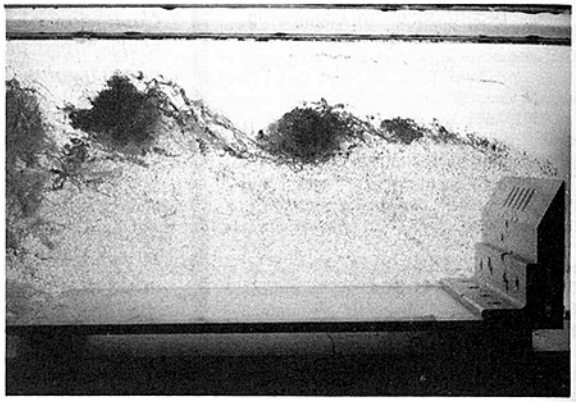

Fig. 5 Advanced stage of cavitation behind the sharp-edged plate, $Re_S = 1.89 \times 10^6$, $\sigma_L = 0.375$

already cavitating at atmospheric conditions. The location of the tap for making velocity and pressure measurements (defined presently as the local values) is specified in Fig. 1. A comparison between the conditions at this point to the pressure behind the knife edge resulted in a constant value of $(P_{BP} - P_L)/(1/2\rho U_L^2) = 0.069$. The amount of air dissolved in the water was controlled with a dearating system (see Ooi (1981) for details) and was measured with a van slyke device.

Results

Figures 2 and 3 are side views and Fig. 4 is a top view of the early states of cavitation behind the sharp-edged plate. As is evident from these micro-second flash photographs, the cavitation first appears as a series of narrow *axial-streamwise* "strings" located in the turbulent shear layer and distributed across the span of the water tunnel. In a more developed state (lower σ), as shown in Fig. 5, the cavitation appears primarily in the shape of the large scale *spanwise* eddy structure, although the existence of the axial strings is still evident between the large lateral vortices. These spanwise eddies do not appear in Figs. 2-4; as a matter of fact, it seems that the early

Nomenclature

P_L = local pressure
P_∞ = pressure at infinity
P_v = vapor pressure at room temperature
P_{BP} = pressure directly behind knife edge
S = distance between knife edge stagnation and separation points
U_L = local velocity, measured above the shear layer
U_∞ = velocity at infinity
C_{PB} = base pressure coefficient
Re_D = diameter Reynolds number, given by $$\frac{U_\infty D}{\nu}$$
Re_S = Reynolds number based on U_L and 2S, given by $$\frac{U_L \cdot 2S}{\nu}$$
ν = kinematic viscosity of water
σ_i = cavitation inception index, given by $$(P_\infty - P_v)\Big/\left(\frac{1}{2}\rho U_\infty^2\right)$$
σ_L = local cavitation inception index, given by $$(P_L - P_v)\Big/\left(\frac{1}{2}\rho U_L^2\right)$$
ρ = density of water

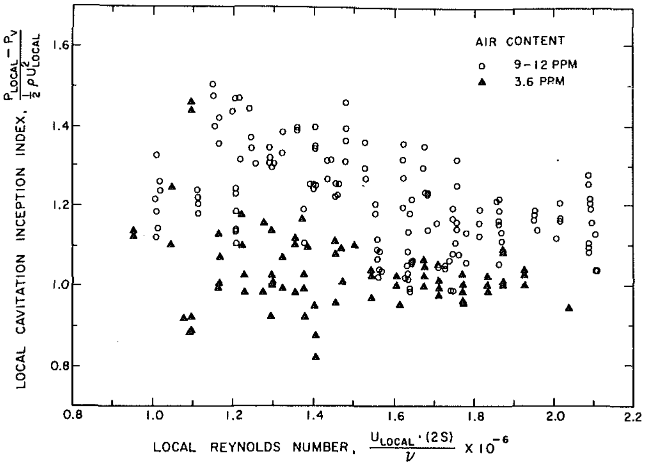

Fig. 6 Cavitation inception indices behind the sharp-edged plate

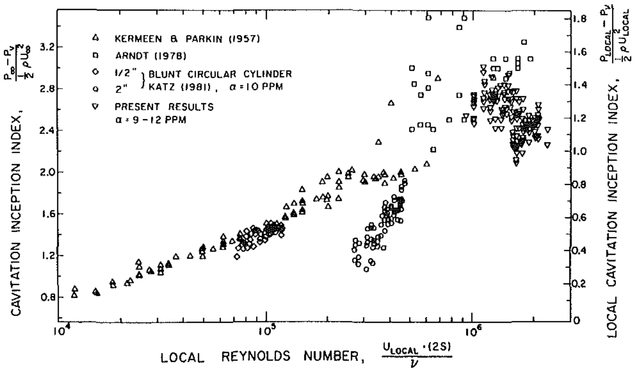

Fig. 7 A collection of cavitation inception indices from various sources

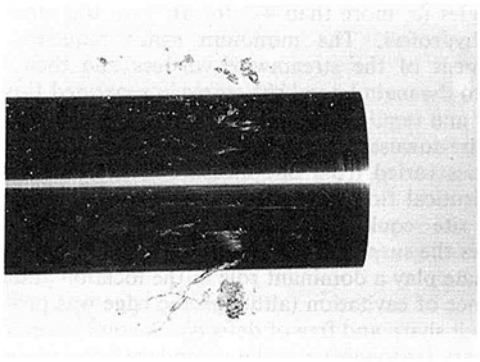

Fig. 8 Inception of cavitation on a blunt circular cylinder. Taken from Katz (1981) $\sigma_i = 1.7$, $Re_D = 3.6 \times 10^5$

stages of cavitation occur mainly between the large eddies. Thus, these photographs provide evidence that although the main flow structure consists of coherent spanwise eddies, the *major contribution* to the onset of cavitation is made by the "secondary" axial vortices of the mixing layer. The existence of these eddies and their relation to the large spanwise structure was reported first by Konrad (1976) and then studied by Breidenthal (1978) and Bernal (1981). The strength of these vortices and their dependence on the flow conditions is not yet known. However, according the Bernal (ibid), the axial vortices originate from disturbances located upstream of their point of appearance. These disturbances are amplified from their origin up to a visible state. The axial location of the visibility threshold can be shifted either upstream or downstream by raising or lowering the Reynolds number. The number of these axial vortices and their spanwise pattern also changes when the velocity is increased. Thus, the present photographs of cavitation and the findings of Bernal may provide the missing link needed for explanation of the dependence of the cavitation inception index on the Reynolds number.

Local cavitation inception indices are plotted against the Reynolds number in Fig. 6. In order to compare the present results to other experimental data, the length scale in the Reynolds number is chosen to be twice the distance between the stagnation point and the separation point (the location of the stagnation point was determined by observation of the motion of small bubbles injected from the front surface pressure taps.) As is evident from Fig. 6, the local cavitation inception indices scatter between 1.0 and 1.4 when the amount of air dissolved in the water is 9-11 ppm and scatter between 0.8 and 1.2 when the air content is 3.5 ppm. Due to the scatter of the present results, and the narrow range of velocities available in the test facility, the inception indices do not display a clear trend with the Reynolds number. Since the population of free stream bubbles in the test facility depends on the amount of air dissolved in the water (see Ooi (1981) and Katz et al (1982)), the results in Fig. 6 suggest a strong dependence of the inception indices on the bubble population density. This point will be explored in the future when the pressure field and the bubble population in this flow will be studied in detail. Figure 7 compares the present results at high air content to the measurements of Kermeen and Parkin (1957) and Arndt (1978) behind sharp-edged disks and those of Katz (1981) around a blunt circular cylinder. Since the present measurements are of the local cavitation inception indices, and the values of σ_i in the other experiments are based on the pressure and velocity at infinity, the coordinates of Fig. 7 were adjusted according to the relation $\sigma_L = (\sigma_i + C_{P_B})/(1 - C_{P_B})$. Here C_{P_B} is the minimum base pressure coefficient which was measured by both Kermeen and Parkin (ibid) and Katz (ibid) and the average value of all of these is taken to be -0.6. The values of the Reynolds number were also adjusted to the local velocity. As is evident in Fig. 7, the present measurements fall within the results of Arndt (1978) and seem to be an extrapolation of the Kermeen and Parkin (ibid) results. Thus even though the presently measured inception indices do not, by themselves, display a clear trend with the velocity, they are in good agreement with the general trend of the cavitation index increase with the Reynolds number.

Discussion

The remarkable physical appearance and location of inception is not unique to the flow geometry described in this paper; the same phenomena has been observed in other types of free shear flows. Figure 8, for example, displays very similar cavities at the onset of cavitation on a flat blunt circular cylinder, as observed in the work of Katz (1981). Similar phenomena were also observed by van der Muelen (1980) in the flow near hydrofoils at high angles of incidence. Thus, there are other types of flows in which the onset of cavitation occurs in the streamwise, secondary turbulent structure of a shear layer. This is not the case, however, in every type of separated flow. For example, this phenomenon has not been observed in cases where the dimensions of the separated regions are too small to allow the development of the streamwise vortices, at least not to a visible size. Examples of these types of flows are hemispherical bodies with and without downstream facing steps (Arakeri (1979), Katz (1981)), and hydrofoils at small angles of attack (van der Muelen (1980)). These flows exhibit inception in the turbulent shear layer, but developing in the lateral (spanwise) structures. The resulting inception indices are usually much lower as is demonstrated by comparing van der Muelen's (ibid) results obtained at small angles of incidence (σ_i about 0.5 for 2°) to those obtained at large angles (σ_i more than 4.0 for 16°) on the same NACA 16-012 hydrofoil. The minimum space required for the development of the streamwise vortices and their strength relative to the main lateral structures in separated flows is not yet clear and requires further study.

Both the downstream and spanwise location of the first visible cavities varied from one measurement to the next, even under identical flow conditions. Therefore, no preferred inception site could be detected. This random behavior eliminates the suspicion that imperfections on the sharp edge of the plate play a dominant role in the location and physical appearance of cavitation (although the edge was protected to maintain it sharp and free of defects). Beyond inception, both the primary (spanwise) and the secondary (streamwise) structures were visible. At the present time, however, we made no attempt to identify whether these turbulent structures appear at distinct number, pattern or location.

A large scatter is seen in the data obtained in the present cavitation tests. The scatter is larger in the lower Reynolds number range, 1.0×10^6 to 1.4×10^6, than in the higher values. The present measurements were carried out using velocity and pressure transducers having a 0.5 percent accuracy, so the measurement error is much smaller than the scatter of the data. Actually, the size of the marks indicating data points in Figs. 6 and 7 (circles or triangles) are larger than the instrumentation error. Since detection of inception was done visually, some error may result from the response of the observer. However, inception could be observed clearly in this flow as it occurred in the free stream far from the test body. Thus, experimental uncertainty played only a minor role in the scatter of the results. The major component of scatter is the fact that the onset of cavitation (in any type of flow) requires the coincidence of at least two events, a low enough pressure (occurring in the streamwise cores in this flow) and a microscopic free stream cavitation nucleus (bubble or particulate containing a gas cavity) of such a size that it becomes unstable at the local pressure. The availability of bubbles is lower at low speeds, therefore, fewer inception sites are available. In addition, the location spacing and pattern of the axial vortices may depend on the Reynolds number, thus altering the number of sites even further. As a result, the probability for inception varies with the velocity. Since the present measurements were carried out by gradually lowering the pressure, the availability of cavitation nuclei and the number of sites at a particular time affects the inception indices measured. Probability studies (such as those of Ooi (1981) in water jets) will require much more knowledge about the basic flow structure and levels of pressure fluctuations. These studies are currently being carried out by the second author.

Summary and Conclusion

Observations of cavitation phenomena in a two-dimensional shear layer behind a sharp-edged plate were carried out in the Caltech Low Turbulence Water Tunnel. Two kinds of vortex motion were observed in these experiments, a spanwise large-scale eddy structure and a secondary axial or streamwise eddy. Cavitation *inception* was found to occur in the axial vortices mainly in the portion between the spanwise eddies. At lower pressures cavitation takes the form of the spanwise vortices but the axial vortices always remain evident.

The cavitation inception indices display a strong dependence on the air content and thus on the population of free stream bubbles. The present results do not, by themselves, display a clear trend with the velocity but are consistent with the assumed trend of the cavitation inception index of sharp-edged bodies to increase with the Reynolds number. No attempt to develop a model to explain the scaling trend of the inception index was made since very little is known about the streamwise secondary vortices. However, since these phenomena of shear flows are currently being studied by several investigators, some answers should be forthcoming in the near future.

Acknowledgment

The authors would like to thank Dr. A. J. Acosta for his advice and guidance during the course of the present study. This work was supported by Naval Sea System Command General Hydro-mechanics Research Program administered by the David Taylor Naval Ship Research and Development Center under Contract No. 00014-75-0378.

References

1 Arakeri, V. H., (1979), "Inception of Cavitation From a Backward Facing Step," *International Symposium on Cavitation Inception*, ASME Winter Annual Meeting, New York, Dec. 2–7, also ASME JOURNAL OF FLUIDS ENGINEERING, Vol. 103, June, pp. 288–293.

2 Arndt, R. E. A., (1976), "Semiempirical Analysis of Cavitation in the Wake of a Sharp-Edged Disk," ASME JOURNAL OF FLUIDS ENGINEERING, Vol. 98, pp. 560–562.

3 Arndt, R. E. A., (1978), "Investigation of the Effects of Dissolved Gas and Free Nuclei on Cavitation and Noise in the Wake of a Sharp-Edged Disk," Joint IAHR/ASME/ASCE Symposium on Fluid Machinery, Ft. Collins, Colo.

4 Bernal, L. P., (1981), "The Coherent Structure of Turbulent Mixing Layers, I. Similarity of the Primary Vortex Structure, II. Secondary Streamwise Vortex Structure," Graduate Aeronautical Laboratories, Calif. Inst. of Tech., June.

5 Breidenthal, R. E., (1978), "A Chemically Reacting Turbulent Shear Layer," Ph.D. thesis, Calif. Inst. of Tech.

6 Brown, G. L., Roshko, A., (1974), "On Density Effects and Large Structure in Turbulent Mixing Layers," *J. Fluid Mechanics*, Vol. 64, pp. 775–816.

7 Hussain, A. K. M. F., Zedan, M. F., (1978), "Effects of the Initial Condition on the Axisymmetric Free Shear Layer: Effects of the Initial Momentum Thickness," Physics of Fluids, Vol. 21, July, pp. 1100–1112.

8 Katz, J., (1981), "Cavitation Inception in Separated Flows," Ph.D. thesis, Calif. Inst. of Tech., Report No. 183-5.

9 Katz, J., Gowing, S., O'Hern, T. J., Acosta, A. J., (1982), "A Comparative Study Between Holographic and Light-Scattering Techniques of Microbubble Detection," Calif. Inst. of Tech., Report No. 261-1, Dec.

10 Kermeen, R. W., Parkin, B. R., (1957), "Incipient Cavitation and Wake Flow Behind Sharp-Edged Disks," Calif. Inst. Tech., Hydrodynamic Lab Report No. 85-4, Aug.

11 Konrad, J. H., (1976), "An Experimental Investigation of Mixing in Two-Dimensional Turbulent Shear Flows with Applications to Diffusion-Limited Chemical Reactions," Ph.D. thesis, Calif. Inst. of Tech., Project SQUID, Technical Report CIT-8-PU.

12 Ooi, K. K., (1981), "Scale Effects on Cavitation Inception in Submerged Jets," Ph.D. thesis, Calif. Inst. of Tech., Report No. 183-6.

13 van der Meulen, J. H. J., (1980), "Boundary Layer and Cavitation Studies of NACA 16-012 and NACA 4412 Hydrofoils," 13th Symposium on Naval Hydrodynamics, Sasakawa Hall, Tokyo, Japan, Oct. 6–10.

Journal of Fluids Engineering

Technical Briefs

Contraction Coefficients for Borda Mouthpieces

Wei-guo Dong[1] **and John H. Lienhard**[1]

Nomenclature

a = distance from a point at which D_j is measured to the point above it, at which we want to know $D_{j,\text{actual}}$
C, C_1 = arbitrary constants
C_C = coefficient of contraction, (jet area)/(aperture area)
C_D = coefficient of discharge, $C_c C_v$
C_v = coefficient of velocity, (jet velocity)/$\sqrt{2gh}$
D, D_j = diameter of a Borda mouthpiece, diameter of the jet from a Borda mouthpiece
g = acceleration of gravity
h = head above a Borda mouthpiece
M = $4([2L/D]^2+1)$
L = length of a Borda mouthpiece
p = pressure in the liquid
Re = Reynolds number, $\rho D\sqrt{2gh}/$(viscosity)
r = radial coordinate around the axis of the Borda mouthpiece
u = liquid velocity
We = Weber number, $\rho D(2gh)/\sigma$
ρ = liquid density
σ = surface tension

Introduction

Figure 1, which is half sketch and half photograph, shows liquid emerging from a Borda mouthpiece; and it establishes some nomenclature. It is well-known that an elementary momentum balance specifies the coefficient of contraction, C_c, (the ratio of the cross-sectional area of the jet to that of the hole) in the following way:

$$C_c = 1/(2C_v{}^2) \tag{1}$$

where C_v is the "coefficient of velocity" or the ratio of the jet velocity to $\sqrt{2gh}$.

Good C_c data for the Borda mouthpiece are very hard to find. The values of 0.5149 (Borda), 0.5547 (Bidone), and 0.5324 (Weisbach) quoted in [1]–without references and without giving the dimensions or proportions of the tube–appear to be the bases upon which textbooks normally quote values between 0.52 and 0.54. It is customary to rationalize a value of $C_c > 0.50$ using equation (1) with an assumed C_v between 0.98 and 0.96.

While the shortage of C_c data clearly reflects the limited practical importance of the Borda mouthpiece, two issues in this matter do merit our attention. One is that of questioning the validity of the routinely-taught momentum balance. The other is that of checking the common implication that substantial mechanical energy is dissipated in conventional orifices.

In 1984 Lienhard V and Lienhard (IV) [2] showed that C_v for a sharp-edged orifice is so close to unity that we can practically forget about any energy dissipation in such discharges. They also noted that, although they did not calculate the dissipation in a Borda mouthpiece, it would certainly be even less than in a sharp edged orifice. Consequently one must look elsewhere than to C_v for the explanation of C_c's greater than 1/2.

The other place where people often look for the cause of the higher value of C_c is in manufacturing imperfections in the lip of the mouthpiece. However, one is hard pressed to see how minor alternations of the lip could affect the momentum balance calculation in any way[2].

We therefore ask how the momentum balance argument itself could fail. A key assumption in the argument is that the liquid is stagnant on the support wall (see Fig. 1.). However, it is clear that there *is* some liquid movement on the wall, and that it must decrease as the length, L, of the mouthpiece is increased. Liquid motion reduces the pressure on the wall; consequently the jet momentum must increase to compensate for it. Since the velocity is constant, it is the area of the jet that must increase.

Our objective is thus to measure C_c as a function of the ratio L/D. The result should verify or deny two matters that we have suggested above. 1) If liquid movement parallel with the support wall affects C_c, then C_c should decrease toward an asymptote as L/D becomes large. 2) If C_v is virtually unity, then that asymptote should be 1/2.

Experiment

Experimental Design. Figure 1 shows the Borda mouthpiece we designed to measure C_c. The apparatus was manufactured entirely from plexiglass. The support wall shown in the figure forms the bottom of 154 cm vertical supply tube with a 15.2 cm inside diameter, which is not shown.

---

[1] Heat Transfer/Phase-Change Laboratory, Mechanical Engineering Department, University of Houston, Houston, Texas 77004. Mr. Wei-guo Dong is a Visiting Scientist on leave from the Thermal Power Engineering Research Institute, Xi-an, Peoples' Republic of China. Professor Lienhard is a Fellow ASME.

Contributed by the Fluids Engineering Division of The American Society of Mechanical Engineers. Manuscript received by the Fluids Engineering Division, July 9, 1985.

[2] We are indebted to A. Degani who triggered this inquiry by questioning the machining argument on this basis, when it was offered in a fluid mechanics class.

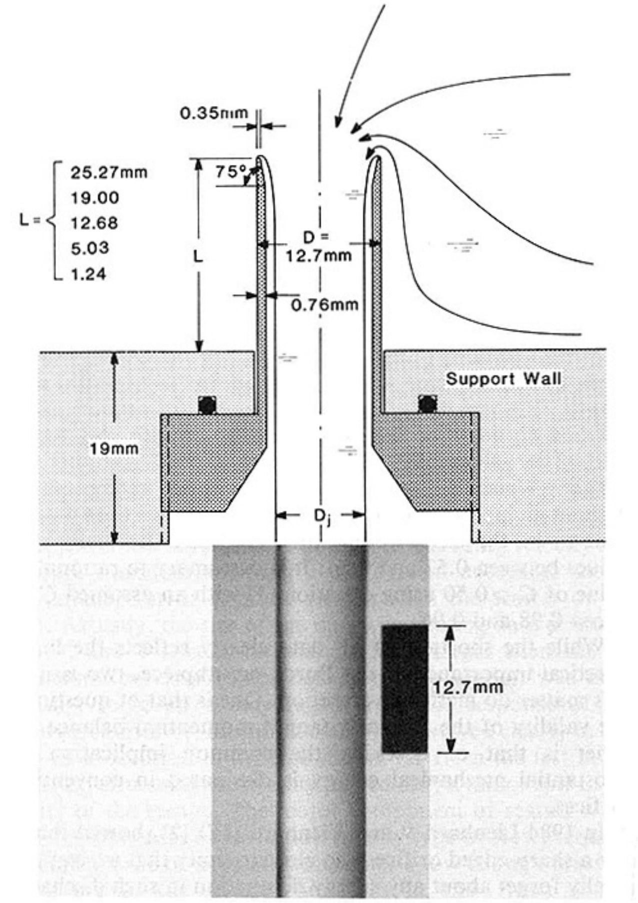

Fig. 1 Borda mouthpiece configuration used in the experiments, and a typical experimental photograph

The five Borda mouthpieces – each of a different length – were separate inserts as shown. Each had a nominal outside diameter of 1.27 cm. Since plexiglass expands by about 0.2 percent when it is wet, actual data are based on the measured outside diameter of the *wet* mouthpieces. The lip of each mouthpiece was examined under a powerful magnifying glass before it was used, and found to be free of perceptible defects.

Tap water was supplied through an overhead tray at the top of the supply tube. All of the jets filled the Borda tube under normal conditions. The separated jet flow pattern had to be initiated by blowing compressed air into the lip region through a small straw[3].

Two kinds of experiment were made. In one, contraction coefficients were obtained from still photographs of the discharging jets, by comparing the jet diameter in the picture with a 1.27 cm marker (which can be seen in the photographic portion of Fig. 1.) All photographs were made after allowing the water several hours of stilling to get rid of air bubbles. We discovered that air bubbles coming out of solution would cling to the lip of the mouthpiece and deform the jets. Stilling the water eliminated most of these bubbles and yielded a higher fraction of perfectly shaped jets.

About 20 photos were made for each mouthpiece. Just over half of these had to be rejected because of deformities in the jet. The probable error of C_c was 1.3 percent. The standard error of the repeated measurements varied slightly, since data were obtained at different heads in each case; but it averaged 1.2 percent which is, predictably, almost the same.

In the second experiment, the loss of liquid from the supply tube was observed as a function of time during draining, and the discharge coefficient, C_D, was obtained from these data. The supply tube was drained from an initial head, to each of about five lower values of head, for each mouthpiece. Each of these 25 points was replicated about 10 times. The probable error of these measurements averaged 0.83 percent.

We made most of these measurements without letting the water stand for hours. But when we did let it stand, C_D was the same within 0.4 percent or less. Nevertheless, these are time-averaged data and, during part of the time in all cases, the jets exhibited imperfections. Therefore these data are less trustworthy than the C_c observations even though their probable error is less.

The velocity coefficients, $C_v = C_D/C_c$, obtained from the data did not deviate significantly or consistently from unity, which bears out the assertion that $C_v = 1$, made in [2]. We therefore take C_d and C_c data as being equivalent.

The ranges of Reynolds and Weber numbers in these tests were:

$$23{,}000 < \mathrm{Re} < 62{,}000 \text{ and } 800 < \mathrm{We} < 4000$$

These ranges, which arose entirely from the variability of h, had no discernable influence on C_c or C_D.

Corrections. The following corrections were applied to the observed jet diameters:

1) *Gravity Correction.* Combining the increase of jet velocity resulting from gravity with the continuity equation we obtain for the jet diameter uninfluenced by gravity, D_j:

$$D_j = (1 + a/2h)^{1/2} D_{j,\text{measured}} \tag{2}$$

where "a" is the distance from the position at which the measurement was made to the positon at which the jet originated, and h is the head above the mouthpiece. Jets that did not match equation (2) within the experimental error, over their length in the photographs, were deemed to be deformed and were rejected.

2) *The Location of the Origin of the Jet.* When a mouthpiece of finite size is located in a gravity field, the formation of the jet is smeared over a variable head region. Where the effective origin of the jet is located is not clear; however it should lie between the lip of the mouthpiece and the support wall.

The gravity correction gave the most consistent results among the various heads when zero head was taken to lie one third of the way from the lip to the support wall. We therefore refer the head to this point in each case. The variation of the value of C_c, as the zero head point for the correction was varied from the lip to the support wall, remained well within the probable error.

3) *Surface Tension.* We are indebted to T. B. Benjamin who made the calculation in the Appendix for us. It shows that the jet dilates slightly under the influence of surface tension. The observed values of C_c had to be reduced between 0.4 and 2 percent, on the average, on the basis of this correction.

Results and Discussion

The fully corrected C_c and C_D data re plotted against L/D in Fig. 2. (Since they are corrected for surface tension, these data represent the high We limit.) They show that C_c exceeds 0.5 when L/D is small, and that it falls off asymptotically toward 0.5 as L/D is increased. The sharp-edged orifice C_c is included at $L/D = 0$. (This is Medaugh-Johnson's [3] value of 0.595 for large We and Re.)

A very simple analytical model serves to illuminate this behavior. We approximate the flow on the support wall by imagining symmetrical sinks located at a distance, L from the

---

[3] We are grateful to Prof. T. B. Benjamin for drawing our attention to this technique, which is needed to operate a Borda mouthpiece.

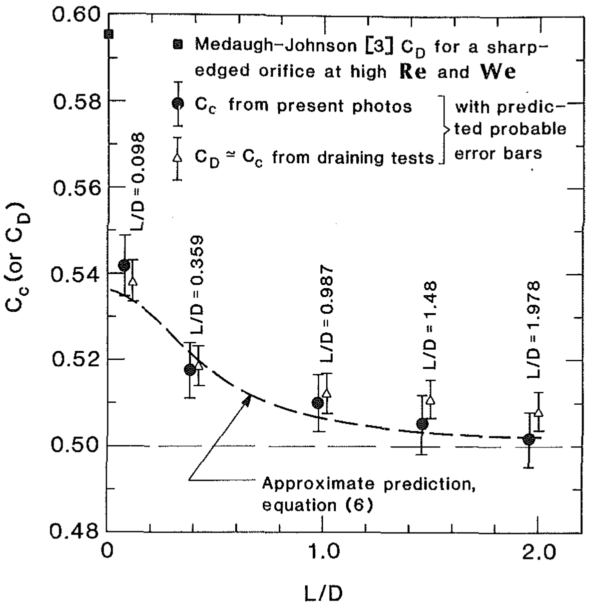

Fig. 2 Experimental results shown the influence of the mouthpiece configuration on contraction

wall on the jet centerline – that is, where the liquid enters the tube, and at its mirror image below. The velocity, u, parallel with the wall is then:

$$u = \frac{C}{(L^2 + r^2)} \tag{4}$$

where r is the radius in the plane of the wall and C is a constant. Then the pressure gradient on the wall is:

$$-\rho u \frac{du}{dr} = \frac{dp}{dr} = \frac{C_1 r}{(L^2 + r^2)^3} \tag{5}$$

where C_1 must be $\rho g h C_c^2 D^4/16$ to make the velocity consistent with the discharge rate.

We obtain C_c from equation (5) in the following way: We first integrate it to estimate the pressure force on a large circular segment of the support wall surrounding the hole of diameter, D. We then add the jet momentum force, $C_c(\pi D^2/4)\rho(2gh)$, to get the total force to the left. This must be balanced by the opposing pressure within the static liquid. Solving the result for C_c, we obtain:

$$C_c = M - (M^2 - M)^{1/2} \tag{6}$$

where $M = 4([2L/D]^2 + 1)$.

Equation (6) is included in Fig. 2. It is suprisingly close to the data, considering what a simplistic model it is. It makes it very clear that fluid movement on the wall is indeed the reason that observed values of C_c are above 1/2.

It is also important to note that neither this simple theory, nor the data, approach the sharp-edged orifice data point at the $L = 0$ limit. Once the tube is removed entirely, the transverse velocity component at $r = D/2$ discontinuously goes to $\surd 2gh$. But for any finite Borda tube, it will be less than this value.

Conclusions

1) Fluid motion on the support wall influences the magnitude of C_c for a finite Borda mouthpiece.
2) C_c for a Borda mouthpiece approaches 1/2 asymptotically as the length of the mouthpiece is increased. For a very short Borda mouthpiece, C_c is a little above 0.54.
3) The coefficient of velocity is virtually unity for a Borda mouthpiece, just as it is for a sharp-edged orifice.
4) The sharp-edged orifice is not the appropriate limit for a very short Borda mouthpiece.
5) The influence of surface tension on C_c for a Borda jet is given by equation (A4).

References

1 *Encyclopaedia Britannica*, 11th ed., Encylopaedia Britannica Inc., New York, *1911, Article on "Hydraulics," pp. 38-56.*

2 Lienhard, J. H., V and Lienhard, J. H., (IV), "Velocity Coefficients of Free Jets from Sharp-Edged Orifices," ASME JOURNAL OF FLUIDS ENGINEERING, Vol. 106, No. 1, 1984, pp. 13-17.

3 Medaugh, F. W., and Johnson, G. D., "Investigation of the Discharge Coefficients of Small Circular Orifices," *Civil Engr.*, Vol. 7, No. 7, 1940, pp. 422-4.

APPENDIX

Influence of Surface Tension on C_c for a Borda Mouthpiece
A Calculation by

T. B. Benjamin, Sedleian Prof. of Natural History
Mathematical Institute
Oxford University

The Bernoulli equation between the stagnant liquid at gauge pressure, ρgh, in the supply tube and the liquid in the jet, is:

$$\rho gh = p + \rho u^2/2 \tag{A1}$$

where the static gauge pressure in the jet is given by the Laplace relation as:

$$p = \frac{\sigma}{(\sqrt{C_c}D/2)} \tag{A2}$$

Neglecting fluid motion on the support wall as being of second order in importance, we write the following momentum balance:

Force on static fluid = momentum of jet
– surface force on the lip
– surface force on the jet.

or:

$$\pi(D^2/4)\rho gh = \pi(C_c D^2/4)[\rho u^2 + \sigma/(\sqrt{C_c}D/2)] - \pi\sqrt{C_c}D\sigma - \pi D\sigma \tag{A3}$$

Substituting equation (A2) in (A1), solving for ρu^2, and using the result in equation (A3), we get a quadratic equation in $\sqrt{C_c}$. Its positive root yields:

$$C_c = \frac{1}{2} + (1 + 3/2\sqrt{2})\,\frac{4}{\mathrm{We}} \tag{A4}$$

after we neglect terms of higher than first degree in (1/We). This result is accordingly limited to We greater than the order of 100. It is also limited to such We's by the fact that the correction is assumed small enough to be superposed additively on the ideal flow.

Prediction of Stack Plume Downwash

F. B. Tatom[1]

Introduction

Downwash in the wake of smokestacks and cooling towers has been a subject of investigation for more than 50 years [1]. The phenomenon occurs when the emerging positively

---

[1] Engineering Analysis, Inc., Huntsville, Ala. 35801

Contributed by the Fluids Engineering Division of THE AMERICAN SOCIETY OF MECHANICAL ENGINEERS. Mauscript received by the Fluids Engineering Division August 15, 1985.

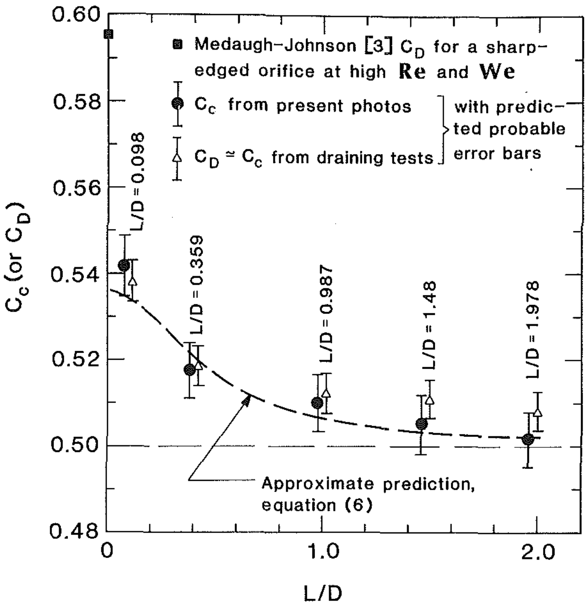

Fig. 2 Experimental results shown the influence of the mouthpiece configuration on contraction

wall on the jet centerline – that is, where the liquid enters the tube, and at its mirror image below. The velocity, u, parallel with the wall is then:

$$u = \frac{C}{(L^2 + r^2)} \tag{4}$$

where r is the radius in the plane of the wall and C is a constant. Then the pressure gradient on the wall is:

$$-\rho u \frac{du}{dr} = \frac{dp}{dr} = \frac{C_1 r}{(L^2 + r^2)^3} \tag{5}$$

where C_1 must be $\rho g h C_c^2 D^4/16$ to make the velocity consistent with the discharge rate.

We obtain C_c from equation (5) in the following way: We first integrate it to estimate the pressure force on a large circular segment of the support wall surrounding the hole of diameter, D. We then add the jet momentum force, $C_c(\pi D^2/4)\rho(2gh)$, to get the total force to the left. This must be balanced by the opposing pressure within the static liquid. Solving the result for C_c, we obtain:

$$C_c = M - (M^2 - M)^{1/2} \tag{6}$$

where $M = 4([2L/D]^2 + 1)$.

Equation (6) is included in Fig. 2. It is suprisingly close to the data, considering what a simplistic model it is. It makes it very clear that fluid movement on the wall is indeed the reason that observed values of C_c are above 1/2.

It is also important to note that neither this simple theory, nor the data, approach the sharp-edged orifice data point at the $L = 0$ limit. Once the tube is removed entirely, the transverse velocity component at $r = D/2$ discontinuously goes to $\sqrt{2gh}$. But for any finite Borda tube, it will be less than this value.

Conclusions

1) Fluid motion on the support wall influences the magnitude of C_c for a finite Borda mouthpiece.
2) C_c for a Borda mouthpiece approaches 1/2 asymptotically as the length of the mouthpiece is increased. For a very short Borda mouthpiece, C_c is a little above 0.54.
3) The coefficient of velocity is virtually unity for a Borda mouthpiece, just as it is for a sharp-edged orifice.
4) The sharp-edged orifice is not the appropriate limit for a very short Borda mouthpiece.
5) The influence of surface tension on C_c for a Borda jet is given by equation (A4).

References

1 *Encyclopaedia Britannica*, 11th ed., Encylopaedia Britannica Inc., New York, *1911, Article on "Hydraulics," pp. 38-56.*

2 Lienhard, J. H., V and Lienhard, J. H., (IV), "Velocity Coefficients of Free Jets from Sharp-Edged Orifices," ASME Journal of Fluids Engineering, Vol. 106, No. 1, 1984, pp. 13-17.

3 Medaugh, F. W., and Johnson, G. D., "Investigation of the Discharge Coefficients of Small Circular Orifices," *Civil Engr.*, Vol. 7, No. 7, 1940, pp. 422-4.

APPENDIX

Influence of Surface Tension on C_c for a Borda Mouthpiece A Calculation by

T. B. Benjamin, Sedleian Prof. of Natural History
Mathematical Institute
Oxford University

The Bernoulli equation between the stagnant liquid at gauge pressure, ρgh, in the supply tube and the liquid in the jet, is:

$$\rho g h = p + \rho u^2/2 \tag{A1}$$

where the static gauge pressure in the jet is given by the Laplace relation as:

$$p = \frac{\sigma}{(\sqrt{C_c}D/2)} \tag{A2}$$

Neglecting fluid motion on the support wall as being of second order in importance, we write the following momentum balance:

Force on static fluid = momentum of jet
– surface force on the lip
– surface force on the jet.

or:

$$\pi(D^2/4)\rho g h = \pi(C_c D^2/4)[\rho u^2 + \sigma/(\sqrt{C_c}D/2)] - \pi\sqrt{C_c}D\sigma - \pi D\sigma \tag{A3}$$

Substituting equation (A2) in (A1), solving for ρu^2, and using the result in equation (A3), we get a quadratic equation in $\sqrt{C_c}$. Its positive root yields:

$$C_c = \frac{1}{2} + (1 + 3/2\sqrt{2})\frac{4}{\text{We}} \tag{A4}$$

after we neglect terms of higher than first degree in (1/We). This result is accordingly limited to We greater than the order of 100. It is also limited to such We's by the fact that the correction is assumed small enough to be superposed additively on the ideal flow.

Prediction of Stack Plume Downwash

F. B. Tatom[1]

Introduction

Downwash in the wake of smokestacks and cooling towers has been a subject of investigation for more than 50 years [1]. The phenomenon occurs when the emerging positively

---

[1] Engineering Analysis, Inc., Huntsville, Ala. 35801

Contributed by the Fluids Engineering Division of The American Society of Mechanical Engineers. Mauscript received by the Fluids Engineering Division August 15, 1985.

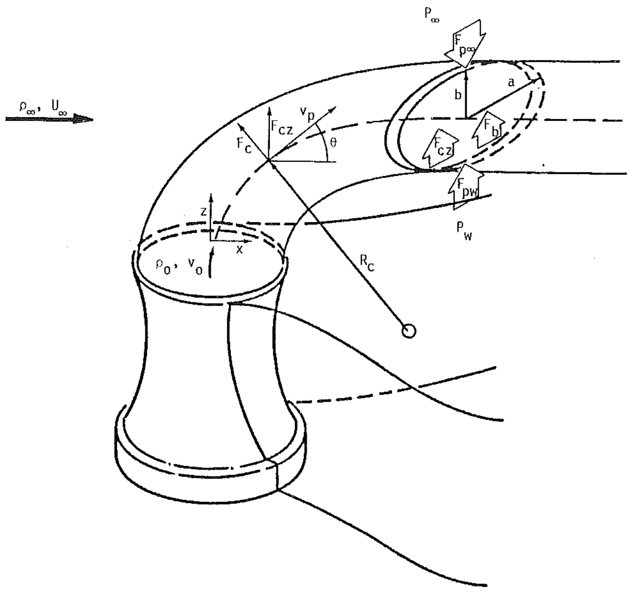

Fig. 1 Dynamics for downwash

buoyant plume becomes entrapped in the wake produced by the wind flowing around the stack or tower from which the plume originated, or in the wake produced by some other nearby building or terrain obstruction. In the current study the objective has been to provide a means of predicting the presence of downwash resulting from the wake *due to the stack*, over a wide range of Froude numbers.

As noted previously [2], most of the studies dealing with downwash have involved either experimental measurements or field observations. The general consensus resulting from such studies has been that for Froude numbers greater than ~ 1.0, to avoid downwash, the ratio of exit velocity to wind velocity should be greater than 1.5 [3]. The observation has been made, however, that for smaller Froude numbers, a smaller value of this velocity ratio should be sufficient [4].

In a relatively recent study by Overcamp [5] all available downwash data were plotted in the form of velocity ratio versus Froude number. The plotted data were correlated by means of an empirical curve, which was consistent with the two basic observations noted in the preceding paragraph.

Based on the results of previous studies it would appear that while there has been considerable measurement and observation involving downwash, a basic understanding of the forces causing this phenomena has not been developed.

Technical Development

The analytical model is based on the premise that *if downwash is to occur the interaction between the plume and wake must commence immediately downstream of the stack or tower.* As indicated in Fig. 1, in the region of interest, four forces (per unit length) are considered to be acting on the plume. The vertical forces due to buoyancy, F_b, centrifugal effects, F_{cz}, and wake pressure, F_{pw}, act in the upward direction, while the ambient pressure force, $F_{p\infty}$, is directed downward. In order for downwash to occur, the net downward pressure force must exceed the combined buoyancy and centrifugal forces or

$$F_{p\infty} - F_{pw} > F_{cz} + F_b \tag{1}$$

As reported by several investigators [6, 7], the cross-section of the plume is kidney-shaped. For simplicity, this shape is approximated by an ellipse with a major axis dimension of $2a$ and a minor axis dimension of $2b$, as indicated in the figure. With this shape, the net pressure force can be written as

$$F_{p\infty} - F_{pw} = (P_\infty - P_w)(2a) \tag{2}$$

The wake pressure, P_w, is assumed to be equal to the pressure on the tower perimeter at the point of separation, P_{sep}. Based on potential flow theory, with viscous drag neglected, P_{sep} can be related to the drag coefficient of the structure, C_D, and thus

$$\begin{aligned} P_w &= P_{\text{sep}} \\ &= P_\infty + \frac{\rho_\infty U_\infty^2}{2}\left[1 - (3C_D)^{2/3}\right] \end{aligned} \tag{3}$$

The net pressure force (acting downward) becomes

$$F_{p\infty} - F_{pw} = \frac{\rho_\infty U_\infty^2}{2}\left[(3C_D)^{2/3} - 1\right](2a) \tag{4}$$

The force due to buoyancy can be written

$$F_b = (\rho_\infty - \rho_p) g \pi a b \tag{5}$$

The vertical component of centrifugal force, as depicted in Fig. 1, is described by the relation

$$F_{cz} = \pi a b \rho_p v_p^2 \cos\theta / R_c(x) \tag{6}$$

The region of interest occurs at $x = D_0/2$ and is thus within the *momentum-dominated near field.* In such a region, based on previous trajectory analysis of deflected buoyant plumes [8], the radius of curvature of the plume centerline $R_c(x)$ can be expressed as

$$R_c(D_0/2) = 2D_0(1 + B^2/4)^{3/2}/B \tag{7}$$

and

$$\cos\theta = 1/\sqrt{1 + B^2/4} \tag{8}$$

where

$$B \equiv R^*/\sqrt{\beta + \alpha R^*} \tag{9}$$

and

$$R^* \equiv \sqrt{\rho_0/\rho_\infty}\, v_0/U_\infty \tag{10}$$

The empirical constants α and β appear in a number of different studies dealing with the behavior of buoyant plumes, and a variety of values have been proposed for each such constant. In the current study

$$\alpha = 0.15$$

and

$$\beta = 0.9,$$

consistent with the values proposed in the original trajectory analysis [8].

As noted previously, the plume cross-section is assumed to be elliptical in shape. For simplicity, and because of the short distance from the exit plane, the area of this cross-section is taken to be equal to that of the exit plane. Based on conservation of mass and geometric considerations, the dimension ($2b$) of the minor axis of the ellipse was taken as a function of the jet exit diameter, D_0, and the parameter, B, according to the relation

$$2b = D_0\left[1 - \exp(-B^2)/2\right] \tag{11}$$

Consistent with equation (11), the major axis dimension can be expressed as

$$2a = D_0/\left[1 - \exp(-B^2)/2\right] \tag{12}$$

When equation (12) is combined with equation (4), the final relation for the net pressure force is

$$F_{p\infty} - F_{pw} = \rho_\infty U_\infty^2\left[(3C_D)^{2/3} - 1\right] D_0/2A \tag{13}$$

where

$$A \equiv 1 - \exp(-B^2)/2 \tag{14}$$

The velocity of the plume, v_p, with entrained mass neglected, is taken to be equal to the exit velocity, v_0, and likewise the density, ρ_p, at the point of interest is assumed equal to the exit density, ρ_0. When these approximations, along with equations (11) and (12) are combined with equation (5), the final result for the buoyancy force is

$$F_b = (\rho_\infty - \rho_0) g \pi D_0^2/4 \tag{15}$$

Equations (7), (8), (11), and (12), along with the same approximations concerning velocity and density as before, when combined with equation (6), produce the final relation for the centrifugal force,

$$F_{cz} = \pi D_0 \rho_0 v_0^2 (2B)/(4+B^2)^2 \tag{16}$$

Based on a combination and rearrangement of equations (1), (13), (15) and (16), the final expression in dimensionless form for the existence of downwash is

$$R^* < \sqrt{\frac{[(3C_D)^{2/3} - 1]}{\pi A [\mathrm{Fr}_0^{-2} + 4B/(4+B^2)^2]}} \tag{17}$$

where

$$\mathrm{Fr}_0 \equiv v_0 \Big/ \sqrt{\left(\frac{\rho_\infty - \rho_0}{\rho_0}\right) g D_0/2} \tag{18}$$

Results

As noted previously, Overcamp [5] has recently provided a compilation of downwash data from a number of different sources, along with an empirical correlation of such data. Although not precisely known, the drag coefficients for the various structures associated with these data would very likely be in the range of 0.4 to 1.2. All of the data noted, including the empirical correlation, are presented in Fig. 2. Also presented in Fig. 2 are the curves produced by the current model corresponding to equation (17), for the range of values of C_D noted. These curves are most encouraging, in that they appear to generally bracket the interface between the data denoting downwash and that denoting its absence. The curve corresponding to $C_D = 1$ strongly resembles Overcamp's recent empirical correlation. Of special significance is the fact that, with a C_D of 1, as the Froude number increases to large values (>10), the critical speed ratio approaches a constant value on the order of 1.5.

Examination of equation (17) indicates that, with $C_D = 1$ for Froude numbers less than ~0.8, the balance of forces is primarily between net pressure and buoyancy, and for this case equation (17) reduces to

$$R^* < \mathrm{Fr}_0 \sqrt{[(3C_D)^{2/3} - 1]/\pi A} \tag{19}$$

In the range of Froude numbers between ~0.8 and ~8.0, centrifugal and buoyancy forces are jointly involved in balancing the net pressure force and the complete version of equation (17) is necessary. For Froude numbers greater than ~0.8, the balance of forces is largely between net pressure and centrifugal forces, and under this condition equation (17) can be reduced to

$$R^* < \left(\frac{4+B^2}{2}\right) \sqrt{[(3C_D)^{2/3} - 1]/\pi A B} \tag{20}$$

Thus, downwash can be pictured as occurring in three separate regimes as indicated in Fig. 3. This result is consistent with the qualitative description provided by Briggs [4].

Conclusions

A simple explanation for downwash in terms of a balance of forces has been demonstrated to correlate all available data quite satisfactorily. The correlation is in basic agreement with,

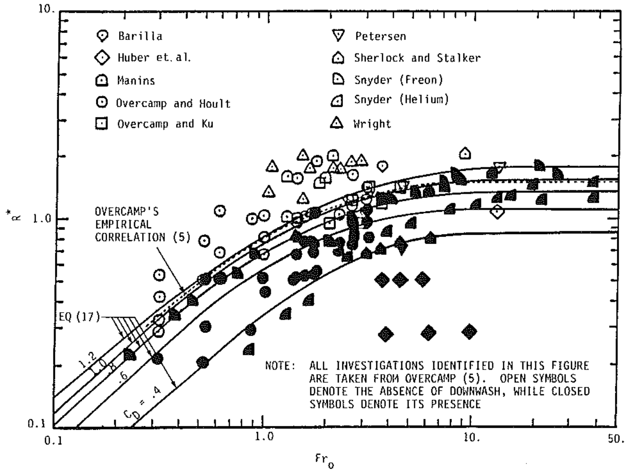

NOTE: ALL INVESTIGATIONS IDENTIFIED IN THIS FIGURE ARE TAKEN FROM OVERCAMP (5). OPEN SYMBOLS DENOTE THE ABSENCE OF DOWNWASH, WHILE CLOSED SYMBOLS DENOTE ITS PRESENCE

Fig. 2 Correlation of downwash data

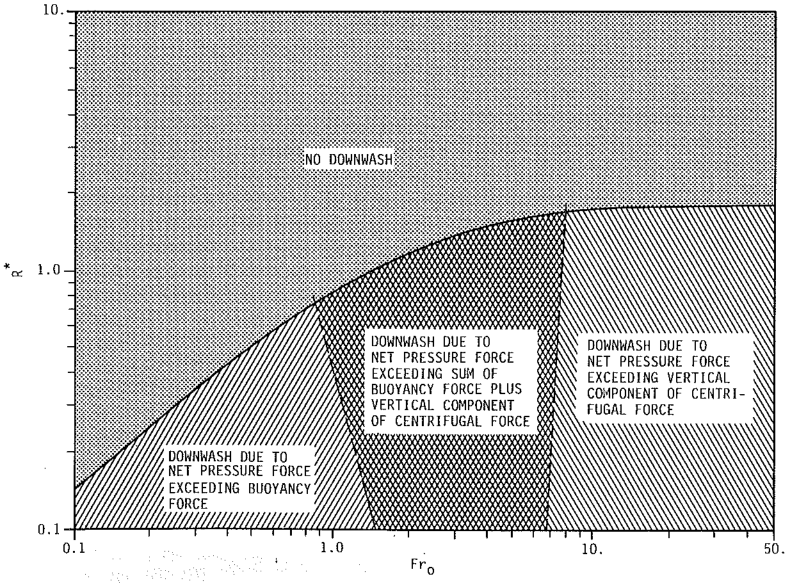

Fig. 3 Downwash regimes

and also explains the rule of thumb that the ratio of exit velocity to wind velocity should be greater than 1.5 to avoid downwash.

The use of the drag coefficient of the structure in the correlation appears of special significance, in that it provides a means of explaining how for a given Froude number, downwash can occur at different velocity ratios for different structures. Because of a lack of detailed drag coefficient information for the various data points collected by Overcamp [5], however, such an explanation cannot be totally accepted at this time. Further study pertaining to the effects of drag coefficients on downwash should be carried out to resolve the matter.

Acknowledgments

This study was funded by the Water Systems Development Branch, Tennessee Valley Authority, under contract TV-49113A.

References

1 Committee Appointed by the Electricity Commissioners, "The Measures Which Have Been Taken in This Country and in Others to Obviate the Emission of Soot, Ash, Grit and Gritty Particles from the Chimneys of Electric Power Stations," Her Majesty's Stationery Office, London, 1932.

2 Tatom, F. B., "Prediction of Downwash," *International Symposium on Modeling Environmental Flows*, Joint ASCE/ASME Mechanics Conference, Albuquerque, New Mexico, June 24-26, 1985.

3 Sherlock, R. H., and Stalker, E. A., "The Control of Gases in the Wake of Smokestacks," *Mechanical Engineering*, Vol. 62, 1940, p. 455.

4 Briggs, G. A., "Plume Rise," *USAEC Report TID-25075*, Environmental Science Services Administration, 1969, pp. 1-69.

5 Overcamp, T. J., "Guidelines for Stack Downwash in Plume Modeling Experiments," *Paper 83-36-3*, 76th Annual Meeting of the Air Pollution Control Association, Atlanta, GA, June 19-24, 1983.

6 Shandorov, G. S., "Flow from a Channel into Stationary and Moving Media," *Zhurnal Teknicheskoi Fiziki*, Vol. 27, No. 1, 1957.

7 Keffler, J. F., and Baines, W. D., "The Round Turbulent Jet in a Cross-Wind," *Journal of Fluid Mechanics*, Vol. 15, Part 4, 1963, pp. 481-496

8 Hoult, D. P., Fay, J. A., and Forney, L. J., "A Theory of Plume Rise Compared with Field Observations," *Journal of the Air Pollution Control Association*, Vol. 19, No. 8, Aug. 1969, pp. 585-590.

Journal of Fluids Engineering Discussion

Effect of Vibrating Upstream Cylinder of Two Circular Cylinders in Tandem Arrangement[1]

M. M. Zdravkovich.[2] The authors are to be complimented for a simple experimental study which revealed a large effect of extremely small amplitudes of an oscillating upstream cylinder on the flow around a stationary downstream cylinder. The most important or primary effect is presumably the influence of the forced oscillation of the upstream cylinder on the flow within the gap between the cylinders. This primary effect causes a secondary effect, that is, the change over of flow regimes around the downstream cylinder. The authors concentrated their experimental study only on the secondary effect and the physical picture of the phenomena involved remained incomplete.

The main feature of a flow around two parallel stationary cylinders arranged in tandem with a spacing ratio $l/d < 3.5$ is that the vortex street cannot be formed behind the upstream cylinder. The free shear layers emanating from the upstream cylinder reattach onto the downstream cylinder. The reattachment produces characteristic peaks in C_p and C_p' at $\theta = 50$ deg as seen in Figs. 5 and 7. The reattached shear layers are turbulent and trip a turbulent boundary layer around the downstream cylinder characterised with a delayed separation at $\theta = 120$ deg (see inflection point of the C_p curve in Fig. 5 and the second C_p' peak in Fig. 7). The delayed separation produces a narrow nearwake which in turn means low drag coefficient, see Fig. 6. It is totally unexpected that such a postcritical, narrow nearwake behind the stationary downstream cylinder could produce an excessive fluctuating lift as found by Arie et al. [2] and confirmed by the authors in Figs. 8 and 9. My comments will be directed towards resolving that puzzle.

The authors proposed that the transverse forced oscillation of the upstream cylinder triggered the "*synchronized*" vortex shedding. The analogy with the synchronization caused by an oscillating single cylinder is not as straightforward as implied by the authors and requires experimental verification which was not given. There are two important differences between the '*synchronization*' behind the upstream cylinder and the synchronization behind the single cylinder. They are as follows:

(i) No vortex shedding was found behind the stationary upstream cylinder for $l/d < 3.5$. When the upstream cylinder is forced to oscillate the *synchronized* vortex shedding is not affected by a tendency of natural vortex shedding at constant Strouhal number.

(ii) There is a threshold amplitude of oscillation $(a/d_{\min}) = .04$ to $.05$ required to initiate the synchronization behind the single cylinder [13]. The range of amplitudes used by the authors was $0 < a/d < 0.029$ which is well below $(a/d)_{\min}$. Hence it looks plausible to look for another explanation of the observed *secondary* effect.

The crucial difference between the nearwakes behind the upstream and single cylinder is that the former is *stable and symmetric* the latter is *unstable and periodic*. Figure 10 taken by Ishigai et al. [14] is the Schlieren image of the flow around two cylinders in tandem arrangement for $l/d = 3$ at $\mathrm{Re} = 3.9 \times 10^3$. The free shear layers gradually roll up into large vortices arranged *symmetrically* relative to the wake axis. The instability of the free shear layers is enhanced by their retardation caused by the downstream cylinder and their subsequent reattachment, as observed in laminar wakes [15, 16]. The instability initiates *in phase* oscillations on both sides of the cylinder and preserves the symmetrical arrangement as found for a single cylinder by Gerrard [17]. If the upstream cylinder is forced to oscillate even at a very small amplitude the free shear layers are disturbed asymmetrically and the initiation of instability is *out-of-phase* on the two sides of the cylinder. This leads to an alternate arrangement of rolled-up vortices which resembles the flow regime for $l/d > 3.5$ behind two stationary cylinders.

The authors found that for $l/d = 3.0$ a bistable range of threshold amplitudes $0.007 < a/d < 0.015$ where either symmetric or alternate arrangement of vortices caused a discontinuous jump or fall in C_D from -0.05 to 0.4, Fig. 6 and in C_L from 0.5 to 0.9, Fig. 8. It is unfortunate that the authors drew smooth curves between experimental points and did not include points related to both regimes in the bistable range. The unexpected second mode of *synchronization* at $f_h/f_k = 1.24$ may be attributed to the instability of free shear layers and should strongly depend on l/d. The authors tested $l/d = 2$ but did not state whether the second mode of synchronization was found. It might be mentioned that Igarashi [18] found another kind of *synchronization* for $1.2 < l/d < 1.6$ which affected the alternate reattachment of free shear layers.

Another puzzling feature is the 'abnormally' high value of C_L measured by Arie et al. [2] and by the authors. Figure 11 reproduced from [19] shows the formation of laminar vortex streets behind the upstream and downstream cylinder for $l/d = 8$. The visible smoke represents free shear layers and it is evident that the second vortex street absorbed all the vorticity

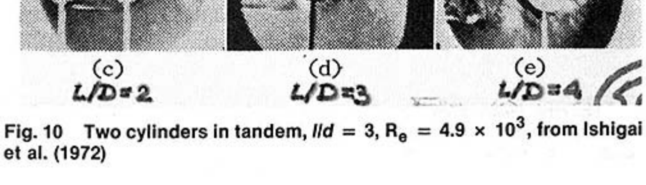

Fig. 10 Two cylinders in tandem, $l/d = 3$, $R_e = 4.9 \times 10^3$, from Ishigai et al. (1972)

---

[1] By M. Moriya and H. Sakamoto published in the June 1986 issue of the JOURNAL OF FLUIDS ENGINEERING, Vol. 108, pp. 180–185.

[2] University of Salford, Salford, U.K. Mem. ASME.

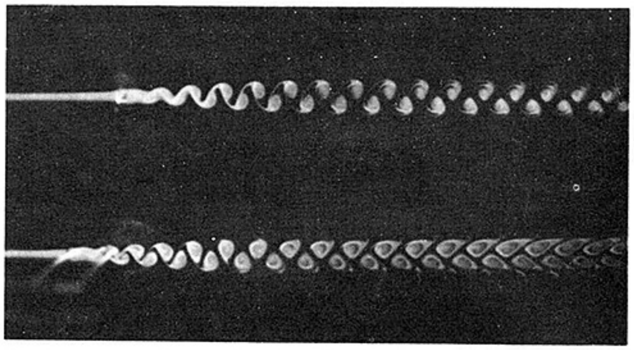

Fig. 11 Two cylinders in tandem $l/d = 8$, $R_e = 92$ from Zdravkovich (1972)

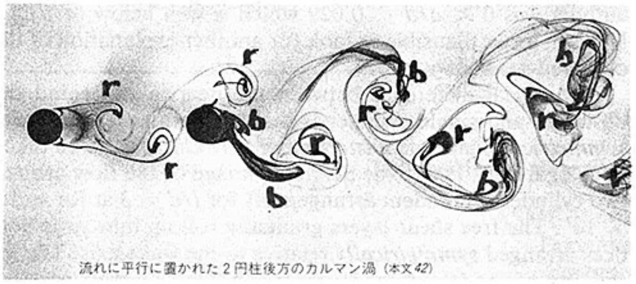

Fig. 12 Two cylinders in tandem $l/d = 5$, $R_e = 10^4$ from Nakayama et al. (1984)

generated by the upstream cylinder. Figure 12 is originally made in color [20] with red dye issued from the upstream cylinder and blue dye from the downstream cylinder. The original color of vortices is marked with *r* and *b*, respectively. Figure 12 reveals that the *r* vortices formed behind the upstream cylinder pair with *b* vortices behind the downstream cylinder in such a way that a *binary* vortex street* is formed.

The measured variation of C_L' with l/d by the authors shown in Fig. 9, can be explained in terms of the strength of binary vortices. They are strongest at $l/d = 3.5$ for stationary cylinders when vortex shedding has just initiated behind the upstream cylinder. The viscous decay and turbulent dissipation gradually weakens the upstream vortices as l/d increases and the strength of the binary vortices decreases asymptotically towards the strength of an ordinary vortex. The oscillating upstream cylinder triggers vortex formation for $l/d < 3.5$ and the binary vortices induce a significant additional C_L' related to the value of a/d as seen in Fig. 9. It is evident in Fig. 8 that for $l/d = 3$ the second mode of *synchronization* at $f_h/f_k = 1.24$ produces stronger binary vortices.

Finally it might be interesting to note that another kind of vortex pairing was observed around the circular cylinder in waves subjected to an oscillatory flow [21, 22]. The vortices formed behind the cylinder during the first half of the wave cycle are carried back around the cylinder by the flow reversal during the second half of the wave cycle. The reversed vortex is paired with a newly formed vortex with opposite circulation. Figure 13 shows the vortex pair at the end of the wave cycle moving away from the cylinder by a self-induced velocity. Despite a significant distortion of streamlines the opposite sign of circulation of two vortices results in the cancellation of the overall circulation. Contrary to that the binary vortex consists of two vortices with the same circulation and the overall circulation is equal to the sum of the two. It seems that these

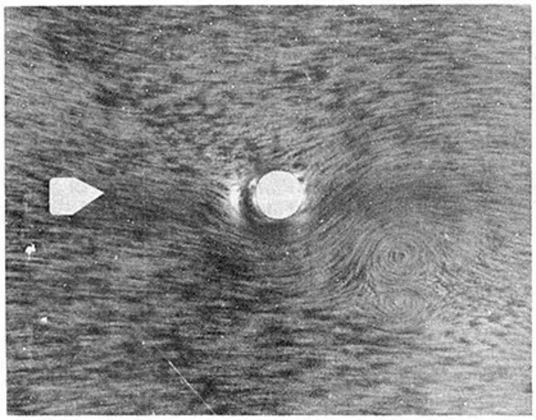

Fig. 13 Fully formed vortex pair, $K_c = 5.3$ (K_c = Keulegen-Carpenter number) from Zdravkovich and Namork (1977)

two intrinsically different kinds of vortex pairing require distinctly different terms as proposed herewith. The most important practical aspect is the suppression of vortex induced oscillation which has been achieved by a variety of means [23]. A significant reduction of the means effectiveness is found for two cylinders in tandem [25] due to interference regimes.

References

13 Zdravkovich, M. M., "Modification of Vortex Shedding in the Synchronisation Range," ASME JOURNAL OF FLUIDS ENGINEERING, Vol. 104, No. 4, 1982, pp. 513-517.

14 Ishigai, S., Nishikawa, E., Nishimura, K., and Cho, K., "Experimental Study on Structure of Gas Flow in Tube Banks with Tube Axes Normal to Flow, Part 1; Karman Vortex Flow Around Two Tubes at Various Spacings," *Bull. Japan Society Mechanical Engineers*, Vol. 15, No. 86, 1972, pp. 949-956.

15 Zdravkovich, M. M., "Smoke Observations of the Wake of a Group of Three Cylinders at Low Reynolds Number," *Journal Fluid Mechanics*, Vol. 32, Part 2, 1968, pp. 339-351.

16 Durgin, W. W., and Karlsson, S. K. F., "On the Phenomenon of Vortex Street Breakdown," *Journal Fluid Mechanics*, Vol. 48, 1971, pp. 507-527.

17 Gerrard, G. H., "The Wakes of Cylindrical Bluff Bodies at Low Reynolds Number," *Philosophical Trans. Royal Society* (London), Series A, Vol. 288, 1978, p. 351-382.

18 Igarashi, T., "Characteristics of the Flow Around Two Circular Cylinders Arranged in Tandem, 2nd Report: Unique Phenomenon at Small Spacings," *Bull. Japan Society Mechanical Engineers*, Vol. 27, 1984, pp. 2380-2337.

19 Zdravkovich, M. M., "Smoke Observations of Wakes of Tandem Cylinders at Low Reynolds Numbers," *The Aeronautical Journal*, Vol. 76, 1972, pp. 108-114.

20 Nakayama (ed. in chief), *Flow; a Photographic Album*, Published by JSME, Maruzen in Tokyo, 1984, in Japanese.

21 Zdravkovich, M. M., and Namork, J. E., "Formation and Reversal of Vortices around Circular Cylinder Subjected to Water Waves," *Proc. ASCE, Journal of Waterways etc.*, Vol. 103, No. WW3, 1977, pp. 378-383.

22 Williamson, C. H. K., "Sinusoidal Flow Relative to Circular Cylinders," *Journal Fluid Mechanics*, Vol. 155, 1985, pp. 141-174.

23 Zdravkovich, M. M., "Review and Classification of Various Aerodynamic and Hydrodynamic Means for Suppressing Vortex Shedding," *Journal Wind Engineering and Industrial Aerodynamics*, Vol. 7, 1981, pp.145-169.

24 Zdravkovich, M. M., "Reduction of Effectiveness of Means for Suppressing Wind Induced Oscillations," *Engineering Structures*, Vol. 6, 1984, pp. 344-349.

25 Williamson, C. H. K., "Evolution of a Single Wake Behind a Pair of Bluff Bodies," *Journal of Fluid Mechanics*, Vol. 159, 1985, pp. 1-18.

Authors' Closure

The authors are grateful to Dr. Zdravkovich for his thoughtful and valuable comments. We especially agree with the physical pictures suggested for our paper. When two stationary cylinders are arranged in tandem with a spacing ratio $l/d < 3.5$, a vortex street cannot be formed behind the upstream cylinder, as pointed out in their comments. Within

---

*The term *binary stars* is used in astronomy for two stars of different size in closed proximity rotating one around the other. This term in Fluid Mechanics context was introduced by Williamson [25].

this range of spacing ratio, the fluctuating pressures and lift forces acting on the downstream cylinder are synchronized by vibration of the upstream cylinder, and this phenomenon is also important. Therefore the present paper did not emphasize the "synchronized" vortex shedding. However, Dr. Zdravkovich's suggestion about binary vortices is useful for our paper. The authors tested spacings of $1/d = 2.0$ and 2.5 but the second mode of synchronization did not arise.